

ulm university universität

uulm

Carbon-based electrode materials in combined atomic force – scanning electrochemical microscopy (AFM-SECM)

DISSERTATION

zur Erlangung des Doktorgrades Dr. rer. nat.

der Fakultät für Naturwissenschaften der Universität Ulm

vorgelegt von

Alexander Eifert

aus Ulm

Ulm, 2015

Amtierender Dekan: Prof. Dr. Joachim Ankerhold

Erstgutachter: PD. Dr. Christine Kranz

Zweitgutachter: PD. Dr. Dr. Christoph Nebel

Tag der Promotion: 16.10.2015

„Fest und stark ist nur ein Baum, der unablässig Windstößen ausgesetzt war, denn im Kampf festigen und stärken sich seine Wurzeln“.

(Seneca; Römischer Philosoph)

Table of Contents

List of papers **8**

List of abbreviations **10**

List of figures **12**

List of tables **22**

1. Motivation and scope of this thesis **23**

2. Theory and state of the art **25**

2.1. Boron-doped diamond (BDD) **25**

2.1.1. Overview 25

2.1.1.1. Diamond growth and doping 26

2.1.1.2. Material properties of boron-doped diamond 28

2.1.2. Applications 31

2.2. Atomic force microscopy (AFM) **33**

2.2.1. Working principles 33

2.2.2. AFM modes 34

2.2.2.1. Contact mode 34

2.2.2.2. Non-contact mode 35

2.2.2.3. Intermittent mode 36

2.2.3. Combined AFM techniques 37

2.3. Scanning electrochemical microscopy (SECM) **38**

2.3.1. Fundamentals 38

2.3.2. SECM imaging modes 40

2.3.2.1. Feedback mode 40

2.3.2.2. Generation-collection mode 44

2.3.3. Applications of SECM 45

2.4. Combined AFM-SECM **46**

2.4.1. Fundamentals 46

2.4.2. Advantages compared to SECM 47

2.4.3. Applications of AFM-SECM 49

3. Electron transfer kinetics of FIB-irradiated BDD samples **50**

3.1. Introduction **50**

3.2. Results & Discussion **52**

3.2.1. Electrochemical characterization 52

3.2.2. Determination of the electron transfer rate constant ... 63
3.2.3. Surface characterization ... 69
3.2.3.1. AFM investigation ... 69
3.2.3.2. Raman spectroscopy ... 71
3.2.3.3. Electron backscatter diffraction (EBSD) investigation after electrochemical treatment ... 74
3.3. Conclusion & Outlook ... 76
4. Combined boron-doped diamond AFM-SECM probes ... 77
4.1. Introduction ... 77
4.2. Results & Discussion ... 78
4.2.1. Milling yield of boron-doped-diamond ... 78
4.2.2. Combined BDD-AFM-SECM probes ... 78
4.2.3. Electrochemical properties ... 80
4.2.4. Combined AFM-SECM measurements ... 83
4.3. Simulations ... 87
4.3.1. Simulated diffusion profiles and calculated currents ... 87
4.3.1.1. Simulated diffusion profiles for bulk conditions ... 88
4.3.1.2. Simulated diffusion profiles for feedback conditions ... 89
4.4. Conclusion & Outlook ... 91
5. Numerical simulations for top-mill-fabricated AFM-SECM probes ... 93
5.1. Introduction ... 93
5.2. Results & Discussion ... 94
5.2.1. Simulations of bulk conditions ... 94
5.2.2. Simulations of SECM feedback experiments ... 98
5.3. Conclusion ... 99
6. Improved signal-to-noise ratio using an integrated amplifier system ... 100
6.1. Introduction ... 100
6.2. Results & Discussion ... 101
6.2.1. Integrated signal transduction and amplification ... 101
6.2.2. Sealing the electrical contact ... 106
6.2.3. Pit formation on passivated iron samples ... 109
6.3. Conclusion & Outlook ... 119
7. Investigation of biological samples ... 120
7.1. Introduction ... 120
7.2. Results & Discussion ... 122
7.2.1. Investigation of supported lipid membranes with incorporated C2IIa heptameres ... 122

7.2.1.1. Supported lipid membrane formation 122
7.2.1.2. C2IIa toxin incorporation 127
7.2.1.3. Redox-mediator transport inhibition with chloroquine (CQ) 133
7.2.1.4. Limitation and improvements 136
7.2.2. Detection of dopamine at combined BDD-AFM-SECM probes in physiologically relevant conditions 137
7.2.2.1. Influence of ascorbic acid on the detection of dopamine 137
7.2.2.2. Detection of dopamine at H-terminated combined BDD-AFM-SECM probes 138
7.2.2.3. Dopamine detection at BDD microelectrode arrays 141
7.3. Conclusion & Outlook 142
8. Summary 144
9. Zusammenfassung 147
10. Experimental 150
10.1. Chapter 3 150
10.1.1. Chemicals and solutions 150
10.1.2. Apparatus 150
10.1.3. Procedures 152
10.1.4. Simulations 152
10.2. Chapter 4 153
10.2.1. Chemicals and solutions 153
10.2.2. Apparatus 153
10.2.3. Procedures 154
10.2.4. Simulations 156
10.2.4.1. Bulk conditions 156
10.2.4.2. Feedback conditions 158
10.2.4.3. CV Simulations 159
10.3. Chapter 5 159
10.3.1. Chemicals and solutions 159
10.3.2. Apparatus 160
10.3.3. Procedures 160
10.3.4. Simulations 160
10.3.4.1. Bulk conditions 160
10.3.4.2. Feedback conditions 161
10.4. Chapter 6 162
10.4.1. Chemicals and solutions 162
10.4.2. Apparatus 162
10.4.3. Procedures 163

10.4.4. Simulations 164
10.5. Chapter 7 164
10.5.1. Chemicals and solutions 164
10.5.2. Apparatus 165
10.5.3. Procedures 166
11. References 169
12. Appendix 192
12.1. List of chemicals and materials 192
12.2. List of equipment 193
12.3. Construction blue prints 194
12.3.1. Rotatable AFM-chip holder for FIB milling 194
12.3.2. Cartridge for mounting combined AFM-SECM probes 197
12.3.3. Glassware for hydrogen termination 198
12.3.4. Shadow mask for gold modification of AFM probes 199
Acknowledgements 206
Curriculum Vitae 208
Eidesstattliche Erklärung 213

List of papers

Parts of this thesis have already been published within the following publications and are reprinted with permission.

Peer-reviewed research articles

Alexander Eifert, Waldemar Smirnov, Stefan Frittmann, Christoph E. Nebel, Boris Mizaikoff, Christine Kranz; Atomic force microscopy probes with integrated boron-doped diamond electrodes: Fabrication and application, Electrochemistry Communications, 2012, 25, 30-34. (**Chapter 4**).

Reprinted from *Electrochemistry Communications, 25, Alexander Eifert, Waldemar Smirnov, Stefan Frittmann, Christoph Nebel, Boris Mizaikoff, Christine Kranz, Atomic force microscopy probes with integrated boron doped diamond electrodes: Fabrication and application, 30-34*, Copyright 2012, with permission from Elsevier.

Alexander Eifert, Philipp Langenwalter, Jonas Higl, Mika Lindén, Christoph E. Nebel, Boris Mizaikoff, Christine Kranz; Focused ion beam (FIB)-induced changes in the electrochemical behavior of boron-doped diamond (BDD) electrodes, Electrochimica Acta, 2014, 130, 418-425. (**Chapter 3**).

Reprinted from *Electrochimica Acta, 130, Alexander Eifert, Philipp Langenwalter, Jonas Higl, Mika Lindén, Christoph E. Nebel, Boris Mizaikoff, Christine Kranz, Focused ion beam (FIB)-induced changes in the electrochemical behavior of boron-doped diamond (BDD) electrodes, 418-425*, Copyright 2014, with permission from Elsevier.

Alexander Eifert, Boris Mizaikoff, Christine Kranz; An advanced fabrication process for combined atomic force-scanning electrochemical microscopy (AFM-SECM) probes, Micron, 2015, 68, 27-35. (**Chapter 5**).

Reprinted from *Micron, 68, Alexander Eifert, Boris Mizaikoff, Christine Kranz, Advanced fabrication process for combined atomic force-scanning electrochemical microscopy (AFM-SECM) probes, 27-35*, Copyright 2015, with permission from Elsevier.

Javier Izquierdo, Alexander Eifert, Ricardo M. Souto, Christine Kranz; Simultaneous pit generation and visualization of pit topography using combined atomic force-scanning electrochemical microscopy, Electrochemistry Communications, 2015, 51, 15-18. (**Chapter 6**).

Reprinted from *Electrochemistry Communications, 51, Javier Izquierdo, Alexander Eifert, Ricardo M. Souto, Christine Kranz, Simultaneous pit generation and visualization of pit topography using combined atomic force–scanning electrochemical microscopy, 15-18*, Copyright 2015, with permission from Elsevier.

Javier Izquierdo, Alexander Eifert, Christine Kranz, Ricardo M. Souto; In situ monitoring of pit nucleation and growth at an iron passive oxide layer by using combined atomic force and scanning electrochemical microscopy, ChemElectroChem, 2015, DOI: 10.1002/celc.201500100 (**Chapter 6**).

Reprinted from *J. Izquierdo, A. Eifert, C. Kranz, R. M. Souto, In situ monitoring of pit nucleation and growth at an iron passive oxide layer by using combined atomic force and scanning electrochemical microscopy, ChemElectroChem*, 2015, DOI: 10.1002/celc.201500100, Copyright 2015, with permission from Wiley-VCH Verlag GmbH & Co. KGaA, Weinheim.

List of abbreviations

AFM	atomic force microscopy
AM-AFM	amplitude modulated atomic force microscopy
ATR	attenuated total reflection
BDD	boron-doped diamond
CV	cyclic voltammogram
CVD	chemical vapor deposition
CQ	chloroquine
ΔE_p	peak separation
EBSD	electron backscatter diffraction
EELS	electron energy loss spectroscopy
FIB	focused ion beam
FFT	fast Fourier-transformation
FM-AFM	frequency modulated atomic force microscopy
HET	heterogeneous electron transfer
iD	intrinsic diamond
IQ	image quality
k^o	heterogeneous electron transfer constant
MEMS	micro-electro-mechanical systems
ODT	1-octadecanthiol
PECVD	plasma-enhanced chemical vapor deposition
PBS	phosphate buffered saline
POPC	1-palmitoyl-2-oleoyl-sn-glycero-3-phophocholine
QAg/AgCl	quasi Ag/AgCl reference electrode
SECM	scanning electrochemical microscopy
SEM	scanning electron microscopy
SICM	scanning ion conductance microscopy
SNOM	scanning near field optical microscopy

SLM	supported lipid membrane
SNR	signal-to-noise ratio
STORM	stochastic optical reconstruction microscopy
TEM	transmission electron microscopy
TOF-SIMS	time-of-flight secondary ion mass spectroscopy
UME	ultra-microelectrode
VDW	van-der-Waals
VPD	volume per dose [μm^3/nC]

List of figures

Fig. 1: Schematic representation of the diamond crystal growth mechanism in a CVD deposition process. 27

Fig. 2: A) Diamond crystal structure; B) electronic diagram of diamond; adapted with permission from M. A. Quiroz, E. R. Bandala, Types of conducting diamond materials and their properties, in: E. Brillas, C. A. Martinez-Huitle (Eds.), Synthetic diamond films preparation, electrochemistry, characterization, and applications, Hoboken, N.J.: Wiley, 2011, pp. 57–75 ; Copyright 2011, John Wiley & Sons, Inc., Hoboken, New Jersey [48]. 28

Fig. 3: Energy diagram of the doping states of differently doped diamonds. 29

Fig. 4: Simplified illustration of the Lennard-Jones potential and corresponding AFM modes. 33

Fig. 5: Optical read-out principle of an AFM system; red: deflection; green: friction. 34

Fig. 6: A) Schematic illustration of an UME; B) optical image of a Pt-UME (50 µm). 38

Fig. 7: A) Planar diffusion profile; B) hemispherical diffusion profile; C) Cottrell equation for macroscopic electrodes; D) modified Cottrell equation for microelectrodes; E) exemplary CV of a macroscopic electrode recorded in 10 mM $[Ru(NH_3)_6]Cl_3$ / 0.1 M KCl; F) CV recorded at a ultramicroelectrode in $K_4[Fe(CN)_6]$ / 0.1 M KCl; CVs are recorded vs. sat Ag/AgCl. 39

Fig. 8: Basic principles of the SECM feedback mode; redox mediator diffusion towards the electrode surface in A) bulk solution; B) between the UME and a conductive surface; C) in the presence of a non-conductive surface. 40

Fig. 9: Approach curves for A) a conductive and B) an insulating substrate; with L = normalized distance (d/r_0); adapted with permission from Ref. [109]; Copyright 1994, The Royal Society of Chemistry. 42

Fig. 10: Influence of the RG-value on theoretical calculated approach curves. Experimental data obtained and reprinted with permission from J. Kwak, A. J. Bard, Scanning electrochemical microscopy. Theory of the feedback mode, Anal. Chem., 61, 1989, 1221–1227; Copyright 1989, American Chemical Society [110]. 43

Fig. 11: Simulated approach curves towards a conductive surface with a subsequent chemical dimerization reaction of the converted redox mediator; with K = normalized (dimensionless) rate constant; reprinted with permission from Ref. [109]; Copyright 1994, The Royal Society of Chemistry. 44

Fig. 12: Exemplary images of A) a hand-made AFM-SECM probe reprinted with permission from J. V. Macpherson, P. R. Unwin, Combined scanning electrochemical-atomic force microscopy, Anal. Chem., 72, 2000, 276–285; Copyright 2000, American Chemical Society [7]; and B) a microfabricated AFM-SECM with recessed Au frame electrode. 47

Fig. 13: SECM current response according to topography and sample property changes. 48

Fig. 14: Exemplary cyclic voltammograms (CVs) recorded at bare and modified electrode surfaces: A) Bare BDD macro electrode (black) and Si_xN_y-insulated electrode (red); adapted from Electrochimica Acta, 130, Alexander Eifert, Philipp Langenwalter, Jonas Higl, Mika Lindén, Christoph E. Nebel, Boris Mizaikoff, Christine Kranz, Focused ion beam (FIB)-induced changes in the electrochemical behavior of boron-doped diamond (BDD) electrodes, 418-425, Copyright 2014, with permission from Elsevier [172]; B) after FIB milling, exposing microdisc BDD electrodes (red) and after electrochemical treatment (black) of a 5x5 array with an electrode spacing of 10 µm and an individual electrode radius of 5 µm; CVs were recorded in 10 mM $K_4[Fe(CN)_6]$ / 0.1 M KCl / 0.016 M Tween 20; all measurements were conducted vs. sat. Ag/AgCl; ν = 100 mV/s; patterning parameters: 16 kV, 15 nA, 50 ns. 52

Fig. 15: A) Schematic illustration of the Ga^+-ion beam orientation during microelectrode fabrication; B) SEM image of a microelectrode array with an electrode spacing of 10 µm and an individual electrode radius of 5 µm. 53

Fig. 16: AFM measurements of FIB-milled electrodes A) before and B) after electrochemical treatment in 2M sulfuric acid. AFM images were recorded in contact mode with Bruker NP general-purpose probes with a nominal spring constant of 0.06 N/m; reprinted from Electrochimica Acta, 130, Alexander Eifert, Philipp Langenwalter, Jonas Higl, Mika Lindén, Christoph E. Nebel, Boris Mizaikoff, Christine Kranz, Focused ion beam (FIB)-induced changes in the electrochemical behavior of boron-doped diamond (BDD) electrodes, 418-425, Copyright 2014, with permission from Elsevier [172]. 54

Fig. 17: Voltammograms recorded in 0.5 M H_2SO_4 vs. sat. Ag/AgCl (ν = 100 mV/s) revealing the potential window after FIB irradiation (red) and after FIB irradiation and cathodic treatment (blue); reprinted from Electrochimica Acta, 130, Alexander Eifert, Philipp Langenwalter, Jonas Higl, Mika Lindén, Christoph E. Nebel, Boris Mizaikoff, Christine Kranz, Focused ion beam (FIB)-induced changes in the electrochemical behavior of boron-doped diamond (BDD) electrodes, 418-425, Copyright 2014, with permission from Elsevier [172]. 55

Fig. 18: Exemplary cyclic voltammogram recorded at a cathodically treated electrode array with 10 µm electrode spacing; CV was recorded in 10 mM $K_4[Fe(CN)_6]$ / 0.1 M KCl / 0.016 M Tween 20 vs. sat. Ag/AgCl; ν = 100 mV/s; patterning parameters: 16 kV, 15 nA, 50 ns. 56

Fig. 19: CVs recorded at cathodically treated non-irradiated BDD electrodes in 10 mM $K_4[Fe(CN)_6]$ / 0.1 M KCl / 0.016 M Tween 20 (black) and 10 mM $[Ru(NH_3)_6]Cl_3$ / 0.1 M KCl / 0.016 M Tween 20 (red); all potentials are reported vs. sat. Ag/AgCl; ν = 100 mV/s. 56

Fig. 20: Peak separation of milled BDD microelectrode arrays after exposure to FIB irradiation and electrochemical treatment in 2 M sulfuric acid. Electrochemical measurements were recorded in a solution containing 10 mM $K_4[Fe(CN)_6]$ / 0.1 M KCl / 0.016 M Tween 20; ν = 100 mV/s; the influence of acceleration voltage on ΔE_p was investigated at a beam current of 15 nA and a dwell time of 1 µs. 59

Fig. 21: Peak separation of milled electrode arrays after exposure to FIB irradiation and electrochemical treatment in 2 M sulfuric acid. Electrochemical measurements were recorded in a solution containing 10 mM $K_4[Fe(CN)_6]$ / 0.1 M KCl / 0.016 M Tween 20; ν = 100 mV/s; the influence of beam current on ΔE_p was investigated at an accelerating voltage of 30 kV and a dwell time of 300 ns (15 nA; 5 nA) and 500 ns (3 nA), respectively. 60

Fig. 22: Peak separation of milled electrode arrays after exposure to FIB irradiation and electrochemical treatment in 2 M sulfuric acid. Electrochemical measurements were recorded in a solution containing 10 mM $K_4[Fe(CN)_6]$ / 0.1 M KCl / 0.016 M Tween 20; ν = 100 mV/s; the influence of the dwell time on ΔE_p was investigated at an accelerating voltage of 16 kV and a beam current of 15 nA. ... 61

Fig. 23: A) Exemplary simulated CV (DigiElch 7) fitted to experimental data using the Butler-Volmer equation (transfer coefficient α = 0.5); B) SEM image of a 5x5 ultra-microelectrode array with an electrode spacing of 100 µm spacing (center-to-center); B) adapted from Electrochimica Acta, 130, Alexander Eifert, Philipp Langenwalter, Jonas Higl, Mika Lindén, Christoph E. Nebel, Boris Mizaikoff, Christine Kranz, Focused ion beam (FIB)-induced changes in the electrochemical behavior of boron-doped diamond (BDD) electrodes, 418-425, Copyright 2014, with permission from Elsevier [172]. ... 64

Fig. 24: HET rate constants for different A) acceleration voltages (15 nA; 300 ns); B) beam currents (30 kV; 300 ns); and C) at different dwell times (HET: 30 kV; 15 nA); adapted from Electrochimica Acta, 130, Alexander Eifert, Philipp Langenwalter, Jonas Higl, Mika Lindén, Christoph E. Nebel, Boris Mizaikoff, Christine Kranz, Focused ion beam (FIB)-induced changes in the electrochemical behavior of boron-doped diamond (BDD) electrodes, 418-425, Copyright 2014, with permission from Elsevier [172]. ... 66

Fig. 25: A) Exemplary comparison of the experimental and the simulated data; B-D) HET rate constants for different transfer coefficient values:, B) acceleration voltages (15 nA; 300 ns), C) beam currents (30 kV; 300 ns), and D) dwell times (30 kV; 15 nA). ... 68

Fig. 26: Ten-point mean surface roughness in correlation to dwell time (16 kV; 15 nA); adapted from Electrochimica Acta, 130, Alexander Eifert, Philipp Langenwalter, Jonas Higl, Mika Lindén, Christoph E. Nebel, Boris Mizaikoff, Christine Kranz, Focused ion beam (FIB)-induced changes in the electrochemical behavior of boron-doped diamond (BDD) electrodes, 418-425, Copyright 2014, with permission from Elsevier [172]. ... 70

Fig. 27: Raman spectra obtained after different fabrication steps of the microelectrode arrays. Raman spectra were acquired using an excitation laser with 532 nm wavelength and 10 mW power. For detection a 100x objective with a 0.9 numerical aperture was used; adapted from Electrochimica Acta, 130, Alexander Eifert, Philipp Langenwalter, Jonas Higl, Mika Lindén, Christoph E. Nebel, Boris Mizaikoff, Christine Kranz, Focused ion beam (FIB)-induced changes in the electrochemical behavior of boron-doped diamond (BDD) electrodes, 418-425, Copyright 2014, with permission from Elsevier [172]. ... 71

Fig. 28: Raman spectra of different patterning parameters; A) after FIB irradiation of an as-grown BDD sample and B) after a subsequent electrochemical treatment in sulfuric acid; adapted from Electrochimica Acta, 130, Alexander Eifert, Philipp Langenwalter, Jonas Higl, Mika Lindén, Christoph E. Nebel, Boris Mizaikoff, Christine Kranz, Focused ion beam (FIB)-induced changes in the electrochemical behavior of boron-doped diamond (BDD) electrodes, 418-425, Copyright 2014, with permission from Elsevier [172]; Optical microscope images of the electrode surface: C) as-grown; D) after FIB irradiation; E) after electrochemical treatment; Raman spectra were recorded inside the blue rectangles (C-E) and subsequently averaged (n = 625). ... 73

Fig. 29: Kikuchi patterns of BDD; A) non-irradiated, cathodically treated BDD B) FIB irradiated and consecutively cathodically treated BDD (30 kV; 15 nA; 50 ns); EBSD measurements were performed at an incident angle of 20° relative to the sample surface with 20 kV, 16 nA; EBSD detector binning 2 x 2; image averaging: 5 frames. ... 74

Fig. 30: A) Z-deviation of the milling depth relative to the target depth for the used VPD parameter; n = 3; B) FIB-milled trenches milled with 30 kV, 46 pA and a dwell time of 1 µs; target depth: 400 nm. 78

Fig. 31: SEM images of the fabrication steps of combined BDD-AFM-SECM probes; A) Parylene-C-insulated cantilever B) after front-cut; C) side view after front cut; D) After 90° reorientation, 2nd cut and tip sharpening; All fabrication steps were performed at 30 kV, 50 pA, 1 µs. 79

Fig. 32: Flow chart for fabricating BDD-AFM-SECM probes. CVs were recorded in 10 mM $[Ru(NH_3)_6]Cl_3$ / 0.1 M KCl vs. sat. Ag/AgCl; ν = 100 mV/s; reprinted from Electrochemistry Communications, 25, Alexander Eifert, Waldemar Smirnov, Stefan Frittmann, Christoph Nebel, Boris Mizaikoff, Christine Kranz, Atomic force microscopy probes with integrated boron doped diamond electrodes: Fabrication and application, 30-34, Copyright 2012, with permission from Elsevier [182] 79

Fig. 33: Exemplary SEM image of a BDD-AFM-SECM probe; tip radius ≈ 50 nm, tip height: 1.2 µm; electrode diameter: 2.4 µm. 80

Fig. 34: CV recorded at an BDD-AFM-SECM probe (r = 1.3 µm) after FIB milling (red); CV after cathodic treatment (black); CVs were recorded in 10 mM $K_4[Fe(CN)_6]$ / 0.1 M KCl vs. sat. Ag/AgCl; ν = 100 mV/s. 81

Fig. 35: CV of a H-terminated BDD-AFM-SECM probe recorded in 0.5 M H_2SO_4 vs. $Hg/HgSO_4$; ν = 200 mV/s. 82

Fig. 36: CVs recorded at a combined BDD-AFM-SECM probe during long time storage; CVs were recorded in 10 mM $K_4[Fe(CN)_6]$ / 0.1 M KCl vs. sat. Ag/AgCl; ν = 100 mV/s. 83

Fig. 37: Combined AFM-SECM measurement: A) topography recorded in contact mode; scan speed: 0.25 line/s; re-shaped AFM tip height: 1.1 µm; B) electrochemistry recorded in 10 mM $[Ru(NH_3)_6]Cl_3$ / 0.1 M KCl; E_{tip}= -400 mV vs. QAg/AgCl; electrode diameter 2.4 µm; magnified view of insulating diamond particle C) topography and D) electrochemical response; reprinted from Electrochemistry Communications, 25, Alexander Eifert, Waldemar Smirnov, Stefan Frittmann, Christoph Nebel, Boris Mizaikoff, Christine Kranz, Atomic force microscopy probes with integrated boron doped diamond electrodes: Fabrication and application, 30-34, Copyright 2012, with permission from Elsevier [182]. 84

Fig. 38: A) Topography image of an abraded diamond particle on the Pt-UME surface; B) cross-sectional view of topography profile (black) and SECM profile (red) obtained at the position marked with the red line in A; scan direction: right-to-left (retrace); scan speed: 0.45 line/s; re-shaped AFM tip height: 1.1 µm; electrochemistry recorded in 10 mM $[Ru(NH_3)_6]Cl_3$ / 0.1 M KCl; E_{tip}= -400 mV vs. QAg/AgCl; electrode diameter 2.4 µm. 86

Fig. 39: A) Electrochemical image at variable potentials B) current profile (top-bottom); electrochemistry recorded in 10 mM $[Ru(NH_3)_6]Cl_3$ / 0.1 M KCl; E_{tip}= -400, -200, -100, -50 mV vs. QAg/AgCl; scan speed: 0.45 line/s; re-shaped AFM tip height: 1.1 µm; electrode diameter 2.4 µm. 87

Fig. 40: A) Simulated diffusion profile for $K_4[Fe(CN)_6]$ at a BDD-AFM-SECM probe; tip height: 0.9 µm, electrode diameter: 2.4 µm, D = $6.3e^{-6}$ cm^2/s [132]; B) CV recorded after H-termination in 10 mM $K_4[Fe(CN)_6]$ / 0.1 M KCl vs. sat. Ag/AgCl; ν = 100 mV/s; (black) and the theoretically obtained steady state current level (red); adapted from Electrochemistry Communications, 25, Alexander Eifert, Waldemar Smirnov, Stefan Frittmann, Christoph Nebel, Boris Mizaikoff, Christine Kranz, Atomic force microscopy probes with integrated boron doped diamond electrodes: Fabrication and application, 30-34, Copyright 2012, with permission from Elsevier [182]. 88

Fig. 41: Simulated diffusion profiles for $[Ru(NH_3)_6]Cl_3$ at a BDD-AFM-SECM probe; tip height: 1.0 µm; electrode diameter: 2.4 µm, D = $7.5e^{-6}$ cm^2/s [132]; A) positive feedback with redox mediator regeneration at the sample surface; B) negative feedback with hindered diffusion towards the electrode caused by an insulating surface. 89

Fig. 42: A) SEM image of intrinsic diamond-insulated BDD coated-AFM probe; B) top-mill fabricated AFM-SECM probe with an integrated BDD electrode; reprinted from Micron, 68, Alexander Eifert, Boris Mizaikoff, Christine Kranz, Advanced fabrication process for combined atomic force-scanning electrochemical microscopy (AFM-SECM) probes, 27-35, Copyright 2015, with permission from Elsevier [208]. 92

Fig. 43: A) Simulated diffusion profile towards a Parylene-C-coated probe fabricated with a top-mill process; electrode diameter 1.0 µm; B) CV recorded in 10 mM $[Ru(NH_3)_6]Cl_3$ with 0.1 M KCl as supporting electrolyte; ν = 100 mV/s; C) SEM image of a top-mill fabricated Parylene-C-coated AFM-SECM probe; adapted from Micron, 68, Alexander Eifert, Boris Mizaikoff, Christine Kranz, Advanced fabrication process for combined atomic force-scanning electrochemical microscopy (AFM-SECM) probes, 27-35, Copyright 2015, with permission from Elsevier [208] 94

Fig. 44: A) Simulated diffusion profile towards a Parylene-C-coated probe fabricated with a standard side-mill process [8]; electrode diameter 1.0 µm; B) CV recorded in 10 mM $[Ru(NH_3)_6]Cl_3$ with 0.1 M KCl as supporting electrolyte; ν = 100 mV/s; C) SEM image of a side-mill fabricated Parylene-C-coated AFM-SECM probe. 95

Fig. 45: A) Simulated diffusion profile towards a Si_xN_y-coated probe fabricated with a top-mill process; electrode diameter 1.0 µm; B) CV recorded in 10 mM $[Ru(NH_3)_6]Cl_3$ with 0.1 M KCl as supporting electrolyte; ν = 20 mV/s; C) SEM image of a top-mill fabricated Si_xN_y-coated AFM-SECM probe; adapted from Micron, 68, Alexander Eifert, Boris Mizaikoff, Christine Kranz, Advanced fabrication process for combined atomic force-scanning electrochemical microscopy (AFM-SECM) probes, 27-35, Copyright 2015, with permission from Elsevier [208]. 96

Fig. 46: Cross-sectional contour plot of the simulated concentration distribution of $[Ru(NH_3)_6]Cl_3$ in respect to the three selected electrode tilts; A) +13°; B) 0°; C) -80°. 97

Fig. 47: Simulated diffusion profiles of $[Ru(NH_3)_6]Cl_3$ at combined AFM-SECM probes with different electrode tilts in A-C) positive feedback; D-F) negative feedback conditions; A&D) -80°; B&E) 0°; C&F) +13°; electrode diameter 1.0 µm. 98

Fig. 48: Scheme of a trans-impedance amplifier circuit. 100

Fig. 49: A) Photograph of an AFM-SECM nosecone (Keysight Technologies) with integrated pre-amplifier; B) Photograph of AFM-SECM cartridge for fast and simple probe replacement with mounted AFM-SECM probe. The contact to the electrical wire is sealed with UV-curable glue and insulating varnish. 101

Fig. 50: Current-time graph recorded with external (red) and internal (black) data acquisition (gain: 1 nA/V); electrochemical data recorded in 10 mM $[Ru(NH_3)_6]Cl_3$ / 0.1 M KCl; E_{tip}= -500 mV vs. QAg/AgCl; sampling rate: 25 Hz (external), 397 Hz (internal); electrode diameter: 1.2 µm (external), 0.7 µm (internal). 102

Fig. 51: AFM-SECM image (relative current) using an external potentiostat for the electrochemical experiment and a top-mill fabricated Parylene-C-coated AFM-SECM probe. The sample reflects milled structures in Pt-coated glass in form of the letter “A”; scan speed: 0.3 line/s; re-shaped AFM tip height: 660 nm; electrode frame length: 1.2 µm; A) topography recorded in contact mode; B) SECM image recorded in feedback mode, images were recorded in 10 mM $[Ru(NH_3)_6]Cl_3$ / 0.1 M KCl; E_{tip}= -500 mV vs. QAg/AgCl; C) electrochemical data after FFT-filtering; D-F) extracted profiles of A-C); G) SEM image of the model sample; 103

Fig. 52: Exemplary FFT-spectrum of a i-t-curve recorded during AFM-SECM measurement in 10 mM $[Ru(NH_3)_6]Cl_3$ / 0.1 M KCl; E_{tip}= -500 mV vs. QAg/AgCl using an external potentiostat. 104

Fig. 53: AFM-SECM image of a model sample (milled structures in Pt-coated glass) recorded with an internal amplifier (gain: 10 nA/V) and a side-mill fabricated Si_xN_y-coated AFM-SECM probe; scan speed: 0.3 line/s; re-shaped AFM tip height: 850 nm; electrode frame length: 0.7 µm; A) topography recorded in contact mode; B) SECM image recorded in feedback mode; C) SECM image after horizontal line correction for drift compensation; D-F) extracted profiles of A-C); G) SEM image of the model sample; electrochemistry recorded in 10 mM $[Ru(NH_3)_6]Cl_3$ / 0.1 M KCl; E_{tip}= -500 mV vs. QAg/AgCl. 105

Fig. 54: Electrochemical signal of a model sample (deposited Pt-structures on Si) recorded with an external potentiostat at a top-mill fabricated Parylene-C-coated AFM-SECM probe; scan speed: 0.3 line/s; re-shaped AFM tip height: 800 nm; electrode frame length: 1.6 µm; A) electrochemistry; B) electrochemistry after horizontal line correction for drift compensation (without FFT-filtering); C) i-t-curve recorded during AFM-SECM measurement; electrochemistry recorded in 10 mM $[Ru(NH_3)_6]Cl_3$ / 0.1 M KCl; E_{tip}= -500 mV vs. QAg/AgCl. 106

Fig. 55: A) Cyclic voltammogram of a Si_xN_y-coated AFM-SECM probe; B) CVs acquired over several hours with the probe constantly immersed in the electrolyte solution (internal data acquisition); C) steady state currents of the AFM-SECM probe during immersion (n=5); electrochemistry recorded in 10 mM $[Ru(NH_3)_6]Cl_3$ / 0.1 M KCl vs. A) sat. Ag/AgCl; B+C) QAg/AgCl; ν = 100 mV/s; electrode frame length: 0.8 µm. 107

Fig. 56: Cyclic voltammograms recorded at a Si_xN_y-coated AFM-SECM probe immersed in redox mediator at A) pH = 1; B) pH = 8.5; CVs were recorded in 10 mM $[Ru(NH_3)_6]Cl_3$ / 0.1 M KCl vs. A) sat. Ag/AgCl; B) QAg/AgCl; ν = 100 mV/s; electrode frame length: 0.9 µm. 108

Fig. 57: Cyclic voltammogram for nitrite oxidation at a combined AFM-SECM probe recorded in 0.5 M NaCl / 0.1 M $NaNO_2$ vs. QAg/AgCl; electrode edge length of 1.07; ν = 100 mV/s; adapted from J. Izquierdo, A. Eifert, C. Kranz, R. M. Souto, In situ monitoring of pit nucleation and growth at an iron passive oxide layer by using combined atomic force and scanning electrochemical microscopy, ChemElectroChem, 2015, DOI: 10.1002/celc.201500100, Copyright 2015, with permission from Wiley-VCH Verlag GmbH & Co. KGaA, Weinheim [215]. 111

Fig. 58: Simulated concentration profile in nitrite solution at an AFM-tip integrated electrode; electrode edge length: 1.07 µm; tip height: 0.46 µm; reprinted from Electrochemistry Communications, 51, Javier Izquierdo, Alexander Eifert, Ricardo M. Souto, Christine Kranz, Simultaneous pit generation and visualization of pit topography using combined atomic force–scanning electrochemical microscopy, 15-18, Copyright 2015, with permission from Elsevier [213]. 112

Fig. 59: 3D AFM topography of a polished iron surface recorded in contact mode with a combined AFM-SECM probe A) before and B) after induced pit formation; AFM images were recorded in 0.5 M NaCl / 0.1 M $NaNO_2$ with an AFM-SECM probe (electrode edge length: 1.07 µm and tip height: 0.46 µm); scan speed: 0.43 lines/s; pit formation was induced at +0.9V vs. QAg/AgCl, while scanning an area of 3x3 μm^2; scan speed: 4.45 µm/s; reprinted from Electrochemistry Communications, 51, Javier Izquierdo, Alexander Eifert, Ricardo M. Souto, Christine Kranz, Simultaneous pit generation and visualization of pit topography using combined atomic force–scanning electrochemical microscopy, 15-18, Copyright 2015, with permission from Elsevier [213]. 112

Fig. 60: Pit depth (□) and volume (Δ) evolution after induced pit formation; AFM images for data extraction were recorded in 0.5 M NaCl / 0.1 M $NaNO_2$ using an AFM probe with a tip height of 0.46 µm; scan speed: 0.34 lines/s; adapted from J. Izquierdo, A. Eifert, C. Kranz, R. M. Souto, In situ monitoring of pit nucleation and growth at an iron passive oxide layer by using combined atomic force and scanning electrochemical microscopy, ChemElectroChem, 2015, DOI: 10.1002/celc.201500100, Copyright 2015, with permission from Wiley-VCH Verlag GmbH & Co. KGaA, Weinheim [215]. 114

Fig. 61: A) AFM image and B) height profile of different corrosion pits induced by varying the scanned area; AFM images recorded in 0.5 M NaCl / 0.1 M $NaNO_2$; scan speed: 0.40 lines/s; pit formation at +0.9V vs. QAg/AgCl, while scanning an area of I) 0.75x0.75 μm^2; II) 0.5x0.5 μm^2; III) 0.25x0.25 μm^2; scan speed: 3.8 µm/s; electrode edge length: 1.07 µm; re-shaped tip height: 0.46 µm. 115

Fig. 62: Plot of pit volume vs. patterning area; scan speed: 1.9 µm/s; pit formation at +0.9V vs. QAg/AgCl in 0.5 M NaCl / 0.1 $NaNO_2$. 116

Fig. 63: AFM contact mode images of corrosion pits induced using a static mode with different exposure times; A) 20s; B) 90s; AFM images recorded in 0.5 M NaCl / 0.1 M $NaNO_2$; immersion time: 155 min; scan speed: 0.34 lines/s; pit formation at +0.9V vs. QAg/AgCl; reprinted from J. Izquierdo, A. Eifert, C. Kranz, R. M. Souto, In situ monitoring of pit nucleation and growth at an iron passive oxide layer by using combined atomic force and scanning electrochemical microscopy, ChemElectroChem, 2015, DOI: 10.1002/celc.201500100, Copyright 2015, with permission from Wiley-VCH Verlag GmbH & Co. KGaA, Weinheim [215]. 117

Fig. 64: AFM topography images and height profile of a polished iron surface recorded in contact mode with a combined AFM-SECM probe; A) before and B&C) after induced pit formation followed by a subsequent scan for iron (II) detection; AFM images were recorded in 0.5 M NaCl / 0.1 M $NaNO_2$ with an AFM-SECM probe with an electrode edge length of 1.07 µm and a tip height of 0.46 µm; scan speed: 0.43 lines/s; pit formation was induced at +0.9V vs. QAg/AgCl; iron (II) detection at + 0.5V vs. Q/Ag/AgCl, while scanning an area of 3x3 μm^2; scan speed: 3.8 µm/s; adapted from J. Izquierdo, A. Eifert, C. Kranz, R. M. Souto, In situ monitoring of pit nucleation and growth at an iron passive oxide layer by using combined atomic force and scanning electrochemical microscopy, ChemElectroChem, 2015, DOI: 10.1002/celc.201500100, Copyright 2015, with permission from Wiley-VCH Verlag GmbH & Co. KGaA, Weinheim [215]. 118

Fig. 65: Scheme of the hybrid lipid membrane formation, incorporation of the C2IIa heptameres and the mass transport inhibition of the heptameric pores using chloroquine; A) self-assembled ODT layer; B) hybrid lipid bilayer; C) hybrid lipid bilayer with incorporated pores; D) pore inhibition using chloroquine. 122

Fig. 66: Exemplary CVs recorded at a bare Au substrate (blue) and an ODT-coated Au substrate (red); CVs recorded in aqueous solution containing 10 mM $[Ru(NH_3)_6]Cl_3$ and 0.1 M KCl, adjusted to pH=6; ν = 100 mV/s. 123

Fig. 67: A) Exemplary CV; B) SEM image of a PtC-composite AFM-SECM probe; CV recorded in 10 mM $[Ru(NH_3)_6]Cl_3$ with 0.1 M KCl as supporting electrolyte vs. Ag/AgCl; ν = 100 mV/s. 124

Fig. 68: Approach curves towards an Au-coated substrate (black) and towards a self-assembled ODT layer (red); approach curves recorded in aqueous solution containing 10 mM $[Ru(NH_3)_6]Cl_3$ and 0.1 M KCl, adjusted to pH=6; E_{tip}: -500 mV vs. QAg/AgCl; A_{el} = 1.94 μm^2. 124

Fig. 69: Chemical structure of 1-hexadecanoly-2-(9Z-octadecanoyl)-sn-glycero-3-phosphocholine (1-palmitoyl-2-oleoyl-sn-glycero-3-phosphocholine / POPC).... 125

Fig. 70: Exemplary CVs recorded at an ODT-coated substrate (red) and at a hybrid bilayer-coated substrate (black); CVs recorded in aqueous solution containing 10 mM $[Ru(NH_3)_6]Cl_3$ and 0.1 M KCl, adjusted to pH=6 vs. QAg/AgCl; ν = 100 mV/s. 126

Fig. 71: Exemplary approach curves towards an Au-coated substrate (black), towards a self-assembled ODT layer (red) and towards the hybrid lipid bilayer (green); approach curves recorded in aqueous solution containing 10 mM $[Ru(NH_3)_6]Cl_3$ and 0.1 M KCl, adjusted to pH=6; E_{tip}: -500 mV vs. QAg/AgCl; A_{el} = 1.46 μm^2. 127

Fig. 72: Exemplary CVs of a SLM (black) and a C2IIa embedded SLM (red); CVs recorded in aqueous solution containing 10 mM $[Ru(NH_3)_6]Cl_3$ and 0.1 M KCl, adjusted to pH=6 vs. QAg/AgCl; ν = 100 mV/s. 128

Fig. 73: Exemplary approach curves towards an Au-coated substrate (black), towards a hybrid lipid bilayer (green) and towards the C2IIa embedded hybrid lipid bilayer (magenta); approach curves recorded in aqueous solution containing 10 mM $[Ru(NH_3)_6]Cl_3$, 0.1 M KCl and 3.48 µg/ml C2IIa, adjusted to pH=6 E_{tip}: -500 mV vs. QAg/AgCl; A_{el} = 1.46 μm^2. 128

Fig. 74: CVs of different C2IIa concentrations in the supernatant liquid phase of the SLM; CVs recorded in aqueous solution containing 10 mM $[Ru(NH_3)_6]Cl_3$, 0.1 M KCl and 1.74-27.84 µg/ml C2IIa, adjusted to pH=6 vs. QAg/AgCl; ν = 100 mV/s. 129

Fig. 75: Calculated pore density according to data from Fig. 74 using Eq. 1; n = 1; D = 7.5e-6 [cm^2/s]; r = 1.35 nm [1]..... 130

Fig. 76: Approach curves towards a SLM with different concentrations of the activated C2IIa in the supernatant solution. Approach curves recorded in aqueous solution containing 10 mM $[Ru(NH_3)_6]Cl_3$, 0.1 M KCl and 1.74-27.84 µg/ml C2IIa, adjusted to pH=6; E_{tip}: -400 mV vs. QAg/AgCl; A_{el} = 0.65 μm^2; inset: zoomed view showing the standard deviation of the recorded approach curves (N = 5)..... 131

Fig. 77: Comparison of the calculated surface coverage (N = 10) and AFM-SECM data (N = 5) correlated to the C2IIa concentration of an alkanethiol supported lipid membrane; I_t/I_∞ values are obtained at surface contact..... 131

Fig. 78: Exemplary approach curves towards a hybrid lipid bilayer before (black) and after (red) $[Ru(NH_3)_6]Cl_3$/PBS solution exchange. Approach curves recorded in aqueous solution containing 10 mM $[Ru(NH_3)_6]Cl_3$ and 0.1 M KCl; E_{tip}: -350 mV vs. QAg/AgCl; A_{el} = 0.33 μm^2; inset: zoomed view showing the standard deviation of the recorded approach curves (N = 6 (hybrid lipid bilayer); N = 5 (after solution exchange))..... 132

Fig. 79: Chemical structure of chloroquine..... 133

Fig. 80: Exemplary electrochemical (A) and approach curve (B) measurements of hybrid lipid bilayers (red); with C2IIa incorporation (orange) and CQ addition (black); CVs and approach curves recorded in aqueous solution containing 10 mM $[Ru(NH_3)_6]Cl_3$ and 0.1 M KCl, adjusted to pH=6; ν = 100 mV/s; E_{tip}: -400 mV vs. QAg/AgCl; A_{el} = 0.96 μm^2; inset: zoomed view showing the standard deviation of the recorded approach curves (N = 5)..... 133

Fig. 81: A) Exemplary CV and B) approach curves for the addition of CQ solution towards an ODT-POPC hybrid lipid bilayer immersed in buffered solution. CVs and approach curves recorded in aqueous solution containing 10 mM $[Ru(NH_3)_6]Cl_3$ and 0.1 M KCl, adjusted to pH=6; ν = 100 mV/s; E_{tip}: -500 mV vs. QAg/AgCl; A_{el} = 0.83 μm^2; inset: zoomed view showing the standard deviation of the recorded approach curves (N = 8 (hybrid lipid bilayer); N = 9 (after CQ addition))..... 135

Fig. 82: Signal decay of a PtC composite electrode after more than 20-25 approach curves; CVs recorded in aqueous solution containing 10 mM $[Ru(NH_3)_6]Cl_3$ and 0.1 M KCl vs. QAg/AgCl; ν = 100 mV/s; A_{el} = 0.83 μm^2..... 136

Fig. 83: Reaction pathways of dopamine and ascorbic acid induced by electrochemical oxidation..... 138

Fig. 84: Exemplary cyclic voltammograms of tip-less cathodically treated BDD-AFM-SECM probes (Fig. 85). CVs recorded in A) 10 mM $K_4[Fe(CN)_6]$ / 0.1 M KCl; B) 5 mM dopamine in PBS solution, pH=7.5 vs. sat. Ag/AgCl; ν = 100 mV/s; A_{el} = 4.52 μm^2..... 139

Fig. 85: Exemplary SEM image of tip-less BDD-AFM-SECM probes; A_{el} = 4.52 μm^2..... 139

Fig. 86: CVs of tip-less cathodically treated BDD-AFM-SECM probes in PBS buffer solution (pH = 7.4) containing 100 µM ascorbic acid (black) spiked with 100 µM dopamine (red); CVs recorded at a combined AFM-SECM probe vs. sat. Ag/AgCl; ν = 100 mV/s; A_{el}= 1.65 μm^2..... 140

Fig. 87: CVs of ascorbic acid in PBS spiked with different concentrations of dopamine; A) 10-100 µM dopamine; B) 100-1000 µM dopamine; C,D) linear regression of the current response of A,B (N = 4); CVs recorded at combined AFM-SECM probe vs. sat. Ag/AgCl; ν = 100 mV/s; A_{el}= 0.96 µm^2 (A,C); A_{el}= 0.58 µm^2 (B,D). 140

Fig. 88: CVs of ascorbic acid in PBS spiked with different concentrations of dopamine; A) 25-100 µM dopamine; B) linear regression of the current response of A recorded at 1V vs. sat. Ag/AgCl (N = 4); CVs recorded at a perpendicular milled BDD electrode array (Fig. 23B); ν = 100 mV/s. A_{el} = 1963 µm². 141

Fig. 89: Schematic illustration of a customized liquid cell for electrochemical measurements. 151

Fig. 90: A) 3D model with solvent box for diffusion simulations and current calculations; B) simulation mesh for combined BDD-AFM-SECM probe. 156

Fig. 91: A) Conversion zones of the diffusion simulation for feedback conditions (pos. feedback); B) bulk solution concentration boundaries for pos. and neg. feedback simulations. 158

Fig. 92: 3D replica of the combined AFM-SECM probes with various electrode angles A) 0°; B) -80°; C) +13°. 160

Fig. 93: SEM images of the PtC-AFM-SECM probe fabrication steps; A) Tip after accessing the Au layer; B) PtC deposition; C) Tip reconstruction via FIB-milling. 166

List of tables

Tab. 1: Exemplary values of peak separations after exposure of the BDD micro-electrode arrays by FIB irradiation and electrochemical treatment; data recorded in a solution containing 10 mM $K_4[Fe(CN)_6]$ / 0.1 M KCl / 0.016 M Tween 20; ν = 100 mV/s; reprinted from Electrochimica Acta, 130, Alexander Eifert, Philipp Langenwalter, Jonas Higl, Mika Lindén, Christoph E. Nebel, Boris Mizaikoff, Christine Kranz, Focused ion beam (FIB)-induced changes in the electrochemical behavior of boron-doped diamond (BDD) electrodes, 418-425, Copyright 2014, with permission from Elsevier [172]. 57

Tab. 2: Overview of peak separations in correlation to the patterning parameters; data were recorded in a solution containing 10 mM $K_4[Fe(CN)_6]$ / 0.1 M KCl / 0.016 M Tween 20; ν = 100 mV/s. 62

Tab. 3 Overview of HET rate constants in correlation to the patterning parameters; data recorded in a solution containing 10 mM $K_4[Fe(CN)_6]$ / 0.1 M KCl / 0.016 M Tween 20; ν = 100 mV/s; rate constants calculated using the Butler-Volmer equation with transfer coefficient α = 0.5. 65

Tab. 4: Overview of HET rate constants in correlation to the patterning parameters; data recorded in a solution containing 10 mM $K_4[Fe(CN)_6]$ / 0.1 M KCl / 0.016 M Tween 20; ν = 100 mV/s; rate constants were calculated using the Butler-Volmer equation with an iterated transfer coefficient α = 0.66. 67

Tab. 5: Surface roughness factors in correlation to the patterning parameters; AFM images were recorded in contact mode in ambient conditions with Bruker NP general-purpose probes with a nominal spring constant of 0.06 N/m. 70

Tab. 6: Calculated current ratios for combined AFM-SECM probes with different electrode tilts; adapted from Micron, 68, Alexander Eifert, Boris Mizaikoff, Christine Kranz, Advanced fabrication process for combined atomic force-scanning electrochemical microscopy (AFM-SECM) probes, 27-35, Copyright 2015, with permission from Elsevier [208]. 97

Tab. 7: Calculated faradaic currents obtained from the simulated diffusion profile for feedback conditions [212]. 98

Tab. 8: Normalized electrode currents of the different electrode tilts for feedback conditions. 98

Tab. 9: Pit depth and volume in correlation to scan area and immersion time. 116

Tab. 10: Surface coverage values at different steps of the hybrid lipid bilayer formation; coverage calculated using Eq. 9. 126

Tab. 11: Peak current determined for the reduction of $[Ru(NH_3)_6]Cl_3$ and relative surface coverage after C2IIa addition; CVs see Fig. 74. 129

Tab. 12: Exemplary change in relative surface coverage after C2IIa addition and CQ inhibition according to Fig. 80A. 134

Tab. 13: Change in relative surface coverage after CQ addition according to Fig. 81A. ... 135

1. Motivation and scope of this thesis

Today a large number of emerging scientific questions arise from processes at the micrometer or nanometer scale ranging from fundamental studies in life sciences to developing new materials. For example, such studies involve investigations at the single cell level (e.g., pore transport [1,2]) or analyzing material transformations (e.g., corrosion processes [3]). Hence, analytical tools providing spatially resolved physical and chemical information are required. Already in the late 1980s and early 1990s, scanning probe techniques providing in particular laterally resolved chemical information have been developed [4–6]. Namely, the scanning electrochemical microscopy (SECM) [5] and the atomic force microscopy (AFM) using chemically modified AFM-tips for molecule-specific detection [6] at a sample surface. Within the last decades, a number of combined scanning probe techniques, including the combination of AFM with SECM [7–9], scanning ion conductance microscopy (SICM) with SECM [10,11], and scanning near field optical microscopy (SNOM) with AFM [12,13] or SICM [14] have emerged, focusing on multifunctional detection of physical and chemical properties with high lateral resolution. Recent developments in this research area are currently focused on improving the achievable physical and chemical resolution (for analyzing processes at steadily decreasing dimensions). Among those techniques, the combination of AFM-SECM is particularly attractive for studying processes at the solid/liquid interface.

During the investigations of biological samples, the main challenge is to discriminate clearly the individual electrochemically active components, and to prevent any (bio)-fouling effects altering or limiting the responsiveness of the chemical probe, i.e., the SECM electrode. Thus, electrode materials facilitating the discrimination of individual electrochemical species while minimizing interference effects are demanded. Boron-doped diamond (BDD) is among the most interesting electrode materials [15], as it is characterized by a wide potential window and high chemical stability. In addition, due to its inertness, electroactive molecules may be detected, which would cause considerable fouling effects at conventional electrode materials [16]. Consequently, a main part of this thesis will focus on the development of a fabrication scheme for tip-recessed BDD-AFM-SECM probes (see chapter 4). BDD-AFM-SECM probes developed within this thesis, with an AFM tip-recessed electrode, are typically

structured using a high energy Ga^+-ion beam [8,17]. The influence of the focused ion beam (FIB) irradiation on the electrochemical behavior of BDD plays a significant role and has been investigated in depth within this thesis (see chapter 3). Furthermore, the effect of electrode geometry of combined AFM-SECM probes is discussed in detail (chapter 5). Typically, the recorded electrochemical signals during AFM-SECM experiments are in the current regime of few nA-to-pA. Given the top-down configuration with the AFM-SECM probe, mounted at a piezoelectric scanner, potential interferences and the achievable signal-to-noise ratio (SNR) are important analytical parameters. Hence, experimental and instrumental improvements of the electrochemical data acquisition and signal quality have been an essential component of this thesis (chapter 6), using a direct current to voltage conversion along with optimized probe mounting strategies. For demonstrating real-world applicability of the AFM-SECM probes, localized corrosion experiments at iron surfaces are discussed in chapter 6.2.3.

In addition, biologically relevant examples for the application of AFM-SECM probes have been demonstrated, such as approach curve measurements at substrate-supported lipid membranes with embedded protein pores (C2IIa of the clostridium botulinum toxin) in chapter 7.2.1, or the detection of dopamine in the presence of ascorbic acid using BDD-AFM-SECM probes (see chapter 7.2.2). The use of BDD as electrode material allowed a simultaneous detection of dopamine and ascorbic acid, which can't normally be discriminated using conventional electrode materials [15].

2. Theory and state of the art

2.1. Boron-doped diamond (BDD)

2.1.1. Overview

As an allotrope of carbon, diamond is considered being one of the most robust crystalline materials on earth concerning its physical and chemical stability, which renders diamond as an excellent material for industrial applications where high mechanical stabilities are required. Therefore, diamond is often used for cutting-, drilling- or grinding tools to reduce wear and tear. Diamond coatings are also applied for device protection in chemical harsh environments. For example, the protection of optical elements from corrosion in strong acids can be achieved by diamond layers [18]. Due to its broad optical transparency from the deep UV to the far IR region of the electromagnetic spectrum [19,20], diamond is an excellent waveguide for spectroscopy. Depending on the chemical composition and grain size of the diamond material, a transparent window between 225-900 nm in the UV-Vis-region [19,20], and <1100 cm^{-1} in the far IR region is observed [19]. Strong research efforts were targeted towards the artificial synthesis of diamond during the 1960s and 1970s. Using chemical vapor deposition (CVD), a successful synthesis with acceptable growth rates was finally achieved [21–25], opening the possibility for industrial applications. In the late 1980s, diamond was also introduced to the field of electrochemistry [26], when dopants of the third or fifth group of the periodic table, like boron, nitrogen or phosphorus, were incorporated into the crystal lattice of the diamond, generating chemical stable and transparent electrodes with a large potential window, low background current and low double layer capacity. The outstanding electrochemical properties of doped diamond films render doped diamond as an attractive electrode material for a variety of electrochemical applications, where conventional electrode materials like platinum or gold (see section 2.1.2) are not suitable. For example, boron-doped diamond is nowadays used as transducer for novel (bio)-sensors. For instance, BDD is an attractive electrode material for detecting neurotransmitters such as dopamine [27–31], which are frequently detected with carbon fiber or glassy carbon electrodes. A common problem thereby are electrode fouling processes [32], or the presence of

other electrochemical active species like ascorbic acid [31,33]. Furthermore, BDD electrodes can be miniaturized, and microelectrodes [29,34] and nanoelectrode arrays [35] have been reported.

2.1.1.1. Diamond growth and doping

Electrochemistry with boron-doped diamond electrodes requires sufficient growth rates and doping, which was obtained with the successful development of a CVD process for growing diamond. The first process reported in literature was demonstrated by Eversole at Union Carbide Corporation at sub-atmospheric conditions, using methane and carbon monoxide [36,37]. Based on the work of Eversole, in the 1970s Angus and coworkers added hydrogen to the fabrication process, thereby increasing the diamond yield during the process by removing unwanted graphitic carbon contents from the deposited diamond phase [38]. Angus and coworkers also demonstrated the first doping of diamond in the early 1970s [39] using a refined CVD process. In the mid-1980s, Setaka and coworkers ultimately developed a CVD process for generating diamond films at an acceptable growth rate for industrial applications, by activating the gas-phase with hot-filament [21,22], microwaves [23] or radio-wave discharge [24,25].

Angus et al. demonstrated the first successful deposition of a conductive diamond film using boron as a dopant [39]. The boron dopant is usually added, depending on the targeted doping level, in small amounts (< 1%) during the deposition process to the source gas. As boron source, commonly diborane [40,41], trimethyl borate [42] or organic borinate ester are used [43], but also solid boron sources have been reported in literature [44].

In order to achieve a diamond formation on the substrate surface, the presence of nucleation sites is required. Therefore, the substrate can either be treated with an abrasive powder to generate nucleation sites by scratching [45], or seeded with nano-crystalline diamond particles. These particles function as “starting points” for the growth of the diamond film, leading to polycrystalline diamond films with various grain orientations due to the statistical distribution of the originally “placed” diamond particles [46]. If a nucleation side is present on the surface, the growth mechanism of the diamond can be described by a hydrogen abstraction and carbon addition process (Fig. 1) [47].

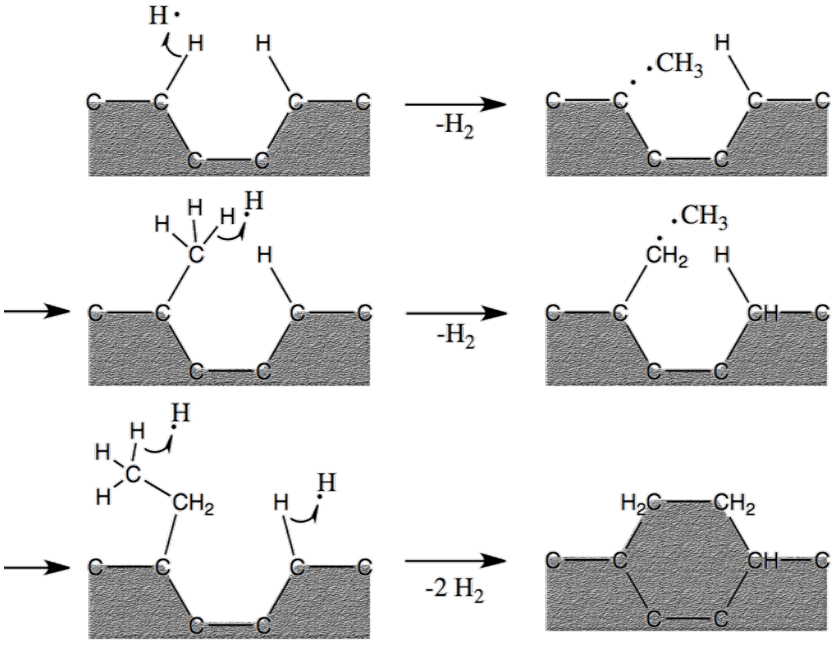

Fig. 1: Schematic representation of the diamond crystal growth mechanism in a CVD deposition process.

Within the reactor, H_2 is decomposed into hydrogen radicals, which react with the hydrogen-terminated surface of the diamond particles, forming H_2. After the hydrogen cleavage, a vacant carbon surface radical is generated. This surface radical can either recombine with other hydrogen radicals in the surrounding volume, or react with a CH_3· radical generated by the reaction of a CH_4 molecule (≤ 1% of the gas mixture) with other hydrogen radicals. This newly attached carbon group can be incorporated into the crystal lattice if another carbon group is attached after activation (hydrogen radical) and an adjacent surface radical is present, resulting in the formation of an atomic bond and the growth of the crystal lattice (Fig. 1). Alternatively, the carbon group may again be etched away or may be desorbed into the gas phase. In addition to the formation of CH_3· radicals, the atomic hydrogen also has a secondary function. If side reactions occur, like the formation of graphitic carbon, these spots are immediately removed due to the presence of the atomic hydrogen in the gas phase, etching non-diamond carbon impurities with a much faster rate than the diamond phase, ensuring the deposition of diamond as impurities are continuously removed. Hence, the growth of the diamond is characterized by simultaneously occurring etching and deposition processes. Therefore, diamond deposition can only be achieved if the deposition rate is higher than the etching

caused by the hydrogen radicals, which are either generated via hot filament or plasma.

2.1.1.2. Material properties of boron-doped diamond

The carbon atoms are arranged in a tetrahedral orientation inside the diamond crystal lattice due to their sp^3-hybridization of the atomic orbitals. All carbon atoms are linked with four adjacent carbon atoms through strong covalent bonds, forming a face-centered-cubic compact three-dimensional crystal structure with an internuclear distance of 1.54Å (as shown in Fig. 2) [48].

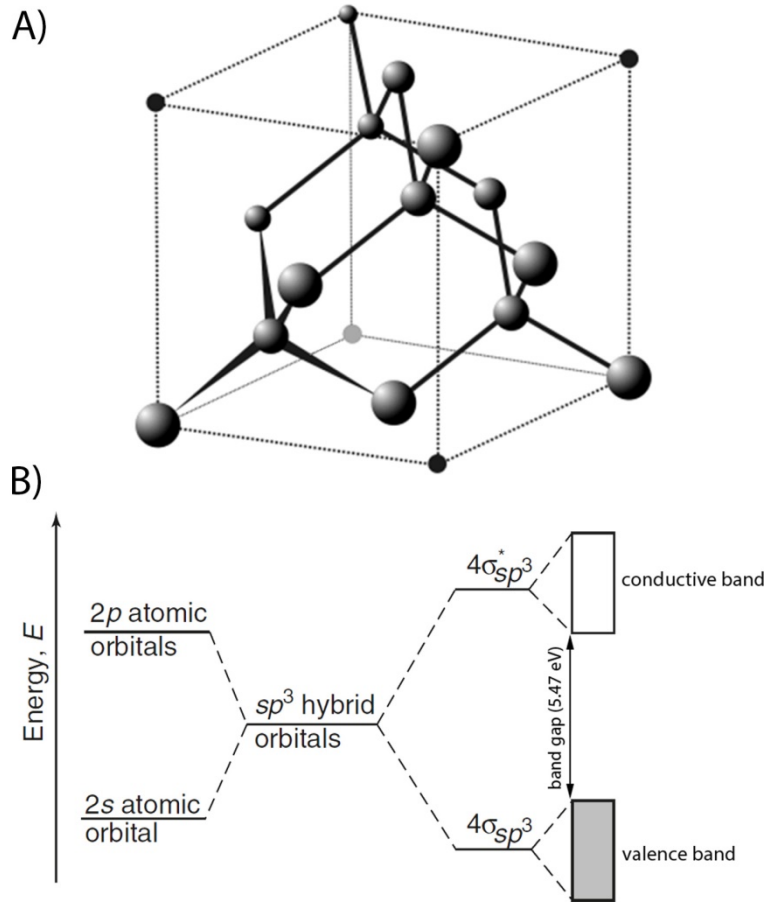

Fig. 2: A) Diamond crystal structure; B) electronic diagram of diamond; adapted with permission from M. A. Quiroz, E. R. Bandala, Types of conducting diamond materials and their properties, in: E. Brillas, C. A. Martinez-Huitle (Eds.), Synthetic diamond films preparation, electrochemistry, characterization, and applications, Hoboken, N.J.: Wiley, 2011, pp. 57–75 ; Copyright 2011, John Wiley & Sons, Inc., Hoboken, New Jersey [48].

The overlap of the sp^3-hybridization of the atomic orbitals results in a large band gap of 5.47 eV between valence and conduction band [49]. This electron distribution also

leads to the strong bonding between the single carbon atoms, resulting in the diamond's superior physical stability and absence of almost any chemical reactivity. The band gap is also responsible for the high thermal stability of diamond as the gap represents an energy barrier, which makes it nearly impossible for electrons to transfer from the valence to the conductive band, resulting in diamond as a non-conductive material in its undoped state. By incorporating boron into the crystal lattice of diamond, a pseudo-conduction band with an acceptor level of 0.37 eV [50] above the diamond valence band is generated (Fig. 3). As boron is a representative of the third element group, the incorporation of this element generates an electron deficiency (hole) inside the crystal structure leading to a p-type semiconductor.

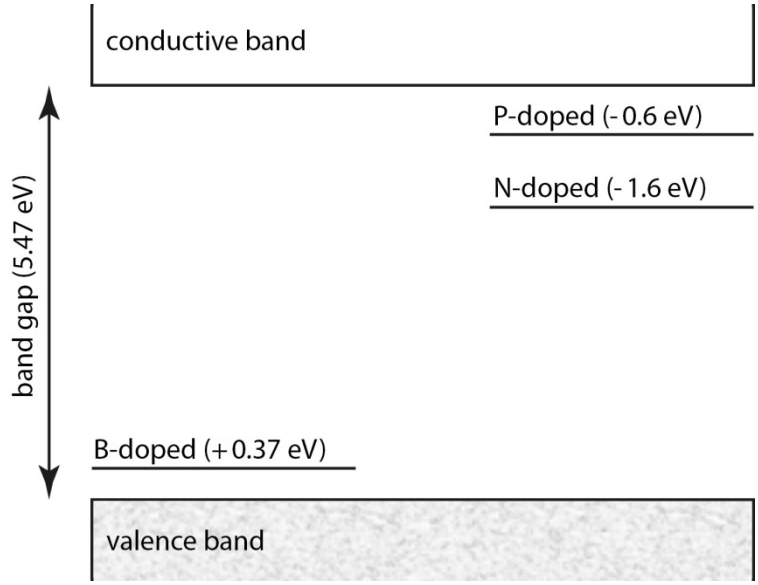

Fig. 3: Energy diagram of the doping states of differently doped diamonds.

With raising boron concentration during the deposition process, the gap between valence band and acceptor level is reduced [51,52], due to the formation of an impurity band. Finally, if the boron concentration exceeds the concentration of 10^{20} - 10^{21} cm^{-3}, the boron-doped diamond achieves semi-metallic characteristics with resistivities lower than 0.001 Ω/cm [53]. One of the most beneficial properties of BDD is related to the high overpotential for oxygen and hydrogen evolution in aqueous solutions compared to other electrode materials such as Pt or Au [54]. This characteristic may be attributed to the absence of surface sites, required for the adsorption of intermediate reaction species for the oxygen/hydrogen evolution. BDD is normally hydrogen-terminated after growth and reveals a chemically inert surface. If non-diamond carbon impurities are present, these surface sites may be available

for adsorption and a smaller potential window of the electrode is usually observed [50,55]. The surface termination of as-grown BDD can be altered to an oxygen-terminated surface, for example by oxygen plasma treatment [56] or anodic treatment in aqueous solution [57,58]. While hydrogen terminated BDD shows hydrophobic surface characteristics and a fast electron transfer behavior, oxygen-terminated BDD reveals, due to the polar oxygen groups at the surface, hydrophilic surface characteristics and additionally, a slow electron transfer behavior for certain redox couples [56,59]. This can be attributed to electrostatic effects occurring between the electrode and the analyte [60]. Additionally, a reduced conductivity of oxygen-terminated BDD films may be observed, related to the loss of surface conductivity. The phenomena of surface conductivity is observed at hydrogen-terminated diamond films in its doped or undoped form, related to the formation of electron holes at the diamond surface due to an electron transfer into the aqueous solution [61]. BDD also shows low background currents and low double-layer capacitance, which can be several orders of magnitude lower compared to standard electrode materials. These low background currents and capacitance may be correlated to the following properties: First, the absence of carbon-oxygen groups at the electrode surface [62], as it has been reported in literature that the absence of these functional groups also influence the background current of other carbon-based electrode materials like glassy carbon [63] and carbon fiber electrodes [64]. Second, the low density of electronic states close to the Fermi energy level at the electrode surface, which is related to the semi-conductor properties of the electrode material [62]. As a consequence, a lower density of counter ions is present at the solid liquid interface if a potential is applied to the electrode. Third, the diamond electrode surface appears mostly in a polycrystalline surface geometry, and therefore may be considered a “microelectrode array” [62], as the boron uptake in the crystal lattice during growth depends on the crystal face orientation, resulting in spots with a higher boron concentration than the surrounding area [65]. Another property of BDD is the low adsorption affinity of electrochemically detectable molecules and their conversion products, resulting in an electrode material less affected by electrode fouling [32]. This may also be explained by the inert surface of the electrode material. Furthermore, BDD electrodes are biocompatible, which makes them suitable for in-vivo studies [66].

2.1.2. Applications

Due to the extended potential window of BDD, one of the most prominent applications at an industrial scale is the use in waste water treatment [50]. The high overpotential of the electrode material for oxygen generation allows hydroxyl radical production with high current efficiencies [67]. This highly reactive oxidizing agent is commonly used for the decomposition of organic water pollutants [50,68]. The high overpotential observed at BDD electrodes renders them attractive materials in electrochemical synthesis, for example, in inorganic chemistry for producing strongly oxidizing agents such as ozone [69] or peroxodisulfate [70]. So far BDD has mainly been used on an industrial scale for electro-synthesis and water treatment, but also for a variety of electroanalytical applications in both macroscopic and microscopic dimensions. For electroanalysis, the outstanding electrochemical properties of BDD have made this electrode material the first choice for specific analytes to overcome common problems like electrode fouling or a too narrow potential window. For example, the detection of cysteine at BDD electrodes doesn't suffer from electrode fouling [16], which is typically observed using Au electrodes. BDD is also superior compared to glassy carbon (GC) electrodes in respect to the detection of sulphur containing species, as the electron transfer at BDD electrodes is the rate determining step in contrast to GC electrodes, where the desorption from the surface determines the conversion rate of cysteine [16]. In addition to cysteine [16,71], BDD has been used for the detection of a variety of bio-molecules like adenosine [72,73], ascorbic acid [27,31,74], catechols and catecholamines [74], dopamine [15,27–29,31,32,75,76], glucose [60,77–83], histamine [84] and serotonin [84,85].

The application range of BDD is not limited to as-grown H-terminated electrodes. Also, a variety of surface modifications have been introduced to improve selectivity. For example, a UV-light induced photo-coupling reaction was used to link the enzyme tyrosinase to a BDD electrode [33] with allylamine as linker molecule. The resulting biosensor resulted in a stable sensing scheme for phenolic derivates, exhibiting an improved linear range, long-term stability and increased sensitivity, which also showed excellent properties for the detection of dopamine in the presence of ascorbic acid.

In addition, the transparency of BDD for electromagnetic radiation, ranging from the UV-Vis (≥225 nm) [20,86] to the deep IR region [87], enables spectro-

electrochemistry. Up to now, tin-doped indium oxide optical transparent electrodes, which use is limited to the UV-Vis region of the electromagnetic spectrum, are frequently applied for spectroelectrochemistry. BDD as conductive transparent material has currently been demonstrated only in two different approaches: as thin BDD film supported by a non-conductive substrate for mechanical stability. As supporting substrate either undoped Si (IR) [87] or quartz (UV-Vis) [86] can be used. Alternatively, free-standing electrodes, like mechanically polished BDD films [20] with thicknesses up to approximately 400 µm or single crystalline diamonds coated with BDD can be applied [88]. Besides spectroelectrochemistry, BDD is also an attractive material for conductive AFM or combined AFM-SECM with integrated BDD electrodes. For example, a BDD electrode at the tip of an AFM cantilever was recently reported [89]. Alternatively, the integration of a BDD microelectrode into an AFM tip, recessed from the AFM tip apex, will be discussed in detail in chapter 4.

2.2. Atomic force microscopy (AFM)

2.2.1. Working principles

Atomic force microscopy, in contrast to classical microscopy methods (light microscopy), is based not on “seeing” objects but more on “feeling” them. When a nanometer-sized sharp tip, which is frequently termed “probe”, is laterally scanned across the sample surface, the interaction forces between the scanning probe and the sample are detected. The forces measured can be described in the simplest case by the Lennard-Jones-potential (Fig. 4), which reflects the intermolecular van-der-Waals (VDW) interactions and Pauli repulsion. Also other interactions between the sharp tip and substrate like electrostatic, dipole-dipole [90] or chemical interactions [6] can be used for surface investigations.

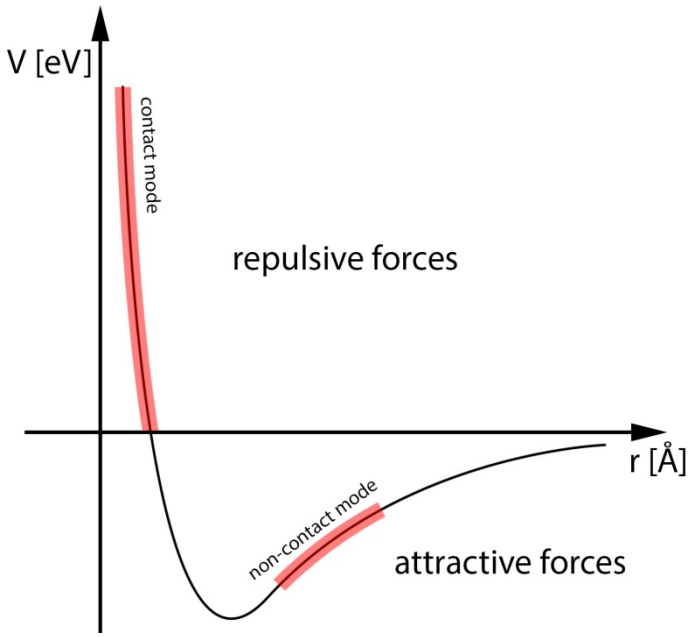

Fig. 4: Simplified illustration of the Lennard-Jones potential and corresponding AFM modes.

The probe consists ideally of an atomically sharp tip at the end of a cantilever arm, which has typically dimensions in the range of 100-200 µm, working as transducer for the intermolecular forces acting on the tip. The occurring forces result in a bending of the cantilever correlated to the change in surface topography, while the tip is in physical contact with the sample (contact mode) or in a change of amplitude or frequency if the cantilever is excited to a periodic oscillation (intermittent or non-contact mode). Commonly the bending/oscillation is detected by an optical read-out.

Therefore, a laser beam is reflected from the backside at the end of the cantilever arm and is detected at a photodiode consisting of four areas with independent readout. By subtracting the photocurrent detected between top and bottom part of the photodiode ((1+2)-(3+4)), the vertical deformation of the cantilever can be monitored (Fig. 5).

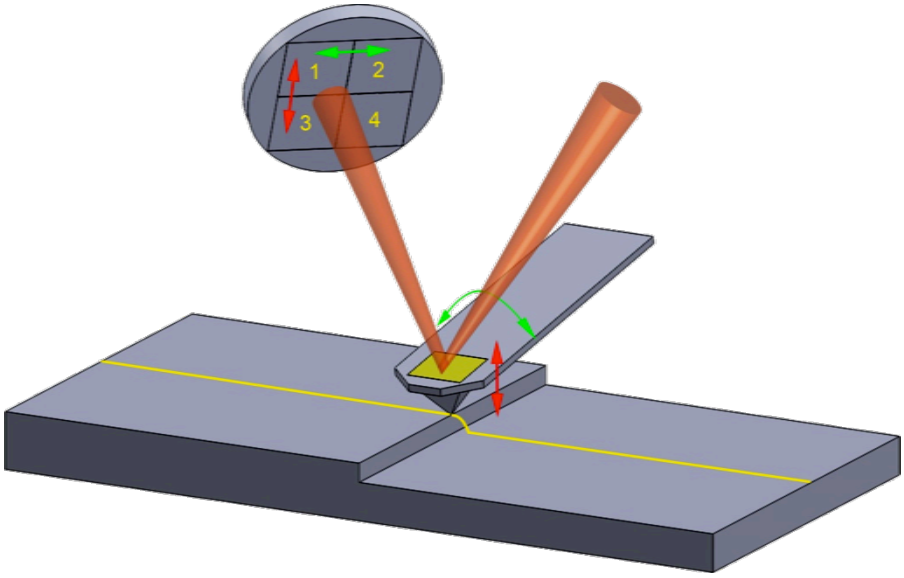

Fig. 5: Optical read-out principle of an AFM system; red: deflection; green: friction.

For topographical imaging commonly the tip is scanned over the sample surface (or vice versa) using piezo-elements for accurate tip-sample positioning with sub-nanometer precision in x,y,z direction.

2.2.2. AFM modes

2.2.2.1. Contact mode

While scanning in contact mode, the AFM tip has physical contact with the surface referring to the repulsive area of the Lennard-Jones potential. These repulsive forces originate from overlapping orbitals of the tip and the sample surface, while applying a pre-specified amount of pressure/force towards the surface. The resulting deformation of the cantilever is constantly measured during scanning by the optical read-out system. Principally, two different approaches of contact mode measurements are possible: constant height or constant force mode.
In constant force mode, the cantilever deflection is kept constant reflecting a constant force, which is related to the force constant by Hook's law. In order to maintain the

applied force, the bending of the cantilever (deflection signal) is continuously monitored during scanning. If the presences of surface objects or change in interaction force result in an increase/decrease of the force, which is related in an actual change of the deflection signal, a software-controlled feedback loop readjusts the force in relation to the force setpoint by applying a relative z-displacement until the specified force is re-established. These z-displacements are mapped relative to the x,y-coordinates of the tip position resulting in a subsequent reconstruction of the sample topography. The quality of the feedback electronic and response time directly correlates with the image quality and possible scan speed. Additionally to the z-displacement, also the torsion along the cantilever axis can be monitored, which is detected by the subtraction of the left and right part of the split photodiode ((2+4)-(1+3); friction; Fig. 5), providing information about material composition due to variations of the lateral forces parallel to the sample surface.

In constant height mode, the feedback loop is disabled and the tip is scanned at a fixed height across the sample surface. The topographical information of the surface is directly obtained by the bending of the cantilever arm. Although a disabled feedback loop enables a higher scan speed, constant height mode can only be used for atomically flat samples, as objects on the surface may result in enhanced physical stress for the cantilever.

Generally, in contact mode scanning over objects may result in damages of fragile samples due to the mechanical interaction.

2.2.2.2. Non-contact mode

In non-contact mode the cantilever has no physical contact as the cantilever is periodically oscillating above the sample surface referring to the attractive region of the Lennard-Jones potential. The information of the surface topography can either be extracted by the detection of an amplitude variation (AM-AFM) or frequency shift (FM-AFM), if the oscillating cantilever is in close proximity to the sample surface. In AM-AFM the cantilever is excited close to its resonance frequency with a fixed excitation amplitude. While approaching to the surface, the tip starts “to feel” at a certain distance the attractive force interaction with the sample surface. With decreasing distance to the sample surface, the amplitude is also linearly decreasing. This linear dependency of amplitude and tip-sample distance can be utilized as signal for the feedback system during data acquisition to maintain a constant

distance. In FM-AFM, the cantilever is excited at a constant oscillation amplitude at its free resonance frequency. When the cantilever is approached to the surface, a frequency shift is induced relatively to the strength of the force interactions. The frequency shift can then be used as feedback signal to maintain a constant tip-sample distance, while scanning the sample surface. By plotting the z-displacement relative to the tip position, the topographical image can be reconstructed. As the tip is not touching the sample surface, damaging fragile and soft samples is avoided, rendering this mode attractive for biological applications, like the investigation of living cells. For high-resolution non-contact AFM (FM-AFM) imaging, the system is operated under (ultra-high) vacuum conditions to avoid undesired long-range capillary forces of liquid monolayers masking VDW forces. While in contrast to contact-mode AFM, the AFM tip can penetrate the liquid monolayers in non-contact AFM, the tip can only acquire a superimposed signal of the monolayers.

2.2.2.3. Intermittent mode

The intermittent mode can be considered as a hybrid mode between contact and non-contact mode. In intermittent mode, the cantilever has only intermittent contact with the sample surface, as the cantilever is only periodically touching the surface through the oscillating excitation of the cantilever in close proximity to the sample surface at its resonance frequency. Therefore, the force impact on the sample surface is significantly reduced (in particular friction forces), while the problems with high resolution non-contact mode measurements due to long-range capillary forces are minimized. Comparable to AM-AFM, the topographical signal is acquired through monitoring the amplitude changes. The decrease in amplitude relative to the free oscillating amplitude reflects therefore the applied force to the sample surface and mostly has direct influence on the image quality [91]. Additionally to the amplitude, also the phase shift (time delay between excitation and cantilever oscillation) is often recorded in intermittent mode experiments. This phase shift is strongly influenced by the tip-sample interactions, in particular by variations in material composition, adhesion, surface friction and viscoelasticity [92,93].

2.2.3. Combined AFM techniques

Complex phenomena are often encountered when studying biological samples, catalytic processes and/or dynamic processes at liquid/liquid or solid/liquid interfaces like in life sciences, corrosion or energy storage research. Such problems require a synergetic analysis of chemical, kinetic and mechanical properties, ideally with high temporal and spatial resolution. A multitude of combined analytical techniques involving AFM have been reported over the years to obtain correlated topographical and chemical data [94].

For instance, fluorescence microscopy represents one of the key methods in life sciences and can be correlated with topographical information obtained by AFM. Hecht et al. used a fluorescence microscope in combination with AFM for the observation of stimulated surfactant release in lung epithelial cells using the fluorescence microscope for the detection of lamellar body fusion and AFM for investigating the changes in the cellular structure [95]. Also more sophisticated fluorescence microscopy methods like stochastic optical reconstruction microscopy (STORM) in combination with AFM have already been reported in literature, achieving optical information beyond the diffraction limit [96]. However, labeling with fluorophores is required. IR- and Raman spectroscopy are considered to be the most important labeling free spectroscopic methods for obtaining molecular information and hence are of significant analytical importance. Comparable to combined fluorescence microscopy–AFM, the combination with far-field IR or Raman is also diffraction limited, but can also be extended beyond the diffraction limit by utilizing surface enhancement effects [97]. The combination of Raman spectroscopy with AFM can either be achieved using a far-field approach [98] (e.g., side-illumination) or tip-enhanced Raman spectroscopy using a metal-coated AFM tip. With the tip in close proximity to the sample surface, an increase of the vibrational signature of the molecules of interest is obtained with resolutions beyond the diffraction limit [99]. A combination of IR-spectroscopy with AFM has been achieved using an ATR crystal as waveguide with a top-down AFM mounted above the ATR crystal. Sample molecules in close proximity to the ATR surface are detected within the evanescent field penetrating into the adjacent medium, while the AFM allows in-situ imaging of the ATR surface [100,101]. This approach grants no access to lateral spectroscopic information - however samples can be imaged in solution. Laterally resolved IR-AFM

combinations, using a metal-coated AFM tip as scattering device for IR radiation have also been demonstrated [102]. Additionally to optical techniques for complementary information, electrochemical methods are attractive for such combinations. Details on the integration of electrochemical techniques into AFM will be discussed in detail in section 2.4.

2.3. Scanning electrochemical microscopy (SECM)

2.3.1. Fundamentals

SECM represents similar to AFM a scanning probe technique, where an electrochemical probe is scanned across the sample surface by using piezoelectric scanners or stepper motors in order to acquire laterally resolved electrochemical information of the sample surface. Therefore, nanoelectrodes or ultramicroelectrodes (UMEs) with an electrode radius ranging from several hundred of nm up to 25 µm are commonly used [103]. The electrodes are usually fabricated by sealing micro wires into glass capillaries, which are then exposed as disc electrode by grinding and polishing (Fig. 6).

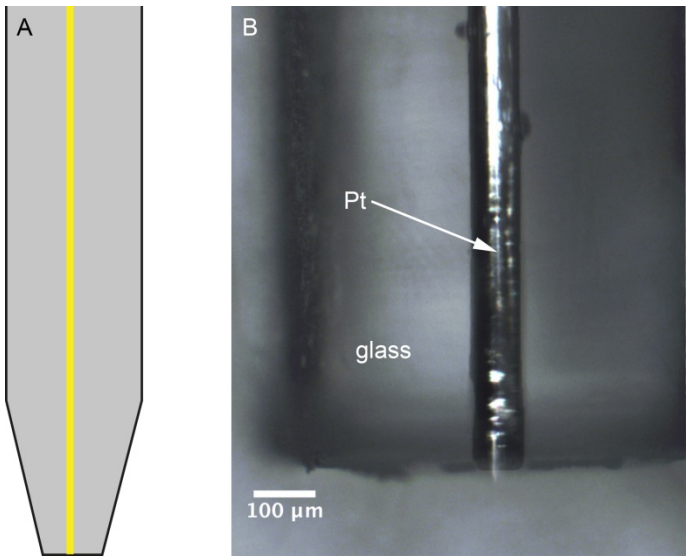

Fig. 6: A) Schematic illustration of an UME; B) optical image of a Pt-UME (50 µm).

In contrast to macroscopic disc electrodes, UMEs are characterized by a reduced double layer capacity, enhanced mass transfer and a reduced ohmic drop [104–106]; these effects are related to the reduced electrode dimensions. The reduced double layer capacity is reciprocal proportional to the size of the UME, resulting in a fast

decrease of non-faradaic current contributions within a fraction of a second [104]. The enhanced mass transfer at the electrode surface is dominated by a hemispherical diffusion profile instead of a planar diffusion (see Fig. 7A,B), observed at macroscopic electrodes. This enhanced mass transfer in combination with the fast decay of non-faradaic current contributions results in well-defined steady state currents (Fig. 7F) compared to the peak-shaped response (Fig. 7E) observed at macroscopic electrodes, which is described by the modified Cottrell equation (Fig. 7D) [106].

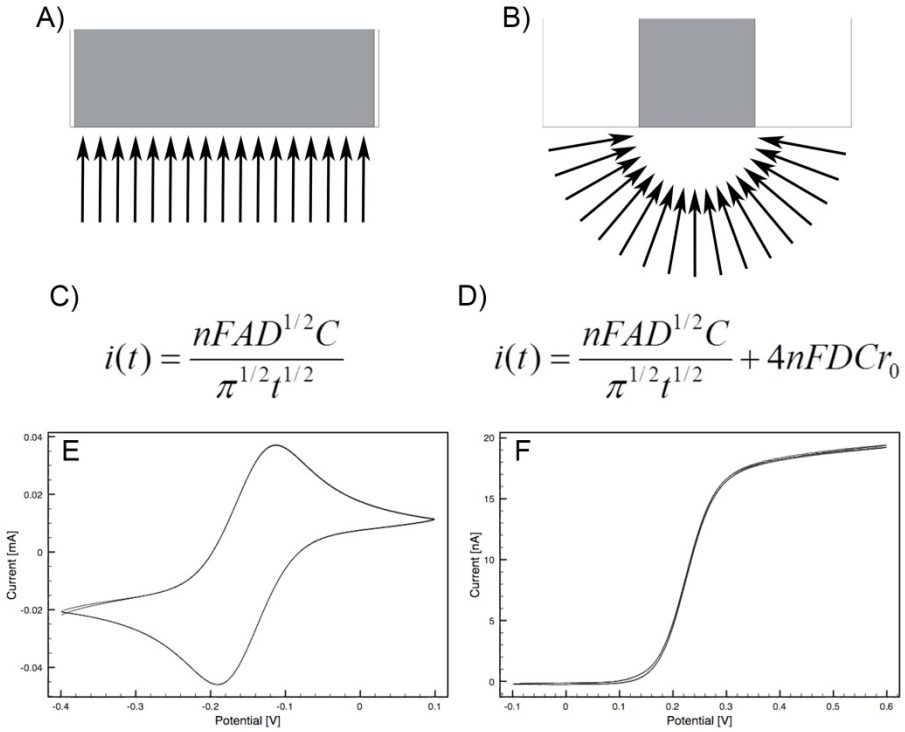

Fig. 7: A) Planar diffusion profile; B) hemispherical diffusion profile; C) Cottrell equation for macroscopic electrodes; D) modified Cottrell equation for microelectrodes; E) exemplary CV of a macroscopic electrode recorded in 10 mM $[Ru(NH_3)_6]Cl_3$ / 0.1 M KCl; F) CV recorded at a ultramicroelectrode in $K_4[Fe(CN)_6]$ / 0.1 M KCl; CVs are recorded vs. sat Ag/AgCl.

UMEs in combination with their inherent properties led in the late 1980s to the introduction of SECM by Bard et al. [4,5]. In SECM the electrochemical information is obtained by recording the current flux of an electrochemical active species at the UME surface relative to the UME position. Depending on the imaging mode, electrochemical surface properties, as well as kinetic information of electrochemical reactions can be obtained (see section 2.3.2).

2.3.2. SECM imaging modes

2.3.2.1. Feedback mode

In feedback mode, the current generated by the conversion of a redox mediator added to solution at the biased UME is monitored relative to the electrode position. In close proximity to the sample surface (several electrode radii), the current is influenced by the sample properties (conductivity, surface activity), the distance and size of the UME. When the tip is far away from the sample surface (several tens of the electrode radii), the measured steady state current of a disc-shaped electrode can be described by the Saito equation [107], if only diffusion is considered responsible for the mass transport towards the electrode (Eq. 1).

$$i_{t,\infty} = 4nFDCr_0$$

Eq. 1: Steady state current of a disc UME in bulk solution; with n = number of electrons; F = Faraday constant; D = diffusion coefficient; C = concentration of the electrochemical active species; r_0 = electrode radius [107].

∞ indicates hereby a distance far away from the sample surface, resulting in diffusion conditions similar to bulk solution and therefore also to similar steady state current values. When the tip is approaching the sample (Fig. 8) surface, following scenarios can be observed depending on the conductivity of the sample surface.

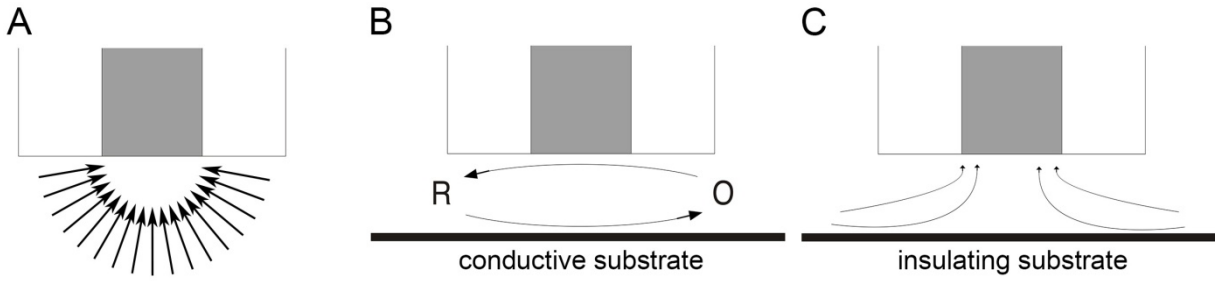

Fig. 8: Basic principles of the SECM feedback mode; redox mediator diffusion towards the electrode surface in A) bulk solution; B) between the UME and a conductive surface; C) in the presence of a non-conductive surface.

Conductive surface: If the UME is in close proximity to a conductive surface, the electrochemically converted redox mediator diffuses to the conductive surface, where it is regenerated to its initial redox state. The regenerated redox mediator can diffuse back to the UME and can be again converted (Fig. 8B). Because the UME is in close proximity to the sample surface, this process occurs at a measureable time scale. As a result of the redox mediator regeneration, the current measured at the UME increases with a decreasing UME-surface distance (Fig. 9A) and an overall increased current ($I_t > I_{t,\infty;}$ positive feedback) is detected, which is described by Eq. 2.

$$\frac{i_t(L)}{i_{t,\infty}} = 0.68 + \frac{0.78337}{L} + 0.3315\exp\left(-\frac{1.0672}{L}\right)$$

Eq. 2: Analytical approximation for the approach towards a conductive substrate as shown in Fig. 9A; with L = normalized distance (d/r_0) [108].

Insulating surface: If the UME approaches an insulating surface, the hemispherical diffusion towards the electrode is hindered, resulting in a reduced mass transfer towards the UME. Therefore, the detected current decreases with decreasing UME-surface distance (and a lower current is detected; $I_t < I_{t,\infty;}$ negative feedback), which is described by Eq. 3 for UMEs with RG ≤ 10 ($RG = r_{glass}/r_0$) [108].

$$\frac{i_t(L)}{i_{t,\infty}} = \frac{1}{0.292 + \frac{1.5151}{L} + 0.6553\exp\left(-\frac{2.4035}{L}\right)}$$

Eq. 3: Analytical approximation for the approach towards an insulating substrat as shown in Fig. 9B; with L = normalized distance (d/r_0); RG = 10 [108].

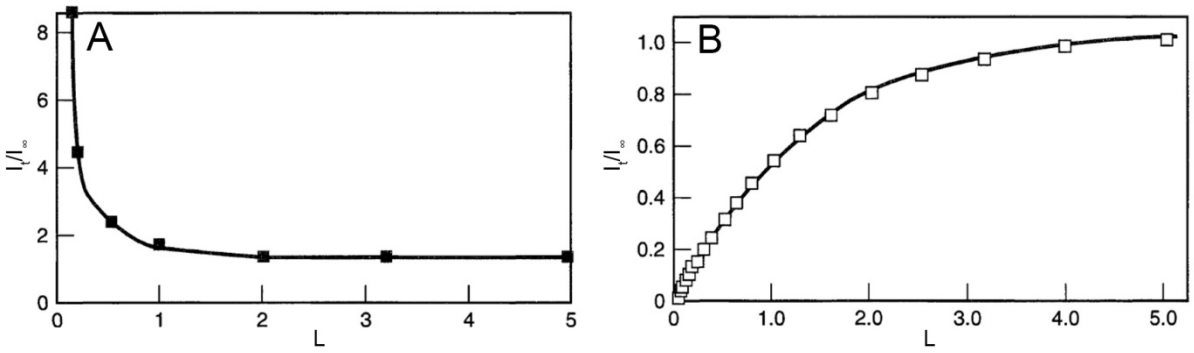

Fig. 9: Approach curves for A) a conductive and B) an insulating substrate; with L = normalized distance (d/r_0); adapted with permission from Ref. [109]; Copyright 1994, The Royal Society of Chemistry.

As shown in Fig. 9, the influence on the current of the redox mediator conversion strongly depends on the distance of the UME to the sample surface. Therefore, the current signal can also be used to position the UME in z-direction relative to the sample surface by acquiring current-distance curves (approach curves). Additionally, the current behavior is also influenced by the RG value and the kinetics of chemical reactions related to the electrochemical conversion (e.g., regeneration rate on the surface or subsequent chemical reaction). A higher RG-value results in a more confined volume between the UME and the sample surface. While approaching a conductive surface, this has little effect on the current-distance behavior, as the regeneration cycle is not significantly influenced. However, the approach towards an insulating surface is severely influenced, as the redox mediator molecules for electrochemical conversion have to diffuse towards the electrode surface from outside the insulating boundary [108]. With increasing RG-value, the required diffusion distance for the redox molecules increases, which results in a more limited diffusive flux and therefore in an earlier onset of decreasing current during approach (Fig. 10).

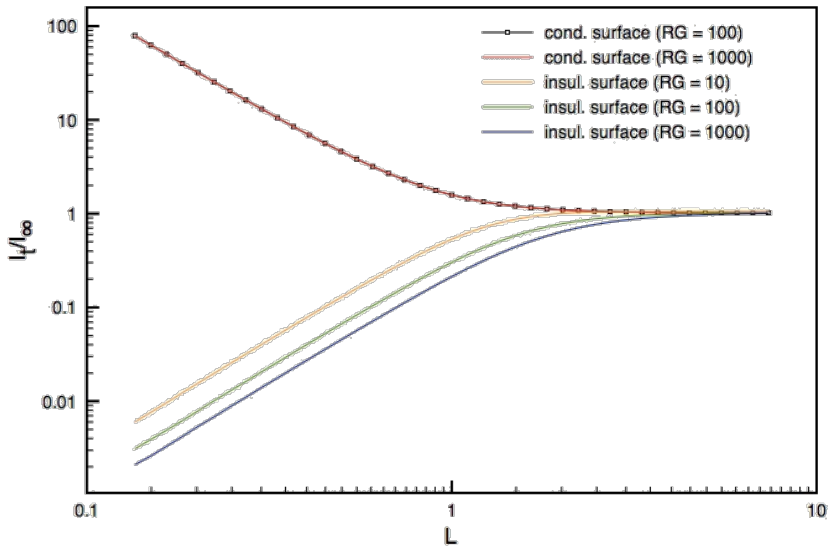

Fig. 10: Influence of the RG-value on theoretical calculated approach curves. Experimental data obtained and reprinted with permission from J. Kwak, A. J. Bard, Scanning electrochemical microscopy. Theory of the feedback mode, Anal. Chem., 61, 1989, 1221–1227; Copyright 1989, American Chemical Society [110].

Increasing rate constants for a subsequent chemical reaction after electrochemical conversion, as shown in Fig. 11, result for example in a decrease of the positive feedback signal until a full negative feedback signal is obtained at an infinite reaction rate. This can be compared to a decrease in the capability of the surface to regenerate the electrochemically converted redox mediator, and represents qualitatively the approach curve transition from a conductor to an insulator.

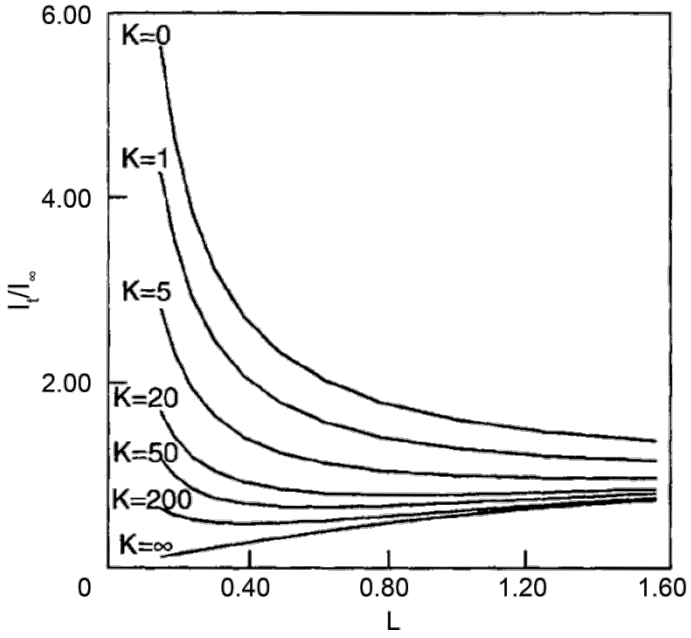

Fig. 11: Simulated approach curves towards a conductive surface with a subsequent chemical dimerization reaction of the converted redox mediator; with K = normalized (dimensionless) rate constant; reprinted with permission from Ref. [109]; Copyright 1994, The Royal Society of Chemistry.

2.3.2.2. Generation-collection mode

The first SECM-type experiments were performed in generation-collection mode [111–113]. In principle, a redox active species generated at the UME can be detected at a conductive sample, which is termed tip generation - sample collection mode (TG-SC). Alternatively, the redox active species may be generated at the sample and collected at the tip (sample generation - tip collection mode (SG-TC)). For example in TG-SC mode, which is considered to be the more efficient technique, the tip is biased to a potential where a redox active species is generated, which can then be detected/collected at the conductive sample surface. As the sample surface is much larger than the electrode surface of the tip and the tip is positioned in close proximity to the sample surface, collection efficiencies of almost 100% can be achieved [103]. With the TG-SC mode also kinetic data can be determined, for example if the produced electroactive species undergoes a reaction during the diffusion towards the sample surface [103].

2.3.3. Applications of SECM

Numerous SECM applications have been demonstrated over the years providing laterally resolved or stationary (fixed tip position) investigations ranging from material related research to life sciences. Holt et al. [114] and Wilson et al. [115] demonstrated laterally resolved imaging of the electrochemical activity of boron-doped diamond electrodes e.g., relative to the boron concentration. Also the investigation of BDD nanoelectrode arrays with an electrode size of 320 nm embedded into non-conductive diamond has been reported recently [116] using shear-force SECM. SECM matured into an important technique in corrosion science e.g., for the investigation of pit formation on iron substrates [117,118]. For pit formation, SECM electrodes are used either producing locally corrosive environment or forming active species inducing localized corrosion pits. Gabrielli et al. [117] utilized a cathodically biased Ag/AgCl microelectrode in close proximity to the iron surface to produce chloride ions, resulting in passivation layer breakdown under controlled conditions. Simultaneously, the occurring iron dissolution current of the surface was measured to evaluate the amount of chloride ions necessary for passivation layer breakdown, in dependency of pH and sample-tip distance. While Gabrielli et al. used chloride ions to facilitate the passivation layer breakdown, Eckhard et al. [118] used the UME as auxiliary electrode in close proximity to the iron surface (working electrode), which was anodically biased. By limiting the current flow to the volume between UME and sample surface, the anodic passivation layer breakdown appeared predominately in close proximity to the UME. After pit formation, the surface was visualized using alternating-current (AC)-SECM. In addition to investigations in material science, SECM has also been used to target biologically relevant problems. Amemiya et al. investigated the ion transfer across a horizontal black lipid membrane by SECM experiments in feedback and generation-collection mode, using voltammetric ion-selective micropipette electrodes [119]. The transfer of redox inactive ions like K^+ through transport channels like gramicidin was demonstrated. Without a concentration gradient across the membrane, no ion transfer in feedback mode could be observed and the feedback signal was similar to an insulating surface. With a concentration gradient, a reduced negative feedback signal was obtained, due to the ion transport across the membrane. Theoretical calculations for the approach curve showed that a first order interfacial rate constant was not sufficient to describe the ion transfer across the membrane. With an

externally applied potential across the artificial membrane as driving force, K^+ ion transfer generation-collection mode analogous experiments could be conducted. The results of these experiments revealed that at least three independent steps were involved in the ion transfer (transfer of K^+ to the pore structure / ion transfer across the membrane / transfer of K^+ to the aqueous phase). Additionally, at sufficient high driving potentials the detected current is limited by the diffusion process, which is potential independent.

Also the detection of secreted electroactive molecules like catecholamines (adrenaline, noradrenaline or dopamine) from cells have been reported using SECM [120]. Hengstenberg et al. monitored temporally resolved the secretion of catecholamines after the cells were stimulated by increasing the K^+ concentration in the surrounding media with a carbon fiber electrode positioned in close proximity of individual cells.

Despite the broad field of applications, SECM in constant height mode is prone to problems related to the current dependency of the electrode-to-sample distance. Whereas, the combination of AFM with SECM enables a constant distance positioning of the electrode (for details see the following section).

2.4. Combined AFM-SECM

2.4.1. Fundamentals

Combining AFM with SECM can be achieved by integrating an electrochemically active area into an AFM tip. As of now two main approaches are described in literature for the fabrication of combined AFM-SECM probes. The first approach describes a relatively cheap and benchtop compatible way to fabricate probes by etching, bending and insulating a conductive wire. These “hand-made” AFM-SECM probes result in small tip apex-located electrodes (Fig. 12A) [7,121,122]. State-of-the-art microfabrication techniques are used for the second approach, where defined tip and electrode geometries can be achieved at the expense of fabrication costs. The microfabricated probes are typically divided into two subcategories: A) Probes with a conductive conical tip apex [89,123–129] and B) with recessed electrodes having different electrode geometries, with one exemplary shown in Fig. 12B [8,17,130–134] (AFM tip-integrated frame electrode).

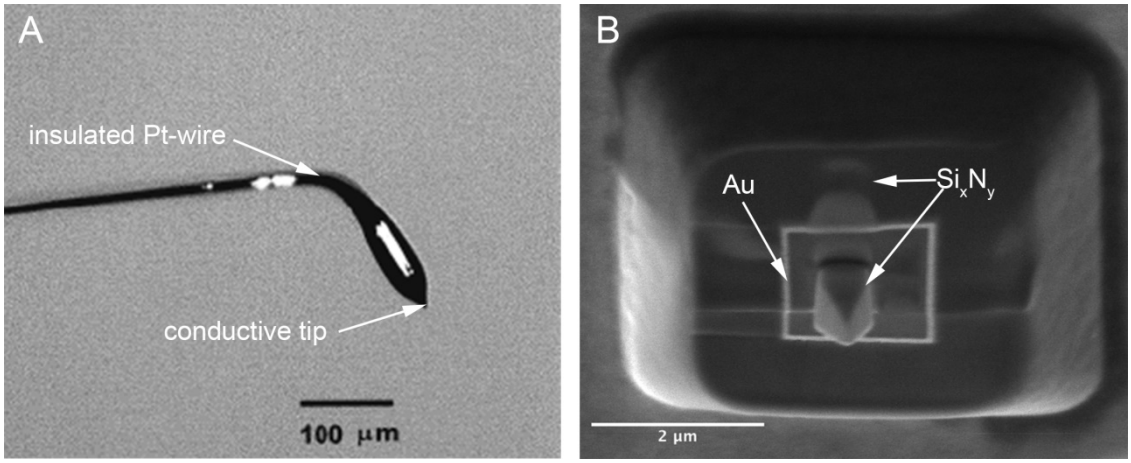

Fig. 12: Exemplary images of A) a hand-made AFM-SECM probe reprinted with permission from J. V. Macpherson, P. R. Unwin, Combined scanning electrochemical-atomic force microscopy, Anal. Chem., 72, 2000, 276–285; Copyright 2000, American Chemical Society [7]; and B) a microfabricated AFM-SECM with recessed Au frame electrode.

2.4.2. Advantages compared to SECM

Conventional SECM (constant height imaging) is based on recording approach curves to determine the distance between UME and sample surface. After positioning the UME at the sample surface in a distance of up to several electrode radii, the UME is scanned in constant height in the x-y plane across the sample surface. To determine the distance between the UME and the sample surface, classically current distance approach curves are recorded and fitted to theoretical calculated current distant curves [108,110,135]. The electrochemical signal recorded at the UME may not only be correlated to the electrochemical properties of the sample but also to changes in the distance in particular for sub-micrometer electrodes. Hence, this so-called constant height mode [136] may result in falsified electrochemical data or artifacts, in case of an unknown sample with a surface roughness in the order of the electrode radius of the UME, or a tilted surface. The electrochemical information may then be convoluted with the topographical information (Fig. 13).

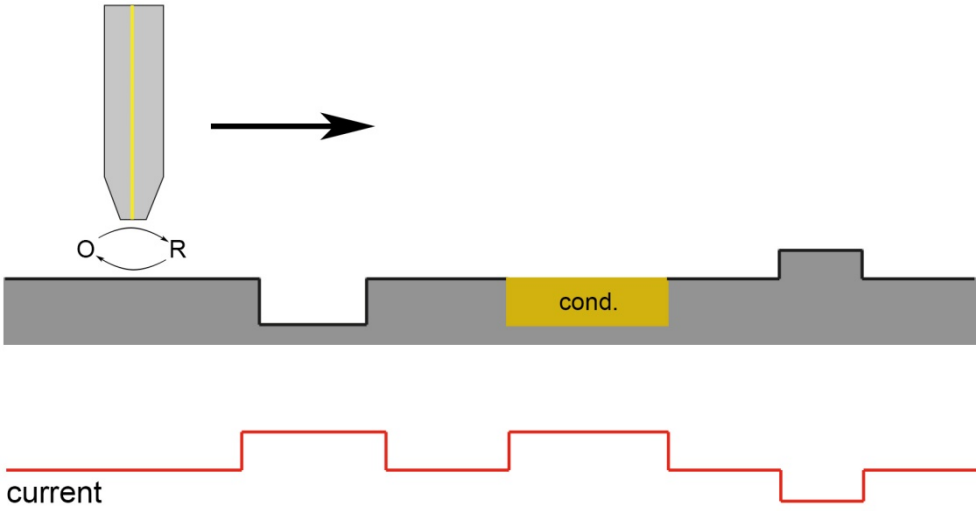

Fig. 13: SECM current response according to topography and sample property changes.

In order to overcome these limitations of the constant-height imaging mode, a shear-force based positioning strategy for UME has been adapted and implemented [137–139], which was derived from near-field scanning optical microscopy [140–142]. Using the oscillation dampening of a laterally vibrating UME allows an accurate positioning of the UME, if the change in amplitude is used as a feedback signal keeping the amplitude at a constant value. As the distance to the surface is continuously corrected with alternating topography, a constant distance is maintained if the topographical variations can be compensated within the temporal resolution of the feedback loop. Nevertheless as the achievable lateral resolution in topography depends on the size of the UME, topographical features cannot be resolved with a resolution comparable to AFM. Although, shear-force based positioning is primarily used for constant distance SECM, alternative strategies such as combined AFM-SECM, STM-SECM [143], NSOM-SECM [144], SICM-SECM [10] or soft electrodes [145] have been reported. An electroactive surface integrated into an AFM probe enables that high topographical lateral resolution of AFM is correlated with simultaneously electrochemical data acquisition. By using recessed integrated electrodes (Fig. 12B), a defined electrode-sample distance is maintained, regardless of the nature of the sample.

2.4.3. Applications of AFM-SECM

Up to now, most of the published research in literature is focused on the development and improvement of combined AFM-SECM probes. The applications of these probes were therefore often limited to model samples like electrode structures or HOPG. For example, Abbou et al. demonstrated the determination of dynamical and structural properties, like end-to-end diffusion coefficient and film thickness, of end-tethered ferrocene moieties linked via poly(ethylene glycol) chains to a gold substrate [146]. These modified polymer chains are capable to shuttle electrons between the combined AFM-SECM probe and the sample surface through the flexible polymer chains. Anne et al. demonstrated a detection scheme, relying upon this flexible polymer chains, to target specific proteins using AFM-SECM and ferrocene-poly(ethylene glycol) marked antibodies for lateral resolved imaging of specific proteins [9]. AFM-SECM has also been used for imaging biologically relevant processes. For example, Kueng et al. demonstrated laterally resolved imaging of enzyme activity and surface topography of oxidoreductase containing polymer spots [130]. Additionally, the mapping of glucose transport through an artificial membrane using an AFM-SECM integrated biosensor was presented by the same group [147]. Also the selective detection of DNA strands have been realized by using immobilized single-stranded DNA on a polypyrrole-modified AFM-SECM probe [148]. Recently, Knittel et al. introduced a novel type of combined probe bearing a conductive polymer tip, which is suitable for force spectroscopy under potential control [149]. Similar to SECM, AFM-SECM has also been used for corrosion studies as shown by Davoodi et al. on aluminum alloys [3,150,151]. They demonstrated the influence of different intermetallic particles [150] on the corrosion behavior by simultaneously recording topographical and electrochemical data. The current in SG-TC mode of the added I^-/I_3^- redox couple was monitored at the combined AFM-SECM probe. With the electrochemical signal, the presence of precursor sites of local corrosion could be detected even before they were actually observable in AFM [3]. Additionally, a size dependency between aluminum dissolution and intermetallic particle size was observed. Large intermetallic particles commonly result in the corrosion of the aluminum alloy around the particles, while small dispersoids seem to be inactive [151].

3. Electron transfer kinetics of FIB-irradiated BDD samples

3.1. Introduction

Over the last two decades, new electrode materials like boron-doped diamond gained considerable significance in the field of electrochemistry due to their outstanding chemical and physical properties [152]. By doping diamond, an insulator with a band gap of 5.47 eV [49], with very high concentrations of boron in the region of 10^{19} - 10^{21} atoms cm^{-3} [153,154], a highly conductive p-type semiconductor with metallic like properties can be obtained. These highly conductive BDD electrodes outmatch most electrode materials concerning chemical inertness [155], potential window [74,153,156,157] and SNR [158]. This outstanding properties grant access to a wide range of electro-analytical applications, especially where the investigated analytes are prone to foul the electrode after electrochemical conversion [16,34]. In addition nano- or micrometer sized BDD electrodes are advantageous due to the small required sample volume [159] and higher current densities leading to improved analytical signals [50,160]. In order to obtain reliable experimental data, the quality of the BDD electrode is of great importance as the electrochemical behavior is influenced by a variety of factors, such as the doping level [65,74,161], structural defects [162], non-diamond carbon impurities [114], crystallographic grain orientation [163], fraction of grain boundaries [114,163], surface termination [58,66,161], and surface modifications [164,165]. The use of hydrogen-terminated BDD for analytical applications is preferred due to a well faceted and hydrophobic surface, as well as a low surface energy [166]. However, it has to be noted that the hydrogen-terminated surface lacks of stability under certain conditions like pH ≤ 6 and an applied anodic potential higher than 1.0 V vs. SCE leading to a (partially) oxygen-terminated surface and as a consequence to a change of the electrochemical properties [58]. However, hydrogen termination can be easily restored by applying cathodic electrochemical treatments [57,167]. In order to fabricate BDD UMEs or electrode arrays, standard micro-fabrication techniques like reactive ion etching [31,168,169] or FIB-based structuring are employed [170,171]. State-of-the-art FIB-technology utilizes gallium ion beams with a beam diameter smaller than 10 nm. Therefore a highly precise prototyping and micro-fabrication at the micrometer scale with nanometer precision can be achieved. As the milling yield (volume of removed substrate material [μm^3]

per amount of accelerated primary Ga^+ ions [nC]) of diamond is low, ranging from 0.07 μm^3/nC [172] (see section 4.2.1) to 0.09 μm^3/nC [173,174], a homogeneous milling behavior, resulting in smooth surfaces [173] can be observed compared to other electrode materials like gold [175]. Nevertheless one disadvantage of using FIB technology for micro-fabrication of BDD electrodes is related to the fact that the impact of accelerated Ga^+ ions with a kinetic energy up to 30 keV results in changes of the surface structure of the irradiated sample area. These changes are related to Ga^+ ion implantation and amorphization of the surface layers in the range of several tens of nanometers [162,174,176–178]. As this amorphization and change of the upper crystal lattices may not affect the functionality of other diamond based devices like micro-electro-mechanical systems (MEMS), it has been shown that the amorphization of doped diamond electrodes have significant impact on the heterogeneous electron transfer behavior of surface sensitive redox species [162,179]. Hence, this requires a fundamental characterization of the FIB milling parameters in relation to the resulting heterogeneous rate constants and how the chosen parameters affect the overall performance of the FIB-modified electrodes. In the past, the degree of damage inflicted by ion beam irradiation on BDD has been investigated employing transmission electron microscopy (TEM) [174,180], Raman spectroscopy [162,176], cyclic voltammetry [162], µ-photoluminescence [178], time-of-flight secondary ion mass spectroscopy (TOF-SIMS) [178] and electron energy loss spectroscopy (EELS) [180]. Also approaches to repair/reduce the FIB-induced damage of the surface have been the focus of research efforts. For example, the influence of gas-assisted fabrication [174] or milling at an incident angle different from 90 degree to the sample surface [162,174] to reduce the damage to the upper crystal layers have been investigated. Also efforts to remove/repair the damaged layers by hydrogen plasma treatment [178], annealing [176,181], electrochemical [182] or chemical treatment [59,183] have been reported. Despite the diversity of studies reported in literature, no quantitative correlation between patterning parameters, electrochemical properties and surface properties were so far discussed. Within this chapter the influence of different milling parameters used for FIB micro-fabrication, and the effect of an electrochemical post-fabrication treatment [57,182] on the heterogeneous electron transfer behavior and surface properties of highly doped BDD microelectrode arrays were investigated. In particular, the influence of accelerating voltage, beam current and dwell time (beam-on time per pixel) are

considered. Parts of this chapter have already been published and are reprinted from *Electrochimica Acta, 130, Alexander Eifert, Philipp Langenwalter, Jonas Higl, Mika Lindén, Christoph E. Nebel, Boris Mizaikoff, Christine Kranz, Focused ion beam (FIB)-induced changes in the electrochemical behavior of boron-doped diamond (BDD) electrodes, 418-425*, Copyright 2014, with permission from Elsevier [172].

3.2. Results & Discussion

3.2.1. Electrochemical characterization

To characterize the electrochemical response of the FIB-fabricated UME arrays, potassium ferrocyanide was chosen as redox mediator. It is known that the potassium ferro/ferricyanide redox couple ($[Fe(CN)_6]^{4-}/[Fe(CN)_6]^{3-}$) [179] is surface sensitive in comparison to hexaammineruthenium (III) chloride ($[Ru(NH_3)_6]Cl_3$), which heterogeneous electron transfer occurs via an outer-sphere redox mechanism [132,184]. The ferro/ferricyanide redox couple is known to be a “marker” for chemical groups on carbon based electrodes and amorphous carbon materials due to a “sluggish” electron transfer behavior [59,183,185,186].

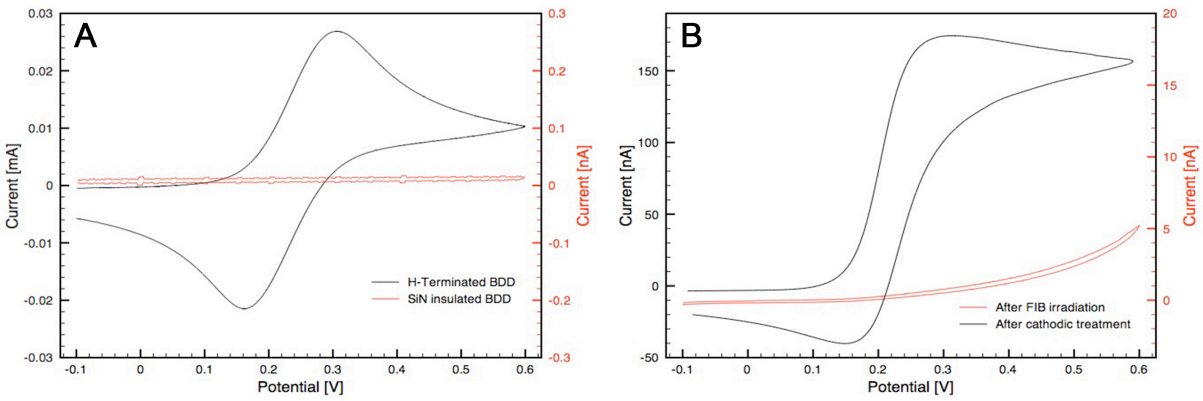

Fig. 14: Exemplary cyclic voltammograms (CVs) recorded at bare and modified electrode surfaces: A) Bare BDD macro electrode (black) and Si_xN_y-insulated electrode (red); adapted from Electrochimica Acta, 130, Alexander Eifert, Philipp Langenwalter, Jonas Higl, Mika Lindén, Christoph E. Nebel, Boris Mizaikoff, Christine Kranz, Focused ion beam (FIB)-induced changes in the electrochemical behavior of boron-doped diamond (BDD) electrodes, 418-425, Copyright 2014, with permission from Elsevier [172]; B) after FIB milling, exposing microdisc BDD electrodes (red) and after electrochemical treatment (black) of a 5x5 array with an electrode spacing of 10 µm and an individual electrode radius of 5 µm; CVs were recorded in 10 mM $K_4[Fe(CN)_6]$ / 0.1 M KCl / 0.016 M Tween 20; all measurements were conducted vs. sat. Ag/AgCl; ν = 100 mV/s; patterning parameters: 16 kV, 15 nA, 50 ns.

Fig. 14A shows the cyclic voltammogram of a hydrogen-terminated boron-doped diamond film used for the ultra-microelectrode array fabrication (black curve). As expected, a peak-shaped cyclic voltammogram for a macroscopic electrode surface with a quasi-reversible electron transfer behavior was observed. The quasi-reversible electron transfer can be derived from an actual peak separation of 140 mV and a peak current ratio of the oxidation and reduction cycle of one for the CV recorded in potassium ferrocyanide ($K_4[Fe(CN)_6]$). In the following, the peak separations of the oxidation/reduction peak of ferrocyanide derived from recorded CVs were used as analytical tool to evaluate the heterogeneous electron transfer behavior of the fabricated boron-doped diamond ultra-microelectrode arrays. After Si_xN_y insulation, the characteristic peaks for oxidation and reduction of the redox mediator disappear, (Fig. 14A; red) indicating a sufficient insulation of the highly conductive BDD film. The microelectrode arrays were then exposed by FIB milling with the ion beam oriented perpendicular to the sample surface using different sets of milling parameters (Fig. 15).

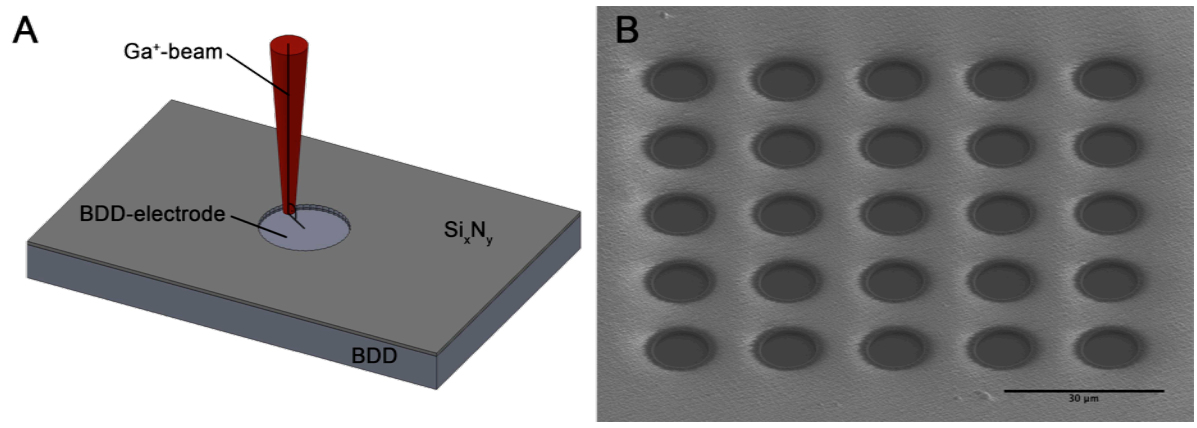

Fig. 15: A) Schematic illustration of the Ga^+-ion beam orientation during microelectrode fabrication; B) SEM image of a microelectrode array with an electrode spacing of 10 µm and an individual electrode radius of 5 µm.

Fig. 14B (red) shows that the electrochemical behavior is changing dramatically after the ion beam irradiation. An irreversible electron transfer behavior is now observed, where a peak separation can no longer be detected, indicating a “sluggish” electron transfer for the ferrocyanide species. The slow electron transfer can be attributed to the modified state of the electrode surface and the formation of amorphous carbon material, generated by the highly energized ion beam bombardment [162,176,180,182]. Employing an anodic electrochemical treatment step at + 2.5 V,

followed by a cathodic treatment at -4.0 V in a two-electrode setup using a Pt counter electrode results in a significant improvement of the observed electron transfer kinetics, as shown in Fig. 14B (black curve).

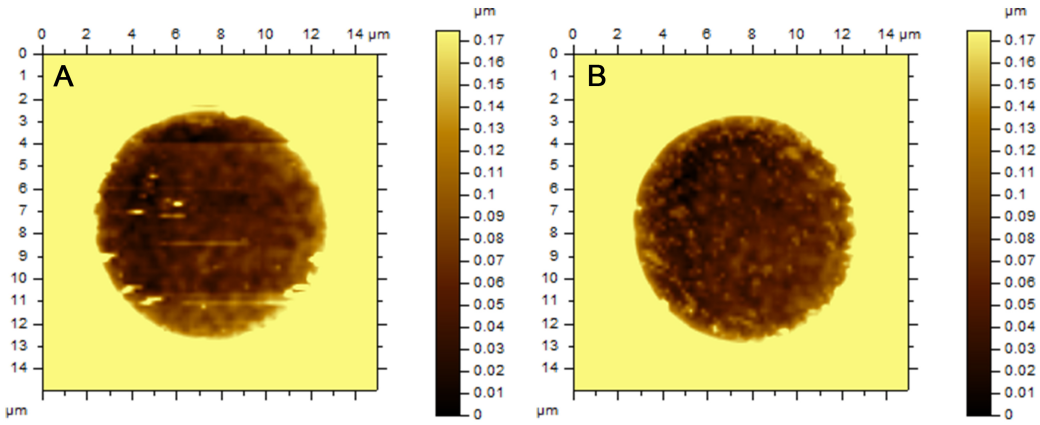

Fig. 16: AFM measurements of FIB-milled electrodes A) before and B) after electrochemical treatment in 2M sulfuric acid. AFM images were recorded in contact mode with Bruker NP general-purpose probes with a nominal spring constant of 0.06 N/m; reprinted from Electrochimica Acta, 130, Alexander Eifert, Philipp Langenwalter, Jonas Higl, Mika Lindén, Christoph E. Nebel, Boris Mizaikoff, Christine Kranz, Focused ion beam (FIB)-induced changes in the electrochemical behavior of boron-doped diamond (BDD) electrodes, 418-425, Copyright 2014, with permission from Elsevier [172].

This immediate improvement of the electron transfer behavior after the electrochemical treatment in combination with the observed topographical changes as shown in Fig. 16 (further details see section 3.2.3.1) indicates a partial restoration of the initial electrode surface properties and therefore likely the removal of at least the majority of the amorphous carbon layer. Also CVs recorded in 0.5 M sulfuric acid for the determination of the potential window support this assumption. The potential window of the BDD electrode shows before the electrochemical post-fabrication treatment signs of surface contaminants, which are no longer observable after treatment (Fig. 17).

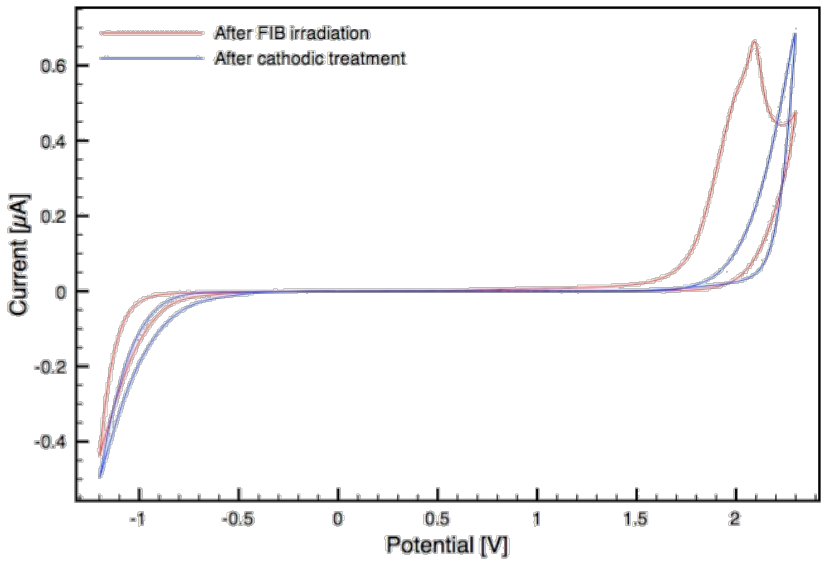

Fig. 17: Voltammograms recorded in 0.5 M H_2SO_4 vs. sat. Ag/AgCl (ν = 100 mV/s) revealing the potential window after FIB irradiation (red) and after FIB irradiation and cathodic treatment (blue); reprinted from Electrochimica Acta, 130, Alexander Eifert, Philipp Langenwalter, Jonas Higl, Mika Lindén, Christoph E. Nebel, Boris Mizaikoff, Christine Kranz, Focused ion beam (FIB)-induced changes in the electrochemical behavior of boron-doped diamond (BDD) electrodes, 418-425, Copyright 2014, with permission from Elsevier [172].

For the determination of the peak separation, an electrode array (5x5) with an individual electrode radius of 5 µm and 10 µm electrode spacing was used. Due to the relatively small distance between the individual electrodes, an overlap of the diffusion profiles is visible [106] resulting in a planar diffusive flux. Hence in contrast to microelectrodes showing a sigmoidal CV, rather a peak-shaped characteristic (Fig. 18) is obtained, which allows retrieving the peak separation data.

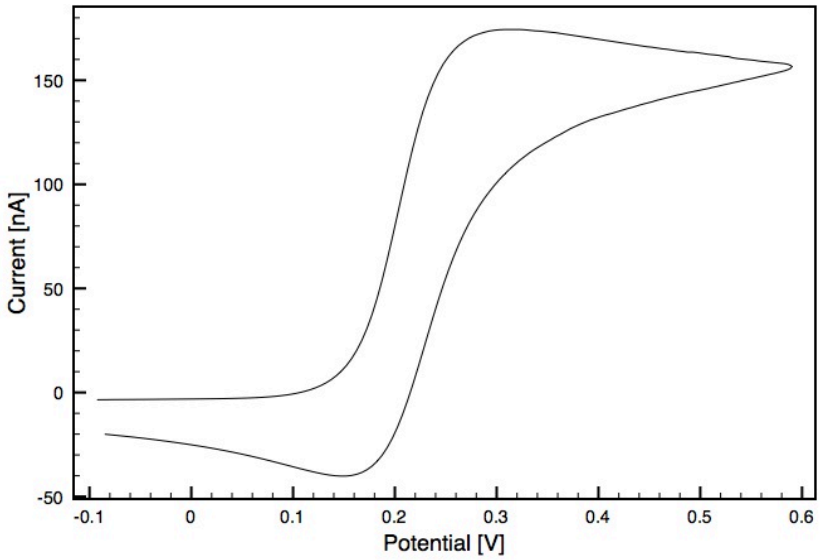

Fig. 18: Exemplary cyclic voltammogram recorded at a cathodically treated electrode array with 10 µm electrode spacing; CV was recorded in 10 mM $K_4[Fe(CN)_6]$ / 0.1 M KCl / 0.016 M Tween 20 vs. sat. Ag/AgCl; ν = 100 mV/s; patterning parameters: 16 kV, 15 nA, 50 ns.

The performance of the BDD electrode arrays due to surfaces changes induced by FIB irradiation was investigated in dependence of the milling parameters. The peak separation and the heterogeneous electron transfer rate (k^0) (see section 3.2.2) were compared after the electrochemical treatment with non-irradiated cathodically treated BDD electrodes. For the non-irradiated BDD samples, a peak separation ΔE_p of 90 mV in $([Ru(NH_3)_6]Cl_3$ and 140 mV in $K_4[Fe(CN)_6]$ (Fig. 19) is observed.

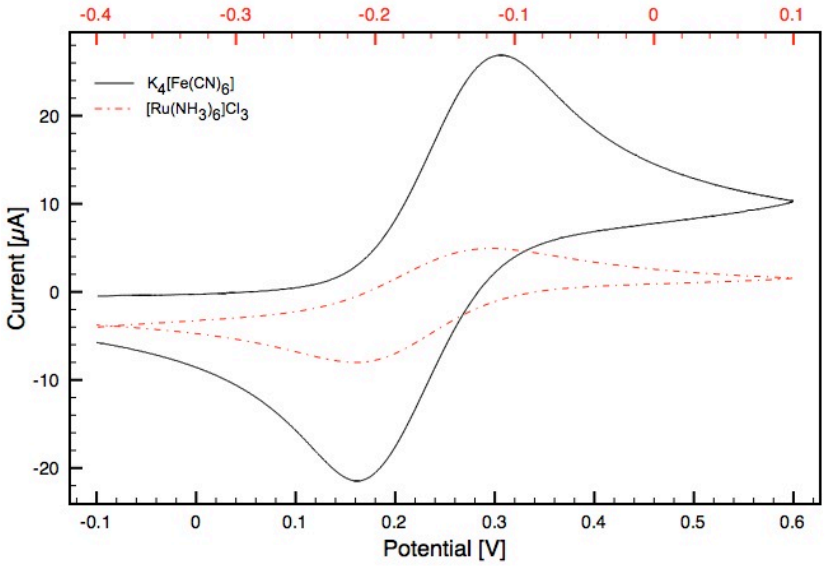

Fig. 19: CVs recorded at cathodically treated non-irradiated BDD electrodes in 10 mM $K_4[Fe(CN)_6]$ / 0.1 M KCl / 0.016 M Tween 20 (black) and 10 mM $[Ru(NH_3)_6]Cl_3$ / 0.1 M KCl / 0.016 M Tween 20 (red); all potentials are reported vs. sat. Ag/AgCl; ν = 100 mV/s.

The obtained values for the investigated BDD electrode in the different redox mediators are in good agreement with peak separations reported in literature [66,187]. Although for $K_4[Fe(CN)_6]$, a peak separation closer to the theoretical peak separation for an one electron process is reported in literature. This may be attributed to the pre-milling surface termination. First an anodic potential was utilized promoting the formation of hydroxyl and other functional oxygen groups on the electrode surface [35], which were then converted to a hydrogen-terminated surface by switching the potential to cathodic values. The applied cathodic potential is thereby of importance concerning the quality of the hydrogen-terminated BDD surface [57]. Therefore, a moderate potential of -4.0 V (see section 10.1.3) and a relatively large surface area, resulting in low current densities, may lead to a BDD electrode surface with partial oxygen termination and may explain the obtained results for ΔE_p of 140 mV in $K_4[Fe(CN)_6]$ for the cathodically treated BDD electrode. For oxygen-terminated BDD electrodes ΔE_p values up to 500 mV were reported in literature [58]. As shown in Tab. 1, the peak separation for $K_4[Fe(CN)_6]$ increases for all applied milling parameters compared to the non-milled cathodically treated BDD from 140 mV up to 430 mV, suggesting a significant change of the surface structure of the electrode crystal lattices.

Acc. voltage [kV]	Beam current [nA]	Dwell time [ns]	Peak separation [mV|
30	15	300	430
16	15	300	215
30	5	300	230
30	15	1000	324

Tab. 1: Exemplary values of peak separations after exposure of the BDD microelectrode arrays by FIB irradiation and electrochemical treatment; data recorded in a solution containing 10 mM $K_4[Fe(CN)_6]$ / 0.1 M KCl / 0.016 M Tween 20; ν = 100 mV/s; reprinted from Electrochimica Acta, 130, Alexander Eifert, Philipp Langenwalter, Jonas Higl, Mika Lindén, Christoph E. Nebel, Boris Mizaikoff, Christine Kranz, Focused ion beam (FIB)-induced changes in the electrochemical behavior of boron-doped diamond (BDD) electrodes, 418-425, Copyright 2014, with permission from Elsevier [172].

The different milling parameter sets result in different peak separations across the range of the patterning parameters, suggesting a correlation between the heterogeneous electron transfer and the milling parameters. Reasons for the obtained peak separation values will be discussed in the following. As the milling yield of diamond is low compared to frequently used materials in microfabrication (0.07 μm^3/nC (section 4.2.1) to 0.09 μm^3/nC [174]), a smooth surface with reduced

surface roughness, which probably consist of an amorphous carbon layer, can be expected using a perpendicular ion beam [174,178,180]. For example, milling diamond with a Ga^+ ion beam acceleration voltage of 20 kV and an ion dose of 10^{18} ions/cm^2 leads to an amorphous carbon layer on top of the crystal lattice of about 28 nm [174]. Different accelerating voltages, dwell times and beam currents for FIB structuring diamond-based materials are expected to change the thickness of the formed amorphous carbon layer. For example, the penetration depth of the primary ions directly correlates with the accelerating voltage [188], and therefore the thickness of the damaged layer. Furthermore, it is expected that the electrochemical treatment of FIB-fabricated microelectrodes only partially removes the amorphous carbon layer. This is also documented in the presented studies with the change of the peak separation from the non-irradiated BDD electrodes to the obtained values after milling and electrochemical treatment as shown in Tab. 1.

With declining accelerating voltage, a decrease in the measured peak separation after electrochemical treatment can be observed, indicating an attenuation of the FIB-induced damage to the crystalline electrode surface and therefore an increase in the heterogeneous electron transfer rates. Milling with a primary ion beam acceleration voltage of 30 kV (15 nA; 1 µs) results in a peak separation of 324 mV. With a decrease of the acceleration voltage from 30 kV to 16 kV also a decrease of 23.2% of the peak separation to 249 mV can be observed. Milling with further reduced accelerating voltages such as 8 kV (12 nA) results in a reduction by 10.8% to 214 mV.

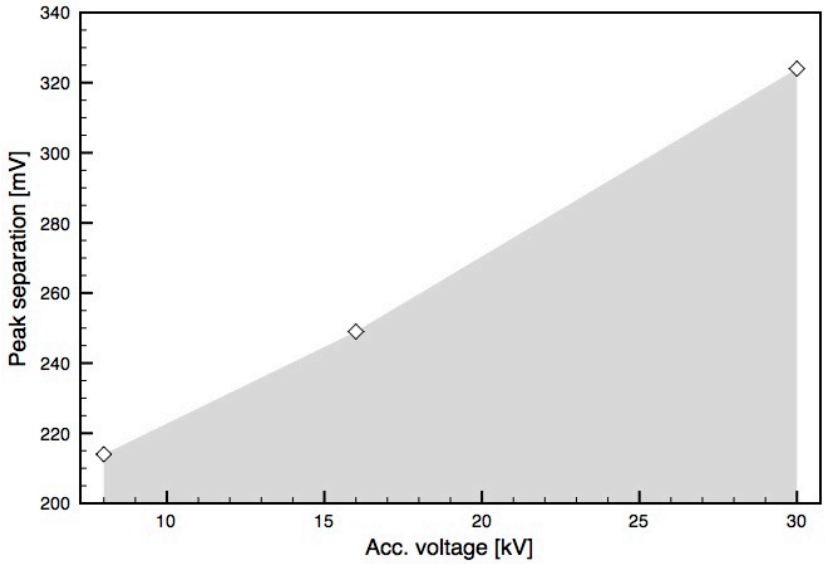

Fig. 20: Peak separation of milled BDD microelectrode arrays after exposure to FIB irradiation and electrochemical treatment in 2 M sulfuric acid. Electrochemical measurements were recorded in a solution containing 10 mM $K_4[Fe(CN)_6]$ / 0.1 M KCl / 0.016 M Tween 20; ν = 100 mV/s; the influence of acceleration voltage on ΔE_p was investigated at a beam current of 15 nA and a dwell time of 1 µs.

As shown in Fig. 20, a linear correlation exists between acceleration voltage and peak separation. In general, the implantation of Ga^+ ions into the substrate surface layers can be expressed by a three dimensional Gaussian profile [189,190] and depends on the kinetic energy of the accelerated ions. Therefore, the damaged volume of the electrode material directly correlates with the accelerating voltage, and thus, also the electrochemical behavior in terms of electron transfer rate.

Similar experiments with different beam currents at a fixed accelerating voltage and dwell time also reveal a dependence of the peak separation. While maintaining a constant accelerating voltage of 30 kV, a linear decrease in the peak separation can be observed with decreasing beam currents. Starting at 430 mV at 15 nA (300 ns), a decrease by 46.5% to 230 mV at 5 nA (300 ns) and by 53.4% at 3 nA (500 ns) can be observed as shown in Fig. 21.

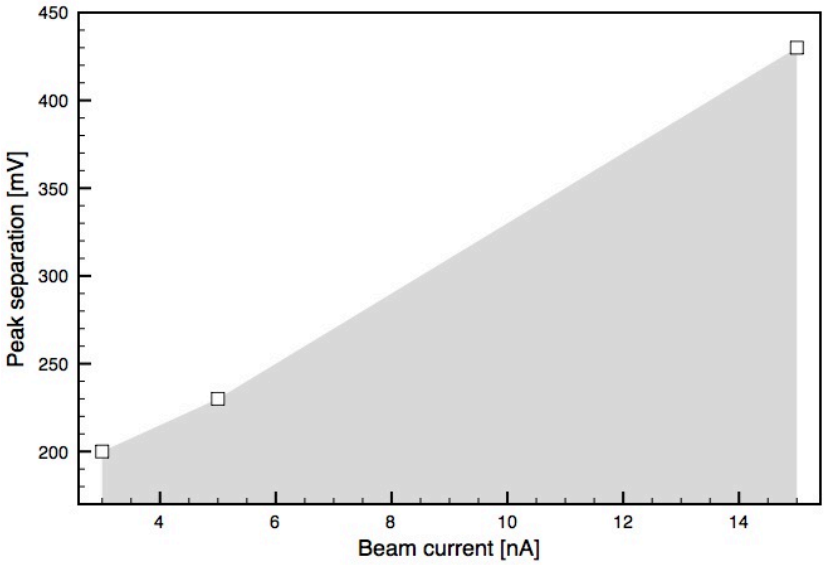

Fig. 21: Peak separation of milled electrode arrays after exposure to FIB irradiation and electrochemical treatment in 2 M sulfuric acid. Electrochemical measurements were recorded in a solution containing 10 mM $K_4[Fe(CN)_6]$ / 0.1 M KCl / 0.016 M Tween 20; ν = 100 mV/s; the influence of beam current on ΔE_p was investigated at an accelerating voltage of 30 kV and a dwell time of 300 ns (15 nA; 5 nA) and 500 ns (3 nA), respectively.

The actual ion beam is generated via a set of filters and apertures from a primary ion beam and the beam current distribution can be approximated by a Gaussian profile [190]. A change of beam current, while the same beam overlap is maintained, results in a more inhomogeneous ion dose distribution. Whereas the beam diameter is linearly increasing with the increasing size of the used aperture (pixel size), the beam current is following the Gaussian ion dose distribution profile of the primary ion beam generated by the liquid metal ion source. Thus the overlapping regions of the patterning spots (pixel) suffer from an additional exponential drop of the beam current distribution at the outer edge of the ion beam (beam tail) resulting in an inhomogeneous ion dose distribution, which is increasing with increasing beam diameter / pixel size. Additionally, the remaining beam intensity in the region of the beam tail is not sufficient to sputter material, but is sufficient to cause amorphization [190]. Therefore, an enhanced amorphization in the region of the beam tail is given, resulting in the variation of the electron transfer behavior. Compared to accelerating voltage and beam current, the dwell time reveals a more complex influence on the electrochemical properties.

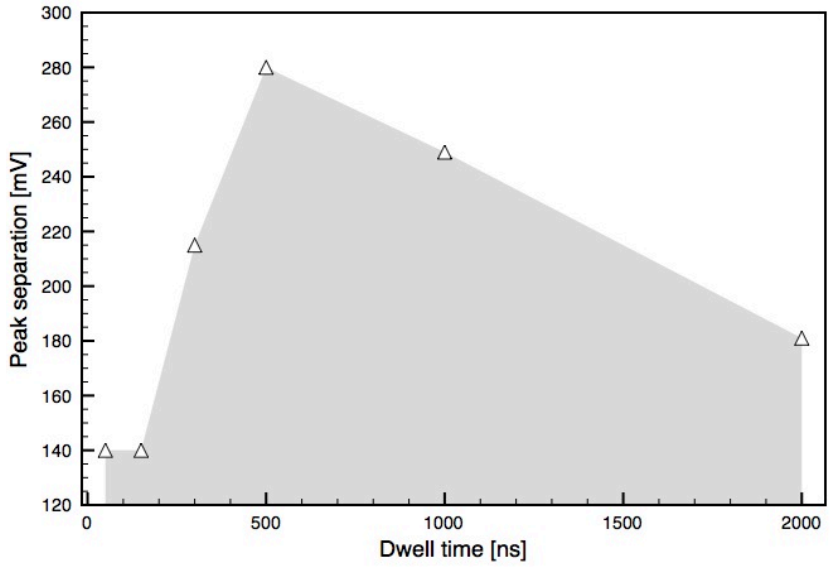

Fig. 22: Peak separation of milled electrode arrays after exposure to FIB irradiation and electrochemical treatment in 2 M sulfuric acid. Electrochemical measurements were recorded in a solution containing 10 mM $K_4[Fe(CN)_6]$ / 0.1 M KCl / 0.016 M Tween 20; ν = 100 mV/s; the influence of the dwell time on ΔE_p was investigated at an accelerating voltage of 16 kV and a beam current of 15 nA.

At very short dwell times <100 ns or very high dwell times >1500 ns, the lowest values of peak separation within the set experimental parameters are observed (<200 mV) (Fig. 22), indicating a higher electron transfer rate compared to the dwell times of 300 - 1500 ns. For short dwell times, it is anticipated that the short beam-on phase per pixel results in reduced crystal damage due to the possibility of the crystal structure to equilibrate before more energy is added to the system by kinetic impact. Therefore, the level of amorphization is reduced, as the energy required for the amorphization threshold [191] is reached at a later point in time of the patterning process. It is assumed that longer dwell times generate a surplus of energy inside the crystal structure, leading to the generation of localized heat. This localized heating may induce a sort of annealing effect, which can be responsible for restoring partially the diamond structure of the underlying diamond crystal structure [176,181] leading to more favorable peak separations. For dwell times of 200 – 500 ns, the added energy results in a steady increase of the peak separation as a continuous flow of energy above the amorphization threshold is maintained during patterning. Above 500 ns the annealing effects dominate, resulting in a steady decrease of the peak separation. In Tab. 2 an overview of the obtained peak separations in correlation to the patterning parameters is given:

Acc. voltage [kV]	Beam current [nA]	Dwell time [ns]	Peak separation [mV]
30	15	1000	324
16	15	1000	249
8	12	1000	214
30	15	300	430
30	5	300	230
30	3	500	200
16	15	50	140
16	15	150	140
16	15	300	215
16	15	500	280
16	15	1000	249
16	15	2000	181

Tab. 2: Overview of peak separations in correlation to the patterning parameters; data were recorded in a solution containing 10 mM $K_4[Fe(CN)_6]$ / 0.1 M KCl / 0.016 M Tween 20; ν = 100 mV/s.

3.2.2. Determination of the electron transfer rate constant

As already indicated by the change of peak separation (shown in Tab. 2), the heterogeneous electron transfer (HET) is influenced by the FIB milling parameters. Therefore, in addition to the peak separation values, the rate constants for the HET were calculated by fitting simulated data using the Butler-Volmer equation (Eq. 4). For initial calculations, an electron transfer coefficient of α = 0.5, which is typically used for the determination of electron transfer rates and represents an agreeable approximation for all transfer coefficients of 0.3 – 0.7 [192], was used to evaluate the recorded CVs (Fig. 23). A transfer coefficient of α = 0.5 is also in good agreement with the obtained peak ratio of the anodic to cathodic current of the non-irradiated cathodically treated BDD electrode (Fig. 14A).

$$i = nFAk^0 \left[C_O(0,t) e^{-\alpha \frac{nF}{RT}(E-E^{0'})} - C_R(0,t) e^{(1-\alpha)\frac{nF}{RT}(E-E^{0'})} \right]$$

Eq. 4: Butler-Volmer equation; i: current, n: number of transferred electrons, F: Faraday constant, A: electrode area, k^0: HET rate constant, $C_O(0,t)$, $C_R(0,t)$: surface concentration of oxidized/reduced species, respectively; α: electron transfer coefficient, R: gas constant, T: temperature, E: potential, $E^{0'}$: formal potential [192].

The CVs for determining k^0 were acquired with FIB-exposed ultra-microelectrode arrays (5x5) with a center-to-center spacing of 100 µm to ensure hemispherical diffusion profiles at the individual electrodes of the array leading to sigmoidal shaped CVs. For experimental details see section 10.1.

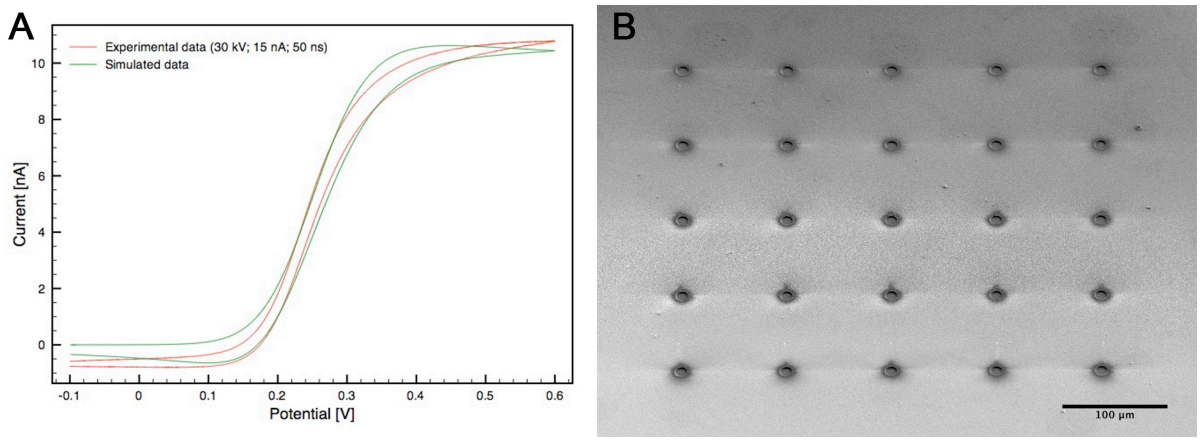

Fig. 23: A) Exemplary simulated CV (DigiElch 7) fitted to experimental data using the Butler-Volmer equation (transfer coefficient α = 0.5); B) SEM image of a 5x5 ultra-microelectrode array with an electrode spacing of 100 µm spacing (center-to-center); B) adapted from Electrochimica Acta, 130, Alexander Eifert, Philipp Langenwalter, Jonas Higl, Mika Lindén, Christoph E. Nebel, Boris Mizaikoff, Christine Kranz, Focused ion beam (FIB)-induced changes in the electrochemical behavior of boron-doped diamond (BDD) electrodes, 418-425, Copyright 2014, with permission from Elsevier [172].

Directly after FIB irradiation, a significant decrease in the HET rate constant by four orders of magnitude is observed in comparison to the cathodically treated BDD macroelectrode. The rate constant for the redox couple ($K_4[Fe(CN)_6]/K_3[Fe(CN)_6]$) used as a “benchmark” for FIB-induced crystal damage drops from k^0 = 0.001 cm/s (ΔE_p = 140 mV; partially oxygen terminated) Fig. 14A (black) to $k^0 = 2.71*10^{-7}$ cm/s, which can be attributed to the surface amorphization. After electrochemical treatment in sulfuric acid, a significant increase of the HET rate constant up to k^0 = 0.004 cm/s is observed. This increase in the HET rate constant by at least a factor of two compared to the rate constant of the partially oxygen-terminated boron-doped diamond indicates the restoration of an almost completely H-terminated boron-doped diamond surface.

Acc. voltage [kV]	Beam current [nA]	Dwell time [ns]	Rate constant [cm/s]
30	15	300	0.0019
16	15	300	0.0022
30	15	300	0.0019
30	7.5	300	0.0021
30	5	300	0.0022
30	15	50	0.0040
30	15	150	0.0029
30	15	300	0.0019
30	15	500	0.0018
30	15	1000	0.0025
30	15	2000	0.0035

Tab. 3 Overview of HET rate constants in correlation to the patterning parameters; data recorded in a solution containing 10 mM $K_4[Fe(CN)_6]$ / 0.1 M KCl / 0.016 M Tween 20; ν = 100 mV/s; rate constants calculated using the Butler-Volmer equation with transfer coefficient α = 0.5.

As shown in Tab. 3, the calculated heterogeneous rate constants are in excellent agreement with the obtained peak separation values. By reducing the acceleration voltage from 30 kV to 16 kV, an increase in k^0 from 0.0019 cm/s (30 kV; 15 nA; 300 ns) to 0.0022 cm/s (16 kV; 15 nA, 300 ns) is obtained. Also as anticipated from the peak separation experiments, the rate constant increases with decreasing current. The rate constant increases from 0.0019 cm/s (30 kV; 15 nA; 300 ns) up to 0.0022 cm/s (30 kV; 5 nA; 300 ns).

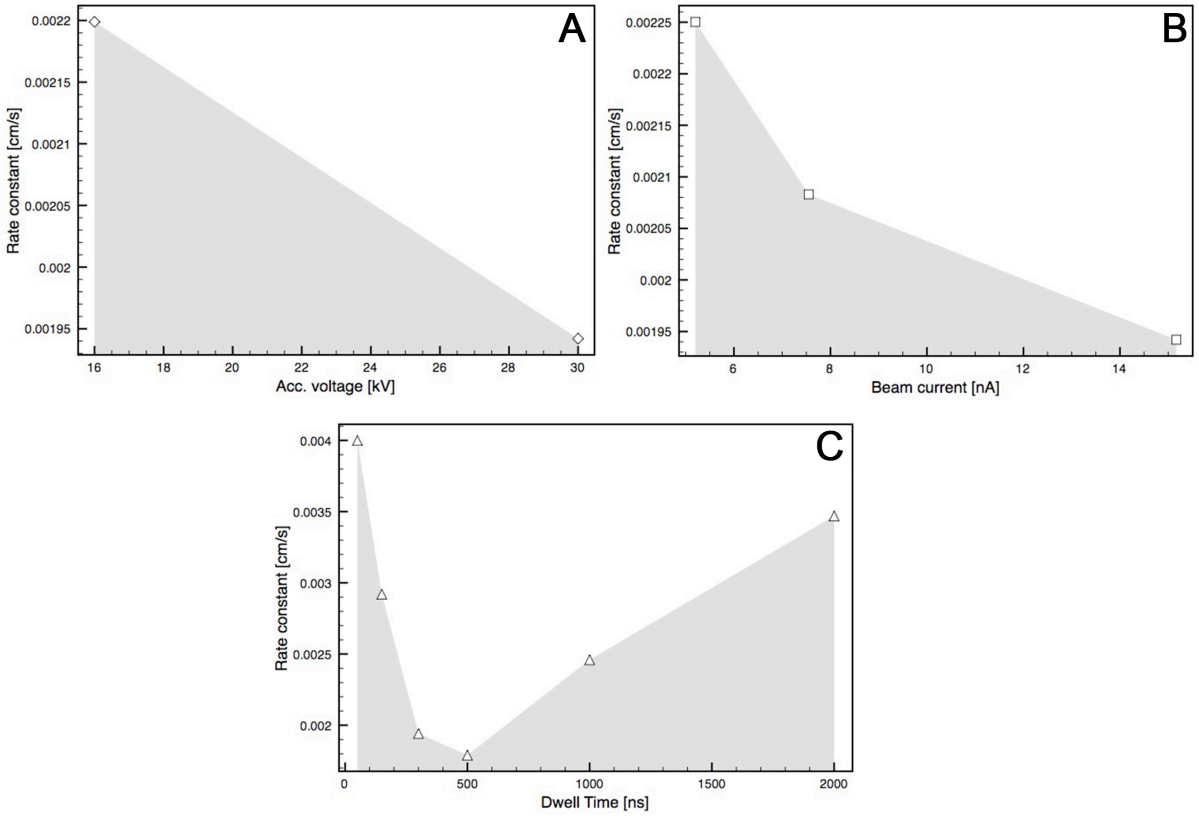

Fig. 24: HET rate constants for different A) acceleration voltages (15 nA; 300 ns); B) beam currents (30 kV; 300 ns); and C) at different dwell times (HET: 30 kV; 15 nA); adapted from Electrochimica Acta, 130, Alexander Eifert, Philipp Langenwalter, Jonas Higl, Mika Lindén, Christoph E. Nebel, Boris Mizaikoff, Christine Kranz, Focused ion beam (FIB)-induced changes in the electrochemical behavior of boron-doped diamond (BDD) electrodes, 418-425, Copyright 2014, with permission from Elsevier [172].

Comparing the peak separation values of the FIB-irradiated and electrochemically treated BDD samples with the calculated HET rate constants as shown in Fig. 24C, also visualizes the anticipated correlation shown in Fig. 22. The calculated rate constants vary from 0.0040 cm/s (30 kV; 15 nA; 50ns) to 0.0018 cm/s (30 kV; 15nA; 500 ns). As shown in Fig. 24C, the highest HET rate constants (> 0.003 cm/s) are observed at dwell time values below 100 ns and above 1500 ns.

The electrochemical properties of BDD are strongly influenced by a variety of parameters [58,65,66,74,114,161–163] such as surface termination and crystal defects. Therefore, it may also be assumed that a transfer coefficient of α = 0.5 is not entirely correct, which is supported by a peak current ratio deviating from one and a peak separation (ΔE_p) >100 mV for FIB-fabricated microelectrode arrays with 10 µm spacing. Hence, the simulations of the CVs (100 µm spacing) are refined in order to achieve a better fit to the experimental data. The electron transfer coefficient is

iterated during data fitting. As a result, an average transfer coefficient of $\alpha \approx 0.66$ is determined. Due to a different electron transfer coefficient also a different set of HET rate constants are determined as the two parameters are linked by the Butler-Volmer equation.

Acc. voltage [kV]	Beam current [nA]	Dwell time [ns]	Rate constant [cm/s]
30	15	300	0.0039
16	15	300	0.0042
30	15	300	0.0039
30	7.5	300	0.0041
30	5	300	0.0043
30	15	50	0.0073
30	15	150	0.0054
30	15	300	0.0039
30	15	500	0.0035
30	15	1000	0.0045
30	15	2000	0.0057

Tab. 4: Overview of HET rate constants in correlation to the patterning parameters; data recorded in a solution containing 10 mM $K_4[Fe(CN)_6]$ / 0.1 M KCl / 0.016 M Tween 20; ν = 100 mV/s; rate constants were calculated using the Butler-Volmer equation with an iterated transfer coefficient α = 0.66.

The calculated rate constants range now from k^0 = 0.0035 cm/s to 0.0073 cm/s as displayed in Tab. 4. Despite the change of the HET rate constant, as anticipated no change in the behavior relative to the patterning parameters are observed (Fig. 25).

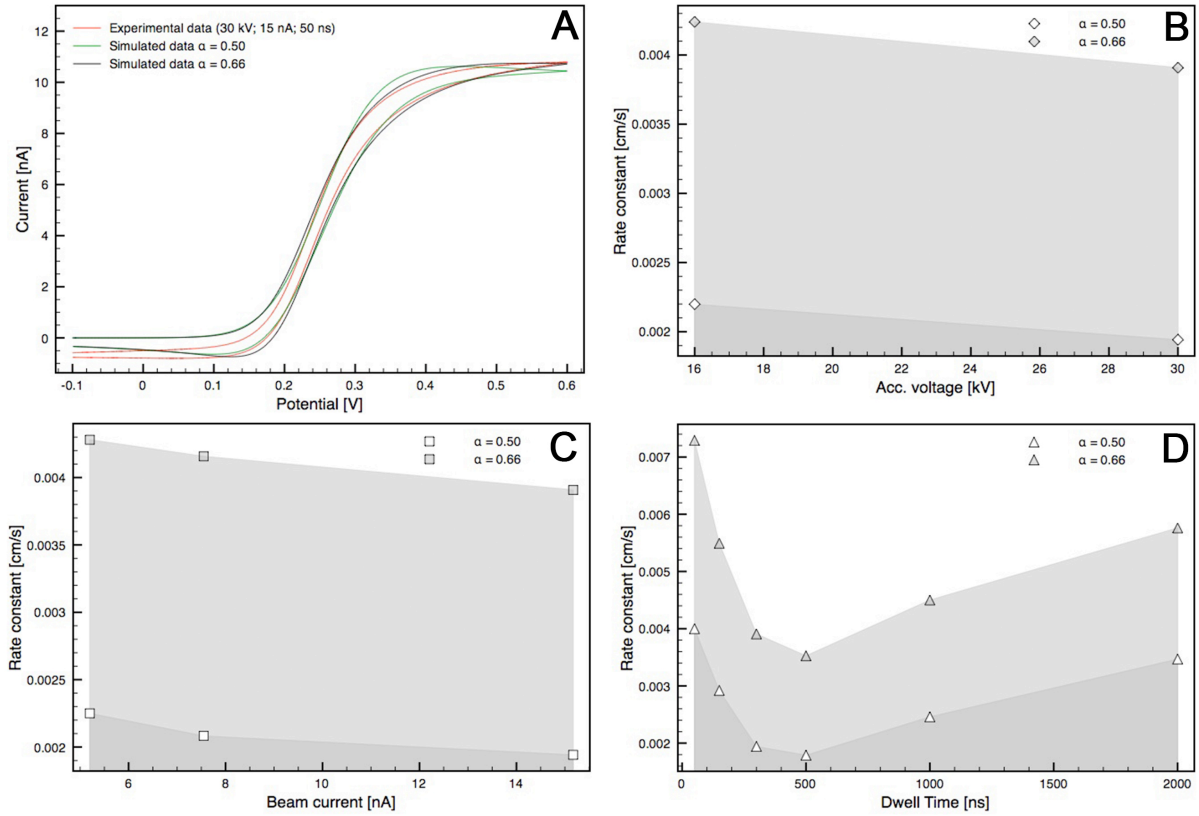

Fig. 25: A) Exemplary comparison of the experimental and the simulated data; B-D) HET rate constants for different transfer coefficient values:, B) acceleration voltages (15 nA; 300 ns), C) beam currents (30 kV; 300 ns), and D) dwell times (30 kV; 15 nA).

For a change in accelerating voltage from 30 kV to 16 kV, now an increase of 7.6% from k^0 = 0.0039 cm/s to k^0 = 0.0042 cm/s is obtained. Also the decrease of beam current from 15 nA to 7.5 nA and finally to 5 nA results in an increase of k^0 from k^0 = 0.0039 cm/s (15 nA) by 5.1% to k^0 = 0.0041 cm/s (7.5 nA) and by 10.2% to k^0 = 0.0043 cm/s (5 nA). The rate constants related to different dwell times show an increase of 108% from k^0 = 0.0035 (500 ns) to k^0 = 0.0073 (50 ns) and by 62.8% to k^0 = 0.0057 (2000 ns).

3.2.3. Surface characterization

The change in surface structure caused by FIB-patterning was observed by topographical and spectroscopic investigations of the modified BDD samples.

3.2.3.1. AFM investigation

As shown in Fig. 16, AFM imaging reveals topographical changes of BDD after FIB patterning.

To evaluate the topographical surface properties, the ten-point mean surface roughness factor R_z (Eq. 5) was determined and averaged from five different spots on the sample surface.

$$R_Z = \frac{1}{s}\sum_{i=1}^{s} R_{ti} \text{ with } R_t = R_p - R_v$$

Eq. 5: Ten-point mean surface roughness parameter; s = 5; R_{ti} = maximum distance between highest peak and lowest valley per sampling length.

The roughness factor of a non-irradiated BDD electrode is determined to 11 ± 3 nm. FIB milling at an acceleration voltage of 30 kV (15 nA; 1 µs) results in a roughness factor of 133 ± 16 nm, which decreases to 70 ± 15 nm at an applied acceleration voltage of 16 kV (15 nA; 1 µs) and to 34 ± 17 nm at 8 kV (15 nA; 1 µs). Comparatively, the experiments at variable beam currents show a linear correlation of the surface roughness factor. At 15 nA (30 kV, 300 ns) a roughness factor of 21 ± 5 nm is determined, decreasing to 16 ± 5 nm at 5 nA (30 kV, 300 ns) and to 14 ± 4 nm at 3 nA (30 kV, 300 ns). For various dwell times, the surface roughness varies from 37 ± 6 nm (16 kV; 15 nA, 2000 ns) to 75 ± 17 nm (16 kV; 15 nA; 500 ns), which correlates inversely to the HET rate constant. A complete overview of the obtained surface roughness values is listed in Tab. 5 and partially illustrated in Fig. 26. In conclusion, a high surface roughness value leads to an enhanced peak separation (see Fig. 22) and a low HET rate constant (Tab. 5).

Acc. voltage [kV]	Beam current [nA]	Dwell time [ns]	R_z [nm]
30	15	1000	133 ± 16
16	15	1000	70 ± 15
8	15	1000	34 ± 17
30	15	300	21 ± 5
30	5	300	16 ± 5
30	3	300	14 ± 4
16	15	50	51 ± 14
16	15	150	60 ± 19
16	15	500	75 ± 17
16	15	1000	70 ± 15
16	15	2000	37 ± 6

Tab. 5: Surface roughness factors in correlation to the patterning parameters; AFM images were recorded in contact mode in ambient conditions with Bruker NP general-purpose probes with a nominal spring constant of 0.06 N/m.

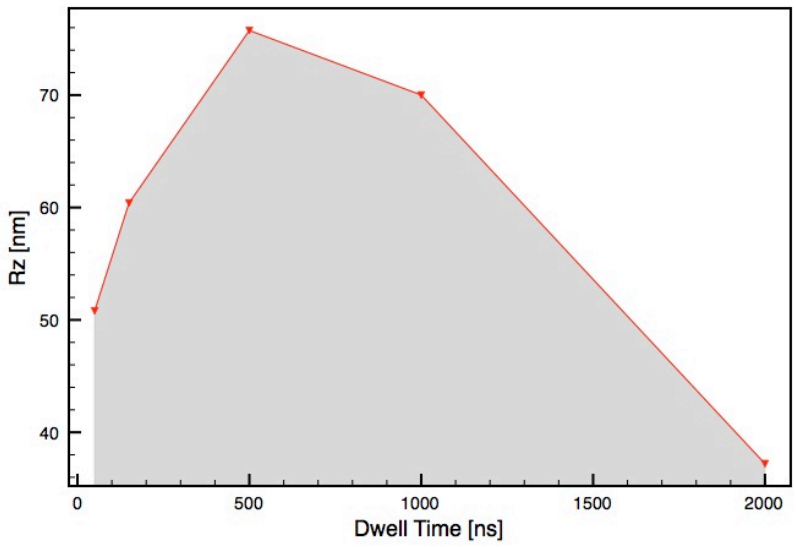

Fig. 26: Ten-point mean surface roughness in correlation to dwell time (16 kV; 15 nA); adapted from Electrochimica Acta, 130, Alexander Eifert, Philipp Langenwalter, Jonas Higl, Mika Lindén, Christoph E. Nebel, Boris Mizaikoff, Christine Kranz, Focused ion beam (FIB)-induced changes in the electrochemical behavior of boron-doped diamond (BDD) electrodes, 418-425, Copyright 2014, with permission from Elsevier [172].

3.2.3.2. Raman spectroscopy

In order to determine the change of the crystal lattice, in particular the upper layers of the milled structures, Raman spectra were recorded at different fabrication steps.

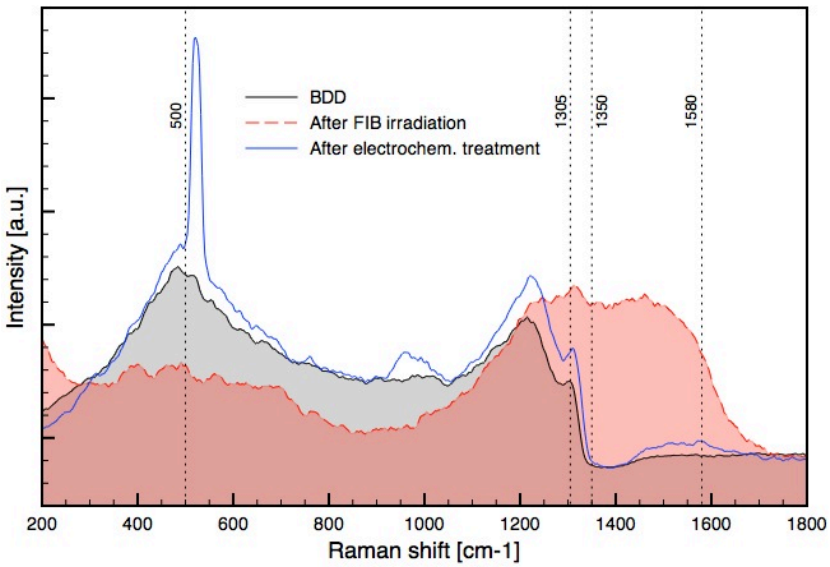

Fig. 27: Raman spectra obtained after different fabrication steps of the microelectrode arrays. Raman spectra were acquired using an excitation laser with 532 nm wavelength and 10 mW power. For detection a 100x objective with a 0.9 numerical aperture was used; adapted from Electrochimica Acta, 130, Alexander Eifert, Philipp Langenwalter, Jonas Higl, Mika Lindén, Christoph E. Nebel, Boris Mizaikoff, Christine Kranz, Focused ion beam (FIB)-induced changes in the electrochemical behavior of boron-doped diamond (BDD) electrodes, 418-425, Copyright 2014, with permission from Elsevier [172].

The Raman spectrum of the non-irradiated nanocrystalline BDD shows broad bands around 500 cm^{-1} and 1200-1250 cm^{-1} [193–196], which are characteristic for nanocrystalline diamond. The broad band between 1100-1280 cm^{-1} and the band around 500 cm^{-1} can be assigned to a disordered sp^3 phase [176,197], which increases with rising boron concentration, respectively due to incorporation of boron into the crystal lattice [193,195]. A second characteristic Raman feature for nanocrystalline diamond is the sharp band edge observable around 1330 cm^{-1}. Furthermore, the band at 1305 cm^{-1} can be attributed to a hexagonal diamond structure [198,199] with one diamond layer of cubic diamond shifted along the (111) plane [198]. After FIB irradiation with a beam setting of 30 kV, 15 nA, 50 ns, a significant change in the overall Raman spectra is observed. The most prominent change is the disappearance of the sharp nanocrystalline diamond band edge

around 1330 cm^{-1} indicating the change in the crystal structure. Simultaneously, the appearance of a broad double band between 1100 and 1700 cm^{-1}, which can be assigned to the D-peak between 1200-1350 cm^{-1} and the G-peak between 1400-1580 cm^{-1} of graphite [200], indicates the amorphization of the diamond structure. Additionally, the broad band previously observed around 500 cm^{-1} becomes negligible in comparison to the remaining features of the spectra, in particular to the D- and G-peak. The observed changes of the Raman spectra correlate with the formation of an amorphous carbon layer after FIB irradiation. This observation is also supported by the electrochemical data including the low HET rate constant after FIB exposure. After electrochemical treatment in 2 M sulfuric acid, the characteristic features of nanocrystalline diamond are reappearing in the recorded Raman spectra around 500 cm^{-1}, 1305 cm^{-1} and 1330 cm^{-1}. But in contrast to the native BDD sample, an additional broad band around 1580 cm^{-1} is observed. This indicates the presence of residues of amorphous carbon on the electrode surface, as the band can be attributed to the G-peak of graphite [200], which obviously was not completely removed by the electrochemical treatment.

The electrochemically treated BDD microelectrode arrays investigated by Raman spectroscopy had an original BDD film thickness of approximately 1000 nm. As around 430 nm of the BDD layer had been removed by FIB milling, the underlying Si substrate becomes observable after the electrochemical treatment in the Raman spectra (see Fig. 28B). Si bands can be attributed to the signals at 520 cm^{-1} and 950 cm^{-1}, respectively [200]. In contrast the samples representing the FIB-milled microelectrode arrays, before electrochemical treatment, have a thickness of approximately 1800 nm, and after FIB milling a thickness of 1000 nm. Therefore, the Raman band for Si is not observable. As shown in Fig. 28A, no significant differences in the Raman spectra of the irradiated samples are observable. After electrochemical treatment, a slight change in the relative peak height of the band at 1305 cm^{-1} in comparison to the broad band for the disordered sp^3 phase of diamond between 1100-1280 cm^{-1} (see Fig. 28B) is observable, indicating an increase of the hexagonal diamond content after FIB irradiation.

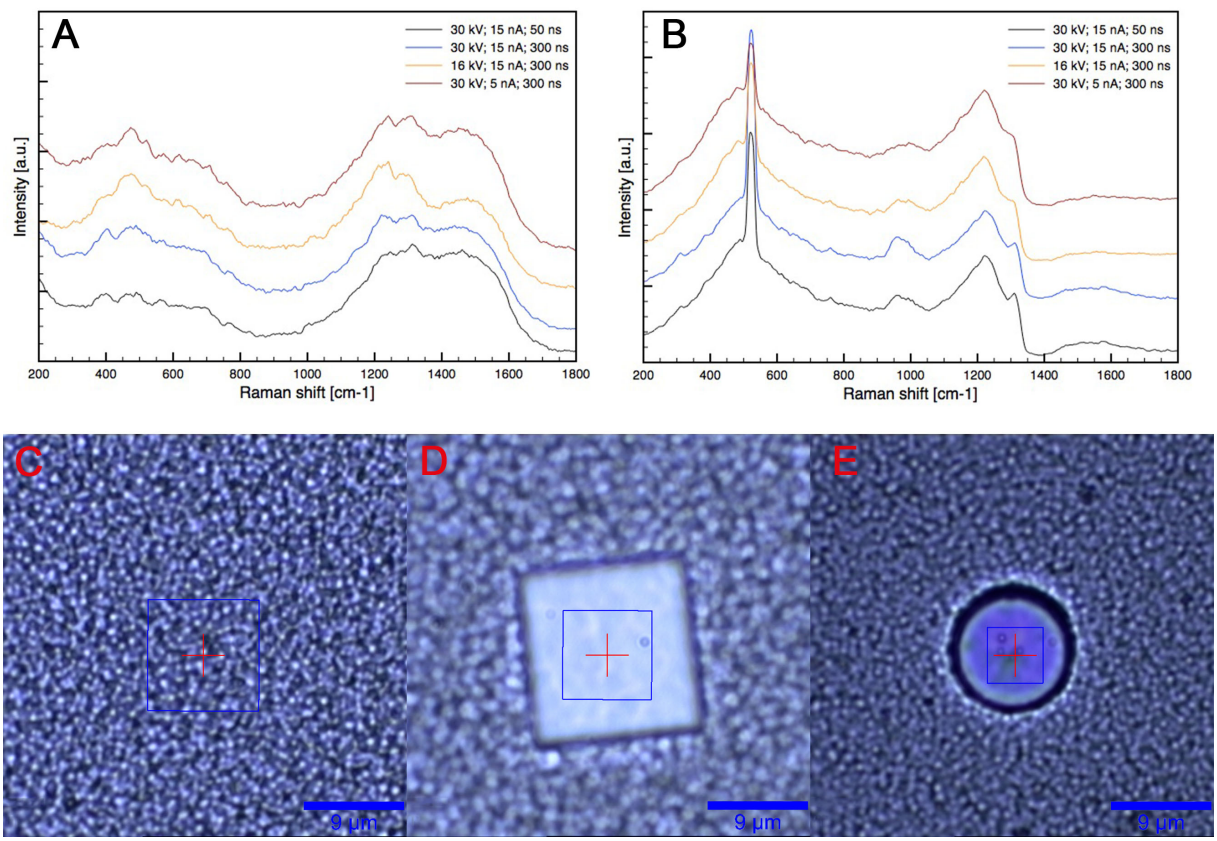

Fig. 28: Raman spectra of different patterning parameters; A) after FIB irradiation of an as-grown BDD sample and B) after a subsequent electrochemical treatment in sulfuric acid; adapted from Electrochimica Acta, 130, Alexander Eifert, Philipp Langenwalter, Jonas Higl, Mika Lindén, Christoph E. Nebel, Boris Mizaikoff, Christine Kranz, Focused ion beam (FIB)-induced changes in the electrochemical behavior of boron-doped diamond (BDD) electrodes, 418-425, Copyright 2014, with permission from Elsevier [172]; Optical microscope images of the electrode surface: C) as-grown; D) after FIB irradiation; E) after electrochemical treatment; Raman spectra were recorded inside the blue rectangles (C-E) and subsequently averaged (n = 625).

3.2.3.3. Electron backscatter diffraction (EBSD) investigation after electrochemical treatment

Additional EBSD measurements were performed to investigate the crystal lattice restoration of the electrochemically treated BDD before and after FIB-exposure. The acquired Kikuchi patterns before and after FIB irradiation are displayed in Fig. 29.

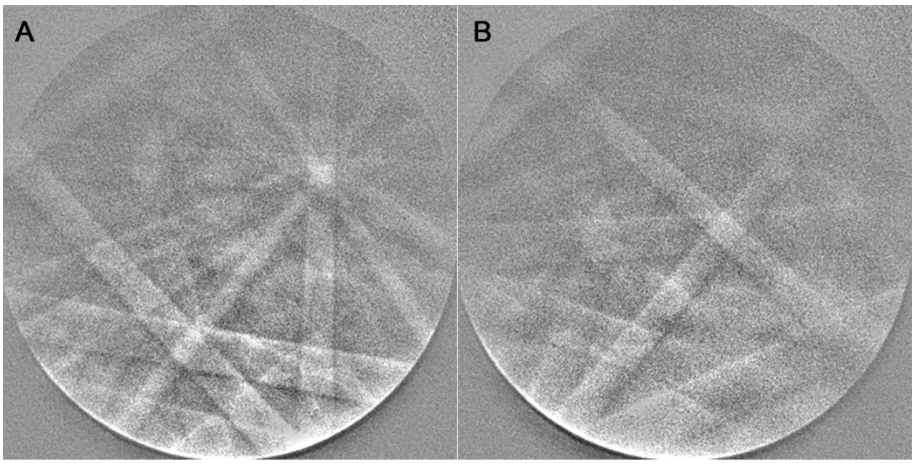

Fig. 29: Kikuchi patterns of BDD; A) non-irradiated, cathodically treated BDD B) FIB irradiated and consecutively cathodically treated BDD (30 kV; 15 nA; 50 ns); EBSD measurements were performed at an incident angle of 20° relative to the sample surface with 20 kV, 16 nA; EBSD detector binning 2 x 2; image averaging: 5 frames.

By orientating the sample at an incident angle of 20° to the electron beam, the upper layers of about 10-20 nm of the crystal surface could be investigated. The obtained Kikuchi pattern for the non-irradiated, cathodically treated BDD reveals a face-centered cubic crystalline structure as expected, unlike the amorphous carbon material generated via FIB irradiation with a thickness layer of about 20-30 nm revealing no pattern at all (image not shown). After electrochemical treatment in sulfuric acid, the EBSD measurement reveals again a Kikuchi pattern indicating a cubic crystalline structure and hence the removal of the amorphous carbon layer. In general, the quality of the EBSD pattern, which is described by the image quality (IQ) value, can be used as an indicator for the amount of crystal defects in the electron interaction volume [201]. The higher the IQ value, the lower the content of crystal defects in the electron interaction volume. The IQ value is defined as the average height of the most prominent peaks in the Hough transform. The evaluation of the EBSD pattern quality after FIB exposure and subsequent treatment reveals an image quality value of IQ = 107.9 ± 8.1 (N = 5) and for non-irradiated, electrochemically

treated BDD a value of IQ = 152.8 ± 6.1 (N = 5), which is in good agreement to materials containing elements of low atomic number [201]. According to the obtained IQ values, it can be assumed that minor residues of amorphous carbon are still present at the electrode surface, which is also in agreement with the obtained Raman data. Although there are remaining residues of amorphous carbon, it can be assumed that the majority of the electrode surface consists of a restored BDD surface, which is also supported by the large potential window (Fig. 17) and the obtained HET rate constants (Tab. 3, Tab. 4).

3.3. Conclusion & Outlook

In the current chapter the influence of FIB milling on the electrochemical behavior of BDD microelectrode arrays was investigated. FIB is nowadays frequently used for prototyping of three-dimensional electrodes, such as electrode arrays [159] or combined SPM probes [8,131]. Hence, it is essential to correlate the influence of FIB irradiation parameters to the electrochemical properties of the electrode materials. This is in particular important for carbon-based materials, such as BDD, where the Ga^+ bombardment results in an alteration of the crystal structure, and as a consequence in a change of the electrochemical properties. In general, the electrochemical treatment after FIB-milling resulted in a significant increase of the HET rate constant up to four orders of magnitude indicating the regeneration of a hydrogen-terminated BDD electrode surface and the removal of the majority of the FIB-induced amorphous carbon layer. Additionally, it could be demonstrated that the electrochemical behavior of the FIB-fabricated BDD microelectrode arrays is also correlated to the milling parameters. In dependency of the patterning parameters, the peak separation, HET rate constant, and the ten-point mean surface roughness were determined and a correlation between the electrochemical parameters and the surface roughness could be observed. Further improvements of the FIB-based fabrication of BDD devices may be achieved by using gas-assisted milling protocols, reducing the formation of amorphous carbon layer during the patterning process [174]. In addition, other post-fabrication steps, such as chemical etching, ozone cleaning or thermal treatment in oxygen rich atmosphere may be explored to remove the remaining amorphous carbon material, which minor content is still observable in the recorded Raman spectra and EBSD patterns.

4. Combined boron-doped diamond AFM-SECM probes

4.1. Introduction

Scanning probe techniques such as AFM or SECM can be combined to obtain complementary data in a single data acquisition pass, benefiting from the advantages of the individual techniques [202] (see also section 2.4.2).

Since the first SECM type experiments in 1986 [4,111], different research groups around the globe have significantly contributed to SECM research including the topic of combining SECM with complementary scanning probe techniques. Such "hyphenated" analytical devices provide correlated high topographical and localized electroanalytical information. The fabrication of combined AFM-SECM probes with an embedded electrode beneath an insulating tip-apex (recessed) is typically achieved via FIB-processing using a high energy Ga^+-ion beam for selective material removal with nanometer precision. As described in section 3.1, BDD represents an outstanding electrode material for electroanalytical chemistry due to its physical and chemical properties along with the possibility of selective surface modifications [33,164,203]. BDD microelectrodes were fabricated by coating, for example, a sharply etched tungsten wire with BDD followed by insulator deposition and electrode exposure [204]. With the advantage of microelectrodes, electrochemical measurements in vivo [29], due to the biocompatibility of BDD, or measurements of redox active species, which are prone to adsorb on the electrode surface (electrode fouling) [32], or measurements in small sample volumes or low concentrations are feasible. Although, first combined BDD-AFM-SECM probes have been reported in literature by Avdic et al. [89], a thorough characterization of such conical electrodes and imaging experiments were absent.

Therefore, the following chapter will focus on the integration of BDD electrodes into AFM probes and their characterization. Combined AFM-SECM measurements providing simultaneous topographical and electrochemical data, as well as simulations of the steady-state current of the fabricated probes will be presented. Parts of this chapter have been already published and are reprinted from *Electrochemistry Communications, 25, Alexander Eifert, Waldemar Smirnov, Stefan Frittmann, Christoph Nebel, Boris Mizaikoff, Christine Kranz, Atomic force*

microscopy probes with integrated boron doped diamond electrodes: Fabrication and application, 30-34, Copyright 2012, with permission from Elsevier [182].

4.2. Results & Discussion

4.2.1. Milling yield of boron-doped-diamond

Diamond is one of the hardest and most robust materials on earth. The boron-doped form of diamond is also considered to show similar physical properties in respect to chemical inertness and mechanical stability. As FIB milling is used for the fabrication of boron-doped diamond AFM-SECM probes, in a first step the volume per dose (VPD) value of the material was determined. The VPD parameter was determined by milling various trenches with a target depth of 400 nm into the sample substrate using different VPD settings. The deviation of the depth is then plotted versus the utilized VPD setting (Fig. 30). The VPD value of the sample material was then extracted from the intersection of the linear fit with the x-axis, resulting in a VPD value for PECVD-deposited BDD of 0.072 μm^3/nC.

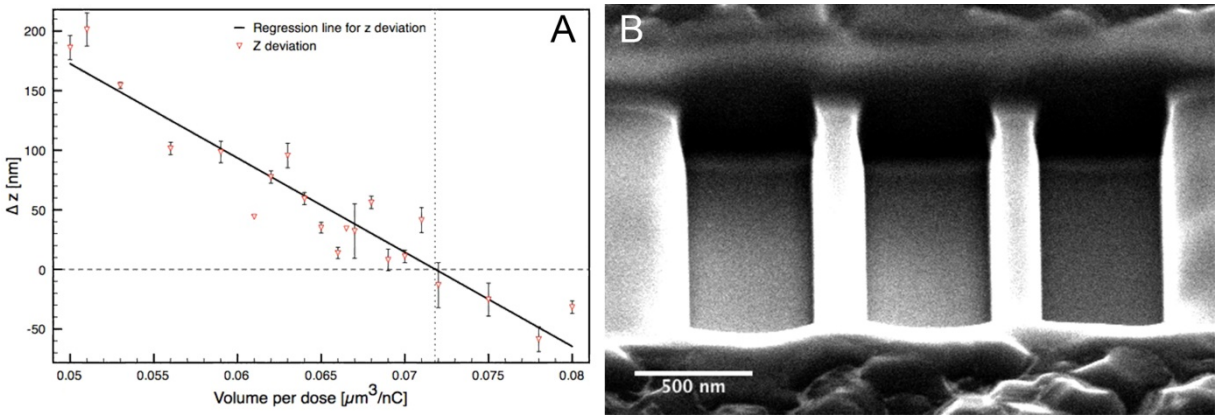

Fig. 30: A) Z-deviation of the milling depth relative to the target depth for the used VPD parameter; n = 3; B) FIB-milled trenches milled with 30 kV, 46 pA and a dwell time of 1 µs; target depth: 400 nm.

4.2.2. Combined BDD-AFM-SECM probes

Combined AFM-SECM probes with an integrated BDD electrode were fabricated from commercially available Si probes (nominal spring constant: 48 N/m; resonance frequency: 190 kHz) coated with a nanocrystalline BDD layer and subsequently modified with an insulation layer (Parylene-C or Si_xN_y) of approximately 900 nm. After modification, the probes show a slightly altered resonance frequency of 206 kHz due

to an increased stiffness of the cantilever. After FIB milling using an adapted process developed by Kranz and coworkers [8,131] (Fig. 31), the combined AFM-SECM probes were electrochemically treated and hydrogen-terminated to remove amorphous carbon material from the surface and to restore a fast electron transfer kinetics as described in chapter 3. Every probe was electrochemically characterized at each step of the fabrication process. SEM images (Fig. 31) and a schematic outline of the fabrication process for combined BDD-AFM-SECM probes is shown in Fig. 32.

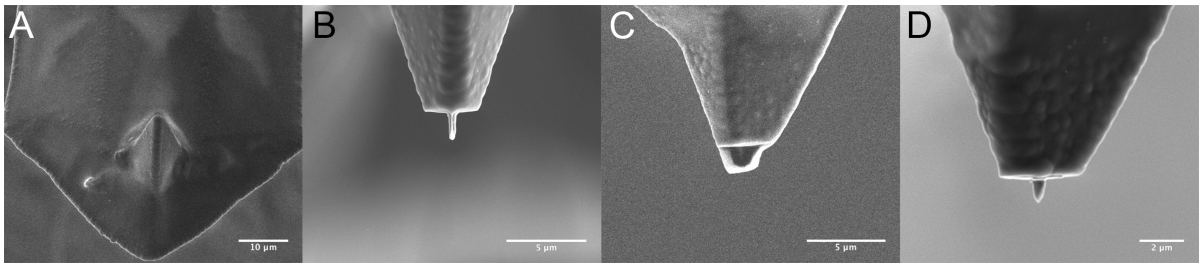

Fig. 31: SEM images of the fabrication steps of combined BDD-AFM-SECM probes; A) Parylene-C-insulated cantilever B) after front-cut; C) side view after front cut; D) After 90° reorientation, 2nd cut and tip sharpening; All fabrication steps were performed at 30 kV, 50 pA, 1 µs.

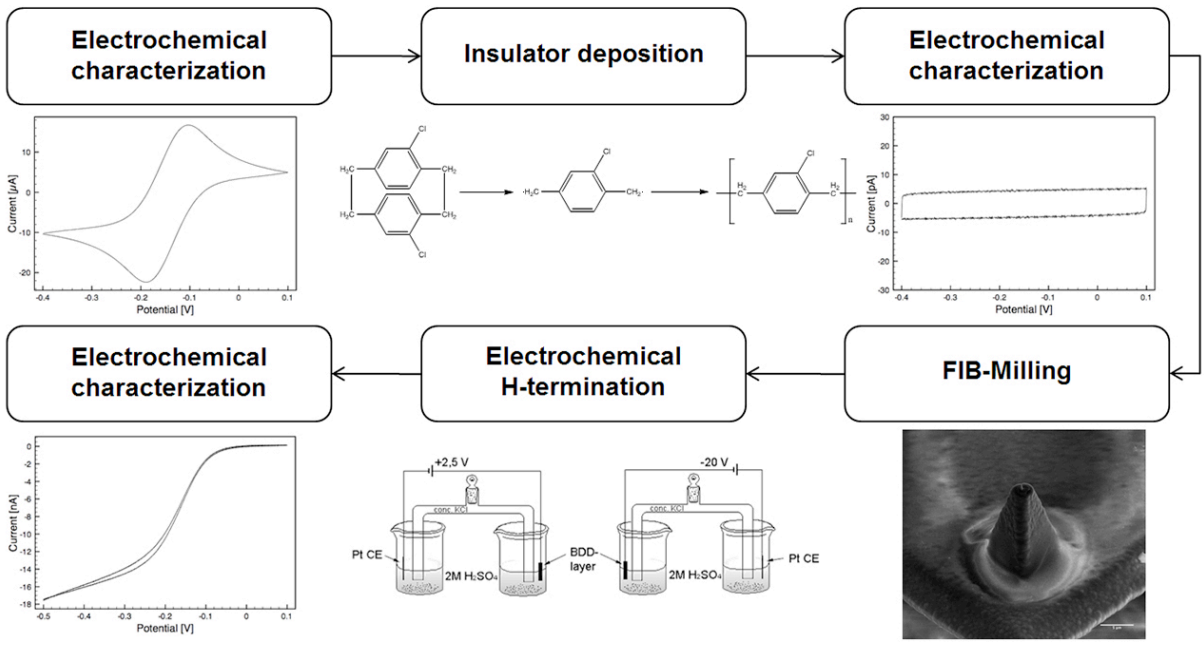

Fig. 32: Flow chart for fabricating BDD-AFM-SECM probes. CVs were recorded in 10 mM $[Ru(NH_3)_6]Cl_3$ / 0.1 M KCl vs. sat. Ag/AgCl; ν = 100 mV/s; reprinted from Electrochemistry Communications, 25, Alexander Eifert, Waldemar Smirnov, Stefan Frittmann, Christoph Nebel, Boris Mizaikoff, Christine Kranz, Atomic force microscopy probes with integrated boron doped diamond electrodes: Fabrication and application, 30-34, Copyright 2012, with permission from Elsevier [182].

As the film thickness of the BDD layer is in the range of approximately 500 nm, a total outer diameter of the electrode area of approximately 2.0 µm is obtained. An exemplary electrode is shown in Fig. 33 with an electrode diameter of approximately 2.4 µm, a tip height of 1.2 µm and an insulation thickness of 740 nm.

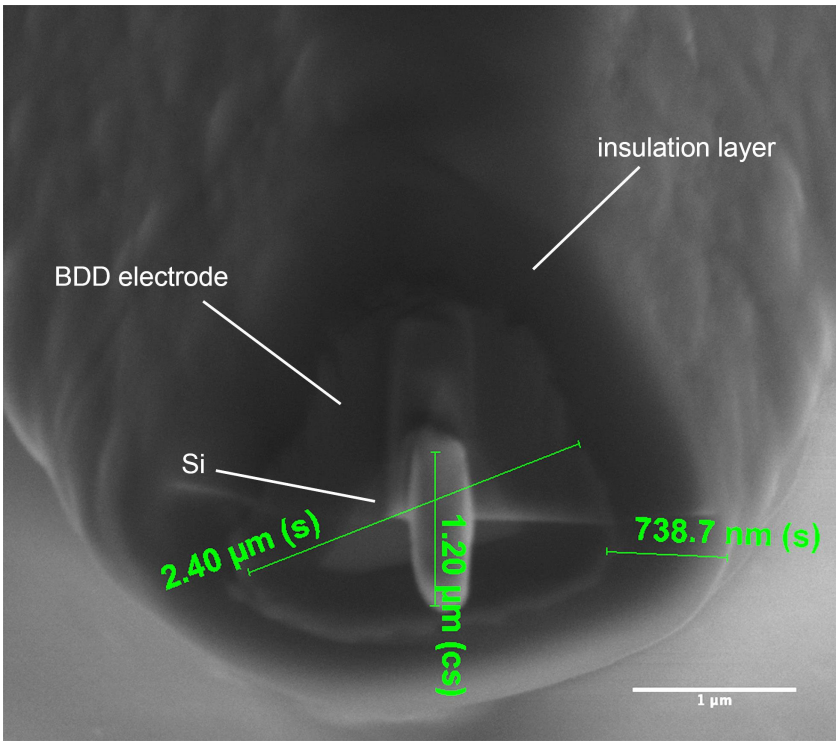

Fig. 33: Exemplary SEM image of a BDD-AFM-SECM probe; tip radius ≈ 50 nm, tip height: 1.2 µm; electrode diameter: 2.4 µm.

4.2.3. Electrochemical properties

Although the FIB milling process was performed with the Ga^+ ion beam parallel to the electrode surface, the lateral Gaussian distribution of Ga^+ ions perpendicular to the ion beam orientation caused a thin layer of amorphous carbon material directly beneath the penetration point due to the ion collision cascade. This amorphous carbon layer results in a slow HET rate and poor electrochemical properties if surface sensitive redox mediators are used (Fig. 34).

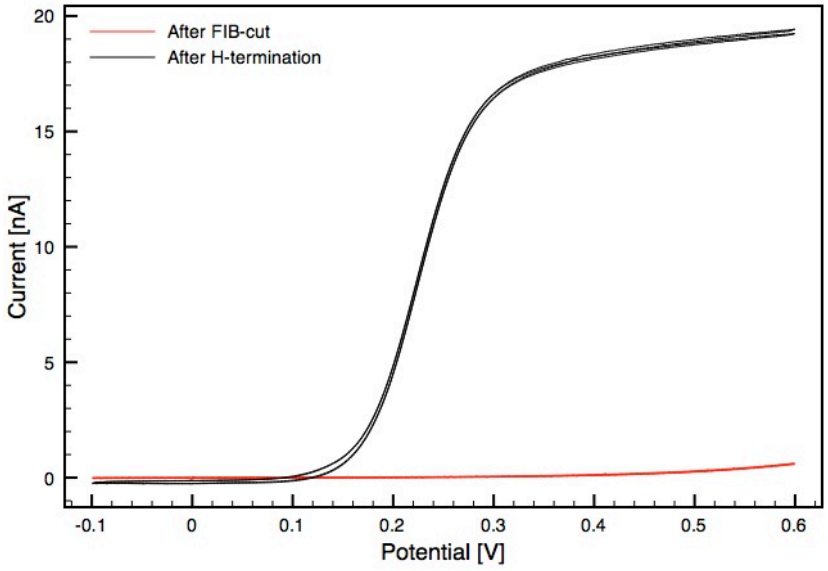

Fig. 34: CV recorded at an BDD-AFM-SECM probe (r = 1.3 µm) after FIB milling (red); CV after cathodic treatment (black); CVs were recorded in 10 mM $K_4[Fe(CN)_6]$ / 0.1 M KCl vs. sat. Ag/AgCl; ν = 100 mV/s.

As already discussed in chapter 3, the ferro/ferricyanide redox couple is frequently used as benchmark system to characterize the electrochemical properties of carbon-based electrode materials such as BDD. Applying an electrochemical H-termination process adapted from Hoffmann et al. [57] results in the restoration of the HET rate and a sigmoidal-shaped CV, as expected for a microelectrode with a radius of 1.3 µm, is observed (Fig. 34).

By fitting simulated data (DigiElch) to the experimentally acquired CVs, the HET rate constants were calculated. The HET rate constant for partially oxygen-terminated BDD not exposed to a Ga^+ ion beam is calculated with k^0 = 0.001 cm/s (α = 0.5) (see section 3.2.2). After FIB milling in a parallel orientation relative to the exposed electrode surface, the HET rate constant drops by 90% to k^0 = 0.0001 cm/s (α = 0.5) due to the amorphization. Compared to the results presented in section 3.2.2, for milled BDD electrodes without electrochemical treatment, a parallel milling orientation results in reduced surface damage and higher electron transfer rates. These results correspond with results already reported by Hu et al. [162], who investigated the impact of FIB irradiation on BDD relative to the milling angle amongst other subjects. After electrochemical treatment, the HET rate constant increases up to k^0 = 0.456 cm/s (α = 0.5) for cathodically treated BDD electrodes. The significant increase in the HET rate constant compared to the partially oxygen-terminated BDD before patterning indicates the restoration of an almost completely H-terminated

boron-doped diamond surface and the removal of almost any amorphous carbon material, generated during probe fabrication.

The quality of the BDD disc electrode can also be evaluated using the potential window of the electrode material (Fig. 35).

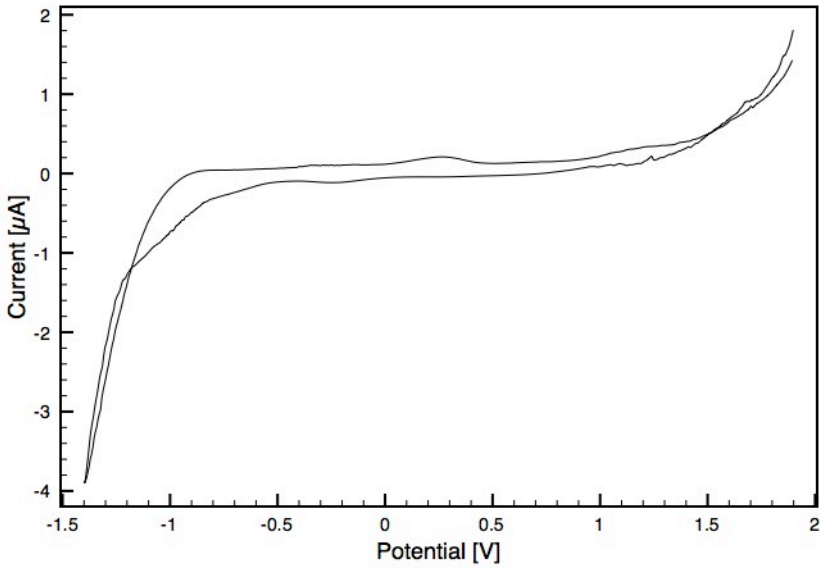

Fig. 35: CV of a H-terminated BDD-AFM-SECM probe recorded in 0.5 M H_2SO_4 vs. $Hg/HgSO_4$; ν = 200 mV/s.

Showing a potential window range similar to BDD electrodes reported in literature [54,156], it can be assumed that the majority of the amorphous carbon impurities have been removed during electrochemical treatment.

The exponential decay of the surface termination of BDD, while storing under ambient conditions, is a known issue [183,205]. Therefore, the electrochemical behavior of H-terminated BDD-AFM-SECM probes was monitored over several weeks.

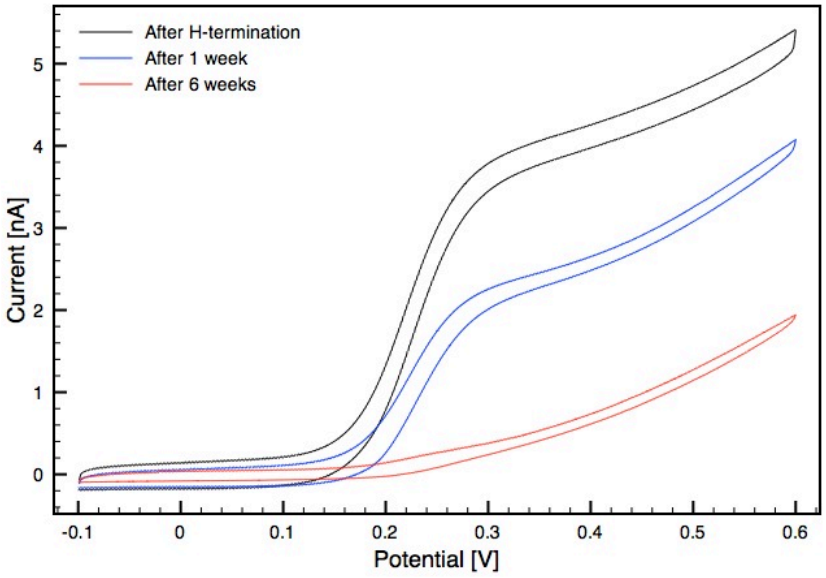

Fig. 36: CVs recorded at a combined BDD-AFM-SECM probe during long time storage; CVs were recorded in 10 mM $K_4[Fe(CN)_6]$ / 0.1 M KCl vs. sat. Ag/AgCl; ν = 100 mV/s.

As shown in Fig. 36, the freshly terminated BDD-AFM-SECM probe shows a sigmoidal-shaped CV. After storage for seven days in ambient conditions, the recorded CV reveals a decrease in the HET rate, which is visible from the altered slope and reduced steady state current of the obtained CV. After six weeks of storage, an electrochemical behavior similar to a FIB-milled BDD electrode without electrochemical treatment (Fig. 34; red) is obtained, indicating the severe decay of the electrochemical surface termination. By repeating the H-termination process, the fast HET rate can be restored. Hence, the electrochemical H-termination procedure is preferable compared to the standard termination procedures such as hydrogen plasma [58] or hot filament treatment [57]. Such procedures may damage the insulation layer, whereas an in situ H-termination is even applicable with the combined probe mounted onto the AFM probe holder.

4.2.4. Combined AFM-SECM measurements

To demonstrate the bifunctional AFM-SECM measurements, a Pt disc microelectrode with a diameter of 25 µm embedded in a glass sheath was imaged with a BDD-AFM-SECM probe. Topographical and electrochemical data were simultaneously acquired in AFM contact mode and SECM feedback mode as shown in Fig. 37.

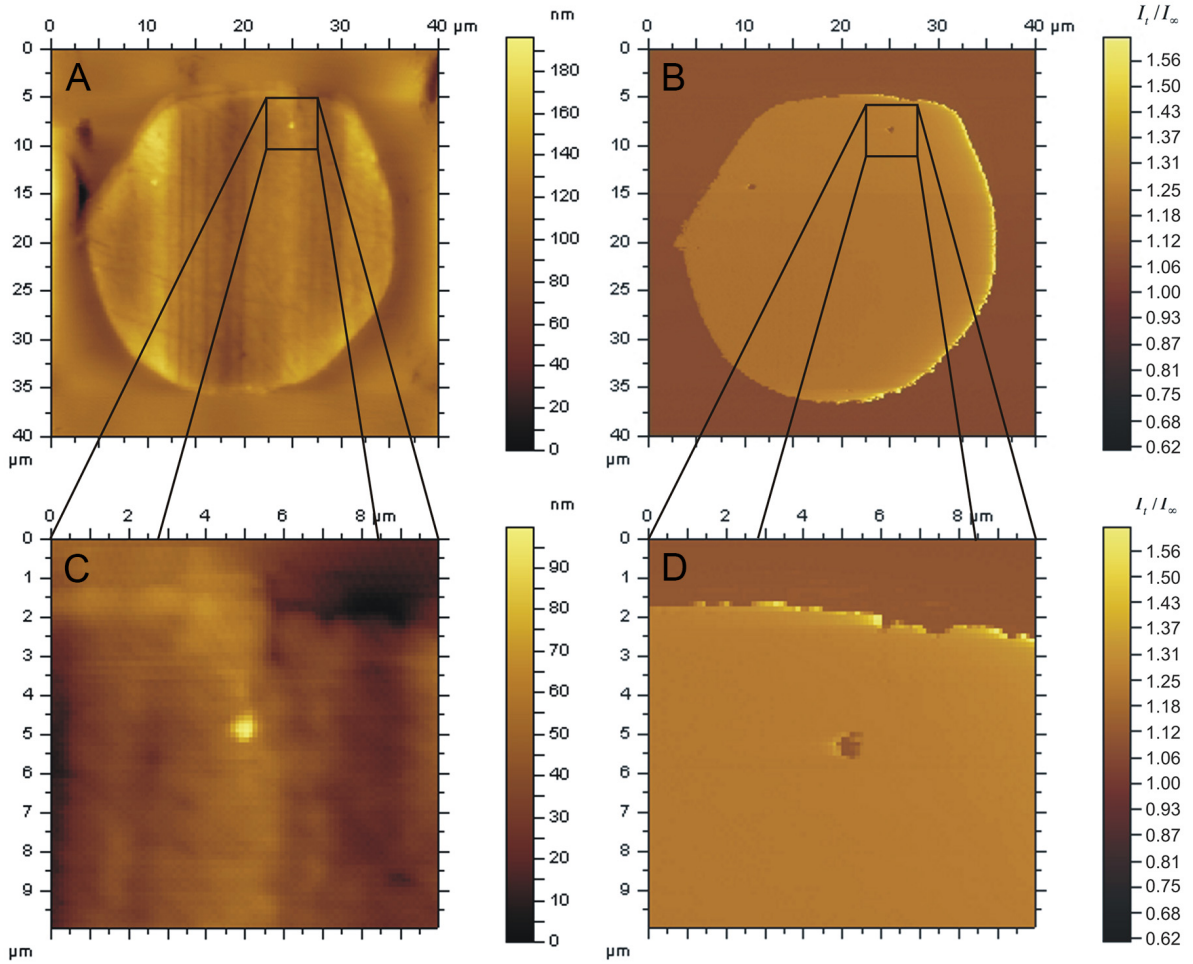

Fig. 37: Combined AFM-SECM measurement: A) topography recorded in contact mode; scan speed: 0.25 line/s; re-shaped AFM tip height: 1.1 µm; B) electrochemistry recorded in 10 mM $[Ru(NH_3)_6]Cl_3$ / 0.1 M KCl; E_{tip}= -400 mV vs. QAg/AgCl; electrode diameter 2.4 µm; magnified view of insulating diamond particle C) topography and D) electrochemical response; reprinted from Electrochemistry Communications, 25, Alexander Eifert, Waldemar Smirnov, Stefan Frittmann, Christoph Nebel, Boris Mizaikoff, Christine Kranz, Atomic force microscopy probes with integrated boron doped diamond electrodes: Fabrication and application, 30-34, Copyright 2012, with permission from Elsevier [182].

The topographical image of the Pt-UME (Fig. 37A) shows vertical features resulting from the grinding and polishing procedures. The final grinding step of the Pt-UME was performed with a 0.5 µm grain-sized diamond lapping film. The trenches created by the grinding particles are clearly visible on the Pt disc. Additionally, two small particles are observable at the Pt-UME surface in the upper part of the AFM image. These particles are probably abraded diamond particles as their size correlate with the grain size of the used lapping film and show a negative feedback effect in the electrochemical response (Fig. 37B,D), as expected for particles with insulating properties. The electroactive area of the Pt-UME shows a positive feedback in

contrast to the surrounding insulating glass. The topographical features are not observed in the electrochemical image, because the polishing grooves show height features in the range of 15-50 nm and the combined measurement is conducted in AFM contact mode, maintaining a constant distance between electrode and sample surface. In contrast, the embedded micrometer-sized abraded insulating diamond particles show a feature in topography and electrochemical response as the diffusive flux of redox mediator is partially blocked while the AFM-SECM probe is scanning over the abraded particle. In general, an insulating particle is expected to result in normalized current values < 1. Because of the size of the particle relative to the entire Pt electrode, only a reduction of the positive feedback is observed. The lateral electrochemical resolution of combined AFM-SECM probes is mainly defined by the diffusion profile of the redox mediator between the embedded electrode and the sample surface. Therefore, the electrode size and the electrode-sample distance are key parameters for imaging resolution. Typically, combined AFM-SECM probes with recessed electrodes were fabricated with a tip height of 70-80% of the electrode frame length. These tip heights result commonly in an electrochemical lateral resolution, where the observed features appear bigger than the electrode diameter (approximately 1.5 times the electrode diameter). A reason why the particle can be observed may be explained with a smaller tip height than originally fabricated. As the combined BDD-AFM-SECM probe is Parylene-C-insulated, which partially forms the top of the reshaped tip apex, an abrasion of this material during scanning is assumed. This abrasion leads to a reduction of the electrode-sample distance and therefore a more confined diffusion profile, ultimately resulting in an enhanced electrochemical resolution. Additionally, to the reduced electrode-to-sample distance, the high background current in the µA region leads to the fact that only the most dominant influences on the electrochemical signal are detected, if a background subtracted image is displayed. The high background current originates from imperfect insulation at the cantilever or the edges of the AFM-chip (which was visualized by copper deposition; results not shown). Therefore, only the center part of the diamond particle can be observed, when the AFM-SECM probe is positioned directly over the insulating spot and the influence on the diffusive flux is on its peak. The reason for possible imperfections in insulation originates from the inert material properties and surface roughness of polycrystalline BDD, resulting in an insufficient adhesion at the edges of the chip for the Parylene-C insulation. Despite the high

background current AFM-SECM measurements are possible as the electrode area in close proximity to the sample surface is the key feature for measurements in feedback mode and not influenced by the relative distant defect sites [206]. Zoomed topography and electrochemistry images of the abraded diamond particle are shown in Fig. 37C,D and Fig. 38, respectively.

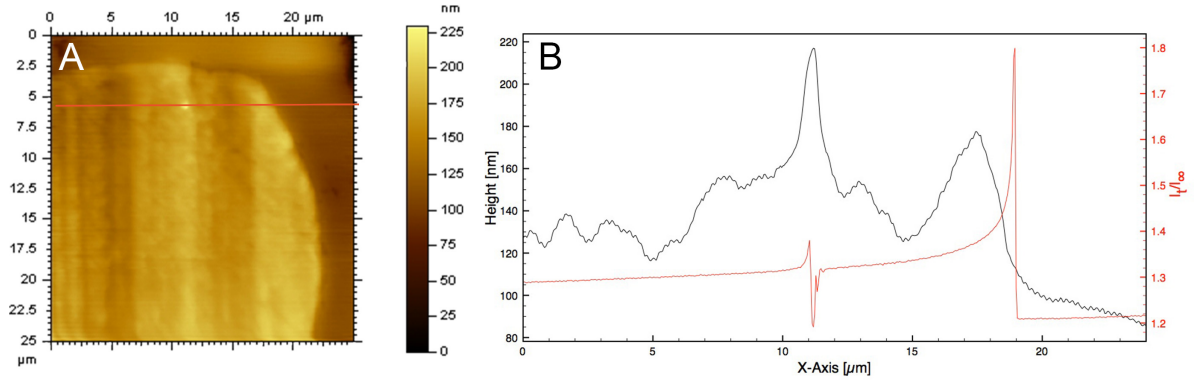

Fig. 38: A) Topography image of an abraded diamond particle on the Pt-UME surface; B) cross-sectional view of topography profile (black) and SECM profile (red) obtained at the position marked with the red line in A; scan direction: right-to-left (retrace); scan speed: 0.45 line/s; re-shaped AFM tip height: 1.1 µm; electrochemistry recorded in 10 mM $[Ru(NH_3)_6]Cl_3$ / 0.1 M KCl; E_{tip}= -400 mV vs. QAg/AgCl; electrode diameter 2.4 µm.

Fig. 38B shows a cross sectional topographical and electrochemical view obtained at the abraded diamond particle (marked as red line in Fig. 38A). The topographical features can be clearly resolved due to the curvature of the reshaped AFM tip, which is comparable to commercially available AFM probes. In contrast, the small electrode-sample distance influences the electrochemical signal. Once the probe is approaching the right edge of the Pt-wire (retrace scan), the AFM tip is still on the glass substrate while parts of the integrated electrode are already over the conductive Pt feature. This results in a decrease of the electrode-sample distance and therefore in an increase of the detectable current (positive feedback), as the Pt-wire is protruded by about 80 nm due to the polishing process. Fig. 38B also shows the exponential decay of the enhanced positive feedback, due to a linear increase of the electrode-sample distance while the AFM tip is moving onto the conductive Pt disc electrode. This behavior can be explained by the current-distance curve for a conductive substrate. When the tip apex finally is on the protruded Pt disc, the electrode-surface distance is re-established and the positive feedback current responds according to the distance of the tip height. The influence of the

applied potential on the recorded current was investigated in a series of experiments as exemplarily shown in Fig. 39. The potential applied to the BDD-AFM-SECM probe has been changed, while the AFM-SECM probe was continuously scanning across the sample surface.

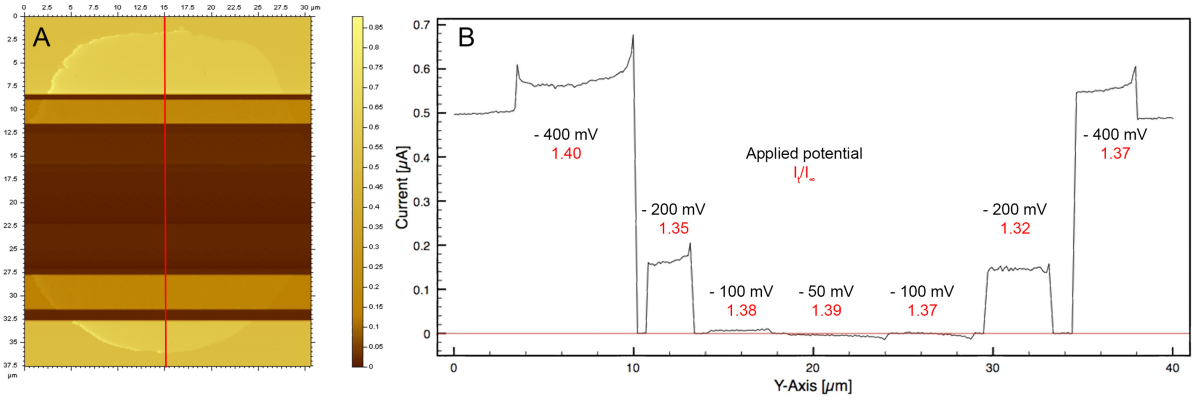

Fig. 39: A) Electrochemical image at variable potentials B) current profile (top-bottom); electrochemistry recorded in 10 mM $[Ru(NH_3)_6]Cl_3$ / 0.1 M KCl; E_{tip}= -400, -200, -100, -50 mV vs. QAg/AgCl; scan speed: 0.45 line/s; re-shaped AFM tip height: 1.1 µm; electrode diameter 2.4 µm.

As shown in Fig. 39, the applied tip potential determines the current response of the AFM-SECM probe. If a potential is applied close to or lower than the formal potential (> -180 mV vs. QAg/AgCl) of the redox species, the turnover rate is significantly reduced and the electrochemical conversion is attenuated (0.4 µA at -400 mV vs. 5.0 nA at -50 mV). Reasons for the overall observed high current values in the µA region have been discussed earlier. Although the turnover rate is changing according to the applied potential, the normalized current values still remain constant (Fig. 39B values indicated in red font). SECM measurements with BDD-AFM-SECM probes may be obtained, even when defect sites are present at the cantilever chip.

4.3. Simulations

4.3.1. Simulated diffusion profiles and calculated currents

Considering only diffusion for mass transport of the redox mediator, the expected steady-state current at the AFM tip-integrated electrode can be calculated using Fick's 2nd law of diffusion taking the appropriate boundary conditions into account (for details see section 10.2.4).

4.3.1.1. Simulated diffusion profiles for bulk conditions

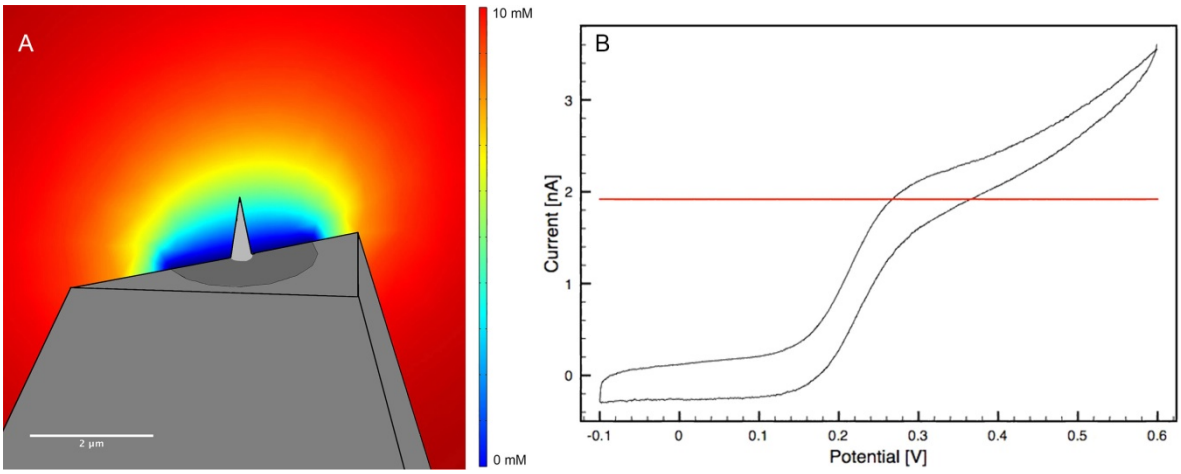

Fig. 40: A) Simulated diffusion profile for $K_4[Fe(CN)_6]$ at a BDD-AFM-SECM probe; tip height: 0.9 µm, electrode diameter: 2.4 µm, D = $6.3e^{-6}$ cm^2/s [132]; B) CV recorded after H-termination in 10 mM $K_4[Fe(CN)_6]$ / 0.1 M KCl vs. sat. Ag/AgCl; ν = 100 mV/s; (black) and the theoretically obtained steady state current level (red); adapted from Electrochemistry Communications, 25, Alexander Eifert, Waldemar Smirnov, Stefan Frittmann, Christoph Nebel, Boris Mizaikoff, Christine Kranz, Atomic force microscopy probes with integrated boron doped diamond electrodes: Fabrication and application, 30-34, Copyright 2012, with permission from Elsevier [182].

Fig. 40A shows a hemispherical (radial) diffusion profile with negligible influence of the AFM tip in the center of the electrode. The steady–state current of the combined AFM-SECM probe can be calculated by integrating the concentration gradient towards the electrode surface multiplied with the diffusion coefficient, the number of transferred electrons and the Faraday constant (Eq. 6).

$$i_{t,\infty} = nFD\int\left(\frac{\partial c}{\partial x}+\frac{\partial c}{\partial y}+\frac{\partial c}{\partial z}\right)dA$$

Eq. 6: Equation for calculating the steady-state current with number of electrons n = 1: Faraday constant F = $9.64853e^4$ C/mol; diffusion coefficient for $K_4[Fe(CN)_6]$ D = $6.3e^{-6}$ cm^2/s.

As a result, a steady-state current for a ring electrode with an outer diameter of 2.4 µm and an inner diameter of 0.3 µm is calculated with 1.92 nA as shown in Fig. 40B. This value is in good agreement with the experimentally obtained data, if the lack in leveling of the steady-state current at a potential higher than 0.35V is considered to originate from hindered diffusion process occurring at the electrode insulator interface due to the rough surface and partial bad adhesion of the insulation

material on the inert BDD, especially when the interface is exposed to the stress of hydrogen termination.

4.3.1.2. Simulated diffusion profiles for feedback conditions

Besides the calculation of the steady-state current for bulk solution, also simulations describing the expected (normalized) current for the conducted AFM-SECM experiments in section 4.2.4 were performed.

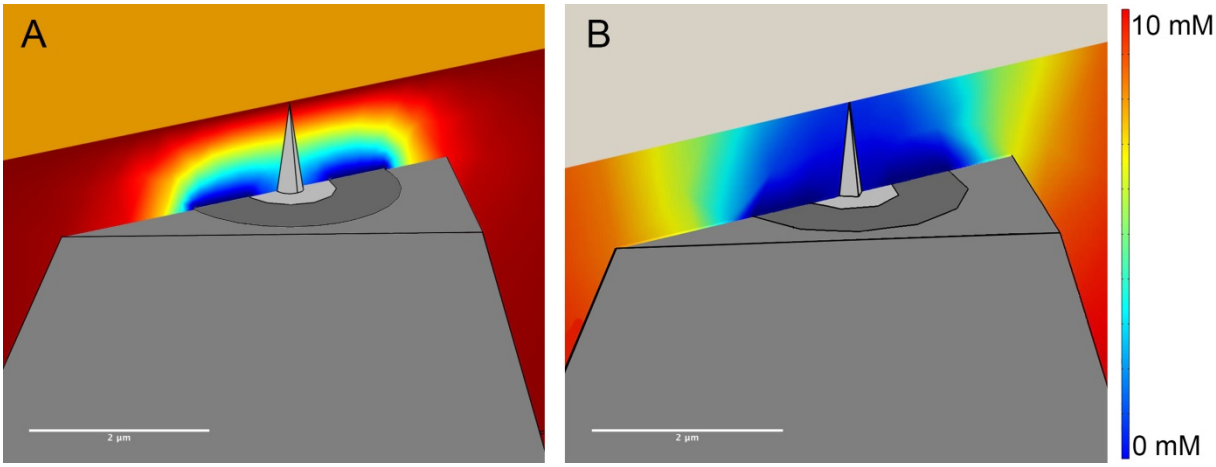

Fig. 41: Simulated diffusion profiles for $[Ru(NH_3)_6]Cl_3$ at a BDD-AFM-SECM probe; tip height: 1.0 µm; electrode diameter: 2.4 µm, D = $7.5e^{-6}$ cm^2/s [132]; A) positive feedback with redox mediator regeneration at the sample surface; B) negative feedback with hindered diffusion towards the electrode caused by an insulating surface.

In case of a positive feedback (conductive substrate), $[Ru(NH_3)_6]^{2+}$ reduced at the tip, is re-oxidized to $[Ru(NH_3)_6]^{3+}$ at the sample surface. Therefore, an almost instantaneous conversion (k = $1e^9$ 1/s) of the previously generated $[Ru(NH_3)_6]^{2+}$ to $[Ru(NH_3)_6]^{3+}$ in close proximity to the sample surface (30 nm) is considered for the simulation. In this case a “compressed radial diffusion profile” is obtained as the regeneration cycle of the redox mediator results in a bulk solution concentration in close proximity to the sample surface (Fig. 41A). For negative feedback, the diffusion profile at the AFM-SECM probe is significantly changed as the redox mediator cannot be regenerated at the sample surface. As shown in Fig. 41B, a cylindrical/conical diffusion profile around the tip of the probe is obtained, as the redox molecules are only supplied by the surrounding solution. Therefore, the impact on the electrochemical signal depends on the flux of the redox mediator towards the electrode, which is influenced by the presence of the sample surface and thickness

of the insulation layer. In both cases (pos/neg feedback), the concentration of the redox mediator, confined between electrode and sample surface, is exponentially rising towards the outer insulator boundary until bulk conditions are reached. Derived from the obtained diffusion profiles, it can be assumed that the electrochemical signal is already influenced laterally and vertically at a distance of 1.5 times the electrode diameter.

The calculated current for positive feedback is 2.58 nA for the chosen redox couple and 1.39 nA for negative feedback, which results in calculated normalized currents of 1.25 for a positive feedback and of 0.67 for a negative feedback, respectively. Although the calculated normalized current for positive feedback is in good agreement with the experimental data obtained from the combined AFM-SECM experiments shown in Fig. 37, the calculated values for negative feedback are not in agreement. This may be attributed to imperfections in the insulation as previously discussed. For positive feedback, the redox mediator cycle in the confined volume between electrode and sample surface is mainly contributing to the normalized current, which is confirmed by the obtained data.

4.4. Conclusion & Outlook

Within this chapter, the FIB-based fabrication of commercially available Si AFM probes with embedded BDD ring electrodes was demonstrated. FIB processing has an adverse effect on the electrochemical characteristics of BDD. By introducing an electrochemical surface treatment step after FIB milling, the amorphous carbon content could be reduced and a hydrogen re-termination of the surface could be achieved. The long-term stability of the surface termination was also investigated. It could be demonstrated that the electrochemical hydrogen termination can be maintained for several days, while the probe is stored under ambient conditions. After longer period of times, the surface termination deteriorates but the BDD electrodes can be H-terminated again, re-establishing the electrochemical properties. In addition to the experimental characterization, the concentration profiles and resulting faradaic currents have been calculated using commercially available software (COMSOL Multiphysics). The obtained experimental results like steady state current in bulk solution and normalized positive feedback currents of combined AFM-SECM experiments are both in agreement with theoretically obtained values. For further improving the performance of combined BDD-AFM-SECM probes, intrinsic diamond (iD) may be used as an insulation layer. An advantage of iD as insulation material is related to a reduced insulator layer thickness of a few hundred nanometers from approximately 1 µm, which is currently required for Parylene-C insulation. As the tip height should be below the electrode diameter, a reduced electrode diameter enabling improved electrochemical resolution requires also a reduced insulator thickness to avoid high RG-values. In all commercial AFM systems, the AFM probes are mounted under an angle between 9-11 degree resulting in a contact between insulation layer and sample if the AFM tip height is smaller than approximately 250 nm and the insulation layer has a thickness of approximately 1 µm. Furthermore, using iD as insulator opens new possibilities for cleaning of the AFM-SECM probes due to its high thermal and physical stability in contrast to Parylene-C. This high thermal stability would allow applying harsh cleaning procedures to remove organic contaminations from BDD electrodes. iD can only be used as insulator material in its O-terminated form, as the surface transfer conductivity of H-terminated iD [49,61] would otherwise result in a conductive iD layer, when immersed into aqueous solution. A further advantage of iD as insulation material is related to the similar

milling rate of BDD and iD, which would allow a more effective top-mill fabrication process [207,208] resulting in as smooth flat electrode and insulation area (Fig. 42).

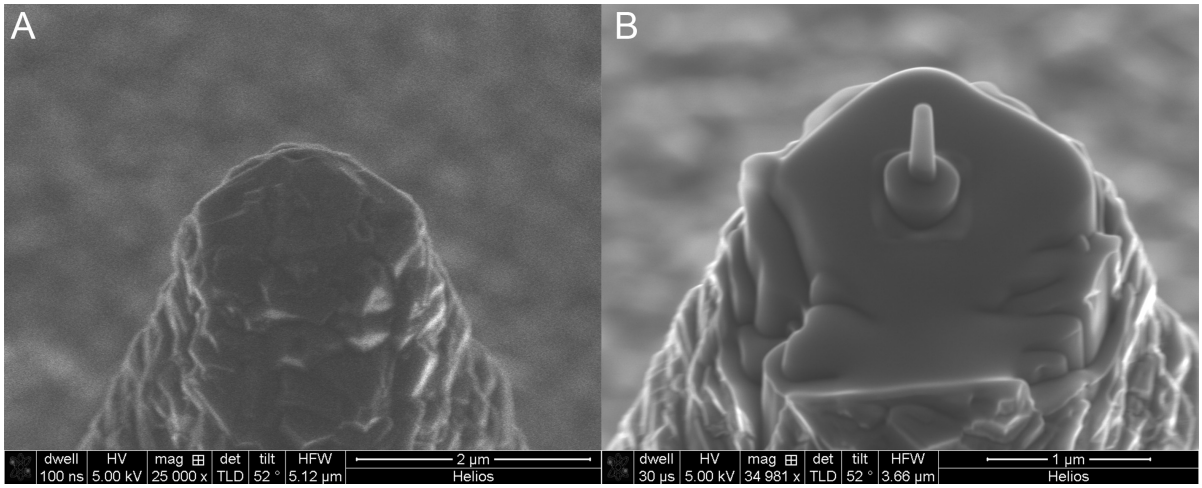

Fig. 42: A) SEM image of intrinsic diamond-insulated BDD coated-AFM probe; B) top-mill fabricated AFM-SECM probe with an integrated BDD electrode; reprinted from Micron, 68, Alexander Eifert, Boris Mizaikoff, Christine Kranz, Advanced fabrication process for combined atomic force-scanning electrochemical microscopy (AFM-SECM) probes, 27-35, Copyright 2015, with permission from Elsevier [208].

5. Numerical simulations for top-mill-fabricated AFM-SECM probes

5.1. Introduction

In AFM-SECM, the probe is scanned in close proximity to the sample surface and the electrochemical signal depends on the diffusive flux of the electroactive species towards the electrode [5,103]. A homogeneous diffusion behavior towards a flat embedded electrode can be observed in bulk solution [103]. The diffusion is thereby influenced by the geometry of the insulating sheath and a possible tilt of the electrode. A tilted electrode may result in a significant change of the diffusive flux, and therefore in a change of the faradaic current. For example, such tilted electrode geometries are generated, if a top-mill process is employed to fabricate combined AFM-SECM probes. In a top-mill process, the ion beam is oriented perpendicular to the cantilever arm, in contrast to a lateral orientation, which is commonly used in the fabrication process [8]. Depending on the milling yields of the material layers inward or outward tilted electrode geometries are obtained [208]. For probes insulated with a layer that has faster milling rates than the underlying conductive layer, an outward tilted electrode is obtained. In turn, an insulating material with lower milling rates results in an inward tilted electrode.

In order to predict the influence of different probe geometries on the faradaic current, numerical simulations have been reported describing the steady state characteristics of different AFM-SECM probe designs as well as the behavior upon the approach to an insulating or conductive surface [123,125,206,209,210]. Also, the effect of irregular geometrical characteristics like defects [211] on the steady-state behavior have been simulated. For example, Dobson et al. performed numerical simulations for triangular-shaped electrodes located at the tip apex, the resulting distortion of the diffusion field around the electrode and the theoretical behavior upon approach to the surface [125]. Davoodi et al. presented numerical simulations to describe the versatility of combined AFM-SECM probes with different electrode geometry [210]. Using finite element analysis, Holder et al. calculated time resolved diffusion profiles for non-insulated AFM-SECM probes to evaluate the spatial resolution for electrogenerated species following a potential step. Thereby they also examined the time resolved diffusion field evolution in close proximity to insulating, conductive and biased surfaces [206].

This chapter focuses on the influence of tilted AFM-SECM electrode geometry obtained in a top-mill fabrication process of the multi-layer multi-material composition on the current response [208]. The calculated currents of differently tilted electrodes are compared to standard FIB-fabricated AFM-SECM probes [8,131,182,209] to evaluate the quality of the top-milled probes for combined AFM-SECM measurements. Also, a comparison to experimental data as described in [208] will be presented. Parts of this chapter have already been published and are reprinted from *Micron, 68, Alexander Eifert, Boris Mizaikoff, Christine Kranz, Advanced fabrication process for combined atomic force-scanning electrochemical microscopy (AFM-SECM) probes, 27-35*, Copyright 2015, with permission from Elsevier [208].

5.2. Results & Discussion

5.2.1. Simulations of bulk conditions

The influence of three different electrode geometries will be compared using numerical simulations (see also section 4.3) to evaluate the versatility of the combined probes for imaging. The different electrode angles result from different material compositions used for the fabrication process (Parylene-C/Au/Si_xN_y; Si_xN_y/Au/Si_xN_y) and the orientation of the milling beam (top-mill [207,208] or side-mill [8]).

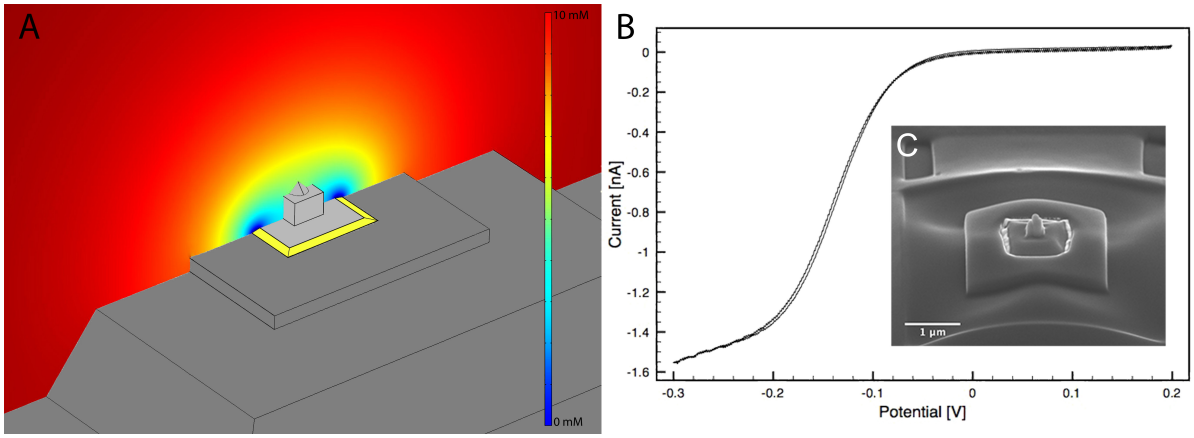

Fig. 43: A) Simulated diffusion profile towards a Parylene-C-coated probe fabricated with a top-mill process; electrode diameter 1.0 µm; B) CV recorded in 10 mM $[Ru(NH_3)_6]Cl_3$ with 0.1 M KCl as supporting electrolyte; ν = 100 mV/s; C) SEM image of a top-mill fabricated Parylene-C-coated AFM-SECM probe; adapted from Micron, 68, Alexander Eifert, Boris Mizaikoff, Christine Kranz, Advanced fabrication process for combined atomic force-scanning electrochemical microscopy (AFM-SECM) probes, 27-35, Copyright 2015, with permission from Elsevier [208].

As shown in Fig. 43C, the fabrication process of the Parylene-C-coated probe, which also requires an additional area of thinned insulator material to avoid topographical scan artifacts, results in an outward tilted electrode surface [207,208]. Due to an increased diffusional flux based on the tilt angle, an increased current is expected compared to flatly embedded electrodes with identical electrode dimensions (Fig. 44A). In analogy to section 4.3, the theoretical current for a 10 mM $[Ru(NH_3)_6]Cl_3$ was calculated using Eq. 6. The current obtained for an electrode as illustrated in Fig. 43A has a theoretical value of 1.47 nA (assuming a tilt angle of +13° for Parylene-C/Au/Si_xN_y; details see [208]), which is in good agreement with previously recorded experimental data (Fig. 43B).

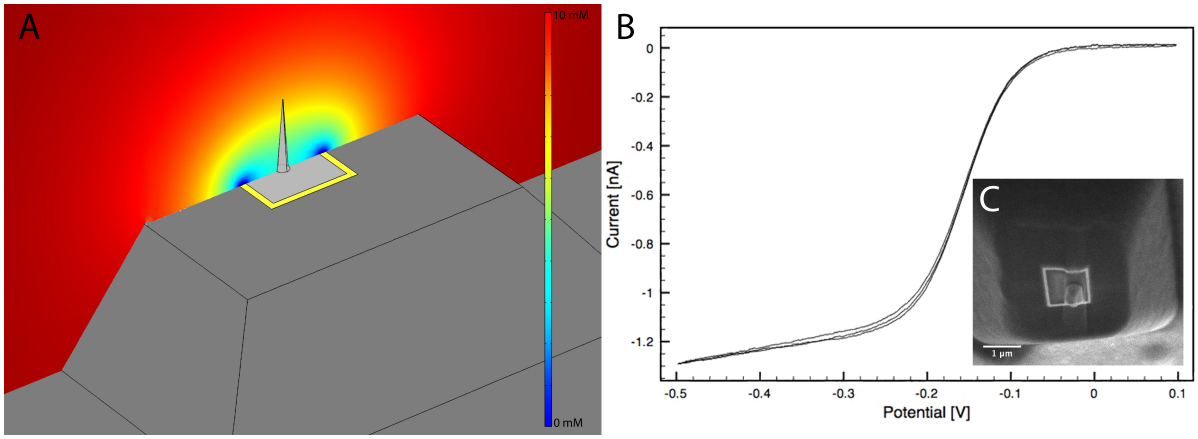

Fig. 44: A) Simulated diffusion profile towards a Parylene-C-coated probe fabricated with a standard side-mill process [8]; electrode diameter 1.0 µm; B) CV recorded in 10 mM $[Ru(NH_3)_6]Cl_3$ with 0.1 M KCl as supporting electrolyte; ν = 100 mV/s; C) SEM image of a side-mill fabricated Parylene-C-coated AFM-SECM probe.

The faradaic current for a flatly embedded electrode with a similar frame length of 1 µm was calculated to 1.22 nA, which is also in good agreement with the experimentally obtained data (Fig. 44B). Both electrodes (0° and +13°; Fig. 43 and Fig. 44) show a similar hemispherical / radial diffusion profile with a homogeneous concentration distribution. As a result, an increased diffusive flux towards the electrode is calculated for the tilted electrode geometry compared to a flatly embedded electrode, which is also reflected in higher calculated and measured faradaic currents.

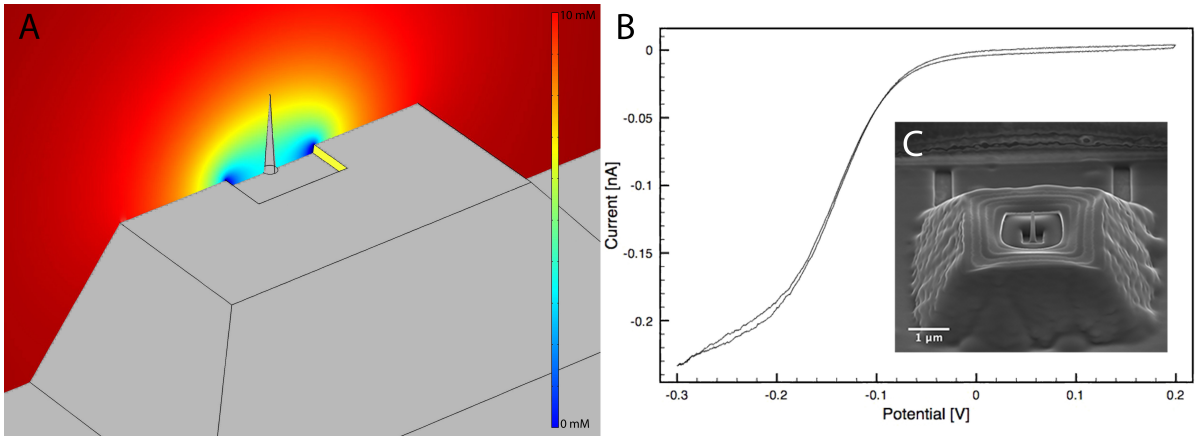

Fig. 45: A) Simulated diffusion profile towards a Si_xN_y-coated probe fabricated with a top-mill process; electrode diameter 1.0 µm; B) CV recorded in 10 mM $[Ru(NH_3)_6]Cl_3$ with 0.1 M KCl as supporting electrolyte; ν = 20 mV/s; C) SEM image of a top-mill fabricated Si_xN_y-coated AFM-SECM probe; adapted from Micron, 68, Alexander Eifert, Boris Mizaikoff, Christine Kranz, Advanced fabrication process for combined atomic force-scanning electrochemical microscopy (AFM-SECM) probes, 27-35, Copyright 2015, with permission from Elsevier [208].

The simulation of the diffusion towards a top-mill-fabricated Si_xN_y-coated probe predicts a concentration profile similar to the previously described electrode geometries. However, the inward tilt of the electrode significantly reduces the diffusive flux towards the electrode. Due to the hemispherical diffusion, the contribution from the electrode edges to the overall current density is highest, which is obstructed by the surrounding insulator material of the electrode for inward tilted electrodes (Fig. 45A). As a result of the obstructed electrode surface, a reduced flux is calculated and is experimentally verified. The calculated current for an inward tilted electrode with a tilt angle of -80° as shown in Fig. 45C is 0.86 nA. This is not in full agreement with the experimentally obtained data, but confirms a clear trend of the tilt influence. In fact, the impact of inward tilt may be even more severe, as the experimentally measured current is only around 0.2 nA (Fig. 45B). Tab. 6 gives a summary of the calculated currents for the different electrode geometries.

Electrode tilt	Current ratio
-80°	0.707
0°	1
+13°	1.202

Tab. 6: Calculated current ratios for combined AFM-SECM probes with different electrode tilts; adapted from Micron, 68, Alexander Eifert, Boris Mizaikoff, Christine Kranz, Advanced fabrication process for combined atomic force-scanning electrochemical microscopy (AFM-SECM) probes, 27-35, Copyright 2015, with permission from Elsevier [208].

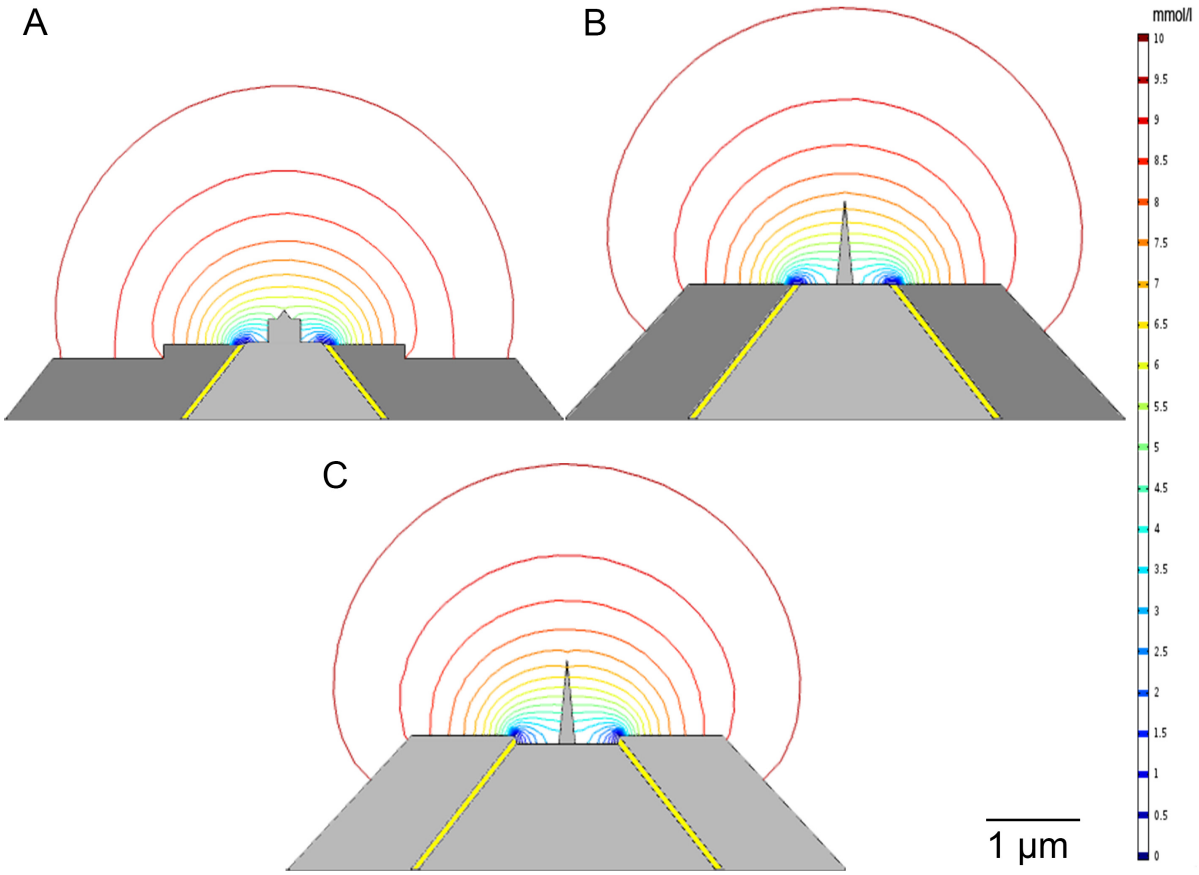

Fig. 46: Cross-sectional contour plot of the simulated concentration distribution of $[Ru(NH_3)_6]Cl_3$ in respect to the three selected electrode tilts; A) +13°; B) 0°; C) -80°.

The contour plot of the redox mediator concentration (Fig. 46) shows the reduced mass transfer towards the -80° tilted electrode compared to the outward tilted and flat electrode designs. The contour lines up to a concentration of 4.5 mM cover a wider volume of the tip geometry, thus indicating a lower concentration gradient and therefore a lower anticipated diffusive flux. In contrast, the contour plot for the combined probes with a tilt ≥ 0° show a narrow concentration distribution and

therefore a higher concentration gradients and mass transports towards the electrode, which are also observed in the experimental data.

5.2.2. Simulations of SECM feedback experiments

Simulations in bulk conditions have shown that the electrode tilt has an influence on the obtained faradaic currents. In a next step, the influence of the electrode tilt on the feedback signal in SECM is evaluated. Feedback simulations were performed following the approach of Zoski et al. [212] with slight adaptations for a three-dimensional geometry (for details see section 10.3.4.2).

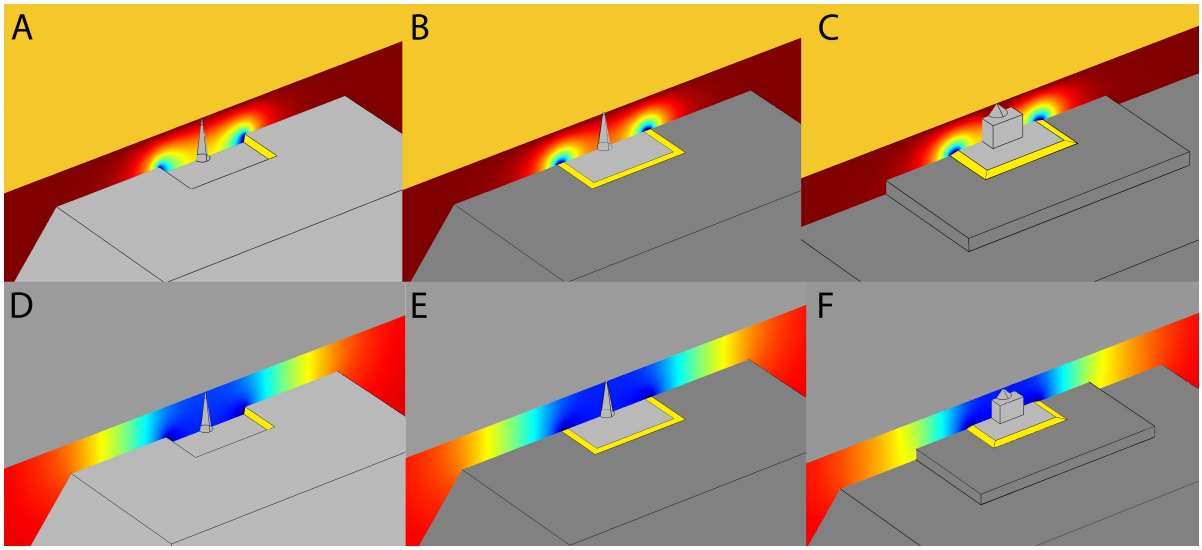

Fig. 47: Simulated diffusion profiles of $[Ru(NH_3)_6]Cl_3$ at combined AFM-SECM probes with different electrode tilts in A-C) positive feedback; D-F) negative feedback conditions; A&D) -80°; B&E) 0°; C&F) +13°; electrode diameter 1.0 µm.

Electrode tilt	I_{pos} [nA]	I_{neg} [nA]
-80°	1.378	0.435
0°	2.024	0.605
+13°	2.445	0.719

Tab. 7: Calculated faradaic currents obtained from the simulated diffusion profile for feedback conditions [212].

Electrode tilt	I_t/I_∞ (pos.)	I_t/I_∞ (neg.)
-80°	1.595	0.503
0°	1.656	0.495
+13°	1.663	0.489

Tab. 8: Normalized electrode currents of the different electrode tilts for feedback conditions.

As shown in Tab. 7 and Tab. 8, the electrode tilt influences the current recorded at the AFM-SECM electrode, while the probe is in close proximity to the sample surface. For the simulated data, the different tilt angles show only minor influence on the normalized currents. The outward tilted and flatly embedded electrodes show comparable current ratios in feedback conditions - in contrast to the negatively tilted electrode, which shows a slightly reduced positive feedback signal (reduced by approximately 6% compared to the values for 0° and +13°). This reduced normalized current of the positive feedback signal can be attributed to a slightly increased distance of the electrode area close to the inner electrode diameter, which is further recessed from the insulation material. For negative feedback conditions, the electrodes show similar normalized current. As shown in Tab. 7, a steady increase of current from the inward to the outward tilt is observed, reflected in an increase by 77.4% from -80° to +13°.

5.3. Conclusion

The different electrode tilts have a significant influence on the simulated currents under bulk conditions. However, no significant influence on the normalized feedback current could be predicted. In conclusion, all probes with different tilt angles of the electrodes should be suitable for combined AFM-SECM experiments. Although, the SNR for negative tilted electrodes may be an issue due the reduced current. Nevertheless, experimental results indicated that for negatively tilted electrode surfaces, unfavorable contaminations of the electrode during imaging prevent their use [207,208].

6. Improved signal-to-noise ratio using an integrated amplifier system

6.1. Introduction

Most of the so far reported AFM-SECM experiments [7,8,121,124,125,128,130,182] were performed using AFM-instruments with individual adaptations for topographical and electrochemical data acquisition. Such an adapted AFM system was also used for the experiments described in section 10.2.3. The electrochemical data are typically recorded using an external potentiostat, thereby requiring a cable connection to the mounted AFM-SECM probe.

The signaling pathways of the measured current at the working electrode (AFM-SECM probe) to the potentiostat are fairly long. Hence, adverse effects such as parasitic couplings lead to undesirable SNRs, which require data processing like Fourier-filtering (see 6.2.1).

This chapter will be focused on improved SNRs and the advantages of a nosecone-integrated signal amplification and transduction. A comparison between external and internal data acquisition shows an improved SNR, which can be achieved for example with a trans-impedance amplifier circuit (Fig. 48) located close to the AFM-SECM probe.

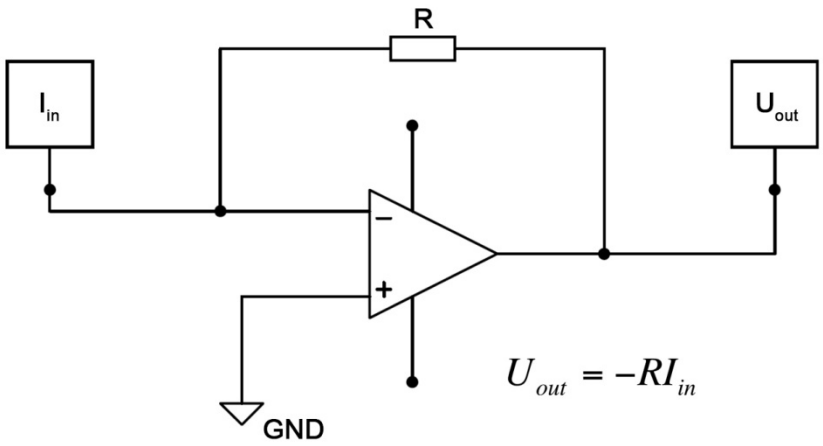

Fig. 48: Scheme of a trans-impedance amplifier circuit.

In combination with the nosecone-integrated signal transduction strategy, a new cartridge-based mounting system for fast and simple mounting and changing

AFM-SECM probes was designed and developed in cooperation with the nanomeasure group of Keysight Technologies. In addition to the evaluation of the integrated system relative to the external data acquisition, applications benefitting from the improved integrated system will be demonstrated. The final design and fabrication of the AFM-SECM nosecone and cartridges were realized by Keysight Technologies (Chandler, AZ, USA).

The application shown within this chapter is a collaborative effort between IABC and Prof. Ricardo Souto and Dr. Javier Izquierdo, University of La Laguna, Spain. Dr. Javier Izquierdo was visiting IABC and during his stay, the pit corrosion experiments were performed in a joint effort.

Parts of this chapter have also already been published in [213-215]; reprinted from *Electrochemistry Communications, 51, Javier Izquierdo, Alexander Eifert, Ricardo M. Souto, Christine Kranz, Simultaneous pit generation and visualization of pit topography using combined atomic force–scanning electrochemical microscopy, 15-18*, Copyright 2015, with permission from Elsevier [213], and reprinted from *J. Izquierdo, A. Eifert, C. Kranz, R. M. Souto, In situ monitoring of pit nucleation and growth at an iron passive oxide layer by using combined atomic force and scanning electrochemical microscopy, ChemElectroChem, 2015, DOI: 10.1002/celc.201500100*, Copyright 2015, with permission from Wiley-VCH Verlag GmbH & Co. KGaA, Weinheim [215].

6.2. Results & Discussion

6.2.1. Integrated signal transduction and amplification

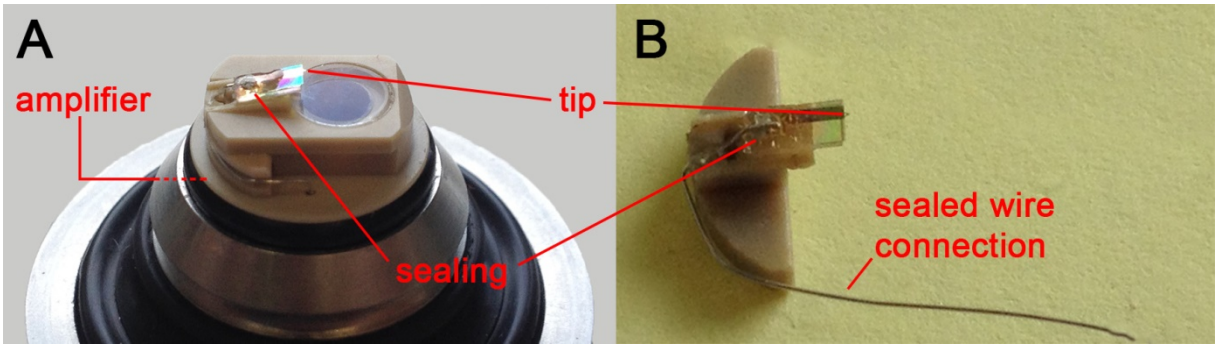

Fig. 49: A) Photograph of an AFM-SECM nosecone (Keysight Technologies) with integrated pre-amplifier; B) Photograph of AFM-SECM cartridge for fast and simple probe replacement with mounted AFM-SECM probe. The contact to the electrical wire is sealed with UV-curable glue and insulating varnish.

As shown in Fig. 49A, the AFM-SECM nosecone is characterized by a shortened signaling pathway through a Teflon-insulated Pt-wire connecting the probe to an amplifier circuit, mounted inside the AFM nosecone. In addition, the cartridges allow a pre-mounting of the AFM-SECM probes. This is a significant advantage, as it permits a fast probe replacement between experiments - if required. As a result of the cartridge with the mounted probe being placed in close proximity to the amplifier, the signaling pathway length of the current signal can be significantly reduced from several tens of centimeters down to 2-3 cm. This reduced length between tip and signal transducer results in a reduced noise level of the current signal (shown in Fig. 50) in comparison to the external setup with a relatively long wire connection, which may lead to significant antenna effects increasing external noise during measurements. In particular, the peak-to-peak noise level reduces from approximately 40-60 pA (external data acquisition) to approximately 10 pA (integrated system). The obtained reduction factor of five allows a higher sensitivity in AFM-SECM measurements. Fig. 51 and Fig. 53 show AFM-SECM measurements of model samples with varying conductivity, clearly demonstrating the improved SNR.

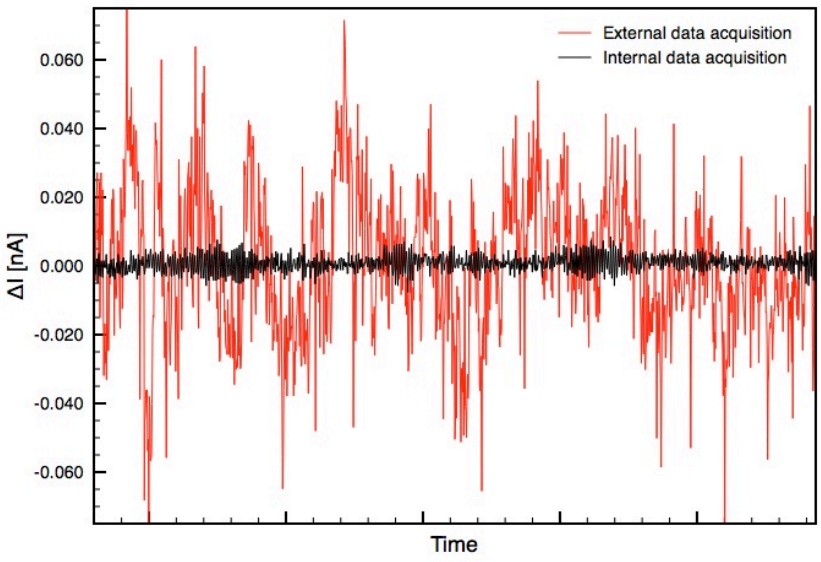

Fig. 50: Current-time graph recorded with external (red) and internal (black) data acquisition (gain: 1 nA/V); electrochemical data recorded in 10 mM $[Ru(NH_3)_6]Cl_3$ / 0.1 M KCl; E_{tip}= -500 mV vs. QAg/AgCl; sampling rate: 25 Hz (external), 397 Hz (internal); electrode diameter: 1.2 µm (external), 0.7 µm (internal).

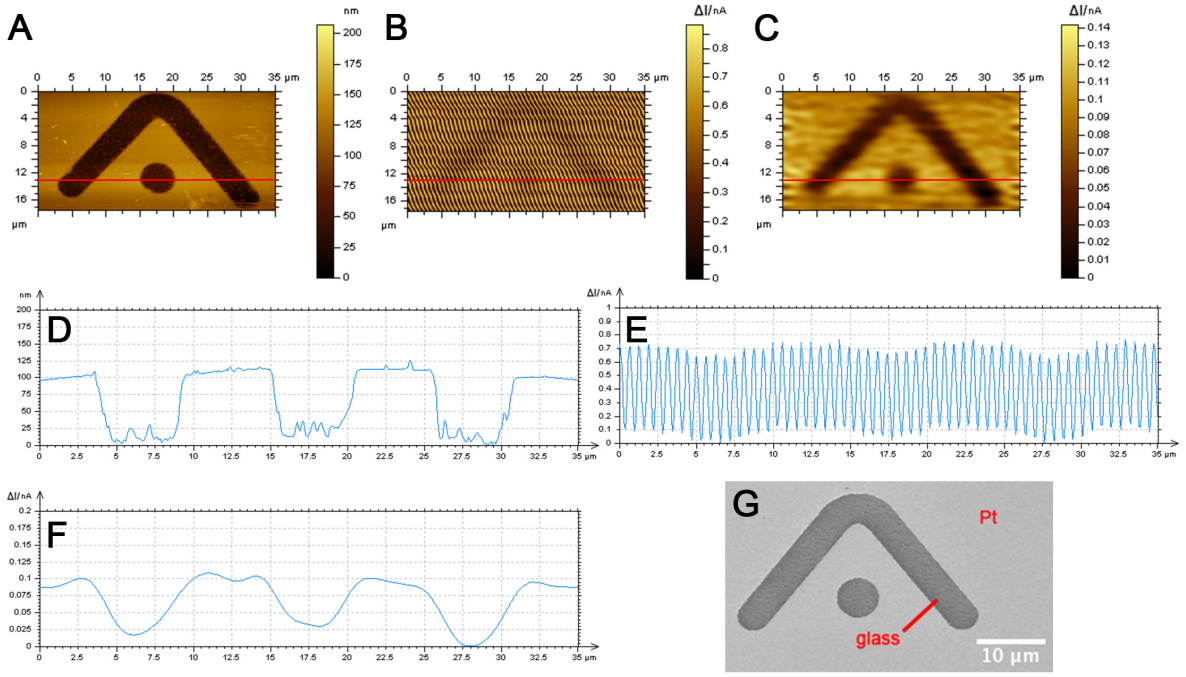

Fig. 51: AFM-SECM image (relative current) using an external potentiostat for the electrochemical experiment and a top-mill fabricated Parylene-C-coated AFM-SECM probe. The sample reflects milled structures in Pt-coated glass in form of the letter “A”; scan speed: 0.3 line/s; re-shaped AFM tip height: 660 nm; electrode frame length: 1.2 µm; A) topography recorded in contact mode; B) SECM image recorded in feedback mode, images were recorded in 10 mM $[Ru(NH_3)_6]Cl_3$ / 0.1 M KCl; E_{tip}= -500 mV vs. QAg/AgCl; C) electrochemical data after FFT-filtering; D-F) extracted profiles of A-C); G) SEM image of the model sample.

Fig. 51 shows a combined AFM-SECM measurement of the letter A (insulating surface), FIB-milled into a conductive Pt layer. The electrochemical data were recorded with an external potentiostat and plotted in relative current values for better comparison with data shown in Fig. 53. As shown in Fig. 51B and E, the electrochemical signal recorded at the tip is superimposed with a dominant periodic signal. The negative feedback effect generated in the area of the letter A is still observable in the raw electrochemical image, but the superimposed periodical signal here is five times larger than the actual feedback current. Hence, post-scan data processing such as FFT-filtering is frequently applied for combined AFM-SECM measurements using an external potentiostat. The strongest superimposed signal corresponds to a coupling of the power net frequency of 50 Hz and the corresponding overtones (net hum) (Fig. 52), which can be removed by frequency filtering leading to an improved electrochemical image of the sample surface (Fig. 51C).

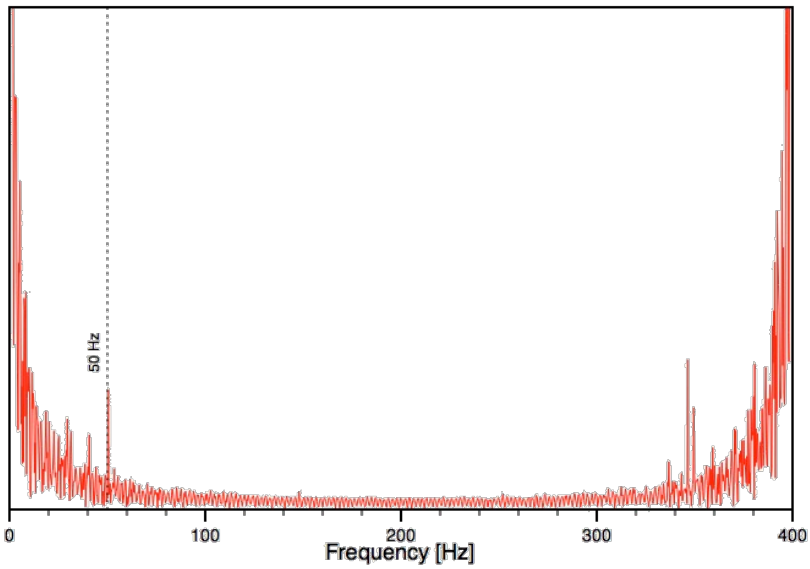

Fig. 52: Exemplary FFT-spectrum of a i-t-curve recorded during AFM-SECM measurement in 10 mM $[Ru(NH_3)_6]Cl_3$ / 0.1 M KCl; E_{tip}= -500 mV vs. QAg/AgCl using an external potentiostat.

The electrochemical data of AFM-SECM measurements recorded with the amplifier-modified nosecone (Fig. 53) shows no significant periodic signal superimposing the electrochemical signal as shown in Fig. 53B. Hence FFT data processing can be omitted, thereby minimizing artifacts related to the data treatment. These filtering artifacts are clearly visible by comparing Fig. 51F and Fig. 53F, where the filtered signal shows a smoother electrochemical profile without further substructures. Additionally, the amplifier-modified nosecone also shows higher relative current values for feedback measurements. This can be attributed to the reduction of the signaling pathway and the associated elimination of electronic resistance generated at the cable junctions, along the signaling pathway for external data acquisition.

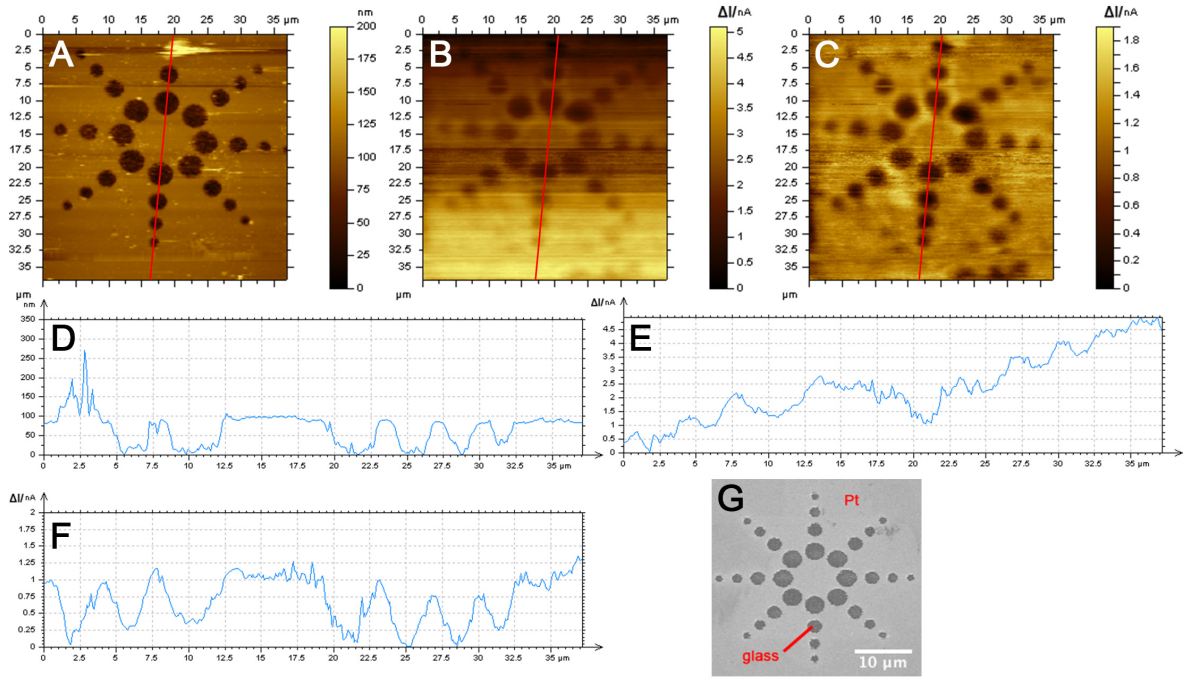

Fig. 53: AFM-SECM image of a model sample (milled structures in Pt-coated glass) recorded with an internal amplifier (gain: 10 nA/V) and a side-mill fabricated Si_xN_y-coated AFM-SECM probe; scan speed: 0.3 line/s; re-shaped AFM tip height: 850 nm; electrode frame length: 0.7 µm; A) topography recorded in contact mode; B) SECM image recorded in feedback mode; C) SECM image after horizontal line correction for drift compensation; D-F) extracted profiles of A-C); G) SEM image of the model sample; electrochemistry recorded in 10 mM $[Ru(NH_3)_6]Cl_3$ / 0.1 M KCl; E_{tip}= -500 mV vs. QAg/AgCl.

Distinct electrochemical surface properties are clearly observable in the raw image (Fig. 53B) without the 50 Hz interference signal. Only, a correction of the linear current drift was performed as data processing (Fig. 53B,E). The observed current drift is probably attributed to the long time stability of the AFM-SECM probe and is not associated to the amplifier, as such a drift is sometimes also observable at long time measurements using an external potentiostat (Fig. 54).

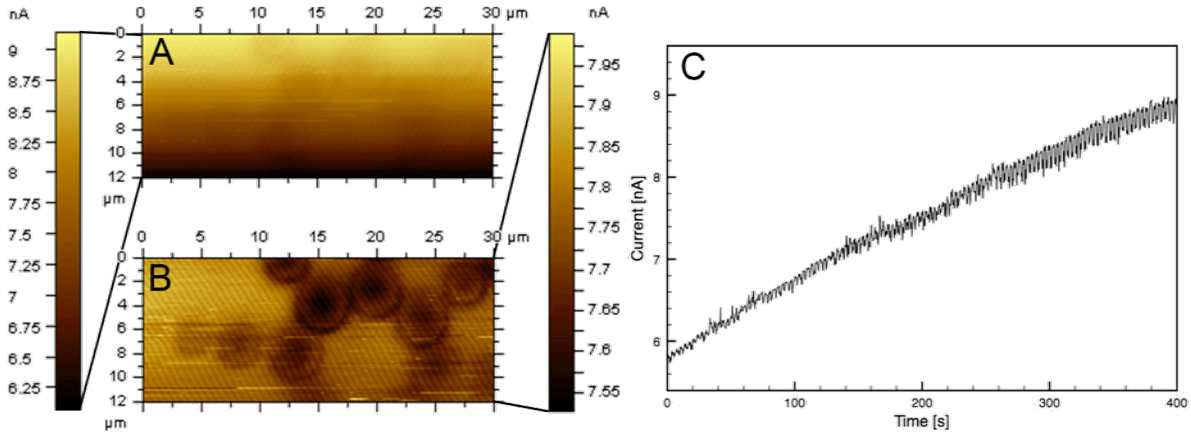

Fig. 54: Electrochemical signal of a model sample (deposited Pt-structures on Si) recorded with an external potentiostat at a top-mill fabricated Parylene-C-coated AFM-SECM probe; scan speed: 0.3 line/s; re-shaped AFM tip height: 800 nm; electrode frame length: 1.6 µm; A) electrochemistry; B) electrochemistry after horizontal line correction for drift compensation (without FFT-filtering); C) i-t-curve recorded during AFM-SECM measurement; electrochemistry recorded in 10 mM $[Ru(NH_3)_6]Cl_3$ / 0.1 M KCl; E_{tip}= -500 mV vs. QAg/AgCl.

6.2.2. Sealing the electrical contact

For long time experiments, the stability of the insulation of the electrical contact at the AFM-SECM chip is a crucial point. Imperfections in the sealing of the wire-chip contact could lead to leakage currents obstructing the electrochemical signal of the AFM-SECM probe. The integrated current-voltage transducer is represented by a single operation amplifier circuit as shown in section 6.1. In the presence of a leakage current, and depending on the used operation amplifier circuit, a signal with a relatively large offset may be observed. In addition, the detection bandwidth of the circuit may not be sufficient leading to saturation of the signal output, and hence loss of any electrochemical information. Drifts in the measured current due to imperfections of the insulating or changes of the electroactive area may be compensated using a drift correction as long as the overall current is not exceeding the amplifier bandwidth. Nonetheless, quantitative interpretation of the electrochemical data requires a long-lasting insulation of the wire contact in order to avoid any leakage. The insulation layer for the wire-chip connection consists of several thin layers of an UV-curable encapsulant and a finishing layer of insulation varnish (details see section 10.4.3).

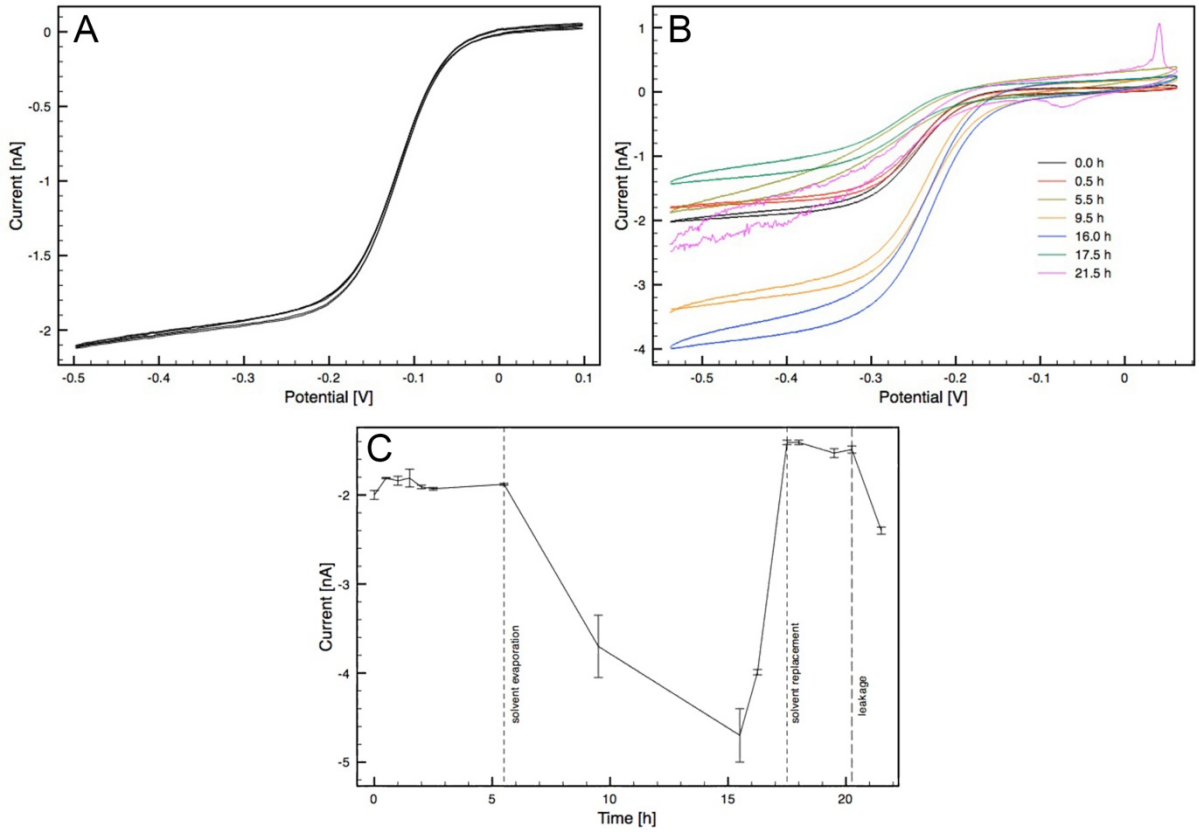

Fig. 55: A) Cyclic voltammogram of a Si_xN_y-coated AFM-SECM probe; B) CVs acquired over several hours with the probe constantly immersed in the electrolyte solution (internal data acquisition); C) steady state currents of the AFM-SECM probe during immersion (n=5); electrochemistry recorded in 10 mM $[Ru(NH_3)_6]Cl_3$ / 0.1 M KCl vs. A) sat. Ag/AgCl; B+C) QAg/AgCl; ν = 100 mV/s; electrode frame length: 0.8 µm.

In Fig. 55B,C the long-term stability of a Si_xN_y-coated AFM-SECM probe is shown. The probe was connected with conductive silver epoxy, and the contact insulated with several thin layers of an UV-curable encapsulant and a finishing layer of insulation varnish. The insulation of the wire contact remains intact for approximately 20 h during immersion in aqueous solution of 10 mM $[Ru(NH_3)_6]Cl_3$ / 0.1 M KCl. Fig. 55C shows the corresponding chronological diagram of the measured steady state currents. The steady state current remained relatively constant for the first 5.5h of immersion. After 5.5h an increase of the steady state current is visible due to the solvent evaporation at room temperature. After 17.5h the solution was exchanged with electrolyte solution containing the original redox mediator concentration. After exchange, the originally observed steady state current value of 1-2 nA was retained. The tip current remained relatively constant for another 4h until a breakdown of the insulation layer was observed, indicated by the appearance of the silver peak at

approximately ± 100 mV vs. QAg/AgCl originating from the exposure of the silver-epoxy contact. Summarizing, the insulation of the contact using UV-curable encapsulant with an additional insulation varnish layer is sufficient for most long-time experiments, as a constant steady state behavior in neutral solution can be maintained for at least 5h.

The insulation quality was also tested under acidic or alkaline conditions. According to the specification of the UV-curable encapsulant, it was assumed that extreme pH conditions result in an insulation layer dissolution/breakdown within a few minutes.

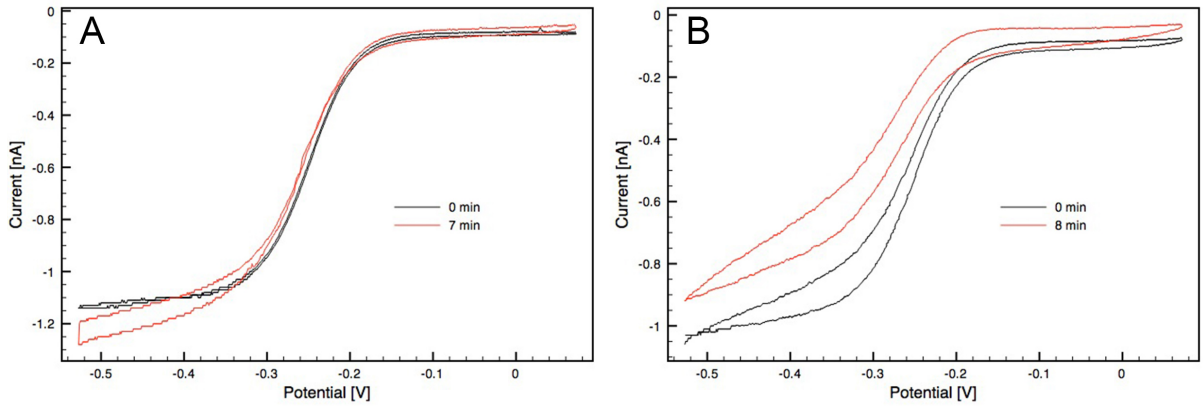

Fig. 56: Cyclic voltammograms recorded at a Si_xN_y-coated AFM-SECM probe immersed in redox mediator at A) pH = 1; B) pH = 8.5; CVs were recorded in 10 mM $[Ru(NH_3)_6]Cl_3$ / 0.1 M KCl vs. A) sat. Ag/AgCl; B) QAg/AgCl; ν = 100 mV/s; electrode frame length: 0.9 µm.

As shown in Fig. 56, the insulation layers are withstanding acidic conditions as low as pH = 1. Redox mediator solutions of pH ≥ 10 result in an insulation layer breakdown already after several minutes (CV data not shown). Therefore, it can be assumed that acidic conditions are less harmful to the insulation layers. Accordingly, the experimental pH range is limited from medium acidic up to neutral / slightly alkaline conditions.

6.2.3. Pit formation on passivated iron samples

In the following, AFM-SECM investigations with the dedicated AFM-SECM nosecone focus on real-world problems such as the observation of pit formation on passive iron samples.

Iron based materials / alloys play a dominant role in industrial manufacturing. Passivation of such iron-based materials is required, forming a barrier for ionic migration and protecting the metal from its environment. Despite the passivation, localized passivation layer breakdown known as pitting corrosion is often observed in the presence of anionic species such as chloride [216,217]. In the event of pit corrosion most of the metal surface remains passivated; only active sites of pit corrosion show high rates of reaction resulting in the propagation of the corrosion pits into the material, ultimately causing failure of metallic structural components [216]. Initially, pitting corrosion starts with the formation of holes or cavities in the micrometer region, and then propagates throughout the material. Microscopic methods employed for the investigation of corrosion pits have been reported in literature, but commonly these investigations are conducted after the formation of randomly occurring pitting corrosion [151,218,219]. In contrast, SECM is highly attractive for pit corrosion experiments, as the corrosion process can be deliberately initiated by generating a corrosive medium in a confined sample volume at a chosen position. For example, chloride precursors dissolved in the electrolyte solution can be reduced at the SECM probe in close proximity to the sample surface locally generating such a corrosive species [117,118], inducing the formation of a single pit. SECM allows also the imaging of such structures [118,220,221]. Although pit corrosion can be locally initiated by SECM, the UME dimensions limit the achievable spot size. Additionally, the imaging mechanism of SECM depends on the electrochemical reactions at the SECM probe in close proximity to the surface and is therefore related to the concentration of electrochemical active species (mediator and corrosion products) at the previously formed pit. The topography change and simultaneous occurring generation of electrochemical active corrosion products makes a deconvolution of topographical and electrochemical information challenging as both parameters are continuously changing during pit formation. With the integration of the SECM functionality into an AFM probe, this issue may be eliminated as the pit is now imaged by the AFM tip. In contrast to the previous

AFM-SECM experiments in this thesis, the AFM tip-integrated electrode was used to generate a reactive species in a confined electrolyte volume, promoting single pit formation on passivated iron samples. The formation of the corrosion pits can be directly monitored by the AFM tip of the combined probe without changing the electrolyte solution. In general, studying pit formation is challenging, as the formation of corrosion pits on homogeneous substrates is fast and the nucleation sites are randomly distributed. In addition, the pits have to be already nucleated in order to be observable. In the example shown here, pit corrosion was induced and promoted by a shift of pH-value instead of generating a critical chloride concentration. The iron sample was immersed into an aqueous solution of sodium chloride and sodium nitrite. Although chloride ions are already present in a fairly high concentration, the presence of nitrite ions leads to the formation of a protective oxide layer on the iron surface. The mechanism of corrosion inhibition of iron in the presence of nitrite ions is related to the oxidation of both, chemically adsorbed and diffusing iron(II) species, released by the corroding metal (Eq. 7) [222,223]. As a result, iron(III) is produced, forming poorly soluble ferric oxide, which precipitates on the iron surface thus preventing further corrosion.

$$2Fe^{2+} + 2\ OH^{-} + 2\ NO_2^{-} \rightarrow 2\ NO + Fe_2O_3 + H_2O$$

Eq. 7: Mechanism of the formation of a passivation layer on iron in the presence of nitrite ions.

As long as the concentration of nitrite is sufficiently high to prevent a passivation layer breakdown, no corrosion process is observed. When the AFM-SECM probe is biased at a sufficiently high potential (+0.9V vs. QAg/AgCl; see Fig. 57), nitrite is oxidized to nitrate leading to a local acidic environment (Eq. 8), which consumes nitrite and hence enables the aggressive attack of chloride.

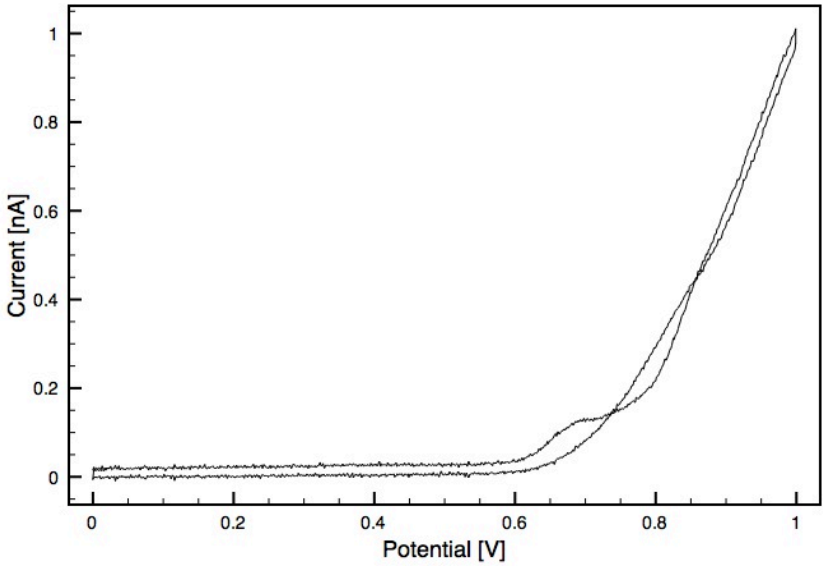

Fig. 57: Cyclic voltammogram for nitrite oxidation at a combined AFM-SECM probe recorded in 0.5 M NaCl / 0.1 M $NaNO_2$ vs. QAg/AgCl; electrode edge length of 1.07; ν = 100 mV/s; adapted from J. Izquierdo, A. Eifert, C. Kranz, R. M. Souto, In situ monitoring of pit nucleation and growth at an iron passive oxide layer by using combined atomic force and scanning electrochemical microscopy, ChemElectroChem, 2015, DOI: 10.1002/celc.201500100, Copyright 2015, with permission from Wiley-VCH Verlag GmbH & Co. KGaA, Weinheim [215].

$$NO_2^- + H_2O \rightarrow NO_3^- + 2H^+ + 2e^-$$

Eq. 8: Nitrite oxidation at +0.9V vs. QAg/AgCl to nitrate and protons [224].

The locally generated highly acidic corrosive medium leads - in combination with the chloride ions - to a reduced local concentration of the corrosion inhibitor and an induced localized pit formation due to a passivation layer breakdown and surface attack. Hence, the passivation layer breakdown is confined to the area around the integrated AFM-SECM probe, as the surrounding iron area is still protected by the presence of nitrite ions in solution as confirmed by the simulated concentration profiles at the AFM-SECM probe (Fig. 58).

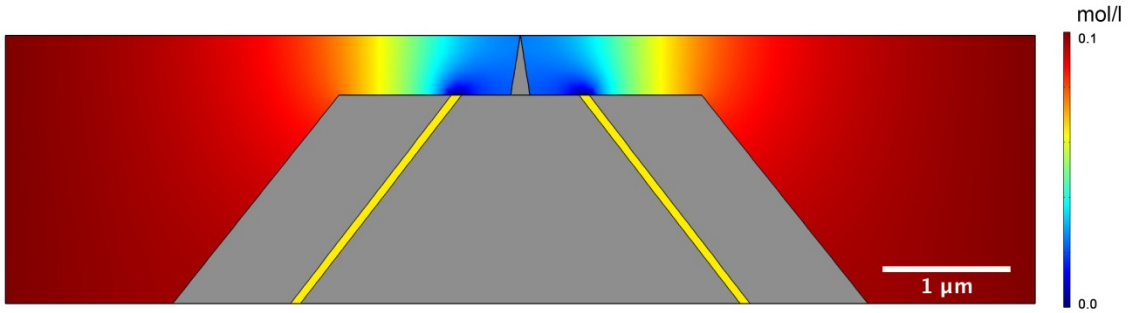

Fig. 58: Simulated concentration profile in nitrite solution at an AFM-tip integrated electrode; electrode edge length: 1.07 µm; tip height: 0.46 µm; reprinted from Electrochemistry Communications, 51, Javier Izquierdo, Alexander Eifert, Ricardo M. Souto, Christine Kranz, Simultaneous pit generation and visualization of pit topography using combined atomic force–scanning electrochemical microscopy, 15-18, Copyright 2015, with permission from Elsevier [213].

Due to the small electrode-sample distance, the volume for nitric acid generation is in the region of 10^{-6} nL, and therefore allows an enhanced lateral resolution for inducing pit generation.

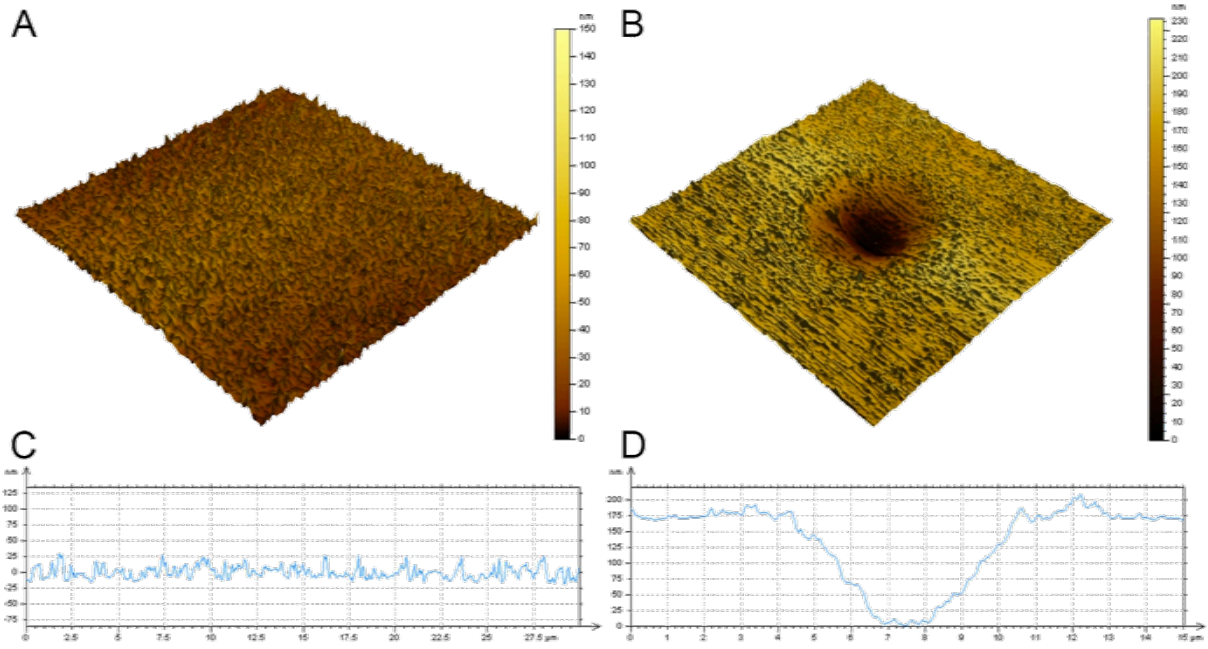

Fig. 59: 3D AFM topography of a polished iron surface recorded in contact mode with a combined AFM-SECM probe A) before and B) after induced pit formation; AFM images were recorded in 0.5 M NaCl / 0.1 M $NaNO_2$ with an AFM-SECM probe (electrode edge length: 1.07 µm and tip height: 0.46 µm); scan speed: 0.43 lines/s; pit formation was induced at +0.9V vs. QAg/AgCl, while scanning an area of 3x3 μm^2; scan speed: 4.45 µm/s; reprinted from Electrochemistry Communications, 51, Javier Izquierdo, Alexander Eifert, Ricardo M. Souto, Christine Kranz, Simultaneous pit generation and visualization of pit topography using combined atomic force–scanning electrochemical microscopy, 15-18, Copyright 2015, with permission from Elsevier [213].

Fig. 59 shows 3D-topographical images of a passivated iron surface in chloride/nitrite solution before (A) and after (B) the formation of a local induced corrosion pit. Fig. 59C and D show the cross sectional data before and after the pitting experiment. Scanning an area of 3x3 μm^2 generated a pit with a depth of approximately 180 nm, a width of 6-7 µm, a surface area of 28.5 μm^2, reflecting a volume of 1.8 μm^3. As shown in Fig. 59D, the diameter of the generated corrosion pit is larger than the scanned area plus the electrode dimension (approx. 4 µm), which can be explained with a broadened concentration profile of nitric acid as shown in Fig. 58. The pit dimension is in good agreement with the surface area covered by the confined volume of the acidic media formed between the combined AFM-SECM tip and the iron surface (Fig. 58). This covered area is approx. 6x6 µm² (3 µm scan size + 1 µm electrode frame length + 2 µm insulator material).

In order to observe the pit evolution after pit formation, a series of AFM images were acquired and the pit volume and depth were measured relative to the elapsed time period. The measurements show that the formed pits are repassivated within minutes, preventing further corrosion, as no further increase in depth and volume are observable. This is attributed to the refreshment of the nitrite concentration above the corrosion pit and the buildup of a passivation layer according to Eq. 7. Further investigation of the pit volume and depth also reveals the growth of the passivation layer, which can be observed in a decrease of depth and volume of the corrosion pit (Fig. 60).

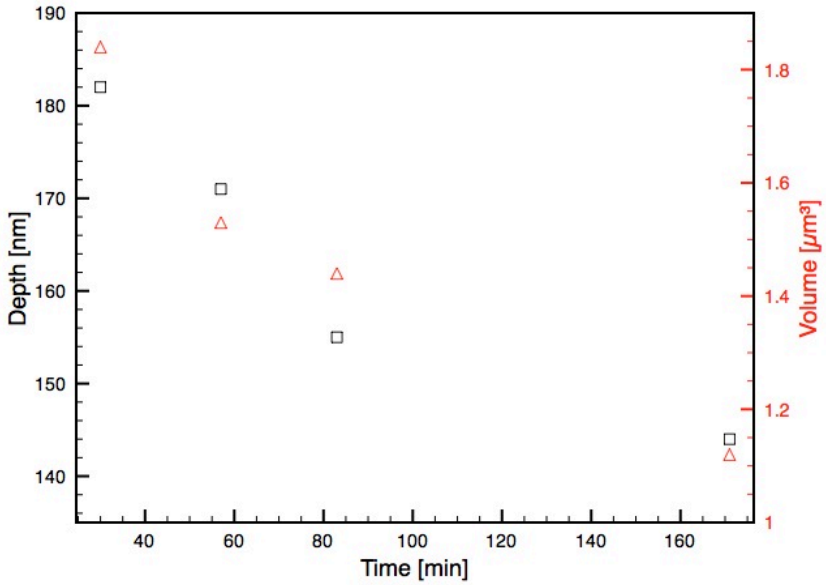

Fig. 60: Pit depth (□) and volume (Δ) evolution after induced pit formation; AFM images for data extraction were recorded in 0.5 M NaCl / 0.1 M $NaNO_2$ using an AFM probe with a tip height of 0.46 µm; scan speed: 0.34 lines/s; adapted from J. Izquierdo, A. Eifert, C. Kranz, R. M. Souto, In situ monitoring of pit nucleation and growth at an iron passive oxide layer by using combined atomic force and scanning electrochemical microscopy, ChemElectroChem, 2015, DOI: 10.1002/celc.201500100, Copyright 2015, with permission from Wiley-VCH Verlag GmbH & Co. KGaA, Weinheim [215].

A growth rate of 0.25 nm/min for the passivation layer is determined, corresponding to a volume decrease of 0.0046 μm^3/min.

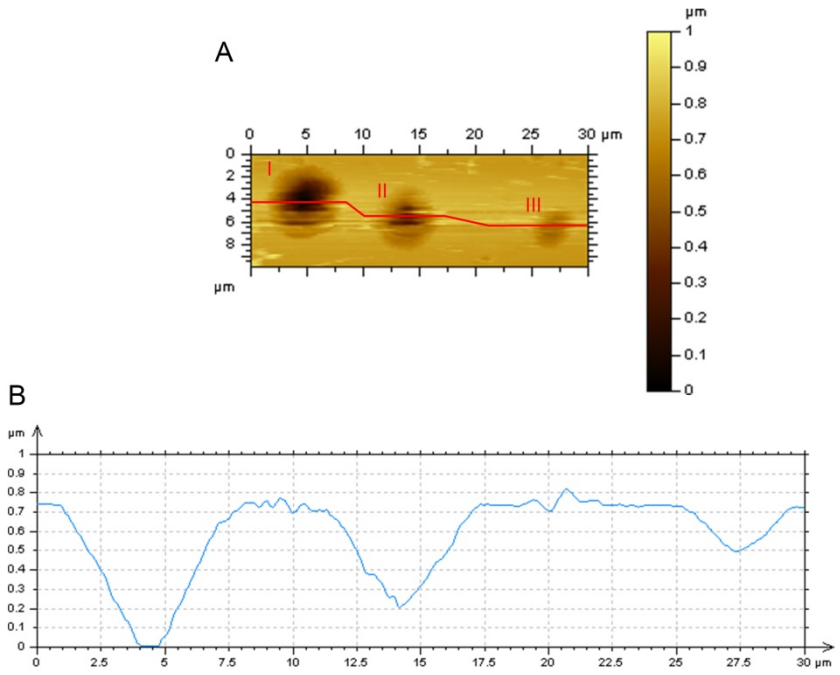

Fig. 61: A) AFM image and B) height profile of different corrosion pits induced by varying the scanned area; AFM images recorded in 0.5 M NaCl / 0.1 M $NaNO_2$; scan speed: 0.40 lines/s; pit formation at +0.9V vs. QAg/AgCl, while scanning an area of I) 0.75x0.75 μm^2; II) 0.5x0.5 μm^2; III) 0.25x0.25 μm^2; scan speed: 3.8 µm/s; electrode edge length: 1.07 µm; re-shaped tip height: 0.46 µm.

By varying the scan size while keeping the AFM-SECM probe biased at +0.9 V vs. QAg/AgCl, the nucleation size can be controlled. It is clearly visible from Fig. 61 that the longer the scan duration, and therefore the more aggressive the conditions, the deeper and the wider is the resulting pit. Starting with a pit depth of 0.7 µm at 0.75x0.75 μm^2, the depth decreases to 0.54 µm at 0.5x0.5 μm^2 to finally 0.24 µm at 0.25x0.25 μm^2. Also, the lateral dimension of the pit decreases from 7.18 µm (33.33 μm^2) to 5.69 µm (21.5 μm^2) and finally to 4.19 µm (7.03 μm^2), as the surface area during scanning is also decreasing. By plotting the pit volume versus the scan area, a linear correlation is observed (Fig. 62).

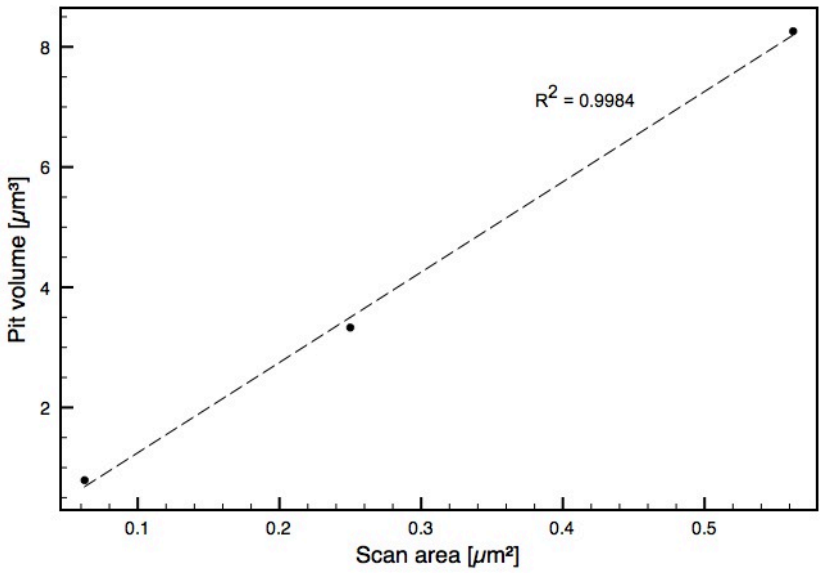

Fig. 62: Plot of pit volume vs. patterning area; scan speed: 1.9 µm/s; pit formation at +0.9V vs. QAg/AgCl in 0.5 M NaCl / 0.1 $NaNO_2$.

It is also observable that the pits displayed in Fig. 61 show a higher pit volume than the previously shown corrosion pits (Fig. 59), which have been produced by scanning an area of 3x3 µm^2. Therefore, it is assumed that not only the scan area is contributing to the pit size, but also the immersion time of the sample. Experiments with various immersion times and scan areas (Tab. 9) support this assumption.

Scan area [µm²]	Depth [nm]	Pit volume [µm³]	Immersion time [min]
3x3	180	1.80	50
3x3	613	7.90	103
1x1	254	1.21	117
0.75x0.75	700	8.26	180
0.50x0.50	540	3.33	184
0.25x0.25	240	0.79	186

Tab. 9: Pit depth and volume in correlation to scan area and immersion time.

With increasing immersion time both pit depth and volume are increasing. Whereas after an immersion time of 50 min, a corrosion pit of only 1.80 µm³ could be achieved using a 3x3 µm² scan with a biased AFM-SECM tip, approximately the same dimensions were achieved after an immersion time of 2h with a scan size of only 1x1 µm². Longer immersion times (3h) result in similar dimensions by further reducing the scan area. Similar results are obtained, if the data from a pit corrosion experiment after 100 min immersion, using a 3x3 µm² scan area, is compared to the corrosion pit

formed after 180 min immersion while a scan area of only 0.75x0.75 µm² is employed.

In the following, the AFM-SECM probe was positioned at a fixed location at the sample surface while biasing the AFM tip-integrated electrode. Hence, pit formation is now induced in a stationary polarization experiment with different durations. The pit volume / size should therefore be depending on the exposure time and should also lead to smaller pits compared to the scanning approach. As shown in Fig. 63, this static corrosion experiments indeed result in smaller dimensions of the corrosion pits, in terms of depth and volume, compared to a pit generation using the scanning approach (see Fig. 61; Tab. 9). The lateral dimensions decrease from 2.15 µm (3.78 μm^2) with the probe biased for 90s to 1.05 µm (1.18 μm^2) for 20s, the measured pit volume decreases from 0.244 μm^3 to 0.018 μm^3; and the depth decreases from 131 nm to 24 nm.

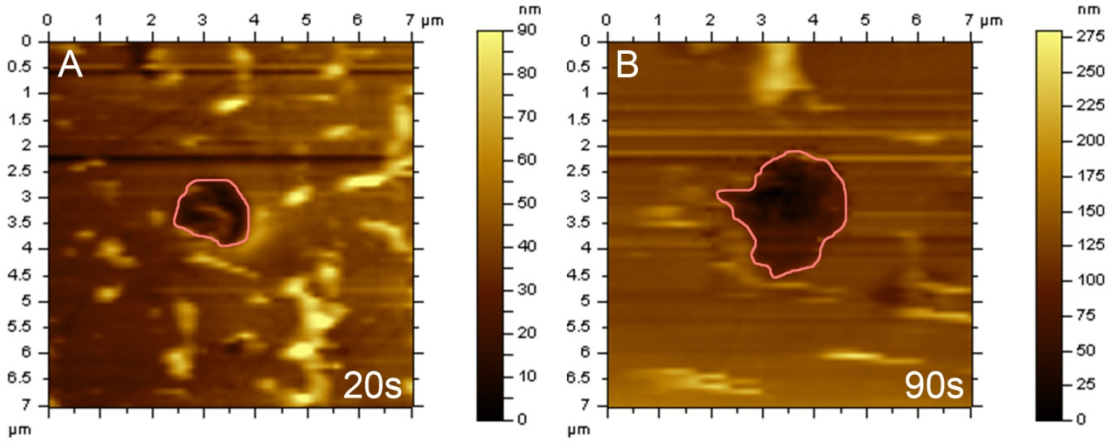

Fig. 63: AFM contact mode images of corrosion pits induced using a static mode with different exposure times; A) 20s; B) 90s; AFM images recorded in 0.5 M NaCl / 0.1 M $NaNO_2$; immersion time: 155 min; scan speed: 0.34 lines/s; pit formation at +0.9V vs. QAg/AgCl; reprinted from J. Izquierdo, A. Eifert, C. Kranz, R. M. Souto, In situ monitoring of pit nucleation and growth at an iron passive oxide layer by using combined atomic force and scanning electrochemical microscopy, ChemElectroChem, 2015, DOI: 10.1002/celc.201500100, Copyright 2015, with permission from Wiley-VCH Verlag GmbH & Co. KGaA, Weinheim [215].

In a next step, the AFM-SECM probe was biased at +0.5V vs. QAg/AgCl, after the pit formation experiment (at +0.9 V vs. QAg/AgCl). At this reduced potential iron (II) released at the active corrosion site is oxidized to iron (III), which forms ferric hydroxides that precipitates [225]. As a result of the reduced potential only the

oxidation of iron (II) to iron (III) is promoted without generating an acidic media caused by the oxidation of nitrite at a potential of +0.9V vs. QAg/AgCl (Fig. 57), which also would prevent the precipitation of ferric hydroxide. With a 3x3 µm² scan for pit formation, the precipitation is forming a circular shape, comparable to the corrosion pit, with a lateral dimension of 5.3 µm and a height of approximately 450-500 nm, resulting in a volume of 5.03 µm³ and a covered surface area of 16.8 µm² (Fig. 64). The size of the area covered with ferric hydroxide is also in good agreement with the surface area covered by the combined AFM-SECM probe during scanning.

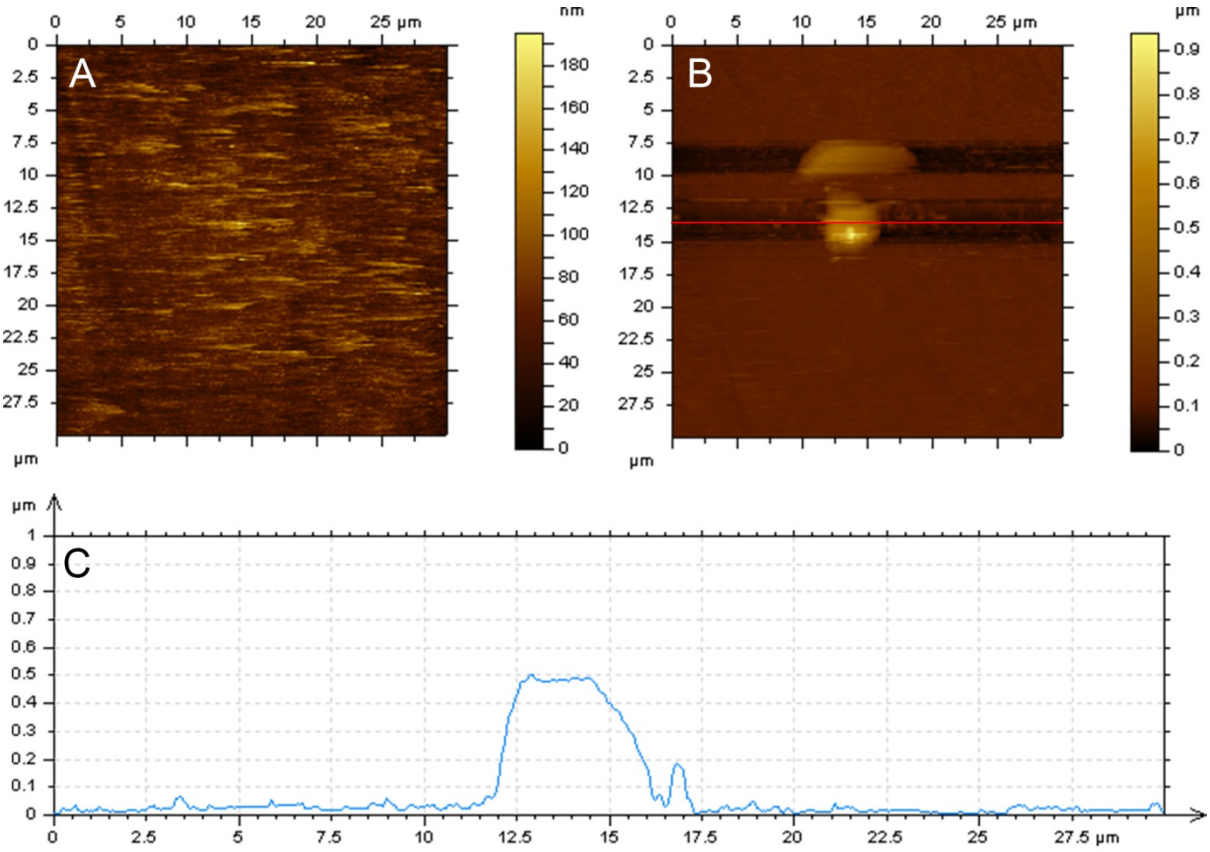

Fig. 64: AFM topography images and height profile of a polished iron surface recorded in contact mode with a combined AFM-SECM probe; A) before and B&C) after induced pit formation followed by a subsequent scan for iron (II) detection; AFM images were recorded in 0.5 M NaCl / 0.1 M $NaNO_2$ with an AFM-SECM probe with an electrode edge length of 1.07 µm and a tip height of 0.46 µm; scan speed: 0.43 lines/s; pit formation was induced at +0.9V vs. QAg/AgCl; iron (II) detection at + 0.5V vs. Q/Ag/AgCl, while scanning an area of 3x3 μm^2; scan speed: 3.8 µm/s; adapted from J. Izquierdo, A. Eifert, C. Kranz, R. M. Souto, In situ monitoring of pit nucleation and growth at an iron passive oxide layer by using combined atomic force and scanning electrochemical microscopy, ChemElectroChem, 2015, DOI: 10.1002/celc.201500100, Copyright 2015, with permission from Wiley-VCH Verlag GmbH & Co. KGaA, Weinheim [215].

6.3. Conclusion & Outlook

Integrating a transducer system based on an operation amplifier circuit directly into the holder (nosecone) of the AFM cantilever significantly reduces the background noise level and external parasitic couplings like the net hum. Therefore, FFT post-scan data processing can be omitted, resulting in improved electrochemical data and minimized imaging artifacts. However, the integrated operation amplifier circuit limits the detection bandwidth and sensitivity to a predefined value, as only one amplifier circuit is available. These limitations restrict adaptations if experimental parameters are changing and exceed the sensitivity or current bandwidth of the amplifier resulting in the loss of electrochemical information. Furthermore, it could be demonstrated that the insulation scheme for tip sealing using UV-curable encapsulant and insulator varnish is suitable for long time measurements up to 20h - if measurements are performed within a pH range of 4.0 - 8.0. In addition to model samples, the performance of the improved system has also been demonstrated with “real-world” investigations like the locally induced formation of single corrosion pits operating in a tip generation substrate collection mode. In comparison with single pit formation using microelectrodes in SECM, not only smaller pits could be generated, but also imaged and characterized by AFM without changing the probe or the pitting medium.

7. Investigation of biological samples

7.1. Introduction

Understanding fundamental biological reaction pathways represents the keystone for advances in medicine, biology and biotechnology. From the large field of biological relevant investigations accessible by combined SPM techniques, pore forming proteins embedded in supported lipid membranes will be investigated within this chapter along with the detection of the neurological important messenger molecule dopamine.

In order to study transport phenomena across cell membranes, frequently lipid membrane model systems are used [226]. Simplified experimental conditions allow studying fundamental processes of cell membrane transport. For example, such models are supported lipid membranes (SLM), which can either be lipid bilayers created via vesicle fusion on a hydrophilic smooth substrate like fused silica, borosilicate glass or SiO_2 [227], or a hybrid bilayer membrane consisting of self-assembled alkanethiols on an Au substrate and phospholipid vesicles. Plasmon resonance [228], electrochemistry [229] or quartz crystal microbalance [230] have been used as analytical techniques to investigate such model membranes. Within this thesis the pore forming protein of interest is the oligomerized C2IIa component of the clostridium botulinum C2 toxin, which presents its large peripheral (hydrophilic) domain only on the outside of the hybrid bilayer system [1,231,232]. The clostridium botulinum C2 toxin is a binary toxin, using a receptor-mediated endocytosis and a C2IIa-mediated translocation of its C2I enzymatic component into the cytosol of mammalian cells, causing an actin-cytoskeleton break-down via actin polymerization inhibition [233]. The pores generated by the C2IIa component represent voltage-dependent cation-selective ion permeable channels [231] with a pore diameter of 27 Å [1].

The detection of dopamine is second problem of interest described within this chapter. Dopamine is an important neurotransmitter within the mammalian brains, which is also involved in the regulation of hormone functions. Furthermore, some neural diseases are related to the loss of dopamine releasing neurons (Parkinson's disease) [234] or abnormal dopamine levels in the nervous system (schizophrenia) [235]. Therefore, the reliable and selective detection of dopamine is of significant

importance in biomedical research. Commonly dopamine is electrochemically detected using e.g., cyclic voltammetry. Although dopamine can be detected at glassy carbon, Pt or Au electrodes, the selective detection is still challenging, as usually ascorbic acid is present in biological samples. Ascorbic acid represents one of the interfering molecules when detecting dopamine in biological media, as the electrochemical generated dopamine-o-quinone is re-reduced by a redox-reaction with ascorbic acid [75], and the oxidation peak of ascorbic acid commonly overlays with the dopamine signal [15]. BDD electrodes are promising for the electrochemical dopamine detection: dopamine and ascorbic acid can be simultaneously detected, as the shift in potential is sufficient to obtain individual signals [15,31].

Within this chapter the formation of a supported hybrid bilayer on an Au substrate, the incorporation of C2IIa heptameres and the inhibition of mass transport through the C2IIa pores will be investigated with combined AFM-SECM. Also, the detection of dopamine in the presence of ascorbic acid at hydrogen-terminated combined BDD-AFM-SECM probes in physiologically relevant conditions will be demonstrated.

Parts of the experimental data of this chapter have been obtained in cooperation with Corinna Frey; Institute for Analytical and Bioanalytical Chemistry; University of Ulm. Corinna Frey contributed to this chapter the preparation of the supported lipid membranes, toxin incorporation, toxin inhibition as well as their electrochemical characterization (CV).

7.2. Results & Discussion

7.2.1. Investigation of supported lipid membranes with incorporated C2IIa heptameres

7.2.1.1. Supported lipid membrane formation

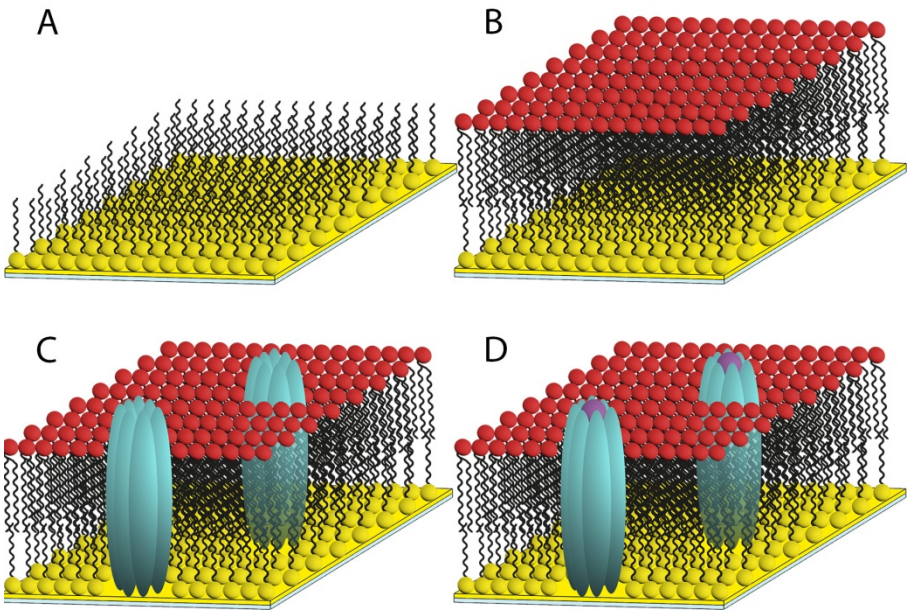

Fig. 65: Scheme of the hybrid lipid membrane formation, incorporation of the C2IIa heptameres and the mass transport inhibition of the heptameric pores using chloroquine; A) self-assembled ODT layer; B) hybrid lipid bilayer; C) hybrid lipid bilayer with incorporated pores; D) pore inhibition using chloroquine.

Bulk electrochemical experiments (CV) have been used to characterize the individual steps of the bilayer formation, the pore incorporation (C2IIa) and the inhibition (chloroquine). In addition, these steps have been investigated with a microscopic approach (recording AFM-SECM approach curves).

The first modification step is the formation of a self-assembled 1-octadecanthiol (ODT) layer on the Au substrate (Fig. 65A). By comparing the peak current of $[Ru(NH_3)_6]Cl_3$ reduction at a bare Au surface and the ODT-coated surface the coverage can be calculated.

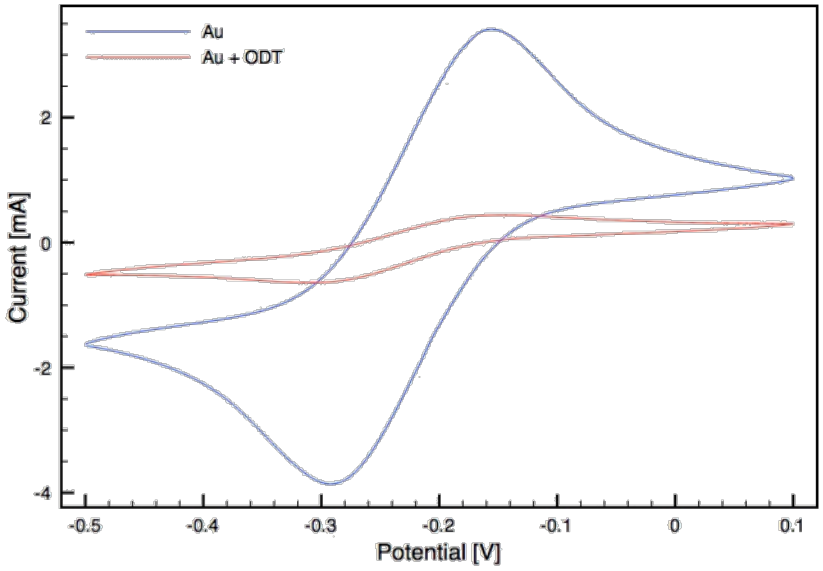

Fig. 66: Exemplary CVs recorded at a bare Au substrate (blue) and an ODT-coated Au substrate (red); CVs recorded in aqueous solution containing 10 mM $[Ru(NH_3)_6]Cl_3$ and 0.1 M KCl, adjusted to pH=6; ν = 100 mV/s.

To calculate the coverage, it is assumed that the recorded current for $[Ru(NH_3)_6]Cl_3$ reduction at the bare Au electrode represents a coverage of 0% and a current of 0 nA represents a coverage of 100%. Hence, the actual coverage is represented by Eq. 9, assuming a homogeneously formed layer.

$$\theta = 100 - \left(\frac{I_{coated}}{I_{Au}} * 100 \right)$$

Eq. 9: Percentage of coverage of the sample surface.

In the following, the coverage is also calculated according to Eq. 9 for all further modification steps to evaluate the impact of the pore-forming proteins on the "permeability" of the supported lipid membrane.

As shown in Fig. 66, the peak current of the $[Ru(NH_3)_6]Cl_3$ reduction drops from -4.05 mA to -0.64 mA resulting in a surface coverage of 84.1%, after immersion of the Au substrate for approximately 24h in an ODT solution. The obtained reduced coverage of less than 100% may be explained as follows. First, the ODT layer is not forming a homogeneously closed monolayer on the macroscopic Au substrate after 24h of immersion. The resulting pinholes result in a measurable current due to the conversion of the redox mediator. Second, the $[Ru(NH_3)_6]Cl_3$ may still be reduced

depending on the orientation of the ODT layer, if the ODT molecules are not perpendicular oriented to the substrate surface [236], as $[Ru(NH_3)_6]Cl_3$ is known to be an outer sphere redox mediator [179]. These collapsed sites can be caused for example by structural defects on the Au surface.

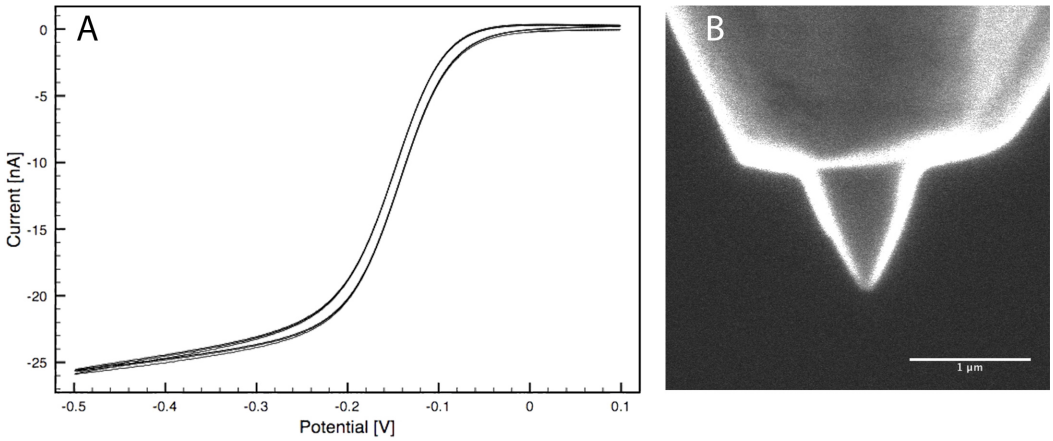

Fig. 67: A) Exemplary CV; B) SEM image of a PtC-composite AFM-SECM probe; CV recorded in 10 mM $[Ru(NH_3)_6]Cl_3$ with 0.1 M KCl as supporting electrolyte vs. Ag/AgCl; ν = 100 mV/s.

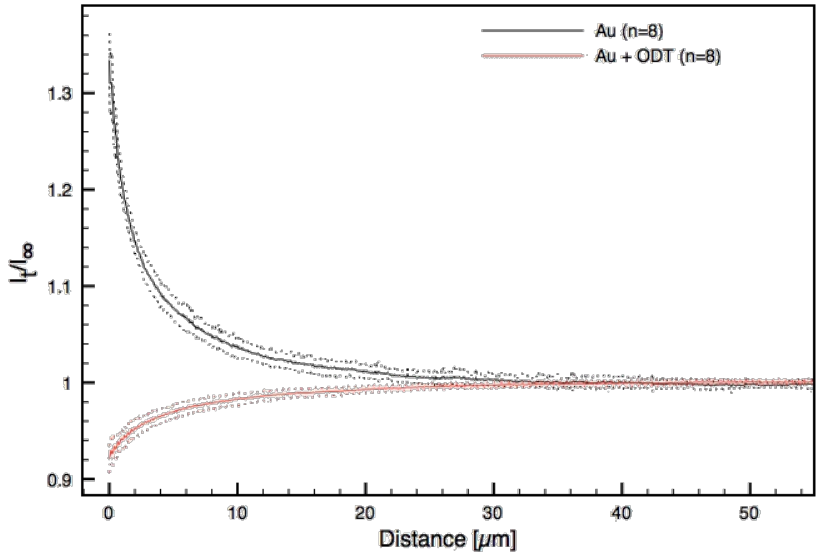

Fig. 68: Approach curves towards an Au-coated substrate (black) and towards a self-assembled ODT layer (red); approach curves recorded in aqueous solution containing 10 mM $[Ru(NH_3)_6]Cl_3$ and 0.1 M KCl, adjusted to pH=6; E_{tip}: -500 mV vs. QAg/AgCl; A_{el} = 1.94 µm^2.

The formation of the ODT layer on the Au coated substrate (Fig. 65A) can be also observed by recording approach curves using AFM-SECM probes with a deposited PtC-composite electrode (Fig. 67) [132]. The positive feedback of the conductive substrate changes, as expected to a negative feedback due to blocking of the

regeneration cycle of the redox mediator. Although a surface coverage of 100% was not achieved during the 24h of immersion, it can be demonstrated that the ODT-layer formation can be successfully observed using AFM-SECM by a drop of 41±3% of the normalized current (Fig. 68). It should be noted that CV data provide an average value over the complete sample surface, whereas approach curves are localized measurements at individual spots. If the supported layer is not formed homogeneously or is partially damaged at the investigated spot of the AFM-SECM experiments, a comparison of the data is difficult. This difference in the investigation technique may lead to quite different results if a homogeneous surface coverage is not ensured.

The next step in forming a supported lipid membrane involves the small unilamellar vesicle fusion for the formation of the hybrid bilayer (Fig. 65B) on top of the ODT layer, acting as anchor groups for the lipid (Fig. 69) [229].

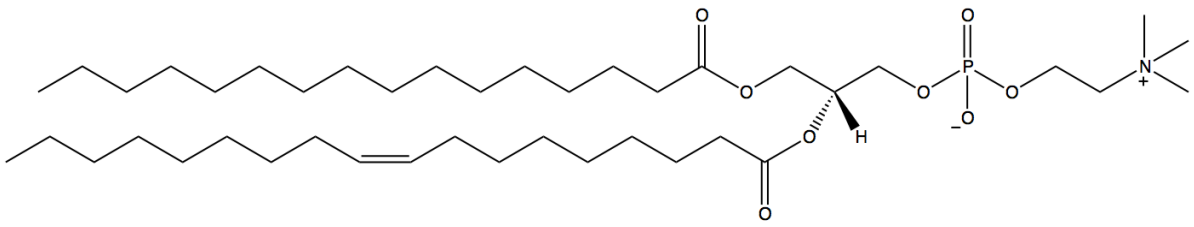

Fig. 69: Chemical structure of 1-hexadecanoly-2-(9Z-octadecanoyl)-sn-glycero-3-phosphocholine (1-palmitoyl-2-oleoyl-sn-glycero-3-phosphocholine / POPC).

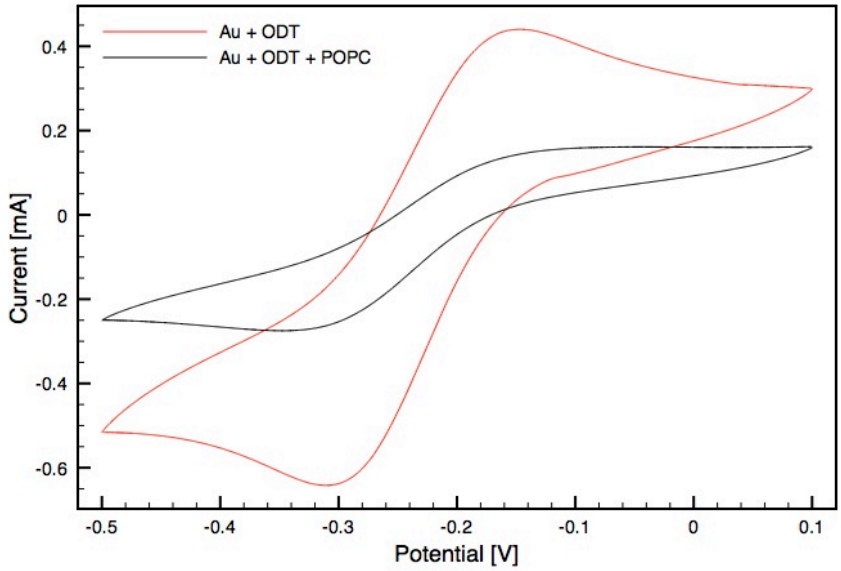

Fig. 70: Exemplary CVs recorded at an ODT-coated substrate (red) and at a hybrid bilayer-coated substrate (black); CVs recorded in aqueous solution containing 10 mM $[Ru(NH_3)_6]Cl_3$ and 0.1 M KCl, adjusted to pH=6 vs. QAg/AgCl; ν = 100 mV/s.

The cathodic peak current of the CV is dropping again after immersion in POPC solution from -0.64 mA to -0.23 mA, as exemplary shown in Fig. 70. The lipid layer is considered to be also impenetrable for the redox species if oriented perpendicular to the sample surface. Calculation of the surface coverage (Eq. 9) results in an increase of the calculated coverage value from 84.1% to 94.3% (Tab. 10).

Sample	Peak Current [mA]	Coverage [%]
Au	-4.05	0.0
Au + ODT	-0.64	84.1
Au + ODT + POPC	-0.23	94.3

Tab. 10: Surface coverage values at different steps of the hybrid lipid bilayer formation; coverage calculated using Eq. 9.

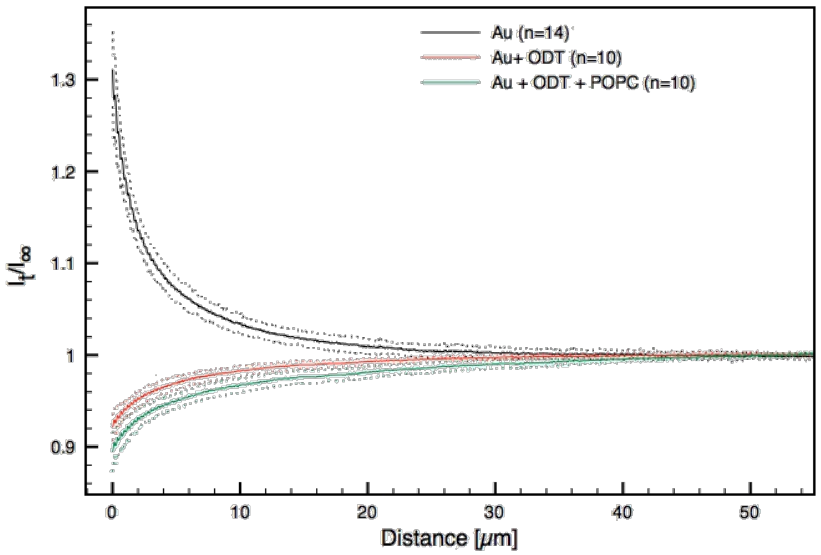

Fig. 71: Exemplary approach curves towards an Au-coated substrate (black), towards a self-assembled ODT layer (red) and towards the hybrid lipid bilayer (green); approach curves recorded in aqueous solution containing 10 mM $[Ru(NH_3)_6]Cl_3$ and 0.1 M KCl, adjusted to pH=6; E_{tip}: -500 mV vs. QAg/AgCl; A_{el} = 1.46 µm^2.

This increase in surface coverage is also observed with AFM-SECM approach curves (Fig. 71) by a further decrease of 2.7±1.3% of the normalized current. Due to the increase of surface coverage and the increase of the negative feedback, it can be assumed that the immersion in POPC solution covers partially the remaining redox-active spots of the ODT layer. It also indicates the presence of the POPC layer. If a perfect ODT layer is assumed, the deposition of an additional POPC layer should not alter the negative feedback current. What might be observable is a change in the capacitive current of the CV, as the POPC deposition should change the capacity of the system.

7.2.1.2. C2IIa toxin incorporation

The incorporation of the activated, trypsin-cleaved, C2IIa pore forming protein (Fig. 65C) was investigated using CV and AFM-SECM approach curves. After the addition of a C2IIa solution, by partially exchanging the $[Ru(NH_3)_6]Cl_3$/KCl solution, covering the supported hybrid lipid bilayer, an increase in the peak current of the CVs can be observed as exemplary shown in Fig. 72.

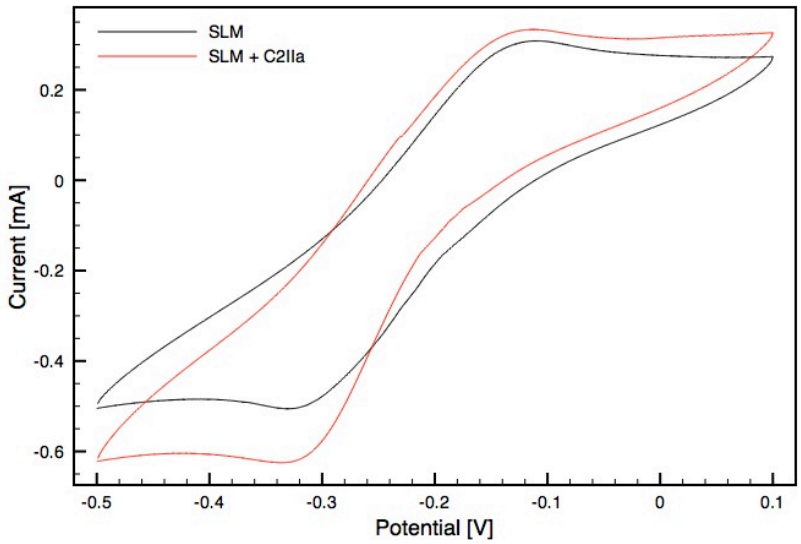

Fig. 72: Exemplary CVs of a SLM (black) and a C2IIa embedded SLM (red); CVs recorded in aqueous solution containing 10 mM $[Ru(NH_3)_6]Cl_3$ and 0.1 M KCl, adjusted to pH=6 vs. QAg/AgCl; ν = 100 mV/s.

Adding the C2IIa results in an increase of the peak current from -0.23 mA to -0.4 mA reflecting a reduction of the calculated surface coverage from 95.5% to 92.0%. If the surface coverage of the lipid membrane is assumed to remain stable after C2IIa addition, the reduction in the calculated surface coverage should be related to pore incorporation, opening channels for a redox mediator transport through the supported lipid membrane. This behavior can also be observed by approach curves (Fig. 73).

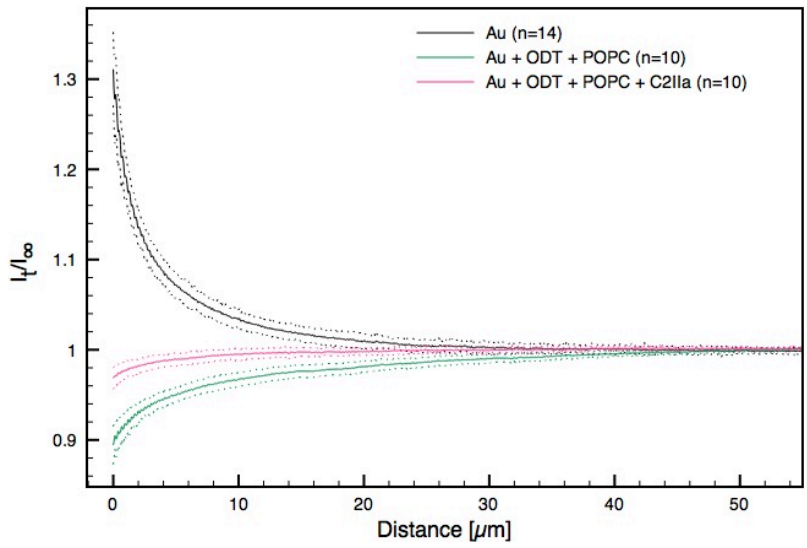

Fig. 73: Exemplary approach curves towards an Au-coated substrate (black), towards a hybrid lipid bilayer (green) and towards the C2IIa embedded hybrid lipid bilayer (magenta); approach curves recorded in aqueous solution containing 10 mM $[Ru(NH_3)_6]Cl_3$, 0.1 M KCl and 3.48 µg/ml C2IIa, adjusted to pH=6 E_{tip}: -500 mV vs. QAg/AgCl; A_{el} = 1.46 µm^2.

The heptameric pores allow now the redox mediator transport through the lipid bilayer, which is observable by an increase of the normalized current by 7.3 ± 2%. As the majority of the surface is still blocked by the (insulating) supported lipid membrane, no positive feedback is expected, but a reduction of the negative feedback effect is observed instead. To further investigate the incorporation of the pores into the supported lipid membrane, a concentration series using standard addition method was performed ranging from 1.74 µg/ml to 27.84 µg/ml of C2IIa in the supernatant liquid phase above the SLM.

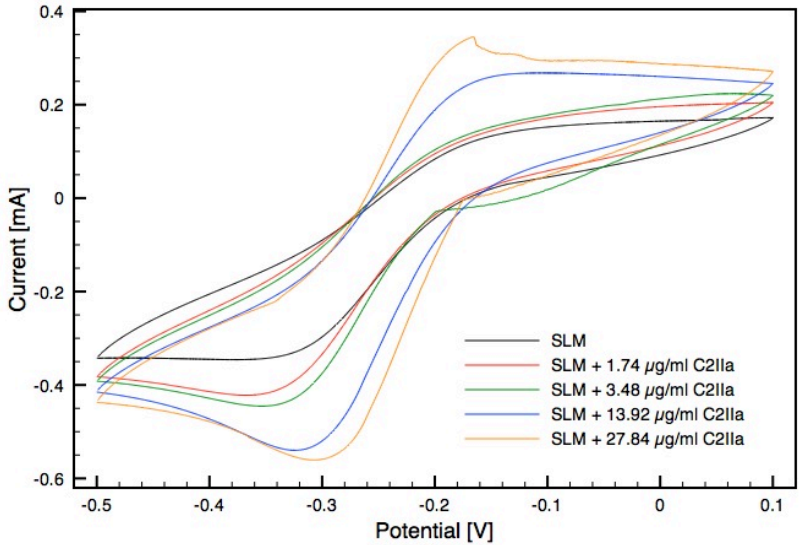

Fig. 74: CVs of different C2IIa concentrations in the supernatant liquid phase of the SLM; CVs recorded in aqueous solution containing 10 mM $[Ru(NH_3)_6]Cl_3$, 0.1 M KCl and 1.74-27.84 µg/ml C2IIa, adjusted to pH=6 vs. QAg/AgCl; ν = 100 mV/s.

Concentration of C2IIa [µg/ml]	Peak current [mA]	Surface coverage [%]
0	-0.29	91.9
1.74	-0.33	90.9
3.48	-0.38	89.5
13.92	-0.49	86.5
27.84	-0.51	85.8

Tab. 11: Peak current determined for the reduction of $[Ru(NH_3)_6]Cl_3$ and relative surface coverage after C2IIa addition; CVs see Fig. 74.

Fig. 74 and Tab. 11 show the peak current for the electrochemical conversion of the redox mediator. The recorded current increases with increasing C2IIa concentration, correlating to a relative surface coverage value (Eq. 9). These results support the hypothesis of a redox mediator mass transport across the supported lipid membrane through the heptameric pores, distributed across the surface (Fig. 65C). Calculations for pore incorporation, according to the obtained peak currents (Fig. 74 and Tab. 11) using Eq. 1, reveal a non-linear increase of the pore density towards an upper saturation limit.

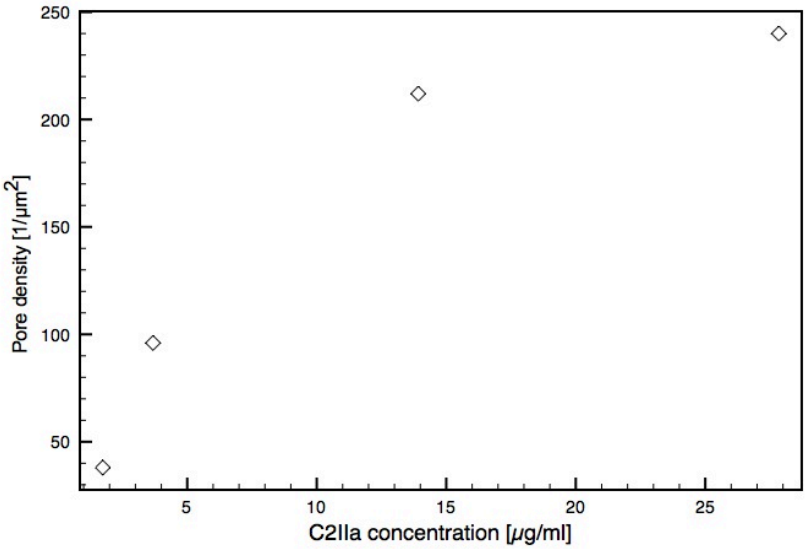

Fig. 75: Calculated pore density according to data from Fig. 74 using Eq. 1; n = 1; D = 7.5e-6 [cm^2/s]; r = 1.35 nm [1].

In addition, AFM-SECM approach curves (Fig. 76) were recorded. Again a subsequent reduction of the negative feedback signal was observed with raising C2IIa concentration. The recorded AFM-SECM approach curves are also in excellent agreement with the calculated pore densities (Fig. 75).

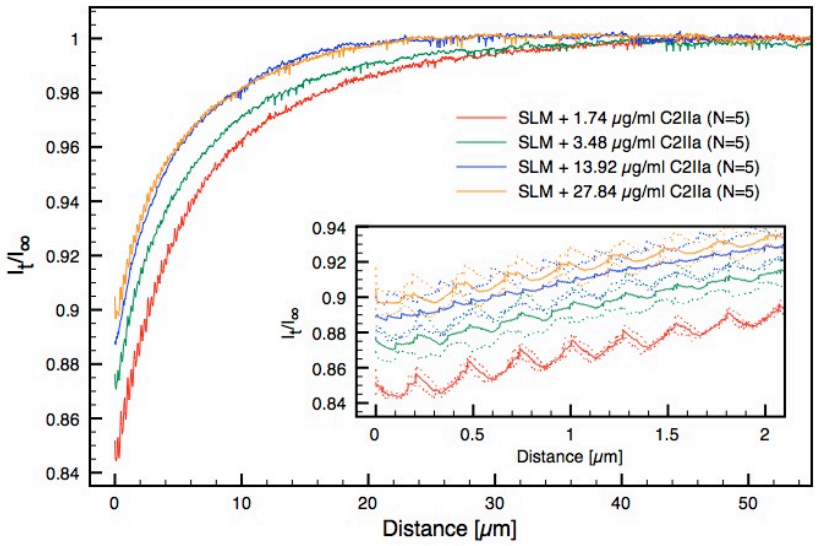

Fig. 76: Approach curves towards a SLM with different concentrations of the activated C2IIa in the supernatant solution. Approach curves recorded in aqueous solution containing 10 mM $[Ru(NH_3)_6]Cl_3$, 0.1 M KCl and 1.74-27.84 µg/ml C2IIa, adjusted to pH=6; E_{tip}: -400 mV vs. QAg/AgCl; A_{el} = 0.65 µm^2; inset: zoomed view showing the standard deviation of the recorded approach curves (N = 5).

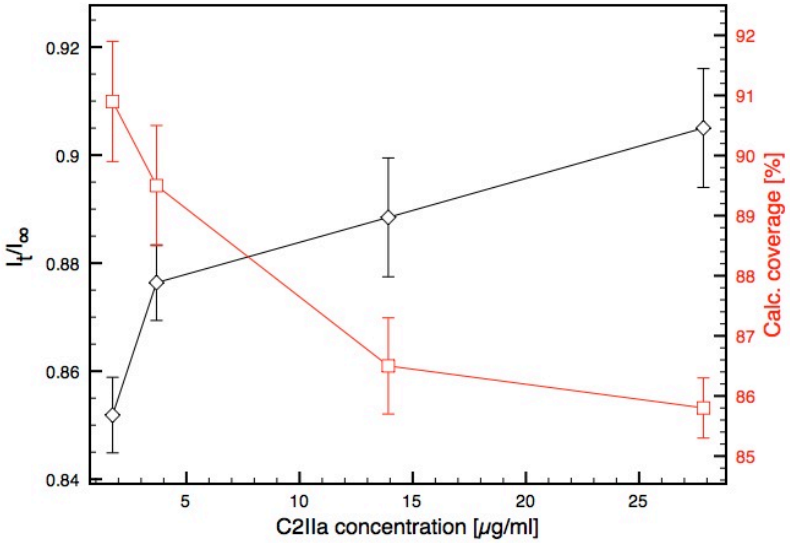

Fig. 77: Comparison of the calculated surface coverage (N = 10) and AFM-SECM data (N = 5) correlated to the C2IIa concentration of an alkanethiol supported lipid membrane; I_t/I_∞ values are obtained at surface contact.

This mass transport phenomenon can be observed independently whether the counter and working electrode are configured to operate on the same side (AFM-SECM; cis-configuration) or on different sides (CV; trans-configuration) of the supported lipid bilayer, as shown in Fig. 77. Hence, it is proven that the applied electrode potential doesn't influence the redox-mediator transport through the pore,

though it is known that the mass transport through the heptameric pores of C2IIa are voltage-dependent as shown for potassium ions in KCl solution by Schmid et al. [231]. In order to prove that the changes in the electrochemical feedback signal of the measurements are not derived from any alterations caused by the solution exchange (PBS/C2IIa), instead of C2IIa incorporation, PBS was added to the $[Ru(NH_3)_6]Cl_3$ solution. The supernatant solution has been partially replaced by this $[Ru(NH_3)_6]Cl_3$/PBS (pH = 6) solution. This exchanged solution was treated similar to the C2IIa toxin solution (C2IIa/$[Ru(NH_3)_6]Cl_3$/PBS) in order to maintain constant and comparable conditions (temperature, pH) to the previously performed experiments of pore embedment.

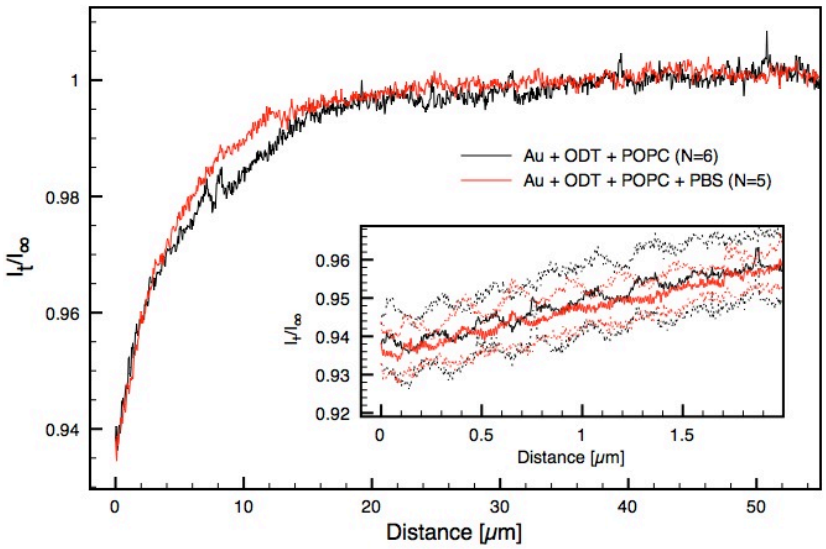

Fig. 78: Exemplary approach curves towards a hybrid lipid bilayer before (black) and after (red) $[Ru(NH_3)_6]Cl_3$/PBS solution exchange. Approach curves recorded in aqueous solution containing 10 mM $[Ru(NH_3)_6]Cl_3$ and 0.1 M KCl; E_{tip}: -350 mV vs. QAg/AgCl; A_{el} = 0.33 µm^2; inset: zoomed view showing the standard deviation of the recorded approach curves (N = 6 (hybrid lipid bilayer); N = 5 (after solution exchange)).

For the approach curves recorded after the partial solution exchange, as shown in Fig. 78, no significant change of the I_t/I_∞ value and hence of the supported lipid membrane is observed. This finding is also supported by the overall shape of the approach curves, which shows no significant changes, or only minor changes that are well within standard deviation of all acquired approach curves.

7.2.1.3. Redox-mediator transport inhibition with chloroquine (CQ)

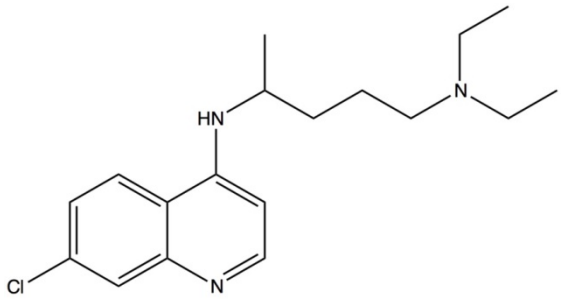

Fig. 79: Chemical structure of chloroquine.

In addition, inhibition experiments were also performed to disable the membrane transport by blocking the transmembrane pores. Previous studies have shown that chloroquine and 4-aminoquinolones may act as inhibitor molecules and block the transmembrane transport through C2IIa heptameric pores [231,237]. Bachmeyer et al. showed in their experiments that the positively charged chloroquine probably forms ionic bonds to the negatively charged environment inside the pore channel (Fig. 65D) and therefore blocks the transmembrane transport.

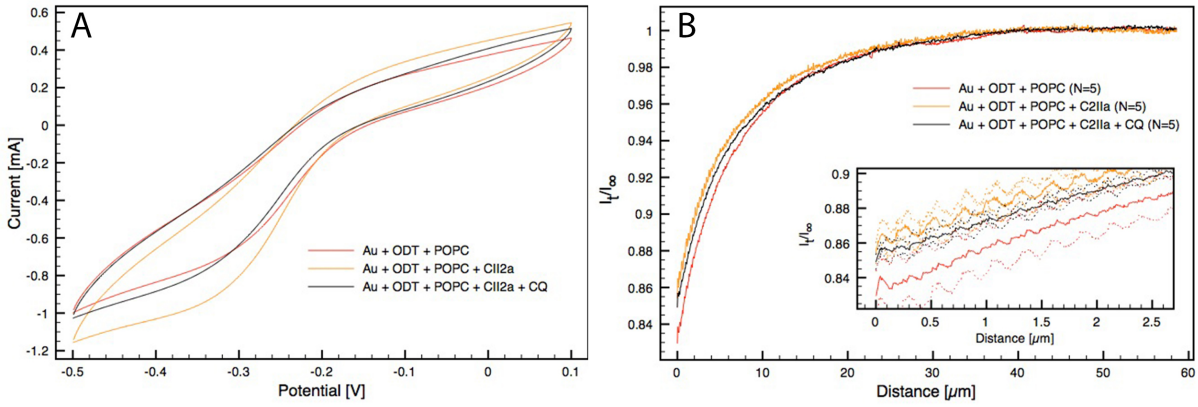

Fig. 80: Exemplary electrochemical (A) and approach curve (B) measurements of hybrid lipid bilayers (red); with C2IIa incorporation (orange) and CQ addition (black); CVs and approach curves recorded in aqueous solution containing 10 mM $[Ru(NH_3)_6]Cl_3$ and 0.1 M KCl, adjusted to pH=6; ν = 100 mV/s; E_{tip}: -400 mV vs. QAg/AgCl; A_{el} = 0.96 μm^2; inset: zoomed view showing the standard deviation of the recorded approach curves (N = 5).

Coating	Surface coverage [%]
Au + ODT +POPC	89.70
Au + ODT + POPC + C2IIa	86.61
Au + ODT + POPC + C2IIa + CQ	89.57

Tab. 12: Exemplary change in relative surface coverage after C2IIa addition and CQ inhibition according to Fig. 80A.

The obtained data, as shown in Fig. 80 and Tab. 12 are based on CV and AFM-SECM measurements, respectively. Corresponding to the CV data, the C2IIa incorporation and inhibition is indicated by an increase (pore incorporation) and following decrease (blocking of pores) of the cathodic peak current to almost its original value reflecting the SLM (Tab. 12). The data acquired with AFM-SECM on supported hybrid lipid membranes also show promising results for the incorporation of C2IIa, however no significant changes were observed concerning transport inhibition. As mentioned, the approach curves shown in Fig. 80B indicate the C2IIa incorporation due to a reduced negative feedback signal, but show only minor changes after the addition of CQ to the solution. Hence, blocking of the pores in the microscopic domain could not be demonstrated at this point as the deviation of the approach curves are within standard deviations. To investigate possible influences of chloroquine addition to the solution, also control experiments were performed, where the supernatant solution was spiked with a similar concentration of the inhibition solution as in the blocking experiment but prior to the spiking, no pores were incorporated. This experiment is comparable to the experiments of PBS solution exchange, as shown in section 7.2.1.2.

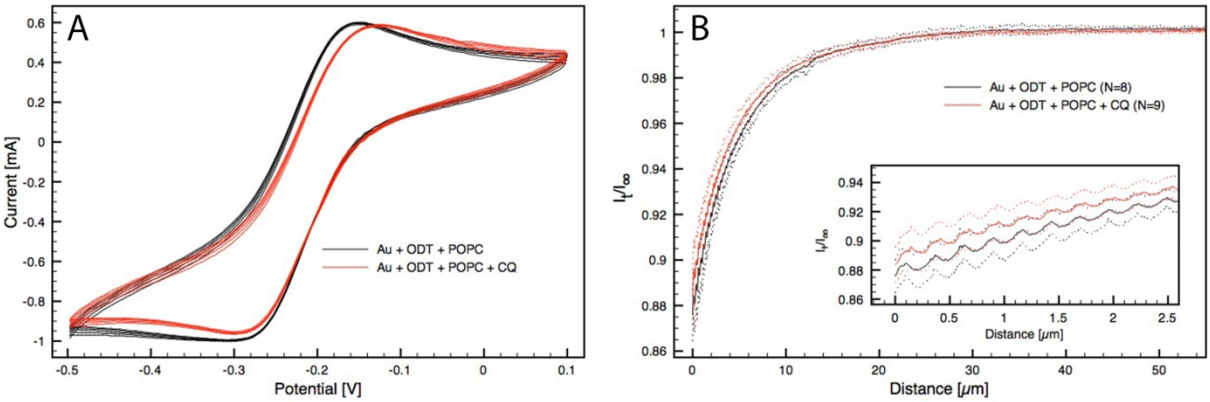

Fig. 81: A) Exemplary CV and B) approach curves for the addition of CQ solution towards an ODT-POPC hybrid lipid bilayer immersed in buffered solution. CVs and approach curves recorded in aqueous solution containing 10 mM $[Ru(NH_3)_6]Cl_3$ and 0.1 M KCl, adjusted to pH=6; ν = 100 mV/s; E_{tip}: -500 mV vs. QAg/AgCl; A_{el} = 0.83 µm^2; inset: zoomed view showing the standard deviation of the recorded approach curves (N = 8 (hybrid lipid bilayer); N = 9 (after CQ addition)).

Coating	Peak current [mA]	Surface coverage [%]
Au + ODT +POPC	-0.911	71.63
Au + ODT + POPC + CQ	-0.912	71.60

Tab. 13: Change in relative surface coverage after CQ addition according to Fig. 81A.

The influence of the addition of CQ to the supernatant solution is shown in Fig. 81 and Tab. 13, respectively. In combination with the results shown in Fig. 80A and Tab. 12, a successful suppression of the transmembrane transport of $[Ru(NH_3)_6]Cl_3$ can be assumed. Additionally, the AFM-SECM results for the addition of CQ to the supernatant solution of a supported lipid bilayer without C2IIa incorporation show some minor deviations, exceeding the standard deviation, in contrast to the PBS solution exchange experiment (Fig. 78). This slight deviation might be the reason why the approach curve, recorded in the previous experiment (Fig. 80), for the transmembrane transport validation did not reveal a significant change after CQ addition. Summarizing the results of both experiments (Fig. 80 and Fig. 81) lead to the conclusion that the redox mediator transport may be successfully blocked by CQ, but may be not directly observed by AFM-SECM with the here shown approach, as adding CQ to solution seems to generate an offset on the recorded approach curve data. Hence, the minute changes due to blocking may be obscured by the changes related to adding CQ to solution.

7.2.1.4. Limitation and improvements

All experiments were performed with PtC composite AFM-SECM probes with the conical electrode as the tip apex. These PtC composite electrodes were fabricated, by depositing Pt/carbon onto an electronically addressable AFM tip apex using FIB induced deposition techniques (for details see subsection 10.5.3). While the conical PtC composite electrodes are relatively easy to fabricate and show high faraday currents up to tens of nA due to their relatively large electrode area, these combined probes also suffer from some disadvantages. As the electrodes are not recessed from the tip apex, the electrodes are frequently in contact with the supported hybrid lipid bilayer leading to contaminations of the electrode surface at longer measurement times. Within the first 20-25 approaches no significant influence on the current at potentials < -400 mV vs. QAg/AgCl due to contaminations were observed, but an extended use of the electrodes may result in a decay of the feedback current (Fig. 82).

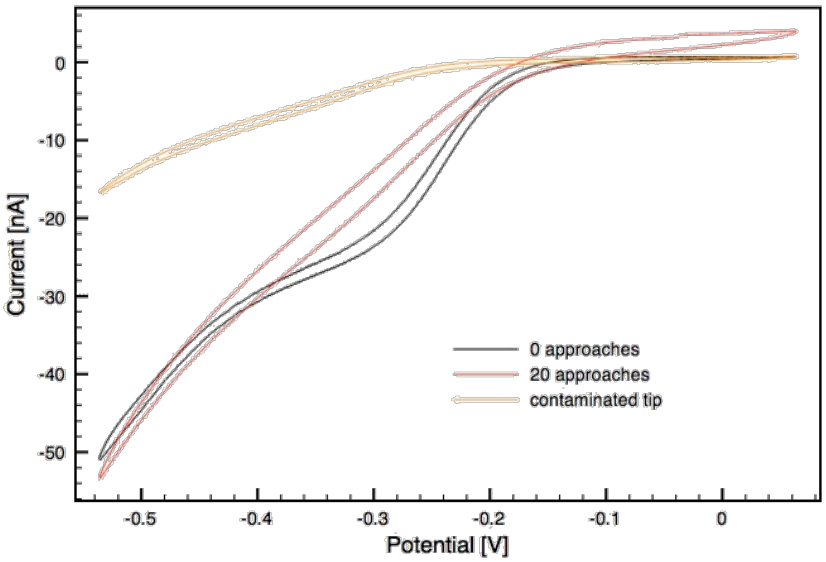

Fig. 82: Signal decay of a PtC composite electrode after more than 20-25 approach curves; CVs recorded in aqueous solution containing 10 mM $[Ru(NH_3)_6]Cl_3$ and 0.1 M KCl vs. QAg/AgCl; ν = 100 mV/s; A_{el} = 0.83 μm^2.

To overcome some of the obstacles in future, electrode materials less prone to adsorption could be used. For example, BDD electrodes might be more suitable as they exhibit less bio-fouling [32,116]. The electrochemical longtime reproducibility of the measurements might be also improved by using recessed electrodes, either with classical electrode materials like Au, Pt or novel materials like BDD [8,182].

7.2.2. Detection of dopamine at combined BDD-AFM-SECM probes in physiologically relevant conditions

7.2.2.1. Influence of ascorbic acid on the detection of dopamine

Detecting dopamine under physiologically relevant conditions includes not only the detection of dopamine in a medium with suitable pH for biological samples such as cells, but refers also to the co-presence of other molecules, which might interfere with the detection of the targeted analyte. For example, ascorbic acid represents such an interfering molecule when electrochemically detecting dopamine. Individually resolved detection of dopamine and ascorbic acid at a glassy carbon electrode is impeded, as the formal oxidation potentials are with 755 mV (dopamine) and 766 mV (ascorbic acid) leading to overlapping signals [15]. However, it has been demonstrated that a resolved electrochemical detection of dopamine and ascorbic acid can be achieved using H-terminated BDD electrodes [15]. Although BDD is generally considered an excellent electrode material, as fouling effects are less observable for most electroactive bio-molecules [32], this is not true for the oxidation of dopamine. Due to the electrochemical conversion, a reaction cascade is triggered leading to the formation of a melanin like polymer (Fig. 83) [75,238] on the electrode surface, rendering the electro active area inert for further measurements. This polymerization pathway can be suppressed by adding stabilizers to solution or by modifications of the electrode surface [238]. Ascorbic acid, which is normally present in a concentration range of 50-100 µM in biological samples, can regenerate the oxidized dopamine o-quinone (Fig. 83). A side effect of this regeneration cycle is an enhanced signal of the dopamine detection, as already converted dopamine is regenerated.

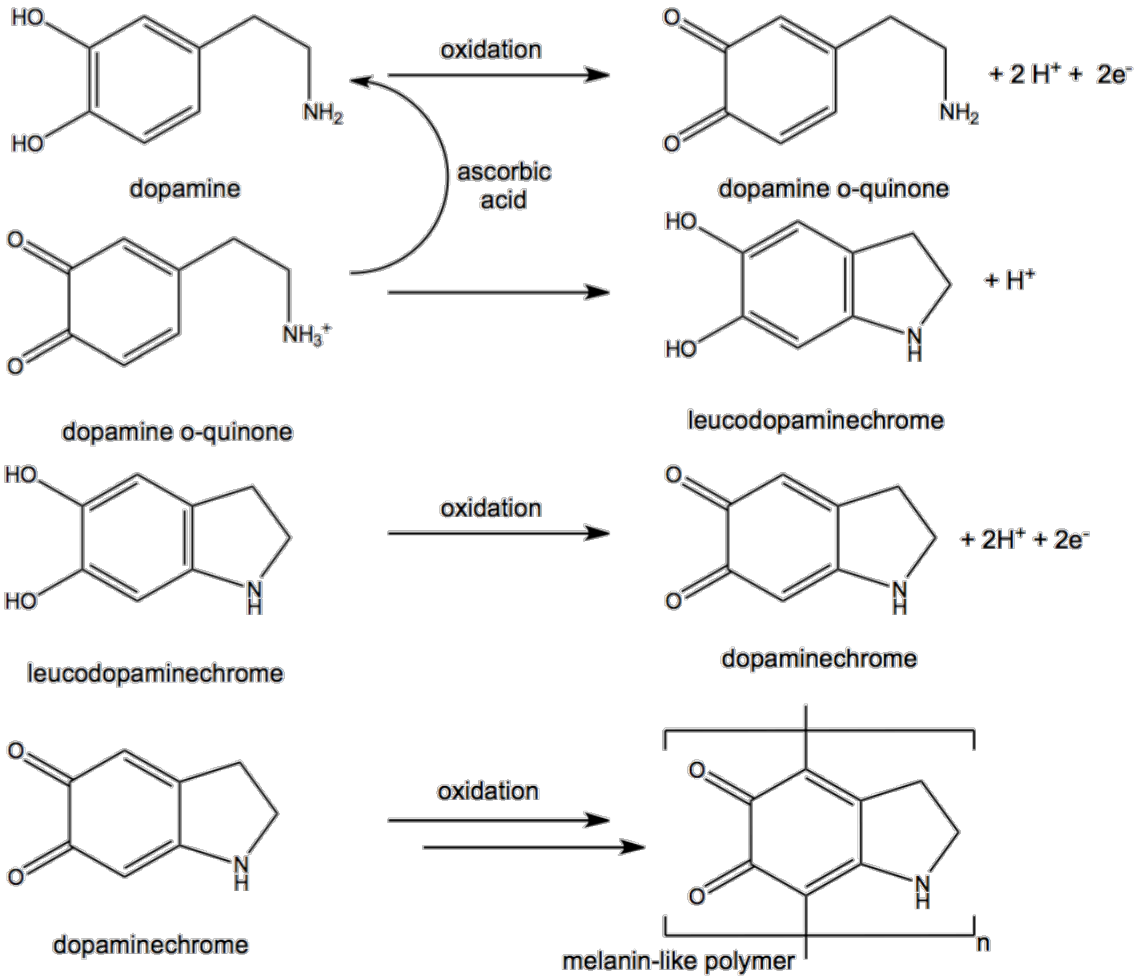

Fig. 83: Reaction pathways of dopamine and ascorbic acid induced by electrochemical oxidation.

7.2.2.2. Detection of dopamine at H-terminated combined BDD-AFM-SECM probes

As stated in the introduction, dopamine represents an important bio-molecule in neural information transfer and altered dopamine levels are also related to several neural diseases. Therefore, the detection of dopamine at physiologically relevant concentrations is important. This is demonstrated with combined BDD-AFM-SECM probes revealing a linear relation of the concentration and the current response, which is necessary for quantification of locally released dopamine.

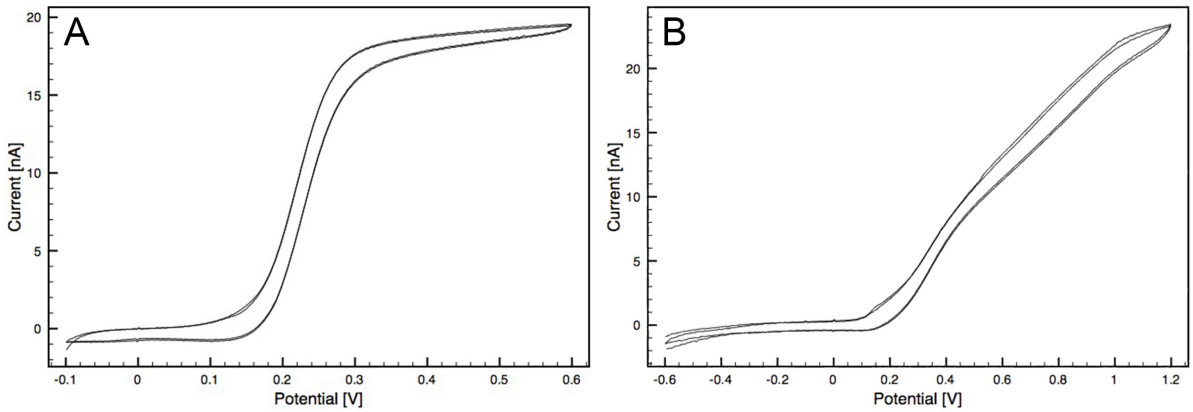

Fig. 84: Exemplary cyclic voltammograms of tip-less cathodically treated BDD-AFM-SECM probes (Fig. 85). CVs recorded in A) 10 mM $K_4[Fe(CN)_6]$ / 0.1 M KCl; B) 5 mM dopamine in PBS solution, pH=7.5 vs. sat. Ag/AgCl; ν = 100 mV/s; A_{el} = 4.52 µm^2.

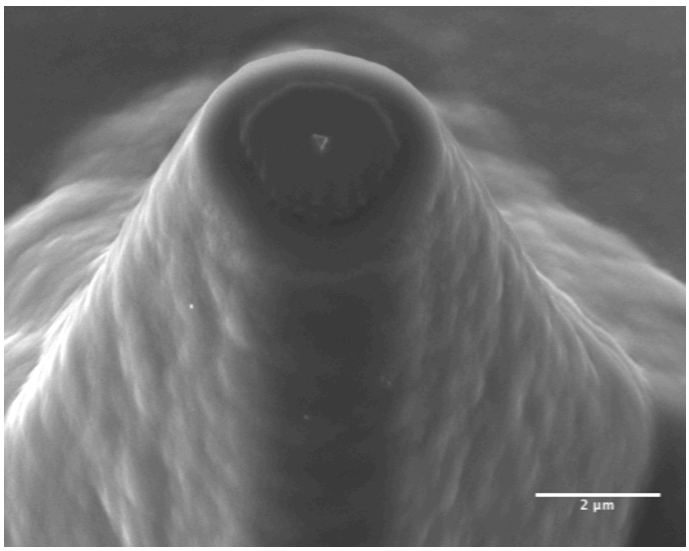

Fig. 85: Exemplary SEM image of tip-less BDD-AFM-SECM probes; A_{el} = 4.52 µm^2.

The BDD-AFM-SECM probes show a sigmoidal CV for the detection of $K_4[Fe(CN)_6]$, but a kinetically hindered electron transfer for the detection of dopamine in PBS solution (Fig. 84). A low electron transfer rate constant in the region of 10^{-4}-10^{-5} cm/s [183] is observed for dopamine on H-terminated BDD electrodes due to the weak adsorption of dopamine and other catecholamines at the electrode surface. The influence of ascorbic acid, which is frequently present in biological samples and is usually co-oxidized in the potential range for dopamine detection, is investigated. Fig. 86 shows the simultaneous detection of dopamine and ascorbic acid in PBS buffer solution (pH = 7.4) at approximately +0.2 V vs. sat. Ag/AgCl (dopamine) and approximately +0.8 V (ascorbic acid), respectively. As shown, both electrochemical signals are well resolved at the BDD-AFM-SECM probe.

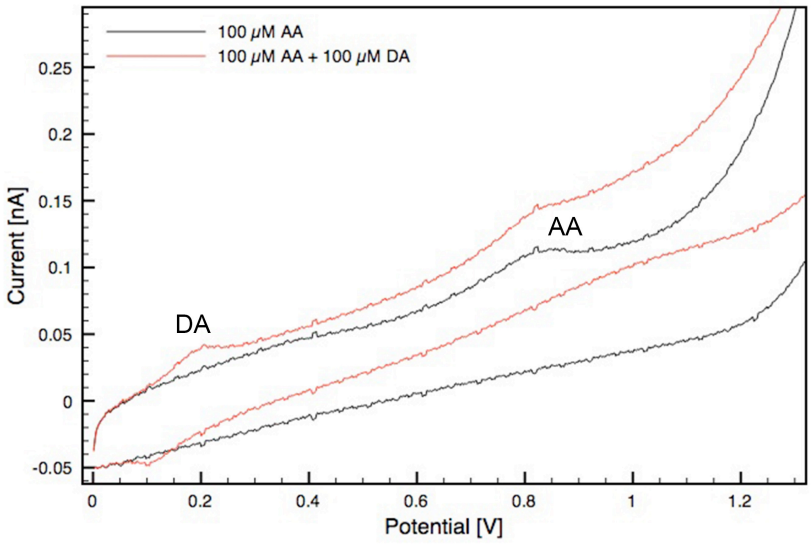

Fig. 86: CVs of tip-less cathodically treated BDD-AFM-SECM probes in PBS buffer solution (pH = 7.4) containing 100 µM ascorbic acid (black) spiked with 100 µM dopamine (red); CVs recorded at a combined AFM-SECM probe vs. sat. Ag/AgCl; ν = 100 mV/s; A_{el}= 1.65 µm^2.

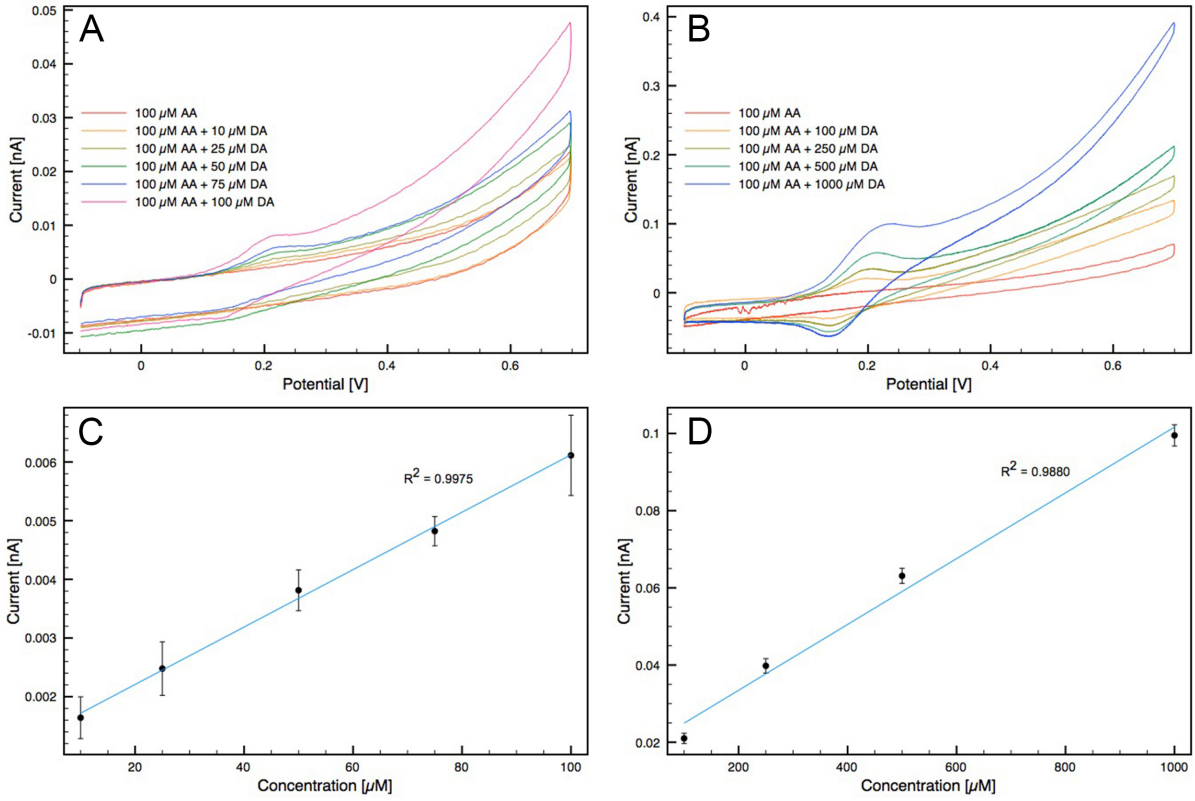

Fig. 87: CVs of ascorbic acid in PBS spiked with different concentrations of dopamine; A) 10-100 µM dopamine; B) 100-1000 µM dopamine; C,D) linear regression of the current response of A,B (N = 4); CVs recorded at combined AFM-SECM probe vs. sat. Ag/AgCl; ν = 100 mV/s; A_{el}= 0.96 µm^2 (A,C); A_{el}= 0.58 µm^2 (B,D).

The BDD electrodes also show a linear response towards the detection of dopamine in the presence of ascorbic acid, as outlined in Fig. 87. This can be used for quantitative analyses, if the ascorbic acid concentration in solution is known, maintained, and the probes are calibrated accordingly. Alternatively, the concentration of dopamine can be determined by standard addition techniques, or by measuring in an ascorbic acid spiked solution in order to maintain a higher ascorbic acid level.

7.2.2.3. Dopamine detection at BDD microelectrode arrays

As outlined in section 4.4, future fabrication of combined BDD-AFM-SECM probes might be realized using a perpendicular to the tip oriented Ga^+ ion beam (top-mill process). This perpendicular orientation of the Ga^+ ion beam leads, compared to a side-mill process, to an increased damaged surface layer as already described in section 4.2.3. As a result, the impact on the electrochemical dopamine detection in the previously used PBS buffer solution containing dopamine and ascorbic acid has been evaluated (Fig. 88), using a top-mill-fabricated BDD microelectrode array (5x5 array; 10 µm individual electrode diameter; 100 µm spacing).

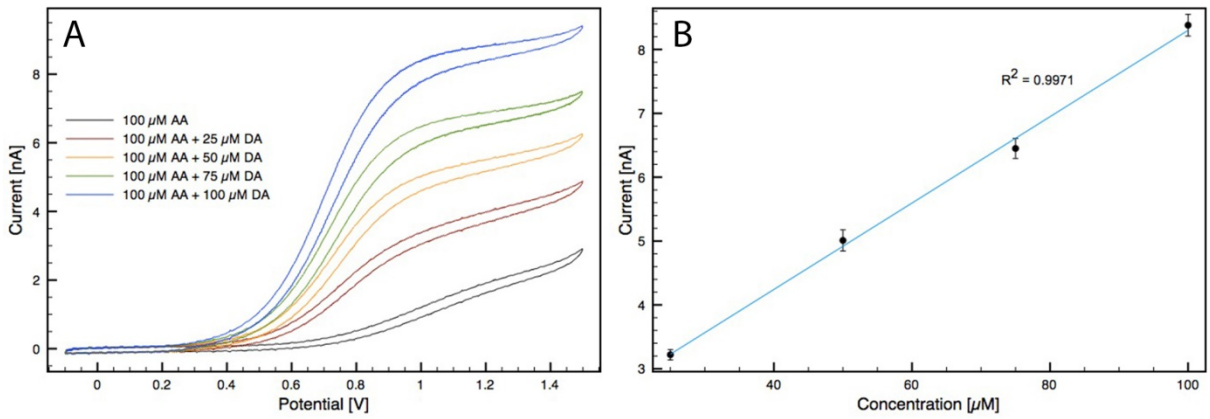

Fig. 88: CVs of ascorbic acid in PBS spiked with different concentrations of dopamine; A) 25-100 µM dopamine; B) linear regression of the current response of A recorded at 1V vs. sat. Ag/AgCl (N = 4); CVs recorded at a perpendicular milled BDD electrode array (Fig. 23B); ν = 100 mV/s. A_{el} = 1963 µm².

The ion beam damage of the surface, even after a cathodic treatment in sulfuric acid shows significant impact on the electrochemical response concerning dopamine detection. The exposure to a perpendicular oriented focused ion beam leads to a shift in the oxidation potential of dopamine of about 600 mV compared to a parallel milled electrode surface. This significant shift of the oxidation potential correlates to

the additional energy requirements for the electrochemical conversion at the amorphous carbon formed on the BDD surface, although it was investigated (chapter 3) that a perpendicular orientation of the Ga^+ ion beam doesn't alter the potential window range significantly. Despite the fact that the oxidation potential of dopamine is shifted to significant higher potentials, and now convoluting with the signal of ascorbic acid, the linear correlation between current and concentration can still be observed, if the concentration of ascorbic acid remains constant.

7.3. Conclusion & Outlook

Within this chapter, it could be demonstrated that changes in the composition of artificially supported hybrid lipid bilayers can be observed by AFM-SECM using PtC composite AFM-SECM probes. In particular, the formation of the supporting structure (ODT) on the substrate, the hybrid lipid membrane, and the embedment of heptameric C2IIa pores using AFM-SECM feedback measurements could be investigated. In addition to the formation and inhibition experiments of the heptameric pores, also validation experiments for solution exchange were conducted, revealing no significant influence on the obtained electrochemical data. Further research may aim towards further miniaturization of the probes and improvement of the long-term stability for prolonged measurements, as the PtC composite AFM-SECM probes show a deactivation of the electroactive area with repetitive exposure towards the lipid membrane. Therefore, BDD may be used as conductive tip, which generally shows less adsorption of bio molecules. Alternatively, an AFM-SECM probe with a recessed electrode may be used. By further miniaturizing the electrode area, a laterally resolved detection of the pore incorporation and activity might be realized allowing a more complex study of the pore forming and transmembrane transport mechanisms. Also more repetitive experiments have to be conducted in order to achieve sufficient statistical data evaluation of the supported lipid membrane formation, C2IIa incorporation and inhibition.

In this chapter also first results on the detection of dopamine at combined BDD-AFM-SECM probes are demonstrated for qualitative as well as for quantitative analysis under physiologically relevant conditions. While side-mill fabricated electrodes (AFM-SECM probes) show a good agreement concerning peak separation of dopamine and ascorbic acid, top-mill BDD-electrodes reveal overlapping signals for dopamine and ascorbic acid, which is commonly observed

with conventional carbon electrode materials. This indicates the presence of an amorphous surface layer, which seems not be removed completely by electrochemical treatment. Although, properties like potential window range and chemical stability of BDD could be restored by the cathodic treatment. AFM-SECM could be in future applied for laterally resolved detection of dopamine e.g., diffusion through artificial pores, as a preliminary step towards a laterally resolved detection of dopamine in biological samples like neurons and other dopamine releasing cells.

8. Summary

Combined atomic force-scanning electrochemical microscopy (AFM-SECM) is a powerful tool for mapping surface activity with high lateral resolution in both topography and electrochemistry at real-world related sample surfaces. Among the most recent developments in this research area are certainly further miniaturization of such combined probes, instrumental improvements towards routine applications and novel electrode materials with superior electroanalytical properties. Hence, the main emphasis of this thesis was related to the development of boron-doped diamond (BDD)-AFM-SECM probes for further advancing this technology.

In the first part of the thesis, the influence of different focused ion beam patterning parameters on the electrode performance (electron transfer rate) was investigated if the focused ion beam was perpendicularly incident at the sample surface. After exposure of such BDD electrodes to the ion beam, an electrochemical post fabrication step was performed in 2 M sulfuric acid. Accelerating voltages of 8 - 30 kV, ion beam currents ranging from 3 - 15 nA and dwell times of 50 - 2000 ns revealed that the heterogeneous electron transfer, the electrochemical peak separation and the ten-point mean surface roughness factor are indeed interrelated. Importantly, it was found that accelerating voltage and beam current are linearly correlated with the heterogeneous electron transfer rate constant k^o. With increasing accelerating voltage and beam current, k^o decreases and the peak separation increases for the conversion of ferrocyanide. For dwell times between 300 – 1500 ns, the electrochemical behavior of the BDD electrodes revealed low electron transfer rates, while dwell times below 200 ns and higher than 1500 ns showed a comparatively fast electron transfer. After detailed investigations, it was concluded that dwell times in the range between 300 – 1500 ns lead to maximum amorphization and to sp^2-hybridized carbon, thereby resulting in low HET rate constants, and a sluggish electron transfer behavior, for surface sensitive electrochemical species.

In the second chapter of the thesis, a fabrication scheme for combined BDD-AFM-SECM probes provided with a recessed embedded ring electrode was outlined. Although a side-mill processing strategy was employed to further reduce the impact of Ga-ion implantation on the modification of the diamond lattice, a post-milling treatment in sulfuric acid to remove amorphous carbon material and restore the required surface termination remained essential. Experiments on model samples,

like Pt-UMEs, proved the versatility of such combined probes. Electrochemical experiments revealed that the H-termination of the surface remained stable for at least several days. Bulk solution measurements furthermore indicated a potential window of approximately 2.5 V. In addition to these experiments, numerical simulations have been performed for predicting the electrochemical response in bulk solution, as well as during combined measurements. Excellent agreement between the simulated behavior and the obtained experimental data has been achieved.

Numerical simulations are a useful tool for evaluating e.g., the impact of various electrode geometries on the analytical measurement. For example, in dependence of the multi-layer device structure, a top-milling fabrication strategy for AFM-SECM probes may lead to a certain electrode tilt. Therefore, the third chapter of this thesis was dedicated to numerical simulations, for predicting the expected current in bulk solution and for SECM feedback conditions. It was demonstrated that in general the predicted currents at steady state conditions indeed coincided with the currents obtained at combined top-milled AFM-SECM probes in bulk solution with minor deviations for inward tilted electrodes.

For optimizing the experimental data acquisition during combined AFM-SECM measurements, maximizing the signal-to-noise ratio (SNR) is of paramount importance. Therefore, the fourth part of this thesis is centered around instrumental improvements in terms of probe mounting and signal transduction using a fully integrated amplifier located in close proximity to the AFM-SECM probe facilitating direct current-to-voltage conversion. This integrated transducer system demonstrated a significant improvement in SNR by a factor of 5 compared to conventional probe mounting and signal extraction strategies, and a significant reduction of external parasitic signals, which may superimpose the electrochemical signal.

In the last part of the thesis two practical applications using the developed AFM-SECM probes were demonstrated, in the area of material science and of biologically/cell physiologically relevant applications. In the first example, electrochemically induced pit corrosion processes were studied and visualized using combined AFM-SECM. It was demonstrated that pit formation and corrosion product precipitation can be controlled via the scanned area, the exposure time, the immersion time, and the applied potential. Increased solution immersion times accelerated the observed pit formation and increased pit dimensions, as visualized via in-situ analysis.

As a second example, for biologically relevant samples, BDD-AFM-SECM probes were applied for simultaneously detecting dopamine and ascorbic acid in a physiologically relevant concentration range. The obtained results clearly encourage future studies targeting laterally resolved quantitative detection of dopamine at live cells, e.g., nerve cells. In addition, it was observed that using a top-milling fabrication approach for BDD electrodes results in a convolution of the dopamine and ascorbic acid signal, which in turn indicates a significant effect of the amorphous carbon residues. Last but not least, supported lipid membranes with embedded protein pores (here, C2IIa toxin) were studied by recording SECM approach curve via AFM-SECM probes using conically shaped PtC electrodes. During these studies, different pore densities have been identified via the variation of the feedback response at the AFM-SECM probes.

9. Zusammenfassung

Die Kombination aus Rasterkraftmikroskopie und elektrochemischer Rastersondenmikroskopie stellt eine leistungsstarke Methode zur hochauflösenden, oberflächensensitiven Untersuchung von Probenoberflächen aller Art dar, und erlaubt simultan die Topographie sowie die elektrochemischen Eigenschaften abzubilden. Von besonderem Interesse in diesem Forschungsbereich ist sicherlich die weitere Miniaturisierung der kombinierten Messsonden, sowie instrumentelle Verbesserungen um dieses Messverfahren in die Routineanalytik einzugliedern. Nicht zuletzt sind neuartige Elektrodenmaterialien mit verbesserten elektroanalytischen Eigenschaften von Bedeutung. Daher lag der Schwerpunkt der vorliegenden Dissertation auf der Entwicklung von kombinierten AFM-SECM Sonden, deren integrierte Elektroden auf bor-dotiertem Diamant (BDD) basieren.

Im ersten Teil der Arbeit wurde der Einfluss unterschiedlicher Fabrikationsparameter, bei der Herstellung von BDD-Elektroden mittels eines senkrecht einfallenden fokussierten Ionenstrahls (FIB) untersucht. Insbesondere wurde das resultierende elektrochemische Verhalten der Elektroden mit der Beschleunigungsspannung des Ga^+-Ionenstrahls (8 – 30 kV), dem Ionenstrom (3 – 15 nA) und der Verweildauer des Strahls pro Pixel (50 – 2000 ns) korreliert. Es hat sich gezeigt, dass nach der Durchführung eines elektrochemischen Nachbearbeitungsschrittes (Anlegen unterschiedlicher Potentiale in 2 M Schwefelsäure), ein eindeutiger Zusammenhang zwischen der erzielbaren Elektronenübertragungsrate, der Peak-Separation und der Oberflächenrauigkeit der BDD Elektroden abgeleitet werden kann. Weitere Untersuchungen zeigten, dass eine umgekehrte Proportionalität zwischen Beschleunigungsspannung bzw. Ionenstrom und dem elektrochemische Verhalten der Elektrode in Hinblick auf die Kinetik des Elektronentransfers besteht. Wurde während des Strukturierungsvorganges eine Verweildauer des Ionenstrahls von 300 – 1500 ns gewählt, zeigte das elektrochemische Verhalten der BDD-Elektroden eine deutlich verringerte Elektronentransferkinetik. Eine Verweildauer von < 200 ns oder > 1500 ns führte zu vergleichsweise schnellen Übertragungsraten. Aus den erzielten Ergebnissen wurde abgeleitet, dass im Bereich von 300 – 1500 ns die Bildung von sp^2-hybridisiertem Kohlenstoff maximiert wird, wodurch es zu deutlich verringerten Elektrodenübertragungsraten und einem trägen Elektrodenverhalten für oberflächensensitive Redox-Spezies kommt.

Im zweiten Kapitel der Arbeit wurde der Herstellungsprozess für kombinierte BDD-AFM-SECM-Sonden mit rückversetzten Ringelektroden entwickelt. Obwohl ein seitlich orientierter FIB-Abtragungsprozess mit seitlicher Ionenstrahleinfallsrichtung implementiert wurde, war weiterhin ein Nachbearbeitungsschritt (anlegen von hohen Potential in Schwefelsäure) zur Entfernung von amorphem Kohlenstoff und zur Wiederherstellung der Wasserstoff-Oberflächenterminierung erforderlich. Erste Experimente an Modellproben, wie z.B. Pt-Ultramikroelektroden, zeigten die Funktionsfähigkeit der kombinierten Sonden. Elektrochemische Experimente belegten weiterhin den Erhalt der Oberflächenterminierung von mehreren Tagen. Nicht zuletzt konnte ein nutzbares Potentialfenster von ungefähr 2.5 V bestimmt werden. Ergänzend zu den Experimenten wurden auch numerische Simulationen durchgeführt, um das elektrochemische Verhalten der entwickelten BDD-AFM-SECM Sonden in Lösung und während kombinierter AFM-SECM Messung im Detail zu beschreiben. Die hierbei erzielten Resultate stimmten größtenteils sehr gut mit den vorhandenen experimentellen Daten überein und eignen sich daher zur Vorhersage des elektrochemischen Verhaltens unter unterschiedlichen Messbedingungen.

Numerische Simulationen wurden auch zur Beschreibung unterschiedlicher Elektrodengeometrien eingesetzt. Der Strukturierungsprozess mittels senkrecht einfallenden Ionenstrahls führt beispielsweise abhängig vom eingesetzten Elektrodenmaterial, Isolationsschicht und Material des AFM-Cantilevers zu unterschiedlichen Neigungswinkeln der integrierten Elektrodenfläche. Daher war das dritte Kapitel dieser Arbeit der Simulation des zu erwartenden Stromflusses in Lösung sowie im SECM Rückkopplungsmodus von AFM-SECM-Messungen gewidmet. Dabei konnte gezeigt werden, dass mittels dieser Simulationen der Stromfluss hinreichend präzise vorhergesagt werden kann, wobei bei sehr hohen Neigungswinkeln der Elektrode noch Einschränkungen zur Genauigkeit der Vorhersage zu berücksichtigen sind.

Zur Verbesserung der experimentellen Durchführung von kombinierten AFM-SECM-Messungen spielt eine optimierte elektrochemische Signalerfassung eine bedeutende Rolle. Deshalb wurden im vierten Kapitel dieser Dissertation eine neuartige Montage von AFM-SECM Sonden, sowie eine verbesserte Strategie zur Signaltransduktion durch direkte Strom-Spannungswandlung nahe der Sonde mittels eines integrierten Verstärkermoduls entwickelt. Die Integration dieses Signalwandlers zeigt eine deutliche Verbesserung des Signal-zu-Rausch-Verhältnisses (SNR) um

einen Faktor 5 gegenüber dem ursprünglichen Messaufbau, und reduziert die Anfälligkeit des elektrochemischen Messsignals gegenüber externen Störsignalen deutlich. Derartige Störsignale überlagern oftmals das elektrochemischen Signals welches im Bereich weniger nA-pA liegt.

Im letzten Teil der Dissertation wurde anhand von zwei Beispielen die Anwendungsmöglichkeiten kombinierter AFM-SECM Sonden im Bereich der Materialwissenschaften, sowie für biologische bzw. zellphysiologische Fragestellungen gezeigt. Die materialwissenschaftlichen Experimente zeigen die Anwendung von AFM-SECM zur gezielten elektrochemischen Induktion und in-situ Visualisierung von relevanten Prozessen in der Lochkorrosion. So konnte beispielsweise die Abhängigkeit des Korrosionsverhaltens von der gescannten Fläche, der Expositionszeit, der Eintauchzeit und des angelegten Potentials anhand der entstandenen Vertiefungen und der Abscheidung von Korrosionsprodukten nachgewiesen werden. Die erzielten Ergebnisse zeigten, dass mit verlängerter Eintauchzeit, die beobachtete Lochkorrosion beschleunigt werden kann, wodurch es was zu größeren Vertiefungsvolumina kommt.

Abschließend wurde gezeigt, dass die in dieser Arbeit entwickelten BDD-AFM-SECM-Sonden zur simultanen Detektion von Dopamin und Ascorbinsäure in physiologisch relevanten Konzentrationsbereichen geeignet sind. Es ist daher zu erwarten, dass in Zukunft die ortsaufgelöste Detektion von Dopamin an lebenden Zellen, beispielsweise Nervenzellen, möglich ist. Im Rahmen dieser Experimente konnte auch nachgewiesen werden, dass die Strukturierung von BDD-Elektroden mittels senkrecht einfallendem Ionenstrahl zu einem deutlichen Anteil an amorphen Kohlenstoff an der Elektrodenoberfläche führt, der eine Überlagerung des Dopamin- und Ascorbinsäuresignals zur Folge hat und somit einen wesentlichen Fabrikationsaspekt in Bezug auf die finale Anwendung der Sonden darstellt. Es wurde außerdem gezeigt, dass eingebettete Proteinporen (hier, C2IIa Toxin) mittels AFM-SECM unter Nutzung integrierter, konischer PtC Elektroden untersucht werden können, sowie die Porendichte mittels SECM Annäherungskurven charakterisiert werden kann.

10. Experimental

10.1. Chapter 3

10.1.1. Chemicals and solutions

Potassium hexacyanoferrate (II) trihydrat ($K_4[Fe(CN)_6]x3H_2O$) p.a., hexaamine-ruthenium (III) chloride ($[Ru(NH_3)_6]Cl_3$) p.a., potassium chloride (KCl) p.a., and polyoxyethylene sorbitan monolaurate (Tween 20) were purchased from Sigma-Aldrich (Steinheim, Germany). Solutions for electrochemical measurements contained 10 mM $K_4[Fe(CN)_6]$ or 10 mM $[Ru(NH_3)_6]Cl_3$, respectively, 0.016 M Tween 20 and 0.1 M KCl as supporting electrolyte. Sulfuric acid 98% p.a. was purchased from Merck (Darmstadt, Germany). 2 M H_2SO_4 was used for electrochemical H-termination and 0.5 M $H_2SO_4$for determining the potential window. All solutions were prepared in Elga high purity water with a resistivity at 25°C of 18.2 MΩ·cm (Elga Labwater, VWS Deutschland GmbH, Celle, Germany) and chemicals as purchased [172].

10.1.2. Apparatus

FIB exposure / microfabrication of the ultra-microelectrode arrays were performed with a DualBeam Quanta 3D FEG (FEI Company, Eindhoven, Netherlands). For electrochemical characterization a CHI potentiostat 660a (CH Instruments Inc., Austin, Texas, USA) with a customized liquid cell (Fig. 89) was used.

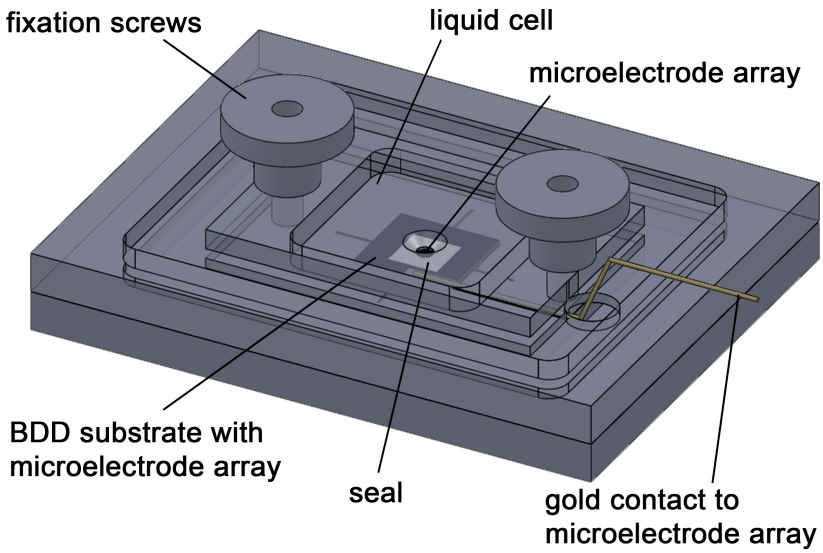

Fig. 89: Schematic illustration of a customized liquid cell for electrochemical measurements.

For electrochemical treatment a Voltcraft plus VSP 2405 HE lab power supply (Conrad Electronic SE, Hirschau, Germany) with a two-electrode setup (working electrode: BDD substrate; counter electrode: Pt-wire) and an designated electrochemical cell with separated counter and working electrode space was used (appendix 12.3.3). The electrochemical characterization was performed in a three-electrode setup using an Ag/AgCl (sat.) reference electrode (ALS Co., Ltd, Tokyo, Japan), a Pt counter electrode and the BDD substrate as working electrode. For determining HET rate constants, experimental data obtained during electrochemical characterization, were fitted to simulated cyclic voltammograms using DigiElch 7 (Elchsoft, Kleinromstedt, Germany).

Surface roughness / AFM measurements were performed with a 5500 atomic force microscope from Keysight Technologies (Chandler, AZ, USA). Surface roughness parameters were obtained in contact mode using Bruker NP silicon nitride cantilevers (nominal spring constant: 0.06 N/m). Raman spectra were recorded with an Alpha300R confocal Raman microscope (WiTec GmbH, Ulm, Germany) equipped with a Nd:YAG laser (532 nm) operated at 10 mW and a 100x objective with a 0.9 numerical aperture. EBSD measurements were performed using a 1.4 megapixel EBSD detector (Ametek GmbH, Meerbusch, Germany) using the electron source of the Quanta 3D FEG operated at 20 kV and 16 nA [172].

10.1.3. Procedures

Nanocrystalline, hydrogen-terminated BDD samples were fabricated in a microwave-assisted PECVD process and provided by the Fraunhofer Institute for Applied Solid State Physics (Freiburg, Germany); the detailed fabrication process and parameters are described elsewhere [169]. The hydrogen-terminated BDD samples were electrochemically characterized using cyclic voltammetry and then insulated with Si_xN_y, with a layer thickness of ≈ 1 µm, deposited in a PECVD process. The insulation properties and quality were tested via cyclic voltammetry prior to the FIB microstructuring. Patterns with different spacing for different characterization experiments were fabricated; for peak separation measurements 5x5 BDD microelectrode arrays with an electrode diameter and spacing of 10 µm were exposed (Fig. 15B) by FIB milling. For HET rate constant determination 5x5 BDD microelectrode arrays with a center-to-center spacing of 100 µm were fabricated (Fig. 23B). Individual nanoelectrode arrays were fabricated with different sets of milling parameters; accelerating voltage ranges from 8 - 30 kV; beam currents from 3 - 15 nA and dwell times from 50 - 2000 ns. In order to evaluate the influence of the milling parameters on the electron transfer rate after electrochemical treatment, the ferro/ferricyanide redox couple was used as a “benchmark” system. The electrochemical treatment consisted of a sequential polarization at various potentials in 2 M sulfuric acid. First the microelectrode arrays were anodically polarized at +2.5V for 1 min, and subsequently cathodically at -4 V for 30 min, following an adapted procedure by Hoffmann et al. [57,172].

10.1.4. Simulations

For the electrochemical CV simulations with DigiElch 7 (Elchsoft, Kleinromstedt; Germany) a one electron redox process was chosen at a µm-sized disc electrode with a radius of 5 µm, and a hemispherical diffusion profile. To calculate the HET rate constant, the simulated data was fitted to the experimentally data. Therefore, the obtained current of the CVs of the 5x5 arrays was divided by 25 to calculate the current of a single electrode, as it is assumed that the diffusion profiles in the microelectrode array with 100 µm spacing are not overlapping and contribute equally to the overall electrochemical signal. For the fitting of the HET rate constant, the electron transfer coefficient was either set to 0.5 (assuming a symmetrical energy barrier for the electron transfer) or to 0.659 for an asymmetrical barrier. The electron

transfer coefficient for the asymmetrical transfer was determined by averaging the electron transfer coefficient of all investigated samples, which were calculated to be between 0.643 and 0.69. To determine the transfer coefficient, the electron transfer coefficient was iterated during fitting with variable electron transfer coefficients. For fitting the untreated macroscopic BDD substrate, a planar diffusion profile and an electrode size of 2 mm in diameter was used to fit the experimental data.

10.2. Chapter 4

10.2.1. Chemicals and solutions

Potassium hexacyanoferrate (II) trihydrat ($K_4[Fe(CN)_6]x3H_2O$) p.a., hexaamine-ruthenium (III) chloride ($[Ru(NH_3)_6]Cl_3$) p.a., and potassium chloride (KCl) p.a. were purchased from Sigma-Aldrich (Steinheim, Germany). Solutions for electrochemical measurements contained 10 mM $K_4[Fe(CN)_6]$ or 10 mM $[Ru(NH_3)_6]Cl_3$, respectively, and 0.1 M KCl as supporting electrolyte. Sulfuric acid 98% p.a. for electrochemical treatment and electrochemical characterization was purchased from Merck (Darmstadt, Germany). 2 M H_2SO_4 was used for electrochemical H-termination and 0.5 M H_2SO_4 for determining the potential window. All solutions were prepared in Elga high purity water with a resistivity at 25°C of 18.2 MΩ·cm (Elga Labwater, VWS Deutschland GmbH, Celle, Germany) and chemicals as purchased. Parylene-C for insulator deposition was obtained from Special Coating Systems Inc. (Indianapolis, IN, USA) [182]. EPO-TEK H2OE silver conductive epoxy for probe connection was purchased from Plano GmbH (Wetzlar, Germany), and insulation varnish RS 199-1480 from RS Components Ltd. (Corby, United Kingdom).

10.2.2. Apparatus

FIB milling of combined AFM-SECM probes was performed with a DualBeam Quanta 3D FEG (FEI Company, Eindhoven, Netherlands), using a custom-made multi-orientation chip mounting device (see appendix 12.3.1), and VPD evaluation of BDD was performed with a Helios NanoLab 600 (FEI Company, Eindhoven, Netherlands). Electrochemical characterization was conducted with a CHI potentiostat 660C (CH Instruments Inc., Austin, Texas, USA). For electrochemical treatment of the BDD-AFM-SECM probes, a Voltcraft plus VSP 2405 HE lab power supply (Conrad Electronic SE, Hirschau, Germany) with a two-electrode setup (working electrode: BDD-AFM-SECM probe; counter electrode: Pt-wire) and a salt-bridge filled with

saturated potassium chloride solution connecting two separated sulfuric acid compartments was used (Fig. 32). Electrochemical characterization was performed in a three-electrode setup using an Ag/AgCl (sat.) reference electrode (ALS Co., Ltd, Tokyo, Japan), a Pt counter electrode and the fabricated BDD-AFM-SECM probe as working electrode. For determining the potential window in 0.5 M H_2SO_4, a $Hg/HgSO_4$ reference electrode was used. HET rate constant were determined with experimental data obtained during electrochemical characterization, and was fitted to simulated cyclic voltammograms using DigiElch 7 (Elchsoft, Kleinromstedt; Germany).

AFM-SECM measurements were performed with a 5500 atomic force microscope (Keysight Technologies, Chandler, AZ, USA), located inside a faraday cage. Simultaneous electrochemical data acquisition during AFM measurements was conducted using a CHI 660C potentiostat. Parylene-C coating was performed using a Parylene Deposition Unit PDS 2010 Labcoter 2 (Specialty Coating Systems Inc.; Indianapolis, IN, USA) [182]. Resonance frequency measurements were performed with a Bioscope Catalyst atomic force microscope (Bruker Corp., Billerca, MA, USA).

10.2.3. Procedures

VPD evaluation of the BDD coating was performed by milling trenches (30 kV; 46 pA) with a targeted depth of 400 nm and assumed VPD values ranging from 0.05 $\mu m^3/nC$ to 0.08 $\mu m^3/nC$ into nanocrystalline BDD. By plotting the deviation of the achieved milling depth vs. the assumed VPD parameters, the precise VPD can be extracted. Therefore, the intersection of the linear regression of the milling depth deviation vs. VPD value with the x-axis is calculated.

For probe fabrication commercial silicon AFM probes (NCL probes, NanoWorld, Neuchâtel, Switzerland) were coated with a nanocrystalline boron-doped diamond layer as described elsewhere [239], and were subsequently coated with a 900 nm insulation layer of Parylene-C or 550-600 nm iD. The electroactive area of the combined BDD-AFM-SECM probes were exposed by FIB milling with a 30 kV Ga^+ beam operating at 50 pA. The detailed fabrication process is described elsewhere (see [8,131] or [207,208]). After electrode exposure via FIB using a side-mill approach, the probes were electrochemically treated in 2 M sulfuric acid, using an adapted procedure from Hoffmann et al. [57]. The electrodes were anodically treated at a potential of +2.5 V for 1 min to remove amorphous carbon material, followed by a

cathodic treatment (hydrogen termination) at -20 V for 1 min or -12 V for 3 min, respectively. After the surface termination in 2 M sulfuric acid, the probes were electrochemically characterized in 10 mM $K_4[Fe(CN_6)]$ / 0.1 M KCl; ν = 100 mV/s. Potential window characterization was performed in 0.5 M H_2SO_4 with a scan rate ν = 200 mV/s to reduce the exposure time of the BDD electrode to anodic potentials under acidic conditions. After characterization, the probes were mounted into nosecone assemblies using fast dry adhesive based on cyanoacrylate. The probes were subsequently connected to a wire using silver epoxy adhesive, and reinsulated with insulation varnish to ensure proper electrochemical data acquisition during the combined measurements. Afterwards the mounted probe was attached to the scanner head and installed into the AFM setup. Combined AFM-SECM measurements were performed in 10 mM $[Ru(NH_3)_6]Cl_3$ / 0.1 M KCl, using contact mode with a scan speed of 0.25 lines/s and 512 data points per line. Electrochemical data was simultaneously acquired at a tip bias of -400 mV vs. QAg/AgCl, if not stated otherwise [182] with an external potentiostat (CHI 660C) and correlated via an auxiliary input channel to the topographical data. Solutions containing $[Ru(NH_3)_6]Cl_3$ were degassed for at least 15 min with Ar prior to usage.

10.2.4. Simulations

10.2.4.1. Bulk conditions

For simulating the mass transport towards the integrated electrode, three-dimensional (3D) virtual replicas (Fig. 90) of the combined BDD-AFM-SECM probe were generated with the simulation software (COMSOL Multiphysics 4.2a, ComSol Multiphysics GmbH, Göttingen, Germany).

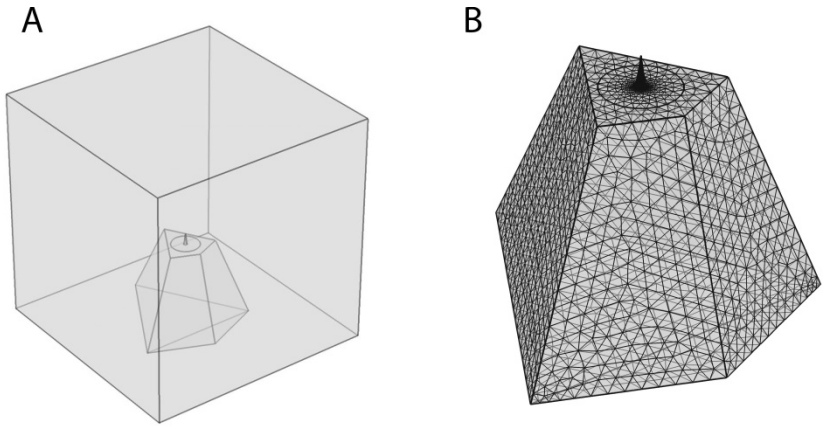

Fig. 90: A) 3D model with solvent box for diffusion simulations and current calculations; B) simulation mesh for combined BDD-AFM-SECM probe.

For the simulation model, the following boundary conditions were set: The concentration of the redox mediator at the edge of the solvent box (20x20x20 µm) was considered to be equal to the bulk solution (10 mM), excluding the bottom of the solvent box, as this part of the simulation represents the surface of the cantilever arm. The concentration of the reduced species of the redox mediator was set to zero at the electrode surface, as an instantaneous electrochemical conversion (oxidation/reduction) was assumed at the electrode. The mass transport of the redox mediator towards the electrode was considered to be solely by diffusion. A diffusion coefficient D = $6.3e^{-6}$ cm^2/s for $K_4[Fe(CN)_6]$, or D = $7.5e^{-6}$ cm^2/s for $[Ru(NH_3)_6]Cl_3$ was used [132]. Diffusion is considered to appear inside the solvent box without penetrating the material walls of the AFM-SECM tip, and equal diffusion coefficients for the oxidized and reduced form of the mediator was chosen. Also no interference between the two electronic states was considered to be present. The concentration of the redox mediator can be described with c(x,y,z) in a Cartesian coordinate

system. The diffusion is described by Fick's 2nd law of diffusion and given by the following partial differential equation:

$$\frac{\partial c}{\partial t} = D\left(\frac{\partial^2 c}{\partial x^2} + \frac{\partial^2 c}{\partial y^2} + \frac{\partial^2 c}{\partial z^2}\right)$$

Eq. 10: Fick's 2nd law of diffusion with c: concentration, D: diffusion coefficient and t: time.

For current simulations a steady state behavior was assumed, which is reached whenever the following equation applies:

$$\frac{\partial c}{\partial t} = 0$$

Eq. 11: Steady-state conditions for diffusion simulations.

By integrating the concentration gradient over the exposed electrode area multiplied with the diffusion coefficient the diffusive flux of the redox mediator can be calculated according to

$$j_{el} = D\int\left(\frac{\partial c}{\partial x} + \frac{\partial c}{\partial y} + \frac{\partial c}{\partial z}\right)dA$$

Eq. 12: Diffusive flux towards the electrode surface with D = $6.3e^{-6}$ cm²/s ($K_4[Fe(CN)_6]$ or D = $7.5e^{-6}$ cm²/s ($[Ru(NH_3)_6]Cl_3$) and A: active electrode area.

Hence, the steady state current can be described by

$$i_{t,\infty} = nFj_{el} = nFD\int\left(\frac{\partial c}{\partial x} + \frac{\partial c}{\partial y} + \frac{\partial c}{\partial z}\right)dA$$

Eq. 13: Steady-state current equation with n = 1: number of electrons; Faraday constant F = $9.64853e^{4}$ C/mol and j_{el} = diffusive flux towards the electrode surface (Eq. 12).

10.2.4.2. Feedback conditions

Simulating feedback conditions requires a modification of the solvent box described in section 10.2.4.1, and the implementation of a surface plane parallel to the electrode surface at a distance of the tip height, representing either an insulating or conductive sample surface (Fig. 91A).

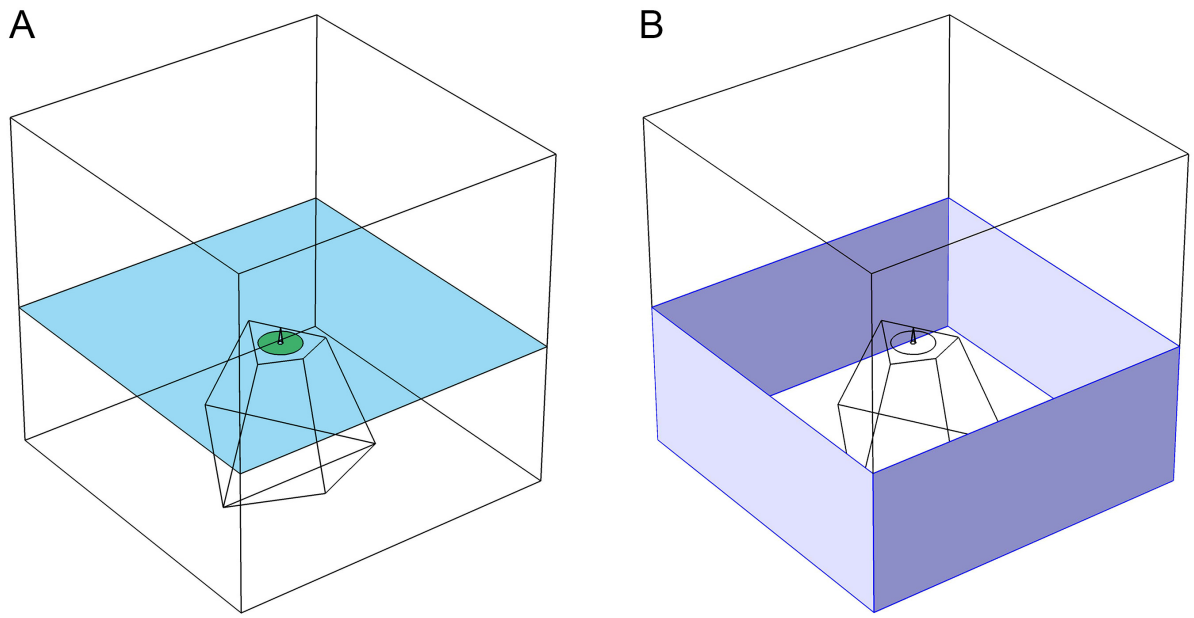

Fig. 91: A) Conversion zones of the diffusion simulation for feedback conditions (pos. feedback); B) bulk solution concentration boundaries for pos. and neg. feedback simulations.

If an insulating surface is modeled, the boundary conditions of the simulation described in section 10.2.4.1 have to be altered regarding the bulk solution concentration boundaries. Therefore, the top edge of the solvent box representing the sample surface is set to a diffusion barrier (instead of the bulk solution concentration), leaving only the side walls set to the bulk concentration and permeable for the diffusion process (Fig. 91B).

If a conductive surface is simulated both electronic states of the redox mediator have to be considered in the simulation (also assuming an equal diffusion coefficient and no interaction between the two different states). Therefore, a reaction volume with a thickness of 30 nm above the electrode and the sample surface extended the negative feedback simulation (Fig. 91A), wherein fast, nearly instantaneous electron transfer was assumed. The electrochemical conversion rate at every coordinate in the reaction zones can then be described by

$$R_{red} = kc_{ox}$$
$$R_{ox} = -kc_{ox}$$

Eq. 14: Conversion rates R_i in the conversion zone close to the electrode surface with k = $1e^9$ 1/s assuming an instantaneous electron transfer; c_i = concentration of the redox mediator species.

$$R_{ox} = kc_{red}$$
$$R_{red} = -kc_{red}$$

Eq. 15: Conversion rates R_i in the conversion zone close to the conductive sample surface with k = $1e^9$ 1/s assuming an instantaneous electron transfer; c_i = concentration of the redox mediator species.

The steady state current described by Eq. 13, is calculated by the diffusive flux of the redox mediator towards the electrode either in negative or positive feedback conditions.

10.2.4.3. CV Simulations

Electrochemical CV simulations were performed as described in section 10.1.4 with an electrode radius of r = 1.3 µm, and a hemispherical diffusion profile. Electrochemical data were used as obtained by CV measurements.

10.3. Chapter 5

10.3.1. Chemicals and solutions

Hexaammineruthenium (III) chloride ($[Ru(NH_3)_6]Cl_3$) p.a. and potassium chloride (KCl) p.a. were purchased from Sigma-Aldrich (Steinheim, Germany). Solutions for electrochemical measurements contained 10 mM $[Ru(NH_3)_6]Cl_3$ and 0.1 M KCl as supporting electrolyte. All solutions were prepared in Elga high purity water with a resistivity at 25 °C of 18.2 MΩ·cm (Elga Labwater, VWS Deutschland GmbH, Celle, Germany) and chemicals as purchased. Parylene-C for insulator deposition was obtained from Special Coating Systems Inc. (Indianapolis, IN, USA) [208].

10.3.2. Apparatus

FIB microfabrication for combined AFM-SECM probes with a top-mill approach was performed with a Helios NanoLab 600 (FEI, Eindhoven, Netherlands) using a custom made AFM-chip holder [207,208]. Flatly embedded electrodes were fabricated in a side-mill process using a Quanta 3D FEG (FEI, Eindhoven, Netherlands). Electrochemical characterization was performed using a CHI potentiostat 832A (CH Instruments Inc. Austin, TX, USA) in a three-electrode setup. The three-electrode cell contained an Ag/AgCl reference electrode (ALS Co., Ltd, Tokyo, Japan), a Pt-wire counter electrode and the AFM-SECM tip as working electrode [207,208]. For Parylene-C insulator deposition a Parylene-coater from Specialty Coating System Inc. (Indianapolis, IN, USA) was used.

10.3.3. Procedures

Modification and fabrication of the combined Parylene-C and Si_xN_y AFM-SECM probes have already been described elsewhere: The procedure for the top-mill approach can be found in [207,208], and for the side-mill approach in [8].

10.3.4. Simulations

10.3.4.1. Bulk conditions

As already described in section 10.2.4.1, the mass transport towards the electrode can be simulated by Fick's 2nd law of diffusion (Eq. 10) and calculated by Eq. 13. Therefore, also 3D replica (see Fig. 92) of the combined AFM-SECM probes were generated, based on the calculated electrode geometry as described elsewhere [207,208].

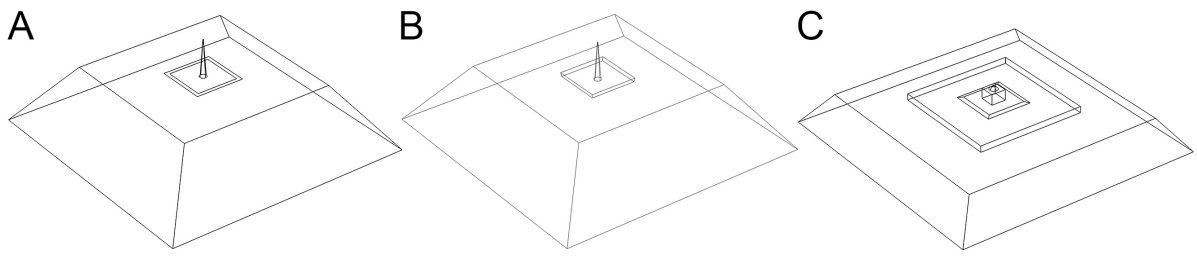

Fig. 92: 3D replica of the combined AFM-SECM probes with various electrode angles A) 0°; B) -80°; C) +13°.

For the simulation under bulk conditions the same boundary conditions as in section 10.2.4.1 are applicable, but with a diffusion coefficient of D = $7.5e^{-6}$ cm^2/s [132] for $[Ru(NH_3)_6]Cl_3$ in a solvent box of 12x12x8 µm.

10.3.4.2. Feedback conditions

In contrast to the previous approach as described in section 10.2.4.2, an adapted approach published by Zoski et al. [212] was used here to simulate the feedback currents of the different electrode geometries. In contrast to Zoski et al., where a two-dimensional approach was used and rotated to calculate the current, a 3D simulation was applied to describe the diffusion towards the electrode. However, similar boundary conditions were used. In particular, the concentration of the redox mediator was set to zero at the electrode surface, and to bulk concentration both at the sample surface and at the edges of the solvent box between sample surface and cantilever (compare Fig. 91B), whenever a conductive surface was simulated. With this approach, feedback simulation can be performed without calculating the diffusion of the reduced electronic state and the conversion reactions. For simulating an insulating surface, the same boundary conditions as described in section 10.2.4.2 were used. In order to compare the different electrode designs, the distance between the electrode surface and the sample was set to 350 nm. The individual tip heights were adapted to fulfill this requirement.

10.4. Chapter 6

10.4.1. Chemicals and solutions

Hexaammineruthenium (III) chloride ($[Ru(NH_3)_6]Cl_3$) p.a., potassium chloride (KCl) p.a., were purchased from Sigma-Aldrich (Steinheim, Germany). Hydrochloric acid (HCl_{aq}) 37%, potassium hydroxide (KOH) p.a., sodium chloride (NaCl) p.a., and sodium nitrite ($NaNO_2$) p.a. were purchased from Merck (Darmstadt, Germany). Solutions for electrochemical characterization and AFM-SECM feedback measurements contained 10 mM $[Ru(NH_3)_6]Cl_3$ and 0.1 M KCl as supporting electrolyte. For corrosion experiments solutions contained 0.5 M NaCl and 0.1 M $NaNO_2$. All solutions were prepared in Elga high purity water with a resistivity at 25°C of 18.2 MΩ·cm (Elga Labwater, VWS Deutschland GmbH, Celle, Germany) and chemicals as purchased. For pH adjustments, solutions of HCl and KOH were used. Iron plates (99.5% Fe) for pit corrosion experiments were purchased from Goodfellow Materials (Cambridge, UK). Parylene-C for insulator deposition was obtained from Special Coating Systems Inc. (Indianapolis, IN, USA) [182]. EPO-TEK H2OE silver conductive epoxy and Acheson silver DAG 1415 for electrochemical probe connection was purchased from Plano GmbH (Wetzlar, Germany), UV-light-curable encapsulant Dymax 9001-E-V3.1 for connection sealing from Dymax Europe GmbH (Wiesbaden, Germany), and insulation varnish RS 199-1480 from RS Components Ltd. (Corby, United Kingdom). 4000 grit SiC lapping film for iron plate preparation was purchased from Allied High Tech Products (Rancho Dominguez, CA), and 0.05 µm alumina slurry for polishing was purchased from Leco Corp. (St. Joseph, MI, USA).

10.4.2. Apparatus

FIB microfabrication for combined AFM-SECM probes with a top-mill approach was performed with a Helios NanoLab 600 (FEI, Eindhoven, Netherlands) using a custom made AFM-chip holder [207,208]. Flatly embedded electrodes were fabricated in a side-mill process using a Quanta 3D FEG (FEI, Eindhoven, Netherlands). Au coating of the AFM cantilevers was performed using a custom-made shadow mask (see 12.3.4). For Parylene-C insulator deposition, a Parylene-coater from Specialty Coating System Inc. (Indianapolis, IN, USA) was used. Electrochemical characterization was performed using a CHI potentiostat 660A (CH Instruments Inc. Austin, TX, USA) in a three-electrode setup. The three-electrode cell contained an

Ag/AgCl reference electrode (ALS Co., Ltd, Tokyo, Japan), a Pt-wire counter electrode and the AFM-SECM tip as working electrode [207,208].
AFM-SECM measurements were performed with a 5500 atomic force microscope (Keysight Technologies, Chandler, AZ, USA), located inside a faraday cage, equipped with a Picostat potentiostat and a SECM nosecone with integrated operation amplifier and replaceable AFM-SECM probe cartridges. External data acquisition was performed with a CHI potentiostat 832A (CH Instruments Inc. Austin, TX, USA). For electrochemical data acquisition the AFM-SECM systems used a three-electrode setup with a QAg/AgCl reference electrode, a ring-shaped Pt counter electrode and the AFM-SECM tip as working electrode.

10.4.3. Procedures

Modification and fabrication of the combined Parylene-C and Si_xN_y AFM-SECM probes have already been described elsewhere: The procedure for the top-mill approach can be found in [207,208], and for the side-mill approach in [8]. After FIB milling, the AFM-SECM probes were electrochemically characterized and mounted for external data acquisition into AFM-SECM nosecones, electronically connected and electrochemically sealed using several layers of an insulation varnish (RS 199-1480). Alternatively, for internal data acquisition, the AFM-SECM probes were mounted into probe cartridges (Fig. 49B), electronically connected and electrochemically sealed using several layers of an UV-curable encapsulant (Dymax 9001-E-V3.1) and insulation varnish (RS 199-1480) prior to installation into the pre-amplifier nosecone. Combined AFM-SECM measurements were performed in 10 mM $[Ru(NH_3)_6]Cl_3$ / 0.1 M KCl, using contact mode with a scan speed of 0.3 lines/s and 512 data points per line. Electrochemical data were acquired simultaneously at a tip bias of -500 mV vs. QAg/AgCl, if not stated otherwise, with an external potentiostat (CHI 832A) and correlated via an auxiliary input channel to the topographical data for external data acquisition or with the Picostat potentiostat and the integrated amplifier circuit for internal data acquisition. Prior to usage, solutions containing $[Ru(NH_3)_6]Cl_3$ were degassed at least for 15 min with Ar. Solutions containing $NaNO_2$ and NaCl were used as prepared.
For corrosion experiments the iron plates were prepared by grinding to a 4000 grit finish using a SiC lapping film, followed by a polishing step with 0.05 µm alumina

slurry. The surface was afterwards degreased with ethanol in an ultrasonic bath, subsequently rinsed with high purity water and dried under an argon gas stream.

10.4.4. Simulations

Mass transport and concentration profile calculations towards the AFM-SECM probe were simulated with COMSOL 4.2a (ComSol Multiphysics GmbH, Göttingen, Germany) using a 3D replica as described in section 10.3.4. For the numerical calculations only diffusion of nitrite towards the electrode was taken into account using a diffusion coefficient of D = 1.912e^{-6} cm^2/s [225]. A detailed description of the simulation can be found in section 10.2.4.

10.5. Chapter 7

10.5.1. Chemicals and solutions

Potassium hexacyanoferrate (II) trihydrat ($K_4[Fe(CN)_6]x3H_2O$) p.a., hexaamine-ruthenium (III) chloride ($[Ru(NH_3)_6]Cl_3$) p.a., potassium chloride (KCl) p.a., dopamine hydrochloride and chloroquine diphosphate salt were purchased from Sigma-Aldrich (Steinheim, Germany). L(+)-ascorbic acid p.a. was purchased from Carl Roth GmbH (Karlsruhe. Germany) and phosphate buffered saline (PBS) solution without Mg^{2+} and Ca^{2+} from Biochrom GmbH (Berlin, Germany). 1-palmitoyl-2-oleoyl-sn-glycero-3-phosphocholine (POPC) was purchased from Avanti Polar Lipids (Alabaster, AL, USA) as chloroform solution (25 mg/ml). 1-octadecanthiol, sulfuric acid 98% p.a., and hydrogen peroxide (H_2O_2; 30%) were purchased from Merck (Darmstadt, Germany).
Solutions for electrochemical measurements contained 10 mM $K_4[Fe(CN)_6]$ or 10 mM $[Ru(NH_3)_6]Cl_3$, respectively, and 0.1 M KCl as supporting electrolyte. Solutions for electrochemical measurements of the supported lipid membranes contained 10 mM $[Ru(NH_3)_6]Cl_3$ and 0.1 M KCl as supporting electrolyte, adjusted to pH = 6. Solutions for C2IIa incorporation contained 17.4 ng/µl C2IIa in PBS, adjusted to pH = 6, and solutions for toxin inhibition contained 200 µM chloroquine in PBS (pH = 6). Solutions for electrochemical treatment of BDD contained 2 M H_2SO_4. Test solutions for the detection of dopamine contained 10-1000 µM dopamine and 100 µM ascorbic acid in PBS solution at pH = 7.4. All solutions were prepared in Elga high purity water with a resistivity at 25°C of 18.2 MΩ·cm (Elga Labwater, VWS Deutschland GmbH, Celle, Germany), if not stated otherwise, and chemicals as purchased. Parylene-C for insulator deposition was obtained from Special Coating Systems Inc. (Indianapolis,

IN, USA) [182]. EPO-TEK H2OE silver conductive epoxy and Acheson silver DAG 1415 for electrochemical probe connection was purchased from Plano GmbH (Wetzlar, Germany), UV-light-curable encapsulant Dymax 9001-E-V3.1 for connection sealing from Dymax Europe GmbH (Wiesbaden, Germany), and insulation varnish RS 199-1480 from RS Components Ltd. (Corby, United Kingdom).

10.5.2. Apparatus

FIB microfabrication of combined AFM-SECM probes was performed with a DualBeam Quanta 3D FEG (FEI Company, Eindhoven, Netherlands), equipped with a Pt deposition gas injection system, using a custom made multi-orientation chip mounting device (see appendix 12.3.1). Electrochemical characterizations of the AFM-SECM probes were conducted with CHI potentiostat 660A or 842B (CH Instruments Inc., Austin, Texas, USA), and characterization of supported lipid membrane samples with a CHI potentiostat 440 (CH Instruments Inc., Austin, Texas, USA) or the electrochemistry module of a 5500 atomic force microscope (Keysight Technologies, Chandler, AZ, USA). Electrochemical experiments for dopamine detection using microelectrode arrays were performed using a CHI potentiostat 660A and a custom-made liquid cell for microelectrode array characterization (Fig. 89). Electrochemical characterization and measurements outside the AFM-SECM setup were performed in a three-electrode setup using an Ag/AgCl (sat.) reference electrode (ALS Co., Ltd, Tokyo, Japan), a Pt counter electrode and the sample/probe as working electrode. Approach curve measurements were performed with a 5500 atomic force microscope (Keysight Technologies, Chandler, AZ, USA), equipped with a SECM module (see chapter 6), located inside a faraday cage. For the electrochemical data acquisition the AFM-SECM systems used a three-electrode setup with a QAg/AgCl reference electrode, a Pt counter electrode, and either the AFM-SECM tip or the sample surface as working electrode. Parylene-C coating during the fabrication process was performed using a Parylene Deposition Unit PDS 2010 Labcoter 2 (Specialty Coating Systems Inc.; Indianapolis, IN, USA) [182]. For electrochemical treatment of BDD-AFM-SECM probes a Voltcraft plus VSP 2405 HE lab power supply (Conrad Electronic SE, Hirschau, Germany) with a two-electrode setup (working electrode: BDD-AFM-SECM probe; counter electrode: Pt-wire) and a salt-bridge filled with saturated potassium chloride solution connecting two separated sulfuric acid compartments was used (Fig. 32). For the preparation of the lipid

vesicles, used for the vesicle fusion to form supported lipid membranes, a Vortex Genie 2 (Scientific Industries; Bohemia, NY, USA) and a W140 Sonifier Cell Disruptor (Branson; Dietzenbach, Germany) was used. For electrochemical detection of dopamine and ascorbic acid at BDD integrated AFM-SECM probes a CHI 660C potentiostat was used in a three-electrode setup.

10.5.3. Procedures

For fabricating combined PtC-AFM-SECM probes, commercially available Si_xN_y probes (NP probes, Bruker Corp., Billerca, MA, USA) were coated with a conductive Au layer of approximately 100 nm, using shadow masks (comparable to those described in section 12.3.4), and subsequently insulated with Parylene-C. After Parylene-C deposition of approximately 800-1000 nm, the tip apex of the cantilever was removed by FIB-milling to access the Au layer embedded inside the layered structure of the modified cantilever (Fig. 93A). A PtC composite material was then deposited using a FIB-induced deposition process, by decomposing $C_9H_{16}Pt$ ((methylcyclopentadienyl) trimethyl platinum) adsorbed onto the substrate surface (Fig. 93B). After Pt deposition at 16 kV; 23 pA, a conductive AFM tip was reconstructed from the deposited material at 30 kV; 50 pA (Fig. 93C) following an adapted procedure from Knittel et al. [149].

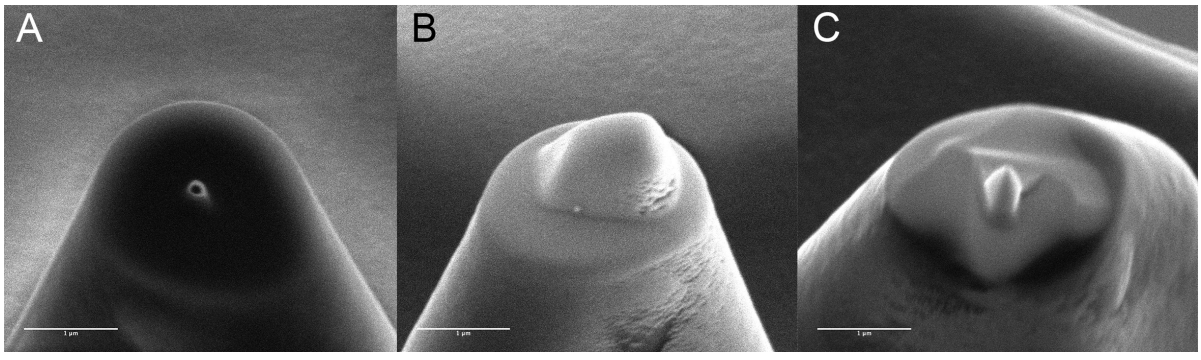

Fig. 93: SEM images of the PtC-AFM-SECM probe fabrication steps; A) Tip after accessing the Au layer; B) PtC deposition; C) Tip reconstruction via FIB-milling.

The PtC-AFM-SECM probes were electrochemically characterized and mounted onto AFM-SECM cartridges (Fig. 49B), electronically connected and electrochemically sealed using several layers of an UV-curable encapsulant (Dymax 9001-E-V3.1) and insulation varnish (RS 199-1480). Approach curves of different supported lipid membrane samples were recorded by recording I-t-curves while approaching the

sample surface with a speed of 0.6 µm/s from a distance of approximately 60 µm. During approach, the tip was biased at a potential of -350 to -500 mV vs. QAg/AgCl for reducing the redox mediator ($[Ru(NH_3)_6]Cl_3$) in solution above the supported lipid membrane. After surface contact of the PtC-AFM-SECM probe, the normalized current-distance curves can be obtained, using the snap-in point as zero-distance point and the current at a distance of 60 µm as $I_{t,\infty}$. If required, the I-t-curves used for obtaining the normalized approach curves were drift corrected using linear regression.

The supported hybrid lipid membranes (ODT-POPC) were formed by small unilamellar lipid vesicle fusion, which were produced by repetitive (20 times) sonication (30 s sonication; 90 s break) of multilamellar lipid vesicles at 0 °C [240] on a self-assembled 1-octadecanethiol layer. The multilamellar vesicles were formed inside a glass vial during slow evaporation of the chloroform of the lipid stock solution under nitrogen flow [240,241] and dissolution of the dried lipid in phosphate buffered saline, while shaking at room temperature [242].

For the self-assembly of the ODT layer gold-coated substrates were immersed for 24 h in a 20 mM ODT/EtOH solution and subsequently rinsed with EtOH and ultra-pure water. For vesicle fusion, the self-assembled ODT-coated gold substrates were immersed into 500 µl of the POPC vesicle solution (1 mg/ml) for 1 h at 60°C following a 30 min period at room temperature. The vesicle solution was then subsequently replaced with a $[Ru(NH_3)_6]Cl_3$ solution in 200 µl steps (25 steps) to ensure a complete solution exchange and an intact supported lipid membrane.

For recording SECM approach curves, different test solutions were added to the formed SLM maintaining the concentration of the $[Ru(NH_3)_6]Cl_3$ solution and the volume of the cell. For solution exchange experiments, 100 µl of the solution inside the AFM liquid cell were replaced with 100 µl of 10 mM $[Ru(NH_3)_6]Cl_3$ in PBS tempered to 37 °C. For the toxin incorporation 100 µl of the solution were exchanged by a 17.4 ng/µl C2IIa/PBS/10 mM $[Ru(NH_3)_6]Cl_3$ solution to maintain the redox mediator concentration, also tempered to 37 °C, leading to a C2IIa toxin concentration of 3.48 µg/ml. For the concentration series measurements, the replaced C2IIa/PBS solution contained a range of the C2IIa toxin leading to solution concentrations from 1.74 µg/ml to 27.84 µg/ml. For the toxin inhibition and chloroquine validation experiments, 3 µl of the 200 µM chloroquine solution was added to the liquid cell prior to recording the SECM approach curves.

The BDD-AFM-SECM probes for the detection of dopamine and ascorbic acid were fabricated according to the scheme outlined in section 10.2.3. Alternatively, 1-2 µm of the insulated tip apex was removed whenever tip-less AFM-SECM probes were used for electrochemical experiments (comparable to Fig. 93A). Top-mill microelectrode arrays were fabricated according to the scheme in section 10.1.3 with 30 kV; 15 nA; 50 ns. Amorphous carbon removal at the exposed BDD electrodes were performed by anodic treatment at a potential of +2.5 V for 1 min, followed by a cathodic treatment (hydrogen termination) at -12 V for 3 min. After the electrochemical treatment in 2 M sulfuric acid, the BDD electrodes were electrochemically characterized in 10 mM $K_4[Fe(CN)_6]$ / 0.1 M KCl solution. The BDD electrodes were immersed into ascorbic acid/PBS solutions, which were subsequently spiked with dopamine up to a concentration of 1 mM.

11. References

[1] C. Schleberger, H. Hochmann, H. Barth, K. Aktories, G. E. Schulz, *Structure and action of the binary C2 toxin from clostridium botulinum,* J. Mol. Biol., 364, **2006**, 705–715.

[2] A. P. Quist, A. Chand, S. Ramachandran, C. Daraio, S. Jin, R. Lal, *Atomic force microscopy imaging and electrical recording of lipid bilayers supported over microfabricated silicon chip nanopores: Lab-on-a-chip system for lipid membranes and ion channels,* Langmuir, 23, **2007**, 1375–1380.

[3] A. Davoodi, J. Pan, C. Leygraf, S. Norgren, *In situ investigation of localized corrosion of aluminum alloys in chloride solution using integrated EC-AFM/SECM techniques,* Electrochem. Solid-State Lett., 8, **2005**, B21–B24.

[4] H. Y. Liu, F. R. F. Fan, C. W. Lin, A. J. Bard, *Scanning electrochemical and tunneling ultramicroelectrode microscope for high-resolution examination of electrode surfaces in solution,* J. Am. Chem. Soc., 108, **1986**, 3838–3839.

[5] A. J. Bard, F. R. F. Fan, J. Kwak, O. Lev, *Scanning electrochemical microscopy. Introduction and principles,* Anal. Chem., 61, **1989**, 132–138.

[6] C. D. Frisbie, L. F. Rozsnyai, A. Noy, M. S. Wrighton, C. M. Lieber, *Functional group imaging by chemical force microscopy,* Science, 265, **1994**, 2071–2074.

[7] J. V. Macpherson, P. R. Unwin, *Combined scanning electrochemical-atomic force microscopy,* Anal. Chem., 72, **2000**, 276–285.

[8] C. Kranz, G. Friedbacher, B. Mizaikoff, A. Lugstein, J. Smoliner, E. Bertagnolli, *Integrating an ultramicroelectrode in an AFM cantilever: Combined technology for enhanced information,* Anal. Chem., 73, **2001**, 2491–2500.

[9] A. Anne, A. Chovin, C. Demaille, M. Lafouresse, *High-resolution mapping of redox-immunomarked proteins using electrochemical-atomic force microscopy in molecule touching mode.,* Anal. Chem., 83, **2011**, 7924–7932.

[10] Y. Takahashi, A. I. Shevchuk, P. Novak, Y. Murakami, H. Shiku, Y. E. Korchev, T. Matsue, *Simultaneous noncontact topography and electrochemical imaging by SECM/SICM featuring ion current feedback regulation,* J. Am. Chem. Soc., 132, **2010**, 10118–10126.

[11] C. A. Morris, C.-C. Chen, L. A. Baker, *Transport of redox probes through single pores measured by scanning electrochemical-scanning ion conductance microscopy (SECM-SICM),* The Analyst, 137, **2012**, 2933.

[12] M. Fujihira, H. Monobe, N. Yamamoto, H. Muramatsu, N. Chiba, K. Nakajima, T. Ataka, *Scanning near-field optical microscopy of fluorescent polystyrene spheres with a combined SNOM and AFM,* Ultramicroscopy, 61, **1995**, 271–277.

[13] A. Ueda, O. Niwa, K. Maruyama, Y. Shindo, K. Oka, K. Suzuki, *Neurite imaging of living PC12 cells with scanning electrochemical/near-field optical/atomic force microscopy,* Angew. Chem., Int. Ed., 46, **2007**, 8238–8241.

[14] Y. E. Korchev, M. Raval, M. J. Lab, J. Gorelik, C. R. W. Edwards, T. Rayment, D. Klenerman, *Hybrid scanning ion conductance and scanning near-field optical microscopy for the study of living cells,* Biophys. J., 78, **2000**, 2675–2679.

[15] Z. Guo-Hua, L. Ming-Fang, L. Ming-Li, *Differential pulse voltammetric determination of dopamine with the coexistence of ascorbic acid on boron-doped diamond surface,* Central Eur. J. Chem., 5, **2007**, 1114–1123.

[16] N. Spãtaru, B. V. Sarada, E. Popa, D. A. Tryk, A. Fujishima, *Voltammetric determination of L-cysteine at conductive diamond electrodes,* Anal. Chem., 73, **2001**, 514–519.

[17] H. Shin, P. J. Hesketh, B. Mizaikoff, C. Kranz, *Batch fabrication of atomic force microscopy probes with recessed integrated ring microelectrodes at a wafer level,* Anal. Chem., 79, **2007**, 4769–4777.

[18] W. B. Yang, F. X. Lü, Z. X. Cao, *Growth of nanocrystalline diamond protective coatings on quartz glass,* J. Appl. Phys., 91, **2002**, 10068–10073.

[19] A. Ogasawara, T. Inushima, T. Shiraishi, S. Ohya, S. Karasawa, H. Shiomi, *Optical and electrical investigation of boron-doped homoepitaxial diamond,* Diamond Relat. Mater., 6, **1997**, 835 – 838.

[20] J. K. Zak, J. E. Butler, G. M. Swain, *Diamond optically transparent electrodes: Demonstration of concept with ferri/ferrocyanide and methyl viologen,* Anal. Chem., 73, **2001**, 908–914.

[21] S. Matsumoto, Y. Sato, M. Kamo, N. Setaka, *Vapor deposition of diamond particles from methane,* Jpn. J. Appl. Phys., Part 2, 21, **1982**, 183–185.

[22] S. Matsumoto, Y. Sato, M. Tsutsumi, N. Setaka, *Growth of diamond particles from methane-hydrogen gas,* J. Mater. Sci., 17, **1982**, 3106–3112.

[23] M. Kamo, Y. Sato, S. Matsumoto, N. Setaka, *Diamond synthesis from gas phase in microwave plasma,* J. Cryst. Growth, 62, **1983**, 642–644.

[24] S. Matsumoto, *Chemical vapor deposition of diamond in RF glow discharge,* J. Mater. Sci. Lett., 4, **1985**, 600–602.

[25] S. Matsumoto, M. Hino, T. Kobayashi, *Synthesis of diamond films in a RF induction thermal plasma,* Appl. Phys. Lett., 51, **1987**, 737–739.

[26] Y. V. Pleskov, A. Y. Sakharova, M. D. Krotova, L. L. Bouilov, B. V. Spitsyn, *Photoelectrochemical properties of semiconductor diamond,* J. Electroanal. Chem., 228, **1987**, 19–27.

[27] A. Fujishima, T. N. Rao, E. Popa, B. V. Sarada, I. Yagi, D. A. Tryk, *Electroanalysis of dopamine and NADH at conductive diamond electrodes,* J. Electroanal. Chem., 473, **1999**, 179–185.

[28] E. Popa, H. Notsu, T. Miwa, D. A. Tryk, A. Fujishima, *Selective electrochemical detection of dopamine in the presence of ascorbic acid at anodized diamond thin film electrodes,* Electrochem. Solid-State Lett., 2, **1999**, 49–51.

[29] A. Suzuki, T. a Ivandini, K. Yoshimi, A. Fujishima, G. Oyama, T. Nakazato, N. Hattori, S. Kitazawa, Y. Einaga, *Fabrication, characterization, and application of boron-doped diamond microelectrodes for in vivo dopamine detection,* Anal. Chem., 79, **2007**, 8608–8615.

[30] K. L. Soh, W. P. Kang, J. L. Davidson, Y. M. Wong, D. E. Cliffel, G. M. Swain, *Diamond-derived ultramicroelectrodes designed for electrochemical analysis and bioanalyte sensing,* Diamond Relat. Mater., 17, **2008**, 900–905.

[31] W. Smirnov, N. Yang, R. Hoffmann, J. Hees, H. Obloh, W. Müller-Sebert, C. E. Nebel, *Integrated all-diamond ultramicroelectrode arrays: Optimization of faradaic and capacitive currents,* Anal. Chem., 83, **2011**, 7438–7443.

[32] R. Trouillon, D. O'Hare, *Comparison of glassy carbon and boron doped diamond electrodes: Resistance to biofouling,* Electrochim. Acta, 55, **2010**, 6586–6595.

[33] Y. L. Zhou, R. H. Tian, J. F. Zhi, *Amperometric biosensor based on tyrosinase immobilized on a boron-doped diamond electrode,* Biosens. Bioelectron., 22, **2007**, 822–828.

[34] H. Zhao, X. Bian, J. J. Galligan, G. M. Swain, *Electrochemical measurements of serotonin (5-HT) release from the guinea pig mucosa using continuous amperometry with a boron-doped diamond microelectrode,* Diamond Relat. Mater., 19, **2010**, 182–185.

[35] J. Hees, R. Hoffmann, A. Kriele, W. Smirnov, H. Obloh, K. Glorer, B. Raynor, R. Driad, N. Yang, O. A. Williams, C. E. Nebel, *Nanocrystalline diamond nanoelectrode arrays and ensembles,* ACS nano, 5, **2011**, 3339–3346.

[36] W. G. Eversole, *Synthesis of diamond,* U.S. Patent US 3030187, **1962**.

[37] W. G. Eversole, *Synthesis of diamond,* U.S. Patent US 3030188, **1962**.

[38] S. P. Chauhan, J. C. Angus, N. C. Gardner, *Kinetics of carbon deposition on diamond powder,* J. Appl. Phys., 47, **1976**, 4746–4754.

[39] D. J. Poferl, N. C. Gardner, J. C. Angus, *Growth of boron-doped diamond seed crystals by vapor deposition,* J. Appl. Phys., 44, **1973**, 1428–1434.

[40] J. Mort, D. Kuhman, M. Machonkin, M. Morgan, F. Jansen, K. Okumura, Y. M. LeGrice, R. J. Nemanich, *Boron doping of diamond thin films,* Appl. Phys. Lett., 55, **1989**, 1121–1123.

[41] N. Fujimori, H. Nakahata, T. Imai, *Properties of boron-doped epitaxial diamond films,* Jpn. J. Appl. Phys., Part 1, 29, **1990**, 824–827.

[42] R. Locher, J. Wagner, F. Fuchs, C. Wild, P. Hiesinger, P. Gonon, P. Koidl, *Boron doped diamond films: Electrical and optical characterization and the effect of compensating nitrogen,* Mater. Sci. Eng. B, 29, **1995**, 211–215.

[43] X. K. Zhang, J. G. Guo, Y. F. Yao, R. Wang, G. M. Chen, W. K. Zhou, S. Yu, *p-type doping of diamond films with a novel organoboron source,* Appl. Phys. A, 56, **1993**, 425–428.

[44] S. A. Grot, C. W. Hatfield, G. S. Gildenblat, A. R. Badzian, T. Badzian, *Electrical properties of selectively grown homoepitaxial diamond films,* Appl. Phys. Lett., 58, **1991**, 1542–1544.

[45] Y. Mitsuda, Y. Kojima, T. Yoshida, K. Akashi, *The growth of diamond in microwave plasma under low pressure,* J. Mater. Sci., 22, **1987**, 1557–1562.

[46] S. Iijima, Y. Aikawa, K. Baba, *Early formation of chemical vapor deposition diamond films,* Appl. Phys. Lett., 57, **1990**, 2646–2648.

[47] J. E. Butler, R. L. Woodin, L. M. Brown, P. Fallon, *Thin film diamond growth mechanism,* Phil. Trans. R. Soc. A, 342, **1993**, 209–224.

[48] M. A. Quiroz, E. R. Bandala, *Types of conducting diamond materials and their properties*, in: E. Brillas, C. A. Martinez-Huitle (Eds.), *Synthetic diamond films preparation, electrochemistry, characterization, and applications*, Hoboken, N.J.: Wiley, **2011**, pp. 57–75.

[49] C. E. Nebel, B. Rezek, D. Shin, H. Watanabe, *Surface electronic properties of H-terminated diamond in contact with adsorbates and electrolytes,* Phys. Status Solidi A, 203, **2006**, 3273–3298.

[50] A. Kraft, *Doped diamond: A compact review on a new, versatile electrode material,* Int. J. Electrochem. Sci., 2, **2007**, 355–385.

[51] Y. F. Tsay, K. P. Ananthanarayanan, P. J. Gielisse, S. S. Mitra, *Electrical conductivity of heavily doped diamond,* J. Appl. Phys., 43, **1972**, 3677–3682.

[52] K. Nishimura, K. Das, J. T. Glass, *Material and electrical characterization of polycrystalline boron-doped diamond films grown by microwave plasma chemical vapor deposition,* J. Appl. Phys., 69, **1991**, 3142–3148.

[53] E. Brillas, C. A. Martínez-Huitle, *Synthetic diamond films preparation, electrochemistry, characterization, and applications*. Hoboken, N.J.: Wiley, **2011**.

[54] C. E. Nebel, B. Rezek, D. Shin, H. Uetsuka, N. Yang, *Diamond for bio-sensor applications,* J. Phys. D: Appl. Phys., 40, **2007**, 6443–6466.

[55] H. B. Martin, A. Argoitia, U. Landau, A. B. Anderson, J. C. Angus, *Hydrogen and oxygen evolution on boron-doped diamond electrodes,* J. Electrochem. Soc., 143, **1996**, L133–L136.

[56] I. Yagi, H. Notsu, T. Kondo, D. a Tryk, A. Fujishima, *Electrochemical selectivity for redox systems at oxygen-terminated diamond electrodes,* J. Electroanal. Chem., 473, **1999**, 173–178.

[57] R. Hoffmann, A. Kriele, H. Obloh, J. Hees, M. Wolfer, W. Smirnov, N. Yang, C. E. Nebel, *Electrochemical hydrogen termination of boron-doped diamond,* Appl. Phys. Lett., 97, **2010**, 52103–52103.

[58] L. A. Hutton, J. G. Iacobini, E. Bitziou, R. B. Channon, M. E. Newton, J. V. Macpherson, *Examination of the factors affecting the electrochemical performance of oxygen-terminated polycrystalline boron-doped diamond electrodes,* Anal. Chem., 85, **2013**, 7230–7240.

[59] M. C. Granger, G. M. Swain, *The influence of surface interactions on the reversibility of ferri/ferrocyanide at boron-doped diamond thin-film electrodes,* J. Electrochem. Soc., 146, **1999**, 4551–4551.

[60] Y. Zhou, J. Zhi, *The application of boron-doped diamond electrodes in amperometric biosensors,* Talanta, 79, **2009**, 1189–1196.

[61] F. Maier, M. Riedel, B. Mantel, J. Ristein, L. Ley, *Origin of surface conductivity in diamond,* Phys. Rev. Lett., 85, **2000**, 3472–3475.

[62] J. Xu, M. C. Granger, Q. Chen, J. W. Strojek, T. E. Lister, G. M. Swain, *Boron-doped diamond thin-film electrodes,* Anal. Chem., 69, **1997**, 591A–597A.

[63] R. DeClements, G. M. Swain, T. Dallas, M. W. Holtz, R. D. Herrick, J. L. Stickney, *Electrochemical and surface structural characterization of hydrogen plasma treated glassy carbon electrodes,* Langmuir, 12, **1996**, 6578–6586.

[64] G. M. Swain, T. Kuwana, *Anodic fracturing and vacuum heat treated annealing of pitch-based carbon fibers,* Anal. Chem., 64, **1992**, 565–568.

[65] H. V. Patten, S. C. S. Lai, J. V. Macpherson, P. R. Unwin, *Active sites for outer-sphere, inner-sphere, and complex multistage electrochemical reactions at polycrystalline boron-doped diamond electrodes (pBDD) revealed with scanning electrochemical cell microscopy (SECCM),* Anal. Chem., 84, **2012**, 5427–5432.

[66] E. Vanhove, J. de Sanoit, J. C. Arnault, S. Saada, C. Mer, P. Mailley, P. Bergonzo, M. Nesladek, *Stability of H-terminated BDD electrodes: An insight into the influence of the surface preparation,* Phys. Status Solidi A, 204, **2007**, 2931–2939.

[67] B. Marselli, J. Garcia-Gomez, P.-A. Michaud, M. A. Rodrigo, C. Comninellis, *Electrogeneration of hydroxyl radicals on boron-doped diamond electrodes,* J. Electrochem. Soc., 150, **2003**, D79–D83.

[68] R. Andreozzi, V. Caprio, A. Insola, R. Marotta, *Advanced oxidation processes (AOP) for water purification and recovery,* Catal. Today, 53, **1999**, 51–59.

[69] N. Katsuki, E. Takahashi, M. Toyoda, T. Kurosu, M. Iida, S. Wakita, Y. Nishiki, T. Shimamune, *Water electrolysis using diamond thin-film electrodes,* J. Electrochem. Soc., 145, **1998**, 2358–2362.

[70] P.-A. Michaud, E. Mahe, W. Haenni, A. Perret, C. Comninellis, *Preparation of peroxodisulfuric acid using boron-doped diamond thin film electrodes,* Electrochem. Solid-State Lett., 3, **2000**, 77–79.

[71] M. Chiku, T. A. Ivandini, A. Kamiya, A. Fujishima, Y. Einaga, *Direct electrochemical oxidation of proteins at conductive diamond electrodes,* J. Electroanal. Chem., 612, **2008**, 201–207.

[72] S. Xie, G. Shafer, C. G. Wilson, H. B. Martin, *In vitro adenosine detection with a diamond-based sensor,* Diamond Relat. Mater., 15, **2006**, 225–228.

[73] Y. Xu, B. J. Venton, *Rapid determination of adenosine deaminase kinetics using fast-scan cyclic voltammetry,* Phys. Chem. Chem. Phys., 12, **2010**, 10027–10032.

[74] M. C. Granger, J. Xu, J. W. Strojek, G. M. Swain, *Polycrystalline diamond electrodes: basic properties and applications as amperometric detectors in flow injection analysis and liquid chromatography,* Anal. Chim. Acta, 397, **1999**, 145–161.

[75] D. Sopchak, B. Miller, R. Kalish, Y. Avyigal, X. Shi, *Dopamine and ascorbate analysis at hydrodynamic electrodes of boron doped diamond and nitrogen incorporated tetrahedral amorphous carbon,* Electroanalysis, 14, **2002**, 473–478.

[76] P. S. Siew, K. P. Loh, W. C. Poh, H. Zhang, *Biosensing properties of nanocrystalline diamond film grown on polycrystalline diamond electrodes,* Diamond Relat. Mater., 14, **2005**, 426–431.

[77] J. Lee, S.-M. Park, *Direct electrochemical assay of glucose using boron-doped diamond electrodes,* Anal. Chim. Acta, 545, **2005**, 27–32.

[78] K. P. Loh, S. Liang Zhao, W. De Zhang, *Diamond and carbon nanotube glucose sensors based on electropolymerization,* Diamond Relat. Mater., 13, **2004**, 1075–1079.

[79] J. Wu, Y. Qu, *Mediator-free amperometric determination of glucose based on direct electron transfer between glucose oxidase and an oxidized boron-doped diamond electrode,* Anal. Bioanal. Chem., 385, **2006**, 1330–1335.

[80] J. Zhao, D. Wu, J. Zhi, *A direct electrochemical method for diabetes diagnosis based on as-prepared boron-doped nanocrystalline diamond thin film electrodes,* J. Electroanal. Chem., 626, **2009**, 98–102.

[81] J. Zhao, L. Wu, J. Zhi, *Non-enzymatic glucose detection using as-prepared boron-doped diamond thin-film electrodes,* Analyst, 134, **2009**, 794–799.

[82] D. Luo, L. Wu, J. Zhi, *Fabrication of boron-doped diamond nanorod forest electrodes and their application in nonenzymatic amperometric glucose biosensing,* ACS nano, 3, **2009**, 2121–2128.

[83] T. Hayashi, I. Sakurada, K. Honda, S. Motohashi, K. Uchikura, *Electrochemical detection of sugar-related compounds using boron-doped diamond electrodes,* Anal. Sci., 28, **2012**, 127–133.

[84] B. V. Sarada, T. N. Rao, D. A. Tryk, A. Fujishima, *Electrochemical oxidation of histamine and serotonin at highly boron-doped diamond electrodes,* Anal. Chem., 72, **2000**, 1632–1638.

[85] J. M. Halpern, S. Xie, G. P. Sutton, B. T. Higashikubo, C. a. Chestek, H. Lu, H. J. Chiel, H. B. Martin, *Diamond electrodes for neurodynamic studies in Aplysia californica,* Diamond Relat. Mater., 15, **2006**, 183–187.

[86] J. Stotter, J. Zak, Z. Behler, Y. Show, G. M. Swain, *Optical and electrochemical properties of optically transparent, boron-doped diamond thin films deposited on quartz,* Anal. Chem., 74, **2002**, 5924–5930.

[87] H. B. Martin, P. W. Morrison Jr, *Application of a diamond thin film as a transparent electrode for in situ infrared spectroelectrochemistry,* Electrochem. Solid-State Lett., 4, **2001**, E17–E20.

[88] D. Neubauer, J. Scharpf, A. Pasquarelli, B. Mizaikoff, C. Kranz, *Combined in situ atomic force microscopy and infrared attenuated total reflection spectroelectrochemistry,* Analyst, 138, **2013**, 6746–6752.

[89] A. Avdic, A. Lugstein, M. Wu, B. Gollas, I. Pobelov, T. Wandlowski, K. Leonhardt, G. Denuault, E. Bertagnolli, *Fabrication of cone-shaped boron doped diamond and gold nanoelectrodes for AFM-SECM,* Nanotechnology, 22, **2011**, 145306–145306.

[90] G. Haugstad, *Overview of AFM*, in: G. Haugstad (Eds.), *Understanding atomic force microscopy: Basic modes for advanced applications*, Oxford: Wiley, **2011**, pp. 1–32.

[91] A. M. Baró, R. G. Reifenberger, *Atomic force microscopy in liquid: Biological applications*. Weinheim: Wiley-VCH, **2010**.

[92] I. Schmitz, M. Schreiner, G. Friedbacher, M. Grasserbauer, *Phase imaging as an extension to tapping mode AFM for the identification of material properties on humidity-sensitive surfaces,* Appl. Surf. Sci., 115, **1997**, 190–198.

[93] K. Babcock, C. Prater, *Phase imaging: Beyond topography,* Bruker Application Note, **2010**.

[94] A. Eifert, C. Kranz, *Hyphenating atomic force microscopy,* Anal. Chem., 86, **2014**, 5190–5200.

[95] E. Hecht, K. Thompson, M. Frick, O. H. Wittekindt, P. Dietl, B. Mizaikoff, C. Kranz, *Combined atomic force microscopy–fluorescence microscopy: Analyzing exocytosis in alveolar type II cells,* Anal. Chem., 84, **2012**, 5716–5722.

[96] J. V. Chacko, F. C. Zanacchi, A. Diaspro, *Probing cytoskeletal structures by coupling optical superresolution and AFM techniques for a correlative approach,* Cytoskeleton, 70, **2013**, 729–740.

[97] P. L. Stiles, J. A. Dieringer, N. C. Shah, R. P. Van Duyne, *Surface-enhanced Raman spectroscopy,* Annu. Rev. Anal. Chem., 1, **2008**, 601–626.

[98] J. Łojewska, A. Knapik, P. Jodłowski, T. Łojewski, A. Kołodziej, *Topography and morphology of multicomponent catalytic materials based on Co, Ce and Pd oxides deposited on metallic structured carriers studied by AFM/Raman interlaced microscopes,* Catal. Today, 216, **2013**, 11–17.

[99] M. S. Anderson, S. D. Gaimari, *Raman-atomic force microscopy of the ommatidial surfaces of Dipteran compound eyes,* J. Struct. Biol., 142, **2003**, 364–368.

[100] M. Brucherseifer, C. Kranz, B. Mizaikoff, *Combined in situ atomic force microscopy-infrared-attenuated total reflection spectroscopy,* Anal. Chem., 79, **2007**, 8803–8806.

[101] J. E. Verity, N. Chhabra, K. Sinnathamby, C. M. Yip, *Tracking molecular interactions in membranes by simultaneous ATR-FTIR-AFM,* Biophys. J., 97, **2009**, 1225–1231.

[102] I. Amenabar, S. Poly, W. Nuansing, E. H. Hubrich, A. A. Govyadinov, F. Huth, R. Krutokhvostov, L. Zhang, M. Knez, J. Heberle, A. M. Bittner, R. Hillenbrand, *Structural analysis and mapping of individual protein complexes by infrared nanospectroscopy,* Nat. Commun., 4, **2013**, 1–9.

[103] A. J. Bard, *Introduction and principles*, in: A. J. Bard, M. V. Mirkin (Eds.), *Scanning electrochemical microscopy*, 2nd ed., New York: CRC Press, **2012**, pp. 1–14.

[104] R. M. Wightman, *Microvoltammetric electrodes,* Anal. Chem., 53, **1981**, 1125A–1134A.

[105] D. O. Wipf, R. M. Wightman, *Voltammetry with microvoltammetric electrodes in resistive solvents under linear diffusion conditions,* Anal. Chem., 62, **1990**, 98–102.

[106] A. J. Bard, L. R. Faulkner, *Basic potential step methods*, in: A. J. Bard, L. R. Faulkner (Eds.), *Elechtrochemical methods: Fundamentals and applications*, 2nd ed., John Wiley & Sons, Inc., **2001**, pp. 156–225.

[107] Y. Saito, *A theoretical study on the diffusion current at the stationary electrodes of circular and narrow band types,* Rev. Polarogr., 15, **1968**, 177–187.

[108] M. V. Mirkin, F.-R. F. Fan, A. J. Bard, *Scanning electrochemical microscopy part 13. Evaluation of the tip shapes of nanometer size microelectrodes,* J. Electroanal. Chem., 328, **1992**, 47–62.

[109] M. Arca, A. J. Bard, B. R. Horrocks, T. C. Richards, D. A. Treichel, *Advances in scanning electrochemical microscopy,* Analyst, 119, **1994**, 719–726.

[110] J. Kwak, A. J. Bard, *Scanning electrochemical microscopy. Theory of the feedback mode,* Anal. Chem., 61, **1989**, 1221–1227.

[111] R. C. Engstrom, M. Weber, D. J. Wunder, R. Burgess, S. Winquist, *Measurements within the diffusion layer using a microelectrode probe,* Anal. Chem., 58, **1986**, 844–848.

[112] R. C. Engstrom, T. Meaney, R. Tople, R. M. Wightman, *Spatiotemporal description of the diffusion layer with a microelectrode probe,* Anal. Chem., 59, **1987**, 2005–2010.

[113] D. H. Craston, C. W. Lin, A. J. Bard, *High resolution deposition of silver in nafion films with the scanning tunneling microscope,* J. Electrochem. Soc., 135, **1988**, 785–785.

[114] K. B. Holt, A. J. Bard, Y. Show, G. M. Swain, *Scanning electrochemical microscopy and conductive probe atomic force microscopy studies of hydrogen-terminated boron-doped diamond electrodes with different doping levels,* J. Phys. Chem. B, 108, **2004**, 15117–15127.

[115] N. R. Wilson, S. L. Clewes, M. E. Newton, P. R. Unwin, J. V. Macpherson, *Impact of grain-dependent boron uptake on the electrochemical and electrical properties of polycrystalline boron doped diamond electrodes,* J. Phys. Chem. B, 110, **2006**, 5639–5646.

[116] C. Dincer, E. Laubender, J. Hees, C. E. Nebel, G. Urban, J. Heinze, *SECM detection of single boron doped diamond nanodes and nanoelectrode arrays using phase-operated shear force technique,* Electrochem. Commun., 24, **2012**, 123–127.

[117] C. Gabrielli, S. Joiret, M. Keddam, H. Perrot, N. Portail, P. Rousseau, V. Vivier, *A SECM assisted EQCM study of iron pitting,* Electrochim. Acta, 52, **2007**, 7706–7714.

[118] K. Eckhard, T. Erichsen, M. Stratmann, W. Schuhmann, *Frequency-dependent alternating-current scanning electrochemical microscopy (4D AC-SECM) for local visualisation of corrosion sites,* Chem. Eur. J., 14, **2008**, 3968–3976.

[119] S. Amemiya, A. J. Bard, *Scanning electrochemical microscopy. 40. Voltammetric ion-selective micropipet electrodes for probing ion transfer at bilayer lipid membranes,* Anal. Chem., 72, **2000**, 4940–4948.

[120] A. Hengstenberg, A. Blochl, I. D. Dietzel, W. Schuhmann, *Spatially resolved detection of neurotransmitter secretion from individual cells by means of scanning electrochemical microscopy,* Angew. Chem., Int. Ed., 40, **2001**, 905–908.

[121] J. Abbou, C. Demaille, M. Druet, J. Moiroux, *Fabrication of submicrometer-sized gold electrodes of controlled geometry for scanning electrochemical-atomic force microscopy,* Anal. Chem., 74, **2002**, 6355–6363.

[122] R. D. Rodriguez, A. Anne, E. Cambril, C. Demaille, *Optimized hand fabricated AFM probes for simultaneous topographical and electrochemical tapping mode imaging,* Ultramicroscopy, 111, **2011**, 973–981.

[123] M. R. Gullo, P. L. T. M. Frederix, T. Akiyama, A. Engel, N. F. deRooij, U. Staufer, *Characterization of microfabricated probes for combined atomic force and high-resolution scanning electrochemical microscopy,* Anal. Chem., 78, **2006**, 5436–5442.

[124] M. A. Derylo, K. C. Morton, L. A. Baker, *Parylene insulated probes for scanning electrochemical-atomic force microscopy,* Langmuir, 27, **2011**, 13925–13930.

[125] P. S. Dobson, J. M. R. Weaver, M. N. Holder, P. R. Unwin, J. V. Macpherson, *Characterization of batch-microfabricated scanning electrochemical-atomic force microscopy probes,* Anal. Chem., 77, **2005**, 424–434.

[126] R. J. Fasching, S. J. Bai, T. Fabian, F. B. Prinz, *Nanoscale electrochemical probes for single cell analysis,* Microelectron. Eng., 83, **2006**, 1638–1641.

[127] R. J. Fasching, Y. Tao, F. B. Prinz, *Cantilever tip probe arrays for simultaneous SECM and AFM analysis,* Sens. Actuators, B, 108, **2005**, 964–972.

[128] Y. Hirata, S. Yabuki, F. Mizutani, *Application of integrated SECM ultra-micro-electrode and AFM force probe to biosensor surfaces,* Bioelectrochemistry, 63, **2004**, 217–224.

[129] A. J. Wain, D. Cox, S. Zhou, A. Turnbull, *High-aspect ratio needle probes for combined scanning electrochemical microscopy — atomic force microscopy,* Electrochem. Commun., 13, **2011**, 78–81.

[130] A. Kueng, C. Kranz, A. Lugstein, E. Bertagnolli, B. Mizaikoff, *Integrated AFM–SECM in tapping mode: Simultaneous topographical and electrochemical imaging of enzyme activity,* Angew. Chem., Int. Ed., 42, **2003**, 3238–3240.

[131] J.-S. Moon, H. Shin, B. Mizaikoff, C. Kranz, *Bitmap-assisted focused ion beam fabrication of combined atomic force scanning electrochemical microscopy probes,* J. Korean Phys. Soc., 51, **2007**, 920–924.

[132] J. Wiedemair, N. Menegazzo, J. Pikarsky, K. S. Booksh, B. Mizaikoff, C. Kranz, *Novel electrode materials based on ion beam induced deposition of platinum carbon composites,* Electrochim. Acta, 55, **2010**, 5725–5732.

[133] M. Salomo, S. E. Pust, G. Wittstock, E. Oesterschulze, *Integrated cantilever probes for SECM/AFM characterization of surfaces,* Microelectron. Eng., 87, **2010**, 1537–1539.

[134] E. Lee, M. Kim, J. Seong, H. Shin, G. Lim, *An L-shaped nanoprobe for scanning electrochemical microscopy–atomic force microscopy,* Phys. Status Solidi RRL, 7, **2013**, 406–409.

[135] A. J. Bard, G. Denuault, C. Lee, D. Mandler, D. O. Wipf, *Scanning electrochemical microscopy-a new technique for the characterization and modification of surfaces,* Acc. Chem. Res., 23, **1990**, 357–363.

[136] F. R. F. Fan, A. J. Bard, P. He, *Instrumentation*, in: A. J. Bard, M. V. Mirkin (Eds.), *Scanning electrochemical microscopy*, CRC Press, **2012**, pp. 15–23.

[137] M. Ludwig, C. Kranz, W. Schuhmann, H. E. Gaub, *Topography feedback mechanism for the scanning electrochemical microscope based on hydrodynamic forces between tip and sample,* Rev. Sci. Instrum., 66, **1995**, 2857–2860.

[138] P. I. James, L. F. Garfias-Mesias, P. J. Moyer, W. H. Smyrl, *Scanning electrochemical microscopy with simultaneous independent topography,* J. Electrochem. Soc., 145, **1998**, L64–L66.

[139] A. Hengstenberg, C. Kranz, W. Schuhmann, *Facilitated tip-positioning and applications of non-electrode tips in scanning electrochemical microscopy using a shear force based constant-distance mode,* Chem. Eur. J., 6, **2000**, 1547–1554.

[140] E. Betzig, P. L. Finn, J. S. Weiner, *Combined shear force and near-field scanning optical microscopy,* Appl. Phys. Lett., 60, **1992**, 2484–2484.

[141] R. Toledo-Crow, P. C. Yang, Y. Chen, M. Vaez-Iravani, *Near-field differential scanning optical microscope with atomic force regulation,* Appl. Phys. Lett., 60, **1992**, 2957–2959.

[142] H. Shiku, R. C. Dunn, *Near-field scanning optical microscopy,* Anal. Chem., 71, **1999**, 23A–29A.

[143] A. R. Kucernak, P. B. Chowdhury, C. P. Wilde, G. H. Kelsall, Y. Y. Zhu, D. E. Williams, *Scanning electrochemical microscopy of a fuel-cell electrocatalyst deposited onto highly oriented pyrolytic graphite,* Electrochim. Acta, 45, **2000**, 4483–4491.

[144] Y. Takahashi, Y. Hirano, T. Yasukawa, H. Shiku, H. Yamada, T. Matsue, *Topographic, electrochemical, and optical images captured using standing approach mode scanning electrochemical/optical microscopy,* Langmuir, 22, **2006**, 10299–10306.

[145] A. Lesch, D. Momotenko, F. Cortés-Salazar, I. Wirth, U. M. Tefashe, F. Meiners, B. Vaske, H. H. Girault, G. Wittstock, *Fabrication of soft gold microelectrode arrays as probes for scanning electrochemical microscopy,* J. Electroanal. Chem., 666, **2012**, 52–61.

[146] J. Abbou, A. Anne, C. Demaille, *Probing the structure and dynamics of end-grafted flexible polymer chain layers by combined atomic force-electrochemical microscopy. Cyclic voltammetry within nanometer-thick macromolecular poly(ethylene glycol) layers,* J. Am. Chem. Soc., 126, **2004**, 10095–10108.

[147] A. Kueng, C. Kranz, A. Lugstein, E. Bertagnolli, B. Mizaikoff, *AFM-tip-integrated amperometric microbiosensors: High-resolution imaging of membrane transport,* Angew. Chem., Int. Ed., 44, **2005**, 3419–3422.

[148] C. dos S. Riccardi, C. Kranz, J. Kowalik, H. Yamanaka, B. Mizaikoff, M. Josowicz, *Label-free DNA detection of hepatitis C virus based on modified conducting polypyrrole films at microelectrodes and atomic force microscopy tip-integrated electrodes,* Anal. Chem., 80, **2008**, 237–245.

[149] P. Knittel, M. J. Higgins, C. Kranz, *Nanoscopic polypyrrole AFM–SECM probes enabling force measurements under potential control,* Nanoscale, 6, **2014**, 2255–2260.

[150] A. Davoodi, J. Pan, C. Leygraf, S. Norgren, *Probing of local dissolution of Al-alloys in chloride solutions by AFM and SECM,* Appl. Surf. Sci., 252, **2006**, 5499–5503.

[151] A. Davoodi, J. Pan, C. Leygraf, S. Norgren, *Integrated AFM and SECM for in situ studies of localized corrosion of Al alloys,* Electrochim. Acta, 52, **2007**, 7697–7705.

[152] J. V. Macpherson, *A practical guide to using boron doped diamond in electrochemical research,* Phys. Chem. Chem. Phys., 17, **2014**, 2935–2949.

[153] T. Yano, *Electrochemical behavior of highly conductive boron-doped diamond electrodes for oxygen reduction in alkaline solution,* J. Electrochem. Soc., 145, **1998**, 1870–1876.

[154] M. Fryda, T. Matthée, S. Mulcahy, A. Hampel, L. Schäfer, I. Tröster, *Fabrication and application of Diachem® electrodes,* Diamond Relat. Mater., 12, **2003**, 1950–1956.

[155] E. Y. Zarechnaya, E. I. Isaev, S. I. Simak, Y. K. Vekilov, L. S. Dubrovinsky, N. A. Dubrovinskaia, I. A. Abrikosov, *Ground-state properties of boron-doped diamond,* JETP, 106, **2008**, 781–787.

[156] F. Bouamrane, A. Tadjeddine, J. E. Butler, R. Tenne, C. Lévy-Clément, *Electrochemical study of diamond thin films in neutral and basic solutions of nitrate,* J. Electroanal. Chem., 405, **1996**, 95–99.

[157] P. Y. Lim, F. Y. Lin, H. C. Shih, V. G. Ralchenko, V. P. Varnin, Y. V. Pleskov, S. F. Hsu, S. S. Chou, P. L. Hsu, *Improved stability of titanium based boron-doped chemical vapor deposited diamond thin-film electrode by modifying titanium substrate surface,* Thin Solid Films, 516, **2008**, 6125–6132.

[158] J. W. Strojek, M. C. Granger, G. M. Swain, T. Dallas, M. W. Holtz, *Enhanced signal-to-background ratios in voltammetric measurements made at diamond thin-film electrochemical interfaces,* Anal. Chem., 68, **1996**, 2031–2037.

[159] N. Triroj, P. Jaroenapibal, H. Shi, J. I. Yeh, R. Beresford, *Microfluidic chip-based nanoelectrode array as miniaturized biochemical sensing platform for prostate-specific antigen detection,* Biosens. Bioelectron., 26, **2011**, 2927–2933.

[160] R. G. Compton, J. S. Foord, F. Marken, *Electroanalysis at diamond-like and doped-diamond electrodes,* Electroanalysis, 15, **2003**, 1349–1363.

[161] M. N. Latto, G. Pastor-Moreno, D. J. Riley, *The influence of doping levels and surface termination on the electrochemistry of polycrystalline diamond,* Electroanalysis, 16, **2004**, 434–441.

[162] J. Hu, K. B. Holt, J. S. Foord, *Focused ion beam fabrication of boron-doped diamond ultramicroelectrodes,* Anal. Chem., 81, **2009**, 5663–5670.

[163] Y. Pleskov, *Electrochemistry of diamond*, in: E. Brillas, C. A. Martinez-Huitle (Eds.), *Synthetic Diamond Films*, John Wiley & Sons, Inc. Hoboken, N. J, **2011**, pp. 79–108.

[164] N. Yang, C. E. Nebel, *DNA-modified diamond films*, in: E. Brillas, C. A. Martinez-Huitle (Eds.), *Synthetic Diamond Films*, John Wiley & Sons, Inc. Hoboken, N. J, **2011**, pp. 551–619.

[165] R. Hoffmann, A. Kriele, H. Obloh, N. Tokuda, W. Smirnov, N. Yang, C. E. Nebel, *The creation of a biomimetic interface between boron-doped diamond and immobilized proteins,* Biomaterials, 32, **2011**, 7325–7332.

[166] Y. Einaga, *Diamond electrodes for electrochemical analysis,* J. Appl. Electrochem., 40, **2010**, 1807–1816.

[167] G. R. Salazar-Banda, L. S. Andrade, P. a. P. Nascente, P. S. Pizani, R. C. Rocha-Filho, L. a. Avaca, *On the changing electrochemical behaviour of boron-doped diamond surfaces with time after cathodic pre-treatments,* Electrochim. Acta, 51, **2006**, 4612–4619.

[168] J. H. T. Luong, K. B. Male, J. D. Glennon, *Boron-doped diamond electrode: Synthesis, characterization, functionalization and analytical applications,* Analyst, 134, **2009**, 1965–1979.

[169] W. Smirnov, A. Kriele, N. Yang, C. E. Nebel, *Aligned diamond nano-wires: Fabrication and characterisation for advanced applications in bio- and electrochemistry,* Diamond Relat. Mater., 19, **2010**, 186–189.

[170] P. Olivero, S. Rubanov, P. Reichard, S. Huntington, B. Gibson, J. Salzman, S. Prawer, D. Jamieson, *Three-dimensional device fabrication in monocrystalline diamond using FIB and a novel lift-off technique,* Microsc. Microanal., 11, **2005**, 856–857.

[171] T. J. Stark, G. M. Shedd, J. Vitarelli, D. P. Griffis, P. E. Russell, *H_2O enhanced focused ion beam micromachining,* J. Vac. Sci. Technol. B, 13, **1995**, 2565–2569.

[172] A. Eifert, P. Langenwalter, J. Higl, M. Lindén, C. E. Nebel, B. Mizaikoff, C. Kranz, *Focused ion beam (FIB)-induced changes in the electrochemical behavior of boron-doped diamond (BDD) electrodes,* Electrochim. Acta, 130, **2014**, 418–425.

[173] A. Stanishevsky, *Patterning of diamond and amorphous carbon films using focused ion beams,* Thin Solid Films, 398,–399, **2001**, 560–565.

[174] D. P. Adams, M. J. Vasile, T. M. Mayer, V. C. Hodges, *Focused ion beam milling of diamond: Effects of H_2O on yield, surface morphology and microstructure,* J. Vac. Sci. Technol. B, 21, **2003**, 2334–2343.

[175] Q. Min, M. J. L. Santos, E. M. Girotto, A. G. Brolo, R. Gordon, *Localized raman enhancement from a double-hole nanostructure in a metal film,* J. Phys. Chem. C, 112, **2008**, 15098–15101.

[176] P. Olivero, S. Rubanov, P. Reichart, B. C. Gibson, S. T. Huntington, J. R. Rabeau, A. D. Greentree, J. Salzman, D. Moore, D. N. Jamieson, S. Prawer, *Characterization of three-dimensional microstructures in single-crystal diamond,* Diamond Relat. Mater., 15, **2006**, 1614–1621.

[177] H. Gnaser, B. Reuscher, A. Brodyanski, *Focused ion beam implantation of Ga in nanocrystalline diamond: Fluence-dependent retention and sputtering,* Nucl. Instrum. Methods Phys. Res., Sect. B, 266, **2008**, 1666–1670.

[178] I. Bayn, A. Bolker, C. Cytermann, B. Meyler, V. Richter, J. Salzman, R. Kalish, *Diamond processing by focused ion beam—surface damage and recovery,* Appl. Phys. Lett., 99, **2011**, 183109–183109.

[179] P. Chen, R. L. McCreery, *Control of electron transfer kinetics at glassy carbon electrodes by specific surface modification,* Anal. Chem., 68, **1996**, 3958–3965.

[180] S. Rubanov, A. Suvorova, *Ion implantation in diamond using 30keV Ga^+ focused ion beam,* Diamond Relat. Mater., 20, **2011**, 1160–1164.

[181] B. Z. Kupfer, R. K. Ahmad, A. Zainal, R. B. Jackman, *Fabrication and characterisation of triangle-faced single crystal diamond micro-cantilevers,* Diamond Relat. Mater., 19, **2010**, 742–747.

[182] A. Eifert, W. Smirnov, S. Frittmann, C. E. Nebel, B. Mizaikoff, C. Kranz, *Atomic force microscopy probes with integrated boron doped diamond electrodes: Fabrication and application,* Electrochem. Commun., 25, **2012**, 30–34.

[183] M. C. Granger, M. Witek, J. Xu, J. Wang, M. Hupert, A. Hanks, M. D. Koppang, J. E. Butler, G. Lucazeau, M. Mermoux, J. W. Strojek, G. M. Swain, *Standard electrochemical behavior of high-quality, boron-doped polycrystalline diamond thin-film electrodes,* Anal. Chem., 72, **2000**, 3793–3804.

[184] R. L. McCreery, *Advanced carbon electrode materials for molecular electrochemistry,* Chem. Rev., 108, **2008**, 2646–2687.

[185] S. Ferro, A. De Battisti, *Electron transfer reactions at conductive diamond electrodes,* Electrochim. Acta, 47, **2002**, 1641–1649.

[186] P. Chen, M. A. Fryling, R. L. McCreery, *Electron transfer kinetics at modified carbon electrode surfaces: The role of specific surface sites,* Anal. Chem., 67, **1995**, 3115–3122.

[187] R. F. Teófilo, H. J. Ceragioli, A. C. Peterlevitz, L. M. Silva, F. S. Damos, M. M. C. Ferreira, V. Baranauskas, L. T. Kubota, *Improvement of the electrochemical properties of "as-grown" boron-doped polycrystalline diamond electrodes deposited on tungsten wires using ethanol,* J. Solid State Electrochem., 11, **2007**, 1449–1457.

[188] N. Yao, *Introduction to the focused ion beam system*, in: N. Yao (Eds.), *Focused ion beam systems: Basics and applications*, Cambridge University Press Cambridge, UK, and New York, **2007**, pp. 1–30.

[189] N. Imanishi, *Interaction of ions with matter*, in: N. Yao (Eds.), *Focused ion beam systems: Basics and applications*, Cambridge University Press Cambridge, UK, and New York, **2007**, pp. 31–66.

[190] A. A. Tseng, *Fabrication of nanoscale structures using ion beams*, in: N. Yao (Eds.), *Focused ion beam systems: Basics and applications*, Cambridge University Press Cambridge, UK, and New York, **2007**, pp. 187–214.

[191] R. Brunetto, G. A. Baratta, G. Strazzulla, *Amorphization of diamond by ion irradiation: A Raman study,* J. Phys.: Conf. Ser., 6, **2005**, 120–125.

[192] A. J. Bard, L. R. Faulkner, *Kinetics of electrode reactions*, in: A. J. Bard, L. R. Faulkner (Eds.), *Elechtrochemical methods: Fundamentals and applications*, 2nd ed., John Wiley & Sons, Inc., **2001**.

[193] C. Mößner, P. Grant, H. Tran, G. Clarke, D. J. Lockwood, H. J. Labbé, B. Mason, I. Sproule, *Characterization of diamond-like carbon by Raman spectroscopy, {XPS} and optical constants,* Thin Solid Films, 317, **1998**, 397 – 401.

[194] S. Prawer, K. W. Nugent, D. N. Jamieson, J. O. Orwa, L. A. Bursill, J. L. Peng, *The Raman spectrum of nanocrystalline diamond,* Chem. Phys. Lett., 332, **2000**, 93–97.

[195] P. W. May, W. J. Ludlow, M. Hannaway, P. J. Heard, J. A. Smith, K. N. Rosser, *Raman and conductivity studies of boron-doped microcrystalline diamond, facetted nanocrystalline diamond and cauliflower diamond films,* Diamond Relat. Mater., 17, **2008**, 105–117.

[196] A. Fabiańska, R. Bogdanowicz, P. Zięba, T. Ossowski, M. Gnyba, J. Ryl, A. Zielinski, S. D. Janssens, K. Haenen, E. M. Siedlecka, *Electrochemical oxidation of sulphamerazine at boron-doped diamond electrodes: Influence of boron concentration,* Phys. Status Solidi A, 210, **2013**, 2040–2047.

[197] P. Gonon, E. Gheeraert, A. Deneuville, F. Fontaine, L. Abello, G. Lucazeau, *Characterization of heavily B-doped polycrystalline diamond films using Raman spectroscopy and electron spin resonance,* J. Appl. Phys., 78, **1995**, 7059–7062.

[198] D. S. Knight, W. B. White, *Characterization of diamond films by Raman spectroscopy,* J. Mater. Res., 4, **1989**, 385–393.

[199] J. Schwan, S. Ulrich, *Raman spectroscopy on amorphous carbon films,* J. Appl. Phys., 80, **1996**, 440–447.

[200] M. A. Tamor, W. C. Vassell, *Raman "fingerprinting" of amorphous carbon films,* J. Appl. Phys., 76, **1994**, 3823–3830.

[201] N. Mateescu, M. Ferry, W. Xu, J. M. Cairney, *Some factors affecting EBSD pattern quality of Ga^+ ion-milled face centred cubic metal surfaces,* Mater. Chem. Phys., 106, **2007**, 142–148.

[202] C. Kranz, *Recent advancements in nanoelectrodes and nanopipettes used in combined scanning electrochemical microscopy techniques,* The Analyst, 139, **2014**, 336–352.

[203] T. A. Ivandini, R. Sato, Y. Makide, A. Fujishima, Y. Einaga, *Pt-implanted boron-doped diamond electrodes for electrochemical oxidation of hydrogen peroxide,* Chem. Lett., 33, **2004**, 1330–1331.

[204] K. B. Holt, J. Hu, J. S. Foord, *Fabrication of boron-doped diamond ultramicroelectrodes for use in scanning electrochemical microscopy experiments,* Anal. Chem., 79, **2007**, 2556–2561.

[205] M. Geisler, T. Hugel, *Aging of hydrogenated and oxidized diamond,* Adv. Mater., 22, **2010**, 398–402.

[206] M. N. Holder, C. E. Gardner, J. V. Macpherson, P. R. Unwin, *Combined scanning electrochemical-atomic force microscopy (SECM-AFM): Simulation and experiment for flux-generation at un-insulated metal-coated probes,* J. Electroanal. Chem., 585, **2005**, 8–18.

[207] A. Eifert, *Focused ion beam based fabrication of combined AFM-SECM probes,* Diploma thesis, University of Ulm, **2010**.

[208] A. Eifert, B. Mizaikoff, C. Kranz, *Advanced fabrication process for combined atomic force-scanning electrochemical microscopy (AFM-SECM) probes,* Micron, 68, **2015**, 27–35.

[209] O. Sklyar, A. Kueng, C. Kranz, B. Mizaikoff, A. Lugstein, E. Bertagnolli, G. Wittstock, *Numerical simulation of scanning electrochemical microscopy experiments with frame-shaped integrated atomic force microscopy-SECM probes using the boundary element method,* Anal. Chem., 77, **2005**, 764–771.

[210] A. Davoodi, A. Farzadi, J. Pan, C. Leygraf, Y. Zhu, *Developing an AFM-Based SECM system; Instrumental setup, SECM simulation, characterization, and calibration,* J. Electrochem. Soc., 155, **2008**, C474–C485.

[211] K. Leonhardt, A. Avdic, A. Lugstein, I. Pobelov, T. Wandlowski, M. Wu, B. Gollas, G. Denuault, *Atomic force microscopy-scanning electrochemical microscopy: influence of tip geometry and insulation defects on diffusion controlled currents at conical electrodes,* Anal. Chem., 83, **2011**, 2971–2977.

[212] C. G. Zoski, B. Liu, A. J. Bard, *Scanning electrochemical microscopy: Theory and characterization of electrodes of finite conical geometry,* Anal. Chem., 76, **2004**, 3646–3654.

[213] J. Izquierdo, A. Eifert, R. M. Souto, C. Kranz, *Simultaneous pit generation and visualization of pit topography using combined atomic force-scanning electrochemical microscopy,* Electrochem. Commun., 51, **2015**, 15–18.

[214] J. Izquierdo, *Microelectrochemical investigation of corrosion processes: Metal passivation and corrosion inhibition by organic substances,* Ph.D. thesis, University of La Laguna, **2014**.

[215] J. Izquierdo, A. Eifert, C. Kranz, R. M. Souto, *In situ monitoring of pit nucleation and growth at an iron passive oxide layer by using combined atomic force and scanning electrochemical microscopy,* ChemElectroChem., **2015**, DOI: 10.1002/celc.201500100.

[216] G. T. Burstein, C. Liu, R. M. Souto, S. P. Vines, *Origins of pitting corrosion,* Corros. Eng., Sci. Technol., 39, **2004**, 25–30.

[217] M. M. Al-Abdallah, A. K. Maayta, M. A. Al-Qudah, N. A. F. Al-Rawashdeh, *Corrosion behavior of copper in chloride media,* Open Corr. J., 2, **2009**, 71–76.

[218] Y. Zhu, D. E. Williams, *Scanning electrochemical microscopic observation of a precursor state to pitting corrosion of stainless steel,* J. Electrochem. Soc., 144, **1997**, L43–L45.

[219] Y. Li, R. Hu, J. Wang, Y. Huang, C.-J. Lin, *Corrosion initiation of stainless steel in HCl solution studied using electrochemical noise and in-situ atomic force microscope,* Electrochim. Acta, 54, **2009**, 7134–7140.

[220] N. Casillas, S. J. Charlebois, W. H. Smyrl, H. S. White, *Scanning electrochemical microscopy of precursor sites for pitting corrosion on titanium,* J. Electrochem. Soc., 140, **1993**, L142–L145.

[221] E. Völker, C. G. Inchauspe, E. J. Calvo, *Scanning electrochemical microscopy measurement of ferrous ion fluxes during localized corrosion of steel,* Electrochem. Commun., 8, **2006**, 179–183.

[222] M. Reffass, R. Sabot, M. Jeannin, C. Berziou, P. Refait, *Effects of NO_2^- ions on localised corrosion of steel in $NaHCO_3$+NaCl electrolytes,* Electrochim. Acta, 52, **2007**, 7599–7606.

[223] D. Y. Lee, W. C. Kim, J. G. Kim, *Effect of nitrite concentration on the corrosion behaviour of carbon steel pipelines in synthetic tap water,* Corros. Sci., 64, **2012**, 105–114.

[224] J. Ufheil, F. M. Boldt, M. Börsch, K. Borgwarth, J. Heinze, *Microstructuring of solid-supported lipid layers using SAM pattern generation by scanning electrochemical microscopy and the chemical lens,* Bioelectrochemistry, 52, **2000**, 103–110.

[225] D. R. Lide, *CRC Handbook of Chemistry and Physics*, 92nd ed. CRC press, **2005**.

[226] G. Menestrina, *Ion transport and selectivity in model lipid membranes carrying incorporated cytolytic protein toxins,* J. Radioanal. Nucl. Chem., 163, **1992**, 169–180.

[227] L. K. Tamm, H. M. McConnell, *Supported phospholipid bilayers,* Biophys. J., 47, **1985**, 105–113.

[228] A. L. Plant, M. Brigham-Burke, E. C. Petrella, D. J. Oshannessy, *Phospholipid/alkanethiol bilayers for cell-surface receptor studies by surface plasmon resonance,* Anal. Biochem., 226, **1995**, 342–348.

[229] A. L. Plant, *Supported hybrid bilayer membranes as rugged cell membrane mimics,* Langmuir, 15, **1999**, 5128–5135.

[230] K. Kastl, M. Ross, V. Gerke, C. Steinem, *Kinetics and thermodynamics of annexin A1 binding to solid-supported membranes: A QCM study,* Biochemistry, 41, **2002**, 10087–10094.

[231] A. Schmid, R. Benz, I. Just, K. Aktories, *Interaction of Clostridium botulinum C2 toxin with lipid bilayer membranes. Formation of cation-selective channels and inhibition of channel function by chloroquine.,* J. Biol. Chem., 269, **1994**, 16706–16711.

[232] E. T. Castellana, P. S. Cremer, *Solid supported lipid bilayers: From biophysical studies to sensor design,* Surf. Sci. Rep., 61, **2006**, 429–444.

[233] K. Aktories, A. Wegner, *Mechanisms of the cytopathic action of actin-ADP-ribosylating toxins,* Mol. Microbiol., 6, **1992**, 2905–2908.

[234] X. Wang, B. Jin, X. Lin, *In-situ FTIR spectroelectrochemical study of dopamine at a glassy carbon electrode in a neutral solution,* Anal. Sci., 18, **2002**, 931–933.

[235] S. R. Ali, Y. Ma, R. R. Parajuli, Y. Balogun, W. Y.-C. Lai, H. He, *A nonoxidative sensor based on a self-doped polyaniline/carbon nanotube composite for sensitive and selective detection of the neurotransmitter dopamine,* Anal. Chem., 79, **2007**, 2583–2587.

[236] P. Diao, D. Jiang, X. Cui, D. Gu, R. Tong, B. Zhong, *Studies of structural disorder of self-assembled thiol monolayers on gold by cyclic voltammetry and ac impedance,* J. Electroanal. Chem., 464, **1999**, 61–67.

[237] C. Bachmeyer, R. Benz, H. Barth, K. Aktories, M. Gilbert, M. R. Popoff, *Interaction of Clostridium botulinum C2 toxin with lipid bilayer membranes and vero cells: Inhibition of channel function by chloroquine and related compounds in vitro and intoxification in vivo,* The FASEB Journal, 15, **2001**, 1658–1660.

[238] J. Weng, J. Xue, J. Wang, J. Ye, H. Cui, F. Sheu, Q. Zhang, *Gold-cluster sensors formed electrochemically at boron-doped-diamond electrodes: detection of dopamine in the presence of ascorbic acid and thiols,* Adv. Funct. Mater., 15, **2005**, 639–647.

[239] W. Smirnov, A. Kriele, R. Hoffmann, E. Sillero, J. Hees, O. A. Williams, N. Yang, C. Kranz, C. E. Nebel, *Diamond-modified AFM probes: From diamond nanowires to atomic force microscopy-integrated boron-doped diamond electrodes,* Anal. Chem., 83, **2011**, 4936–4941.

[240] J. Güldenhaupt, Y. Adigüzel, J. Kuhlmann, H. Waldmann, C. Kötting, K. Gerwert, *Secondary structure of lipidated Ras bound to a lipid bilayer: Secondary structure of Ras bound to lipid bilayer,* FEBS J., 275, **2008**, 5910–5918.

[241] M. Seul, M. J. Sammon, *Preparation of surfactant multilayer films on solid by deposition from organic solution,* Thin Solid Films, 185, **1990**, 287–305.

[242] Y. Barenholz, D. Gibbes, B. J. Litman, J. Goll, T. E. Thompson, F. D. Carlson, *A simple method for the preparation of homogeneous phospholipid vesicles,* Biochemistry, 16, **1977**, 2806–2810.

12. Appendix

12.1. List of chemicals and materials

- Hexaammineruthenium (III) chloride 98% (Sigma-Aldrich)
- Potassium hexacyanoferrate (II) trihydrat p.a. (Sigma-Aldrich)
- Potassium chloride p.a. (Sigma-Aldrich)
- Potassium hydroxide p.a. (Merck)
- Sodium chloride p.a. (Merck)
- Sodium nitrite p.a. (Merck)
- Polyoxyethylene sorbitan monolaurate (Tween 20) (Sigma-Aldrich)
- Sulfuric acid 98% (Merck)
- Hydrochloric acid 37% (Merck)
- Parylene-C (Specialty Coating Systems Inc.)
- Dopamine hydrochloride (Sigma-Aldrich)
- L(+)-ascorbic acid (Carl Roth GmbH)
- Phosphate buffered saline (PBS) solution w/o Ca, Mg; pH = 7.5 (Biochrom GmbH)
- 1-palmitoyl-2-oleoyl-sn-glycero-3-phophocholine (POPC) (Avanti Polar Lipids)
- 1-octadecanthiol (Merck)
- Chloroquine diphosphate salt (Sigma-Aldrich)
- Acheson DAG 1415 silver paint (Plano GmbH)
- EPO-TEK H2OE silver conductive epoxy (Plano GmbH)
- Dymax 9001-E-V3.1 (Dymax Europe GmbH)
- Insulation varnish RS 199-1480 (RS Components Ltd.)
- (Methylcyclopentadienyl)trimethylplatinum

12.2. List of equipment

- Quanta 3D FEG (FEI)
- Helios NanoLab 600 (FEI)
- CHI potentiostat 660A (CH Instruments)
- CHI potentiostat 660C (CH Instruments)
- CHI potentiostat 832A (CH Instruments)
- CHI potentiostat 842B (CH Instruments)
- CHI potentiostat 440 (CH Instruments)
- Ag/AgCl reference electrode (ALS Co., Ltd)
- Voltcraft plus VSP 2405 HE (Conrad Electronic)
- Alpha300R confocal Raman microscope (WiTec)
- AFM 5500 (Keysight Technologies)
- BioScope Catalyst AFM (Bruker Corp.)
- PDS 2010 Labcoter 2 (Specialty Coating Systems Inc.)
- Vortex Genie 2 (Scientific Industries)
- W140 Sonifier Cell Disruptor (Branson)
- Dymax UV lamp Blue Wave® (Dymax Corp.)

12.3. Construction blue prints

12.3.1. Rotatable AFM-chip holder for FIB milling

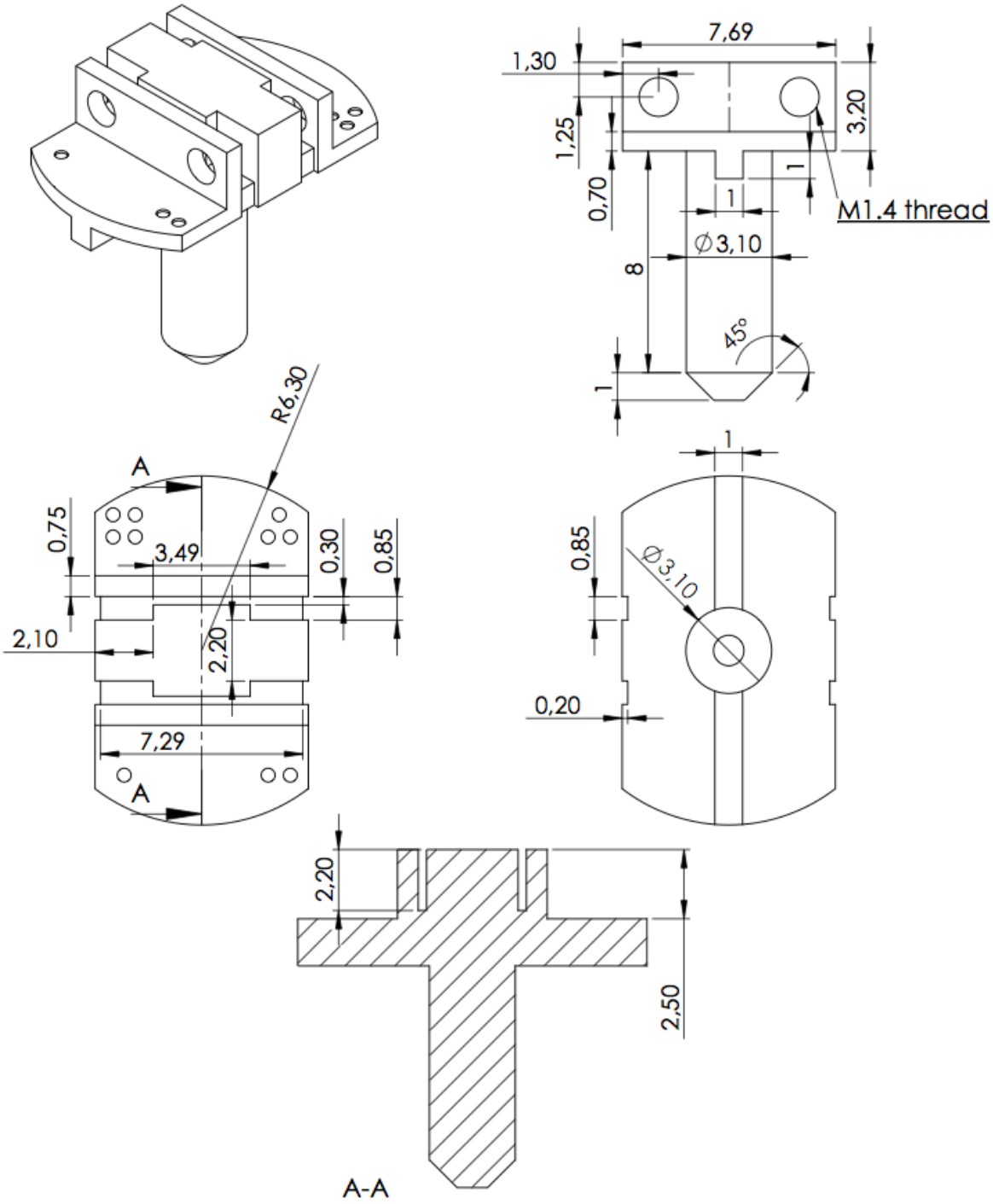

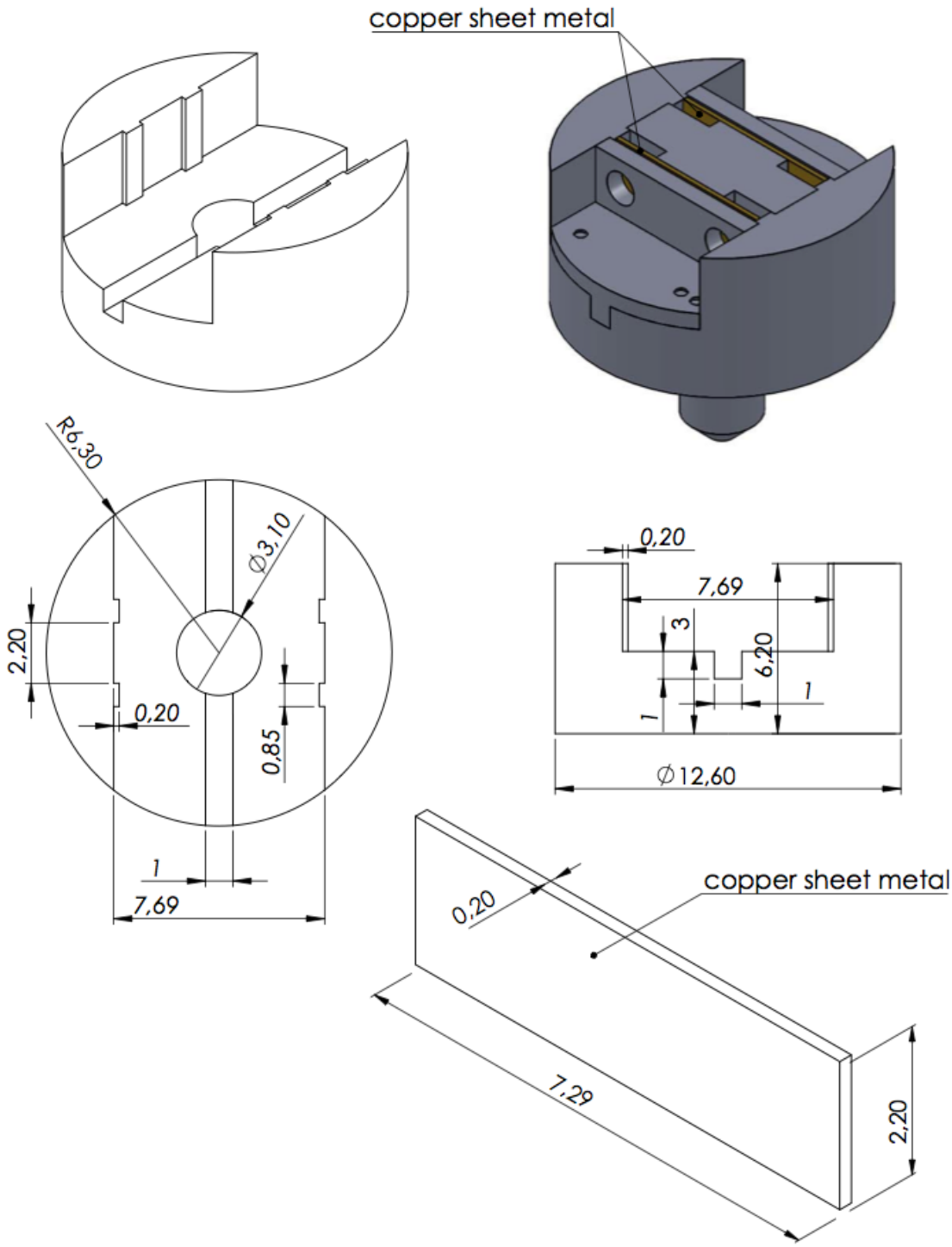
copper sheet metal
R6,30
Ø3,10
2,20
0,20
0,85
1
7,69
0,20
7,69
3
6,20
1
1
Ø12,60
copper sheet metal
0,20
7,29
2,20

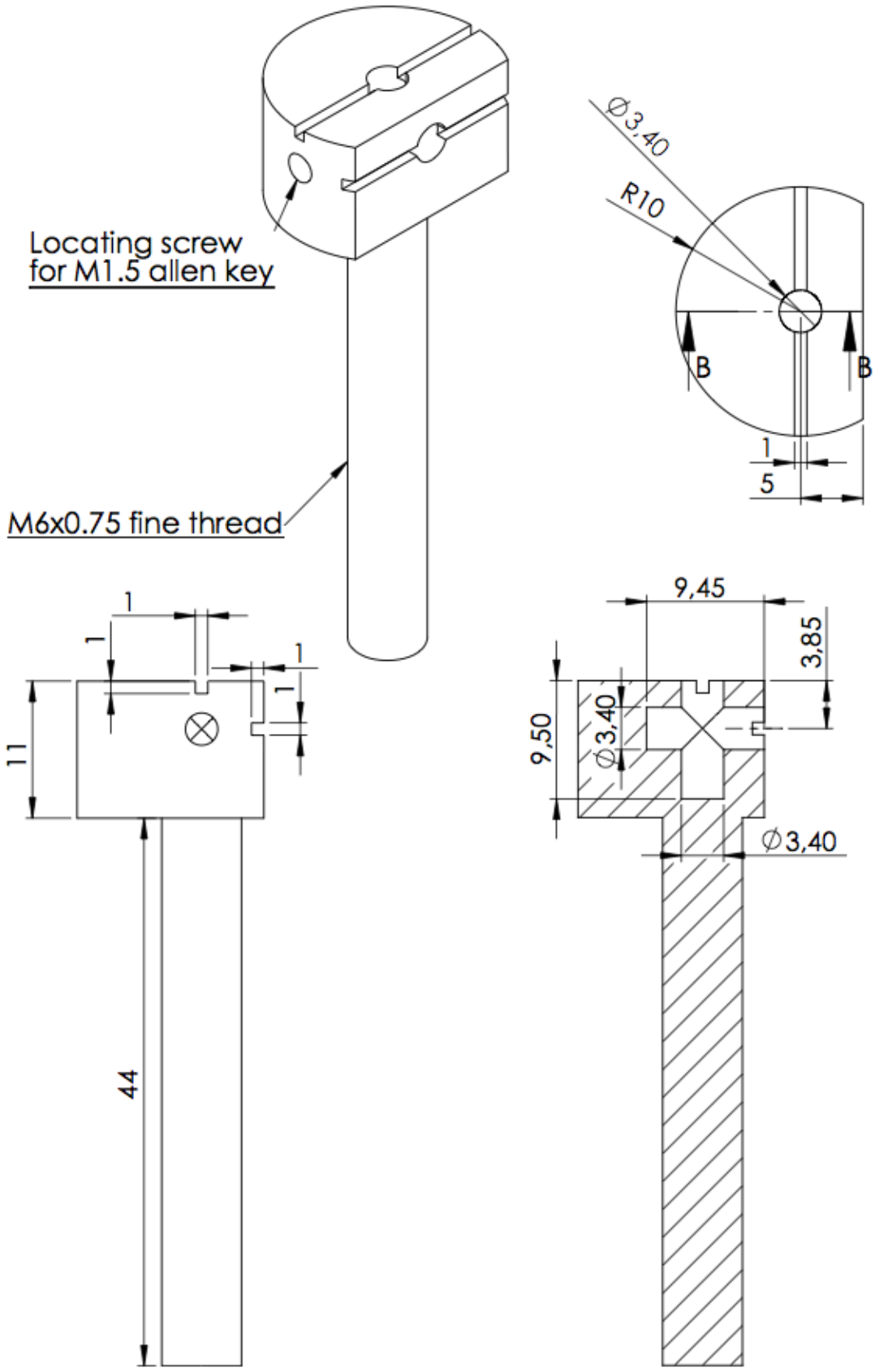
Locating screw
for M1.5 allen key
M6x0.75 fine thread
Ø3,40
R10
B
B
1
5
1
1
1
1
11
44
9,45
3,85
9,50
Ø3,40
Ø3,40

12.3.2. Cartridge for mounting combined AFM-SECM probes

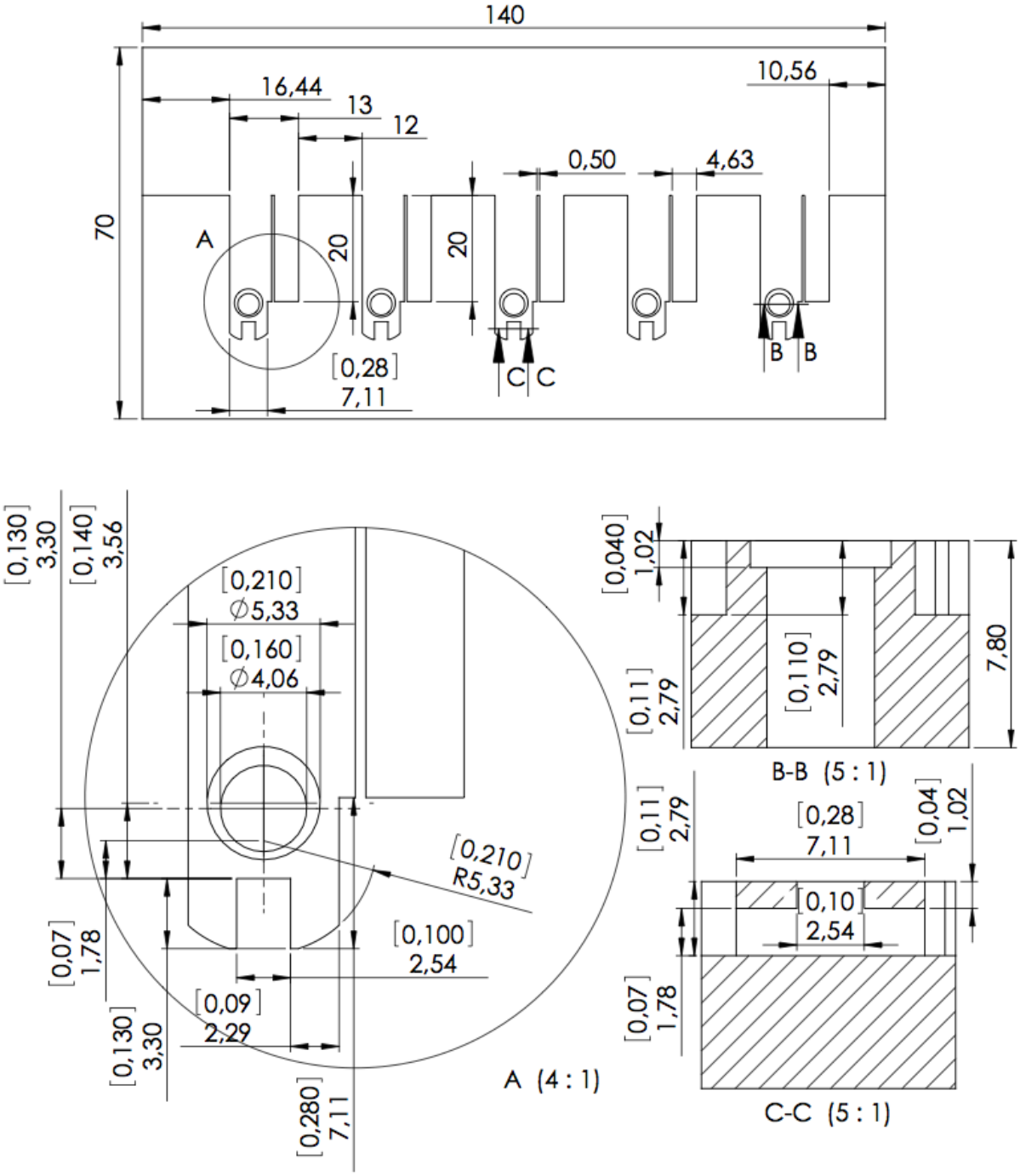

12.3.3. Glassware for hydrogen termination

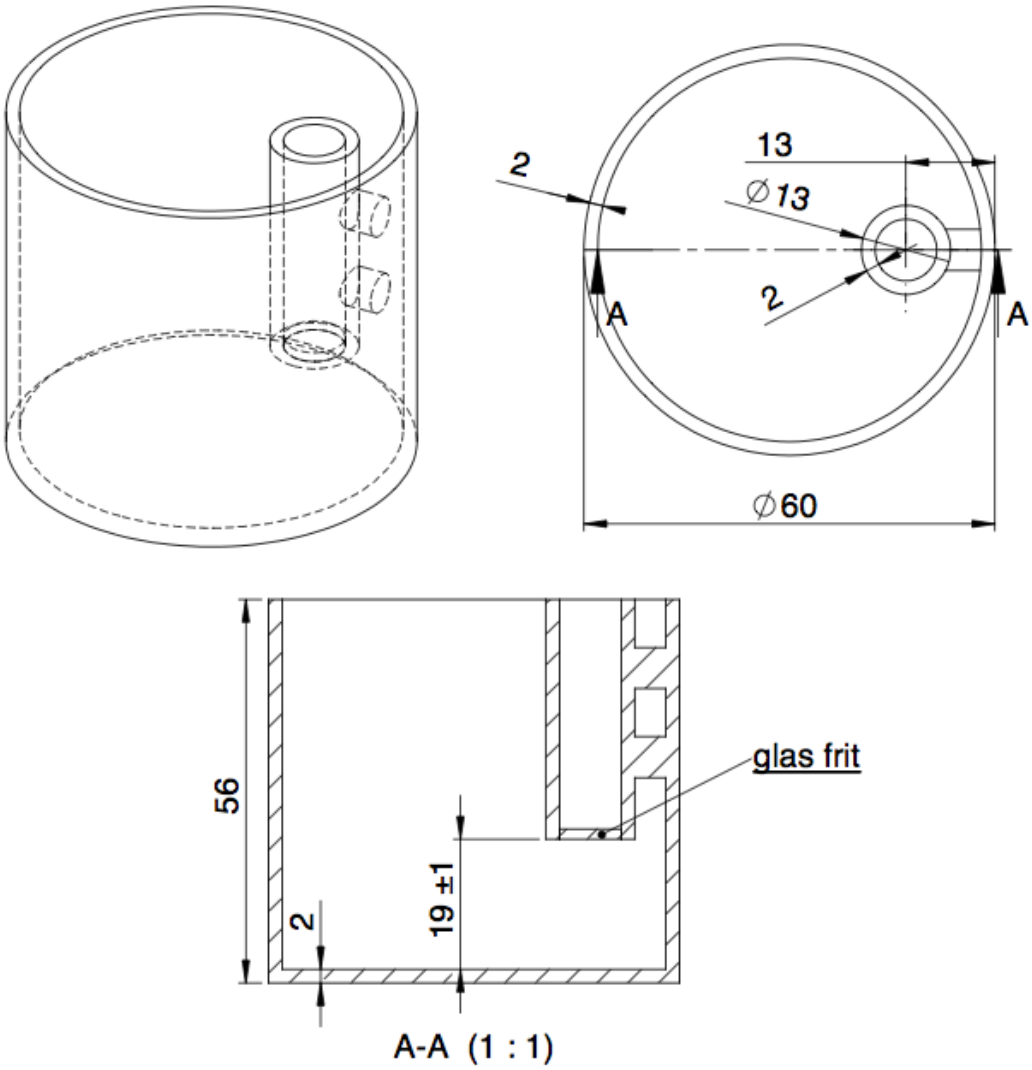

12.3.4. Shadow mask for gold modification of AFM probes

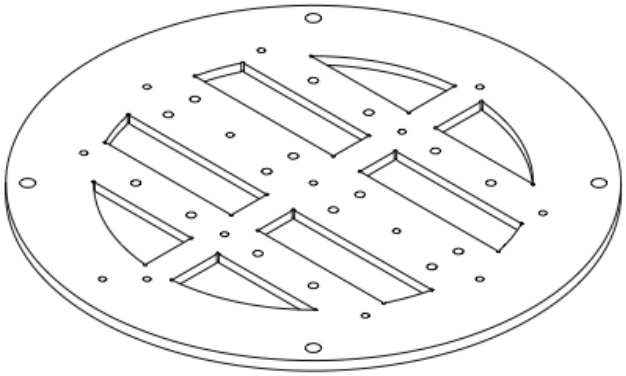

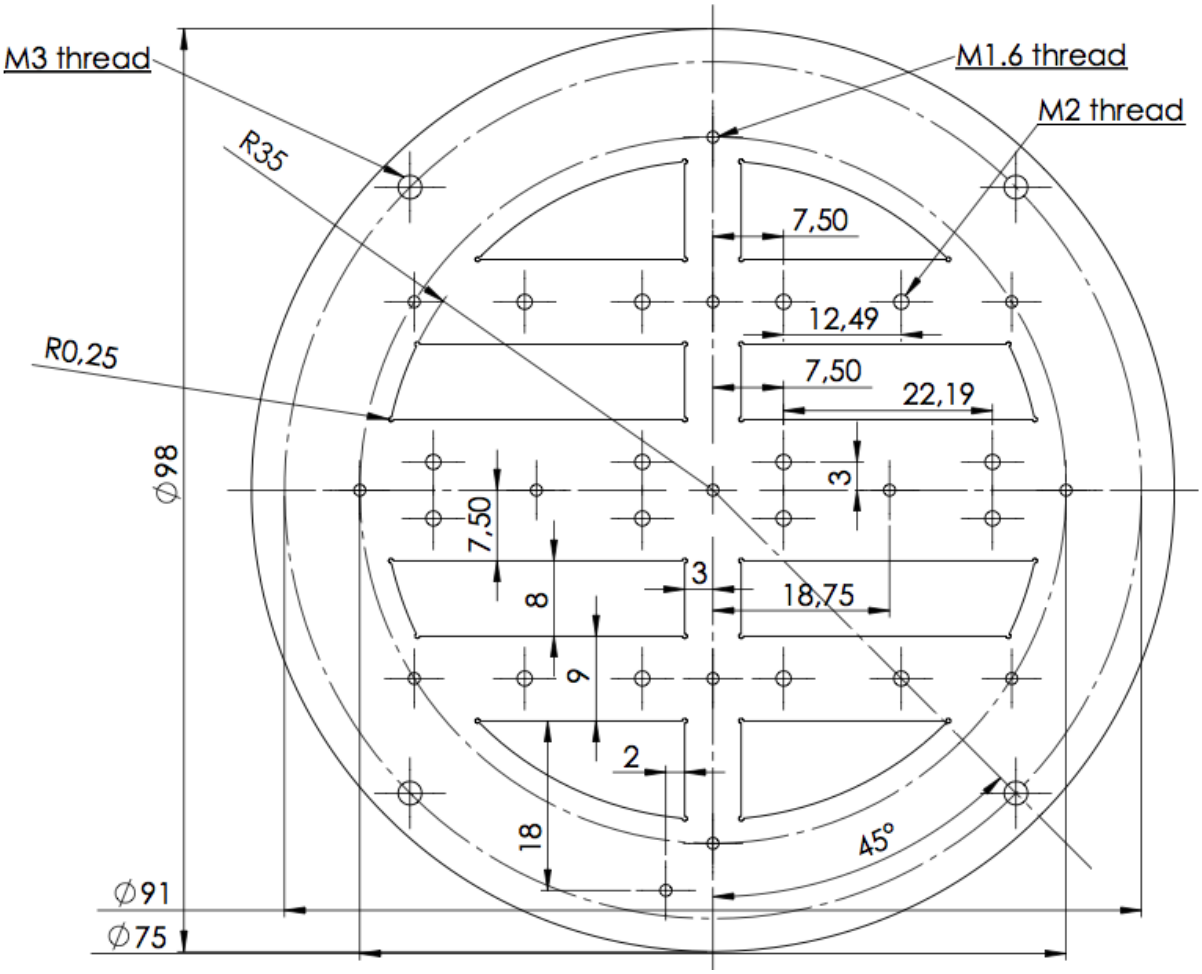

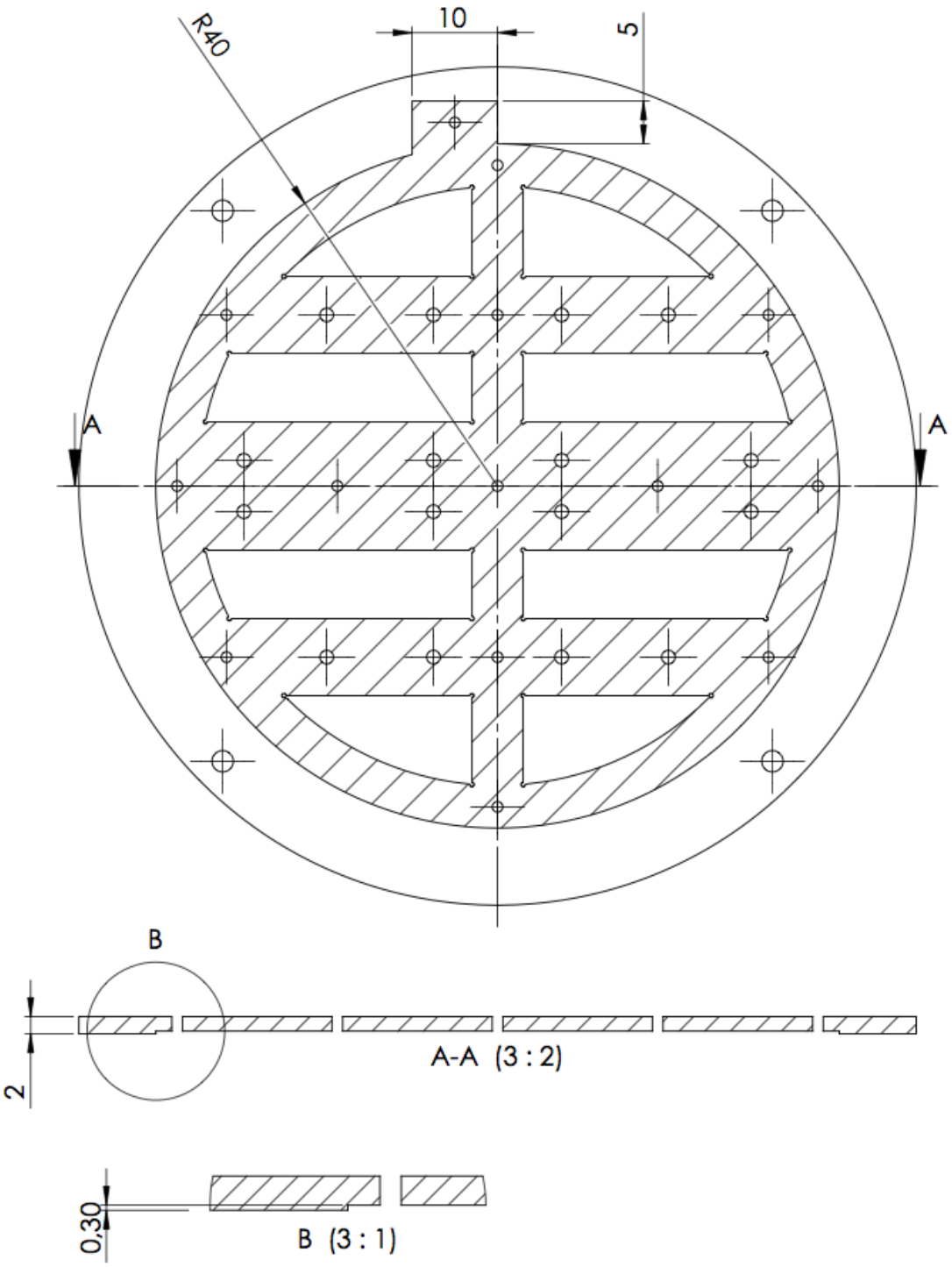
R40
10
5
A
A
B
2
A-A (3 : 2)
0,30
B (3 : 1)

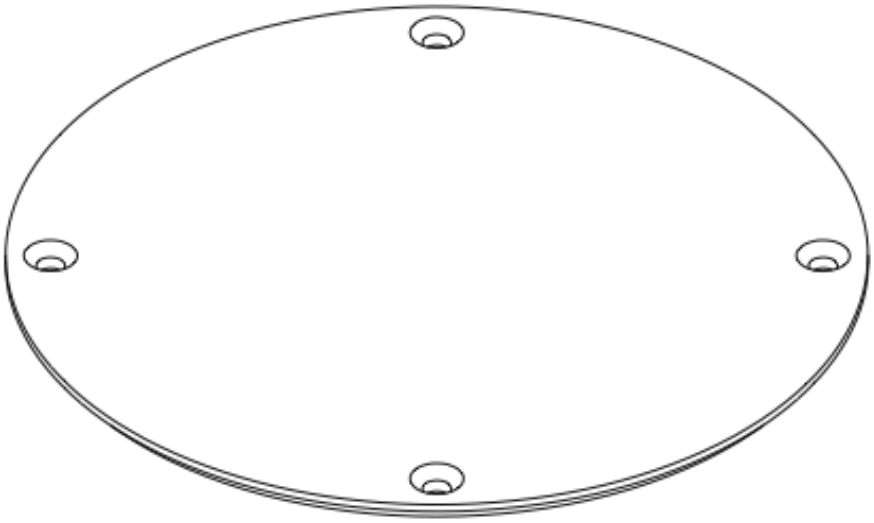

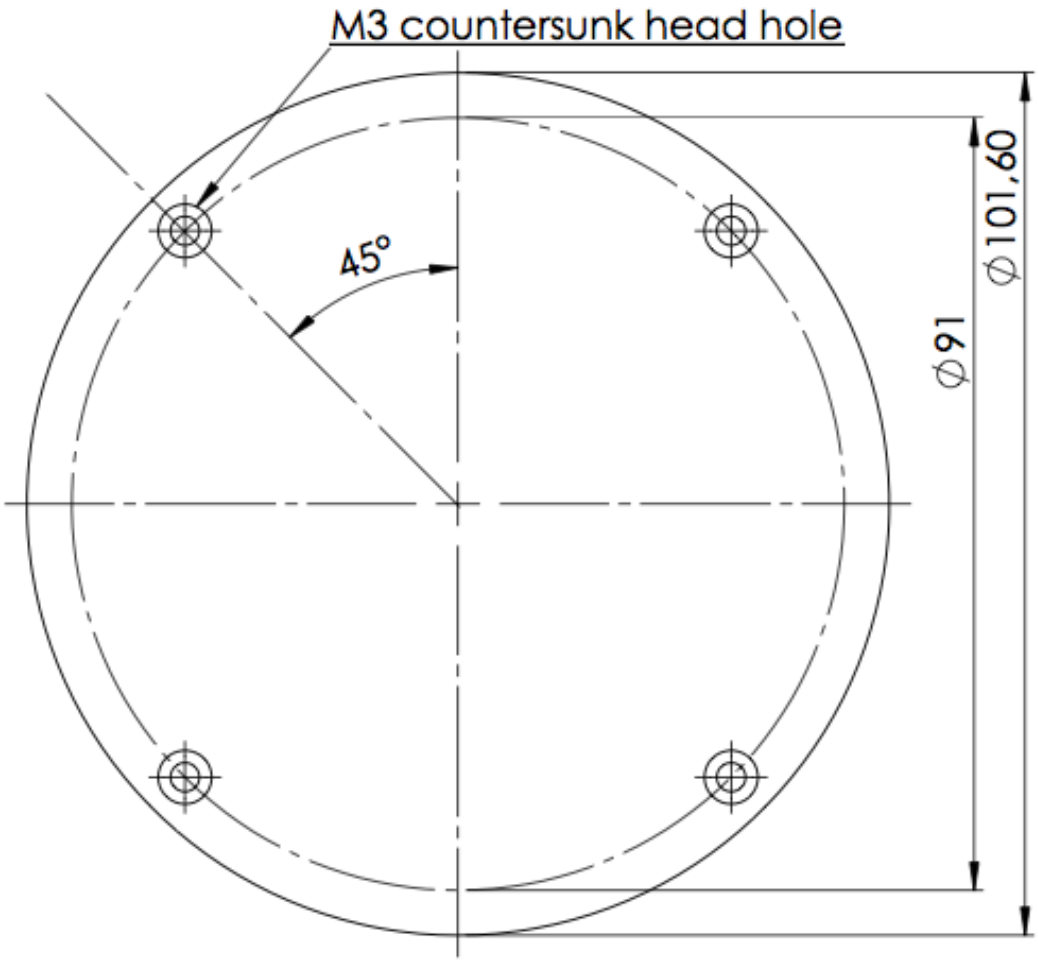
M3 countersunk head hole
45°
ϕ101,60
ϕ91

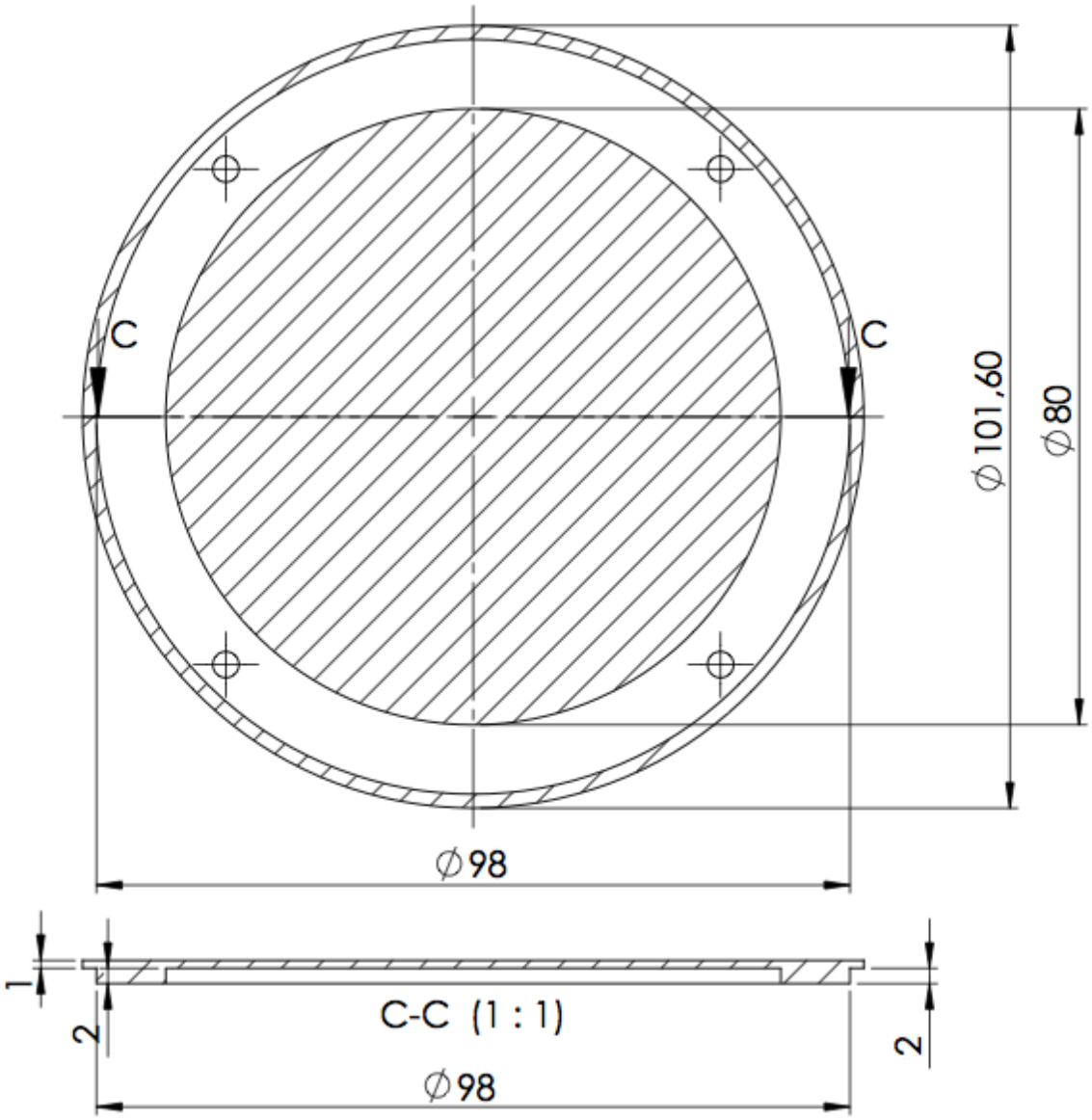
C
C
Ø101,60
Ø80
Ø98
1
2
C-C (1 : 1)
2
Ø98

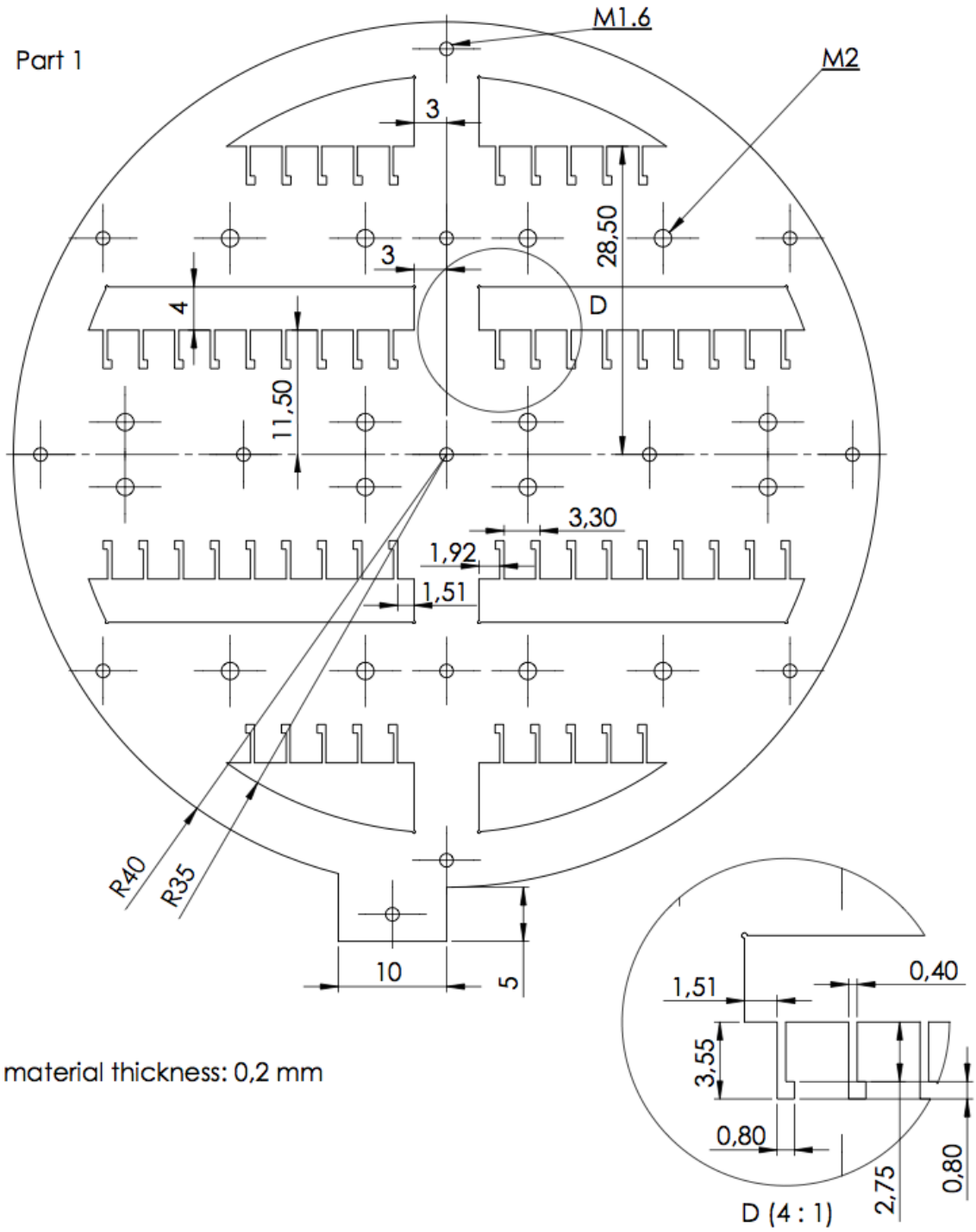

material thickness: 0,2 mm

Part 2

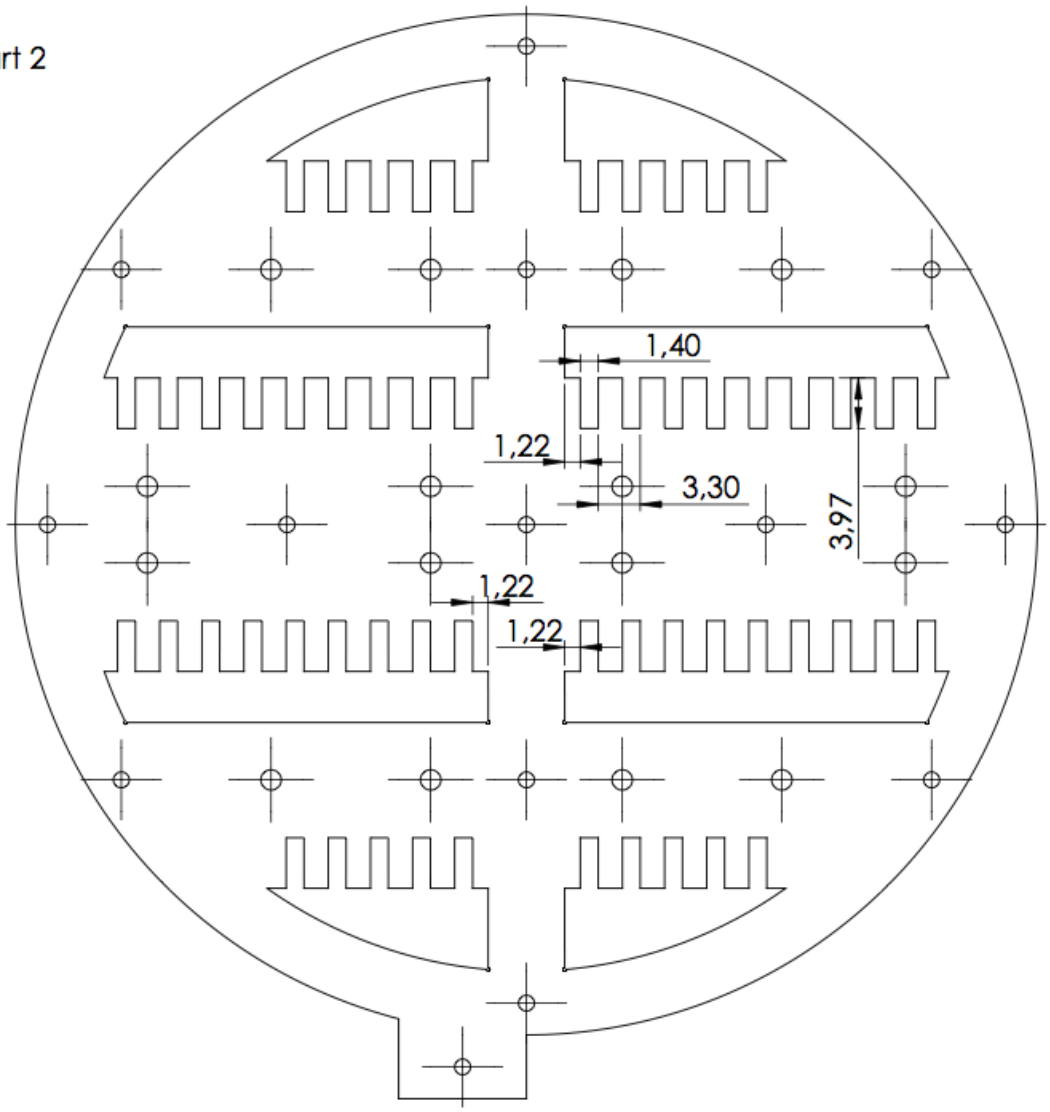

material thickness: 0.1 mm

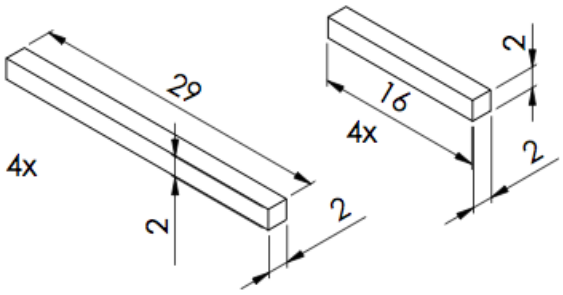

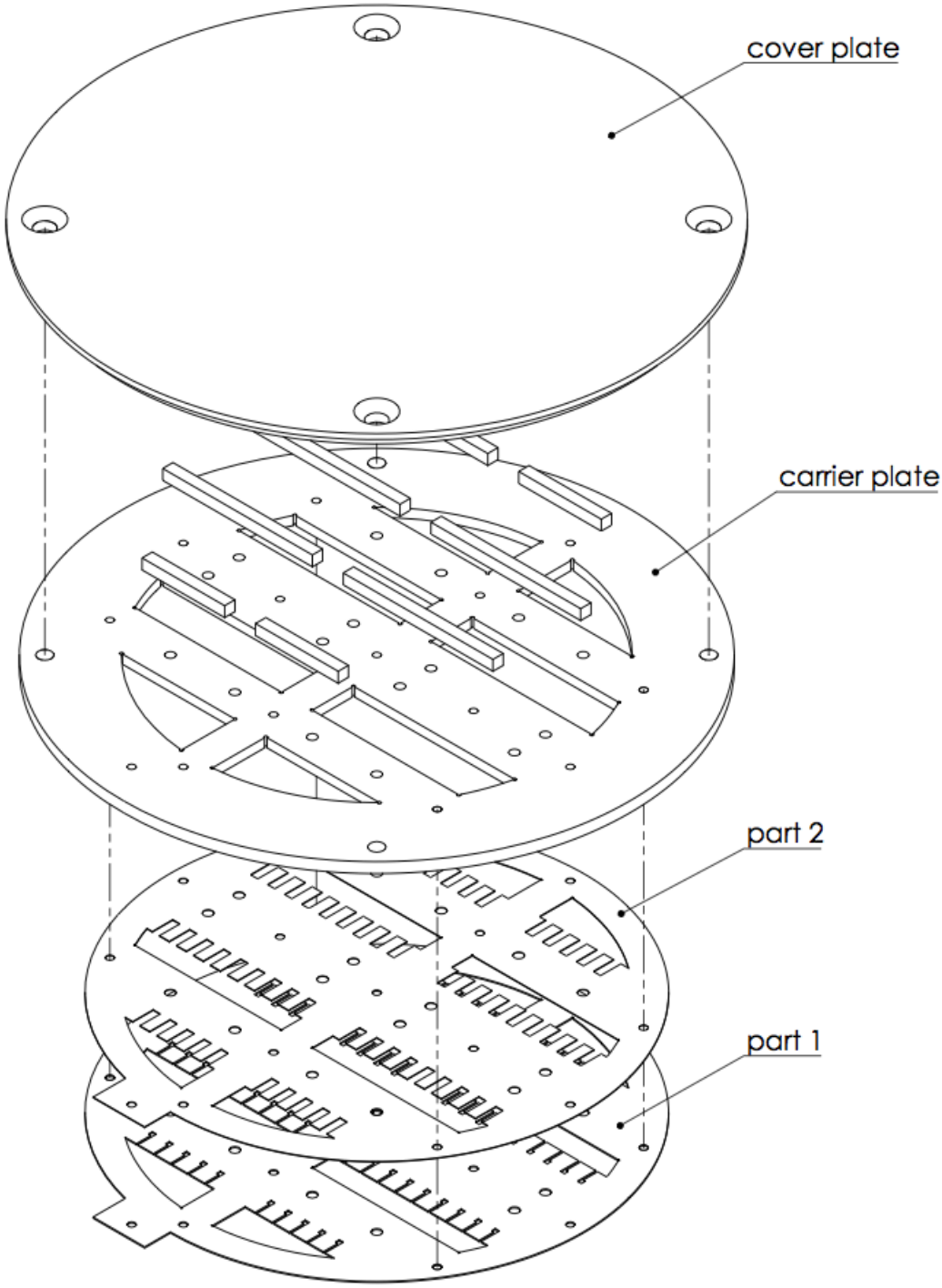
cover plate
carrier plate
part 2
part 1

Acknowledgements

First of all I want to express my deepest gratitude to PD Dr. Christine Kranz for providing the topic, her ongoing support and discussions during my Ph.D. thesis and helpful ideas and comments.

Also great thanks go to Prof. Dr. Boris Mizaikoff for the possibility to complete my Ph.D. thesis at the Institute of Analytical and Bioanalytical Chemistry at the University of Ulm.

Furthermore, I would like to thank PD Dr. Dr. Christoph Nebel, Waldemar Smirnov and Georgia Lewes-Malandrakis for their support during my Ph.D. thesis by supplying boron-doped diamond modified cantilevers and BDD test samples.

Also great thanks to Philipp Langenwalter, Björn Raupers and Hanno Schütz for their experimental support during their Bachelor thesis.

Great thanks go as well to Peter Knittel and Corinna Frey from the Institute of Analytical and Bioanalytical Chemistry at the University of Ulm, for their helpful support.

Special thanks also to Dr. Javier Izquierdo, University of La Laguna for the wonderful and constructive time during the cooperation.

Great thanks go also to Wolfgang Rapp and Martin Feierabend from the mechanical workshop of the University of Ulm as well as to Reinhard Liske and Edgar Zeilmeir from the electronic workshop of the University of Ulm for their helpful support.

I would also like to acknowledge Shijie Wu, Gerald Kada, Matthias Fenner and Michael Hippler from Keysight Technologies.

Great thanks go also to all my colleagues who have supported me throughout the years at IABC:
Charlotte Steinbach, Andreas Hartmann, Sandra Gienger, Gregor Neusser, Andreas Wilk, Margit Bunz, Bärbel Abt, Angelika Holzinger, Cornelia Weber, Florian Meier, Stefan Eppler, Daniel Neubauer, Bettina Pluhar, Nadine Feichtmeier, Jessica Huber, Katharina Wöhrle and Roland Schindl.

Curriculum Vitae

Persönliche Daten

Name:	Eifert
Vorname:	Alexander
Geburtsdatum:	22.12.1985
Geburtsort:	Ulm

Schul- und Hochschulausbildung

01/2011-10/2015	Promotion an der Universität Ulm Institut für Analytische und Bioanalytische Chemie unter der Anleitung von PD. Dr. Christine Kranz. Gesamtbewertung der Dissertation: summa cum laude.
11/2010	Diplom im Fachbereich Chemie; Diplomnote: 1,1.
	Diplomarbeit an der Universität Ulm Institut für Analytische und Bioanalytische Chemie unter der Leitung von Prof. Dr. Boris Mizaikoff Thema: “Focused ion beam based fabrication of combined AFM-SECM probes”.
10/2005-11/2010	Chemie Studium an der Universität Ulm mit Wahlfach Analytische Chemie
09/1996-06/2005	Besuch des Robert-Bosch Gymnasiums Langenau; Allgemeine Hochschulreife
08/1992-07/1996	Grundschule Rammingen / Asselfingen

Lehrtätigkeiten

01/2011-02/2015	Akademischer Mitarbeiter am Institut für Analytische und Bioanalytische Chemie; Betreuung von Praktika und Seminaren im Bereich der analytischen Chemie für Studierende der Studiengänge Chemie und Biologie; Betreuung von Bachelorarbeiten im Fach Analytische Chemie.
11/2007-09/2010	Studentische Hilfskraft an der Universität Ulm; Betreuung von Praktika und Seminaren im Studiengang Chemie.

Weiterbildungen

11/2010	Sachkunde nach §5 der Chemikalien-Verbotsverordnung

Sprachkenntnisse

- Deutsch (Muttersprache)
- Englisch (fließend in Wort und Schrift)
- Französisch (Grundkenntnisse)

EDV-Kenntnisse

- Windows XP / 7 / 8 // Mac OS X
- MS Office (Word, Excel, PowerPoint)
- COMSOL Multiphysics 4.2a
- FEI DualBeam Steuersoftware xT-Server 3.8.x
- FEI Nanobuilder
- SolidWorks 2014
- CorelDRAW 2012
- Adobe Photoshop CS6

Liste der Veröffentlichungen

Peer-reviewed Publikationen

Alexander Eifert, Waldemar Smirnov, Stefan Frittmann, Christoph E. Nebel, Boris Mizaikoff, Christine Kranz; Atomic force microscopy probes with integrated boron-doped diamond electrodes: Fabrication and application, Electrochemistry Communications, 2012, 25, 30-34.

Thomas Schädle, **Alexander Eifert**, Christine Kranz, Yosef Raichlin, Abraham Katzir, Boris Mizaikoff; Mid-infrared planar silver halide waveguides with integrated grating couplers, Applied Spectroscopy, 2013, 67, 1057-1063.

Alexander Eifert, Philipp Langenwalter, Jonas Higl, Mika Lindén, Christoph E. Nebel, Boris Mizaikoff, Christine Kranz; Focused ion beam (FIB)-induced changes in the electrochemical behavior of boron-doped diamond (BDD) electrodes, Electrochimica Acta, 2014, 130, 418-425.

Alexander Eifert, Christine Kranz; Hyphenating atomic force microscopy, Analytical Chemistry, 2014, 86, 5190-5200.

Alexander Eifert, Boris Mizaikoff, Christine Kranz; An advanced fabrication process for combined atomic force-scanning electrochemical microscopy (AFM-SECM) probes, Micron, 2015, 68, 27-35.

Javier Izquierdo, **Alexander Eifert**, Ricardo M. Souto, Christine Kranz; Simultaneous pit generation and visualization of pit topography using combined atomic force-scanning electrochemical microscopy, Electrochemistry Communications, 2015, 51, 15-18.

Javier Izquierdo, **Alexander Eifert**, Christine Kranz, Ricardo M. Souto; In situ monitoring of pit nucleation and growth at an iron passive oxide layer by using combined atomic force and scanning electrochemical microscopy; ChemElectroChem, 2015, DOI: 10.1002/celc.201500100.

Wissenschaftliche Vorträge

Christine Kranz, Jong-Seok Moon, **Alexander Eifert**, Boris Mizaikoff; Nanoelectrochemistry at the AFM tip, Electrochemistry 2010, 13. - 15. Sep. 2010, Bochum, Deutschland.

Alexander Eifert, Waldemar Smirnov, Boris Mizaikoff, Christoph E. Nebel, Christine Kranz; Focused ion beam (FIB)-assisted fabrication of combined boron-doped diamond AFM-SECM probes: Characterization and Application, MRS Fall Meeting 2011, 28. Nov. - 02. Dez. 2011, Boston, MA, USA.

Alexander Eifert, Waldemar Smirnov, Christoph E. Nebel, Christine Kranz; Focused ion beam (FIB)-assisted fabrication of combined boron-doped diamond AFM-SECM probes: FIB influences, characterization and application, Electrochemistry 2012, 17. - 19. Sep. 2012, München, Deutschland.

Christine Kranz, **Alexander Eifert**, Daniel Neubauer; Boron-doped diamond electrodes: From spectroelectrochemistry to AFM tip-integrated electrodes, 65th Annual Meeting of the International Society of Electrochemistry, 31. Aug. - 05. Sep. 2014, Lausanne, Schweiz.

Javier Izquierdo Pérez, **Alexander Eifert**, Christine Kranz, Ricardo Manuel Souto; Local pit corrosion induction on iron surfaces using combined AFM-SECM, 65th Annual Meeting of the International Society of Electrochemistry, 31. Aug. - 05. Sep. 2014, Lausanne, Schweiz.

Alexander Eifert, Daniel Neubauer, Boris Mizaikoff, Christine Kranz; Boron-doped diamond electrodes: From AFM tip-integrated electrodes to mid-IR spectroelectrochemistry, International Workshop of Novel Carbon, 20. - 22. Okt. 2014, Enshi, China.

Alexander Eifert, Christine Kranz; Hyphenated atomic force-scanning electrochemical microscopy, Keysight AFM Users' Meeting 2014, 04 Nov. 2014, Essen, Deutschland.

Posterpräsentationen

Alexander Eifert, Boris Mizaikoff, Christine Kranz; Focused ion beam (FIB)-assisted fabrication of combined AFM-SECM probes: Improved fabrication process using advanced pattering software, 6. ASAC Jugendanalytikerforum, 11. - 12. Jun. 2010, Wien, Österreich.

Alexander Eifert, Boris Mizaikoff, Christine Kranz; Focused ion beam (FIB)-assisted fabrication of combined AFM-SECM probes: An improved fabrication process with milling from top, EPFL Summer School, 21. - 23. Jun. 2011, Lausanne, Schweiz.

Alexander Eifert, Björn Raupers, Waldemar Smirnov, Christoph Nebel, Boris Mizaikoff, Christine Kranz; The influence of focused ion beam (FIB)-milling on the electrochemical behavior of boron-doped diamond (BDD), Forschungstag 2011 – Lebenswissenschaften, 29. Jun. 2011, Heidelberg, Deutschland.

Alexander Eifert, Waldemar Smirnov, Georgia Lewes-Malandrakis, Christoph Nebel, Christine Kranz; Combined boron-doped diamond (BDD) AFM-SECM probes for the detection of biomolecules, 7. SECM Workshop, 17. - 21. Feb. 2013, Ein Gedi, Israel.

Alexander Eifert, Shije Wu, Boris Mizaikoff, Christine Kranz; Integration of scanning electrochemical microscopy (SECM) into a commercially available AFM system: Advantages and Applications, XVI. Annual Linz Winter Workshop, 31. Jan. - 03. Feb. 2014, Linz, Österreich.

Alexander Eifert, Philipp Langenwalter, Jonas Higl, Mika Lindén, Christoph E. Nebel, Boris Mizaikoff, Christine Kranz; Focused ion beam (FIB)-induced changes in the electrochemical behavior of boron-doped diamond (BDD) electrodes, IMC 2014, 07. - 12. Sep. 2014, Prag, Tschechische Republik.

Eidesstattliche Erklärung

Hiermit versichere ich, dass ich die vorliegende Dissertation selbstständig und durch eigene Recherche angefertigt habe. Alle Stellen die wörtlich oder sinngemäß aus Veröffentlichungen entnommen wurden, sind als solche gekennzeichnet. Die verwendete Literatur ist im Quellverzeichnis angegeben.

Ulm, den 13.04.2015 .....

(Alexander Eifert)